

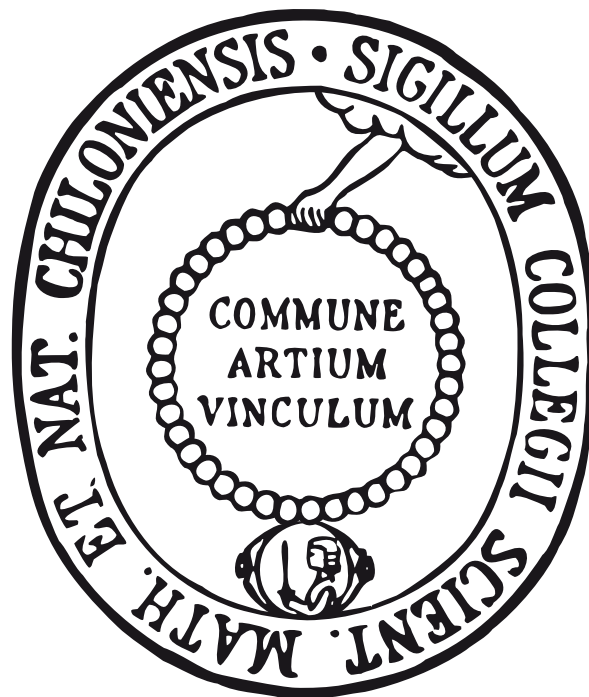
Peruvian Oxygen Minimum Zone dynamics during the last 18 000 years

Kumulative Dissertation

zur Erlangung des Doktorgrades

der Mathematisch-Naturwissenschaftlichen Fakultät

der Christian-Albrechts Universität zu Kiel



Vorgelegt von

Elfi Mollier-Vogel

Kiel 2012

Peruvian Oxygen Minimum Zone dynamics during the last 18 000 years

Kumulative Dissertation

zur Erlangung des Doktorgrades

der Mathematisch-Naturwissenschaftlichen Fakultät

der Christian-Universität zu Kiel

Vorgelegt von

Elfi Mollier-Vogel

Kiel 2012

1. Gutachter und Betreuer: Prof. Dr. Ralph R. Schneider

2. Gutachter: Dr. Philippe Martinez

Eingereicht am: 21.06.2012

Datum der Disputation: 27.07.2012

Zum Druck genehmigt: 12.12.2012

Der Dekan: Prof. Dr. Wolfgang J. Duschl

EIDESSTATTLICHE ERKLÄRUNG

Hiermit erkläre ich an Eides statt, dass die vorliegende Dissertation mit dem Titel «Peruvian Oxygen Minimum Zone dynamics during the last 18 000 years», abgesehen von der Beratung durch meine akademischen Lehrer, in Inhalt und Form meine eigene Arbeit darstellt. Ferner habe ich weder diese noch eine ähnliche Arbeit an einer anderen Hochschule im Rahmen eines Prüfungsverfahrens vorgelegt.

Kiel, den 21.06.2012

E. Mollier-Vogel

Table of contents

ABSTRACT.....	II
ZUSAMMENFASSUNG	15
ACKNOWLEDGEMENTS.....	19
LIST OF ABBREVIATIONS.....	23
LIST OF FIGURES.....	25
LIST OF TABLES.....	27
CHAPTER I. INTRODUCTION	29
I-1. MOTIVATION FOR THIS STUDY	29
I-2. OUTLINE.....	31
I-3. STUDY AREA.....	32
<i>I-3.1. Atmospheric circulation and variability of the system.....</i>	<i>33</i>
I-1.3.1. The ITCZ	33
I-2.3.1. The Walker circulation.....	35
<i>I-3.2. Regional oceanic circulation.....</i>	<i>36</i>
<i>I-3.3. Upwelling and productivity</i>	<i>39</i>
<i>I-3.4. Nutrient cycles and OMZ.....</i>	<i>39</i>
<i>I-3.5. Past variability of the ETSP</i>	<i>41</i>
CHAPTER II. PALEOPROXIES	45
II-1. PALEOPRODUCTIVITY.....	46
II-2. TERRIGENOUS INPUT.....	47
II-3. ALKENONE/SST	48
II-4. NITROGEN ISOTOPES.....	49
II-5. PALEO-STUDIES OF THE REGION.....	50
CHAPTER III. METHODOLOGY.....	55
III-1. SAMPLING AREA	55
III-2. METHODS	57
<i>III-2.1. Analysis of export production-related proxies.....</i>	<i>57</i>
<i>III-2.2. XRF measurements.....</i>	<i>58</i>
<i>III-2.3. Alkenone analyses</i>	<i>58</i>
<i>III-2.4. Nitrogen isotope analyses</i>	<i>60</i>
<i>III-2.5. Radiocarbon and core chronology</i>	<i>61</i>

CHAPTER IV. ALKENONES IN SURFACE SEDIMENTS	63
CHAPTER V. NITROGEN ISOTOPE GRADIENTS OFF PERU AND ECUADOR RELATED TO UPWELLING, PRODUCTIVITY, NUTRIENT UPTAKE AND OXYGEN DEFICIENCY	69
V-1. ABSTRACT.....	69
V-2. INTRODUCTION.....	70
V-3. REGIONAL SETTING.....	72
V-4. SAMPLING AND ANALYTICAL METHODS.....	74
V-5. RESULTS.....	76
<i>V-5.1. Surface sediments: $\delta^{15}N_{sed}$ and export production proxies.....</i>	<i>76</i>
<i>V-5.2. Water column oxygen, nitrate, and $\delta^{15}N$ distribution.....</i>	<i>79</i>
V-6. DISCUSSION.....	80
<i>V-6.1. Possible sedimentary influences on $\delta^{15}N_{sed}$.....</i>	<i>80</i>
<i>V-6.2. Influence of N-loss processes and nutrient uptake in the water column on $\delta^{15}N_{sed}$ gradients</i>	<i>82</i>
<i>V-6.3. Comparison to N. Chile.....</i>	<i>90</i>
V-7. CONCLUSIONS.....	90
V-8. ACKNOWLEDGEMENTS.....	91
CHAPTER VI. NITROGEN ISOTOPE EVOLUTION THROUGH WATER MASS TRANSPORT ALONG THE EASTERN SOUTH AMERICAN MARGIN	93
VI-1. INTRODUCTION.....	93
VI-2. OCEANOGRAPHY ALONG THE WESTERN SOUTH AMERICAN COAST.....	93
VI-3. RESULTS AND DISCUSSION.....	97
CHAPTER VII. MID-HOLOCENE COLLAPSE OF THE PERUVIAN OXYGEN MINIMUM ZONE.....	101
VII-1. ABSTRACT.....	101
VII-2. INTRODUCTION.....	102
VII-3. MATERIAL AND METHODS.....	104
<i>VII-3.1. Core locations.....</i>	<i>104</i>
<i>VII-3.2. Geochemical analyses.....</i>	<i>105</i>
<i>VII-3.3. Age Model.....</i>	<i>109</i>
VII-4. RESULTS AND DISCUSSION.....	111
VII-5. CONCLUSIONS.....	121
VII-6. ACKNOWLEDGEMENTS.....	121

CHAPTER VIII. RAINFALL RESPONSE TO ORBITAL AND MILLENNIAL FORCING IN NORTHERN PERU OVER THE LAST 18 KA	123
VIII-1. ABSTRACT	123
VIII-2. INTRODUCTION	123
VIII-3. REGIONAL SETTINGS	127
VIII-4. MATERIAL AND METHODS	128
VIII-5. RESULTS	131
<i>VIII-5.1. XRF data.....</i>	<i>131</i>
<i>VIII-5.2. Variations in terrigenous input</i>	<i>133</i>
VIII-6. DISCUSSION.....	134
<i>VIII-6.1. Sedimentary patterns</i>	<i>134</i>
<i>VIII-6.2. Review of precipitation changes around equatorial South America during the last 18 ka</i>	<i>135</i>
VIII-7. CONCLUSIONS	138
VIII-8. ACKNOWLEDGEMENTS.....	139
CHAPTER IX. GENERAL CONCLUSIONS	141
IX-1. CONCLUSIONS	141
IX-2. OUTLOOK	143
BIBLIOGRAPHY	145
TABLES	159

Abstract

The Eastern Tropical South Pacific (ETSP) subsurface waters are affected by one of the strongest and shallowest oxygen minimum zone (OMZ) in the World Ocean, which results from the interplay of high regional primary production (PP) and sluggish subsurface ventilation. The recent expansion of the tropical OMZs suggests that these zones are very vulnerable to anthropogenic climate change, but their sensitivity to changes in PP and in nutrient cycling still remains poorly understood and under debate. We present a core-top compilation of nitrogen isotopes ($\delta^{15}\text{N}$) measured on a collection of surface sediment retrieved along the Ecuadorian and Peruvian coasts and compare it to the upper 200 m of water column samples to identify which processes may ultimately influence downcore (i.e. past) changes in the isotopic signature of bulk nitrogen. We overall find that in O_2 -depleted subsurface waters, microbial-mediated NO_3^- -loss to N_2 leaves a ^{15}N -enriched signal in underlying sediments characteristic of water masses affected by denitrification and/or anammox, so called nitrogen-loss (N-loss) processes. We find that phytoplankton nitrate (NO_3^-) uptake in surface waters contributes significantly to the sedimentary signal within the high nutrient, low chlorophyll (HNLC) areas of the studied region. We also detect regional differences in the water column and sedimentary signatures of nitrogen isotopes with respect to contrasting oxygenation and PP status. In the North, between 1°N - 10°S , subsurface O_2 concentrations are too high to allow N-loss processes to take place and account for nitrogen isotopic changes, keeping $\delta^{15}\text{N}_{\text{NO}_3^-}$ values relatively low in the subsurface waters. In contrast, $\delta^{15}\text{N}_{\text{NO}_3^-}$ values increase toward the surface due to partial nitrate utilization in the photic zone. However, an incomplete utilization of NO_3^- probably triggers $\delta^{15}\text{N}_{\text{sed}}$ values being consistently lower than the $\delta^{15}\text{N}$ of the upwelled NO_3^- . Further south, between $10 - 15^\circ\text{S}$ within the perennial upwelling region, HNLC conditions are relaxed, resulting in more intense biological production and its associated phytoplankton uptake of surface NO_3^- . In addition, subsurface O_2 concentration decreases to levels sufficient for N-loss by denitrification and/or anammox to take place, resulting in elevated subsurface $\delta^{15}\text{N}_{\text{NO}_3^-}$ values in waters feeding the coastal upwelling. Various sedimentary proxies for productivity reflect increasingly higher PP southward, and echo a parallel north-south $\delta^{15}\text{N}_{\text{sed}}$ gradient reflecting an increasing subsurface N-loss southwards. In addition, the $\delta^{15}\text{N}$ values measured on core-top sediments and on water column samples increase cross-shelf toward the coast, and highlight an

intensification of coastal upwelling along the shoreline bringing the oxycline and nitracline closer to the surface. Overall, our mapping effort suggests that the degree of N-loss influencing subsurface $\delta^{15}\text{N}_{\text{NO}_3^-}$ values, the degree of upper ocean stratification, and the degree of near-surface nitrate utilization should all be considered for the interpretation of downcore $\delta^{15}\text{N}_{\text{sed}}$ records in an attempt of reconstructing the spatio-temporal variability of the Peruvian OMZ.

Following on this, past changes in the extent of the OMZ were reconstructed on the basis of 4 piston cores selected from regions located outside, at the rim and within the core of the modern OMZ along a latitudinal transect (from 3.5 to 15°S). The $\delta^{15}\text{N}$ values measured on each core cover the entire Holocene and the last deglaciation period. In the northern part along the Ecuadorian margin, the $\delta^{15}\text{N}$ values are low, ranging from 4 to 6‰, with an amplitude of $\sim 1\text{‰}$ during the Holocene and the last deglaciation period. This is likely due to the absence of OMZ conditions within this area. In contrast, the southern cores show values similar to modern core-tops data and a large amplitude ($\sim 4\text{‰}$) over the past, that we interpret as resulting from variable N-loss processes taking place in the core of the OMZ, from modern time up to the beginning of the last deglaciation. In all the studied cores, we generally observe a strong increase first and then a decreasing trend in the $\delta^{15}\text{N}$ values along the time period of the deglaciation, followed by relatively stable $\delta^{15}\text{N}$ signatures during the mid-Holocene. Interestingly, low $\delta^{15}\text{N}$ values ($\sim 5.5\text{‰}$) consistently characterize all the studied cores for the mid-Holocene time interval, indicating an overall absence of heavy nitrate in the surface being subsequently uptaken by phytoplankton. As the proxies for export production suggest that there is no straightforward correlation with $\delta^{15}\text{N}$ values during the mid-Holocene, the changes in $\delta^{15}\text{N}$ values are more likely resulting from modifications of subsurface ventilation rather than of nutrient utilization. An increase in upwelling intensity during the mid-Holocene may have allowed for a more efficient ventilation of the upper part of the water column, preventing any N-loss processes to take place, along with injection of NO_3^- with low $\delta^{15}\text{N}$ within the euphotic zone.

A mid-Holocene increase in upwelling intensity, analogously to modern conditions prevailing during austral winters and La Niña events, should also be mirrored in sedimentary records sensitive to regional shifts in the atmospheric circulation such as latitudinal shifts in the Intertropical Convergence Zone (ITCZ). We further investigated how past changes in precipitation along the Ecuadorian margin has evolved over the last 18 000 years. We used

two high-resolution XRF records to track downcore changes in the Guayas River runoff. The titanium over calcium ratio is supposed to reveal information on paleo-precipitation shifts along the western flanks of the equatorial Andes. When compared to other deglacial to Holocene rainfall records located across the tropical South American continent, different modes of variability become apparent. The records of rainfall variability imply that changes in the hydrological cycle at orbital and sub-orbital timescales were different from western to eastern South America. Orbital forcing caused an antiphase behavior in rainfall trends between eastern and western equatorial South America. In contrast, millennial-scale rainfall changes, remotely connected to the North Atlantic climate variability, led to homogeneously wetter conditions over eastern and western equatorial South America during North Atlantic cold spells. These results may provide helpful diagnostics for testing the regional rainfall sensitivity in climate models and help to refine rainfall projections in South America for the next century, and corroborate the mid-Holocene increase in upwelling activity which was likely responsible for pushing the ITCZ north of the Ecuadorian margin at this time.

Zusammenfassung

Die unteren Oberflächenwassermassen im östlichen tropischen Südpazifik (Eastern Tropical South Pacific, ETSP) sind durch eine der weltweit ausgeprägtesten und direkt unterhalb der Meeresoberfläche befindlichen Sauerstoff-Minimum-Zone (OMZ) charakterisiert. Diese OMZ resultiert aus dem Zusammenspiel einer regional hohen Primärproduktion (PP) und einer schwachen Ventilation der oberflächennahen Wassermassen. Die Ausdehnung der tropischen OMZ während der letzten Jahrzehnte weist darauf hin, dass diese Zonen sehr sensitiv auf den anthropogenen Klimawandel reagieren können, allerdings sind die grundlegenden Prozesse bezüglich des Einflusses von Änderungen der PP und dem Nährstoffkreislauf noch nicht richtig verstanden. Die vorliegende Arbeit ist eine Vergleichsstudie von Stickstoffisotopen-Daten, gemessen an Oberflächensedimenten aus einer Multicorer Beprobung entlang der ecuadorianischen und peruanischen Küste sowie von Nitrat Proben gemessen in der oberen 200m der Wassersäule, um zu verstehen welche Prozesse letztlich die Änderungen der Isotopensignatur in Sediment beeinflussen. Insgesamt wurde festgestellt, dass im O₂-armen unteren Oberflächenwasser die mikrobielle Umwandlung von NO₃⁻ zu N₂ ein ¹⁵N-angereichertes Signal im darunterliegenden Sediment hinterlässt, welches für Denitrifikation und/oder von Anammox beeinflusste Wassermassen charakteristisch ist. Des Weiteren wurde herausgefunden, dass das Ausmaß der partiellen NO₃⁻-Aufnahme durch das Phytoplankton im Oberflächenwasser signifikant zum Sediment-Signal in den nährstoffreichen und chlorophyllarmen (HNLC) Teilen des Untersuchungsgebiets beiträgt. Zudem konnte nachgewiesen werden, dass regionale Unterschiede bezüglich des Sauerstoffgehalts und der PP in Wassersäule und Sediment zu einer unterschiedlichen Stickstoff Isotopen-Signatur ($\delta^{15}\text{N}$) führen. Im Norden, zwischen 1°N–10°S, sind die oberflächennahen O₂-Konzentrationen zu hoch um Prozesse, die zu N-Verlusten führen, zuzulassen. Dies hält die $\delta^{15}\text{N}_{\text{NO}_3^-}$ -Werte auf einem relativ niedrigen Niveau in den unteren Oberflächenwassern. Im Gegensatz dazu steigen die $\delta^{15}\text{N}_{\text{NO}_3^-}$ -Werte mit abnehmender Wassertiefe durch die stärkere partielle NO₃⁻-Nutzung in der photischen Zone an. Dennoch führt eine nur teilweise Nutzung des NO₃⁻ möglicherweise zu konstant niedrigeren $\delta^{15}\text{N}_{\text{sed}}$ -Werten im Vergleich zu den $\delta^{15}\text{N}$ -Werten des aufsteigenden NO₃⁻. Weiter südlich, zwischen 10 – 15°S, innerhalb der Region des permanenten Auftriebs, sind die HNLC Bedingungen schwächer ausgeprägt, was zu einer intensiveren biologischen

Produktion und damit verbundenen NO_3^- -Aufnahme durch Phytoplankton im Oberflächenwasser führt. Zusätzlich verringert sich die oberflächennahe O_2 -Konzentration auf ein Niveau, welches ausreicht um N-Verlust durch Denitrifikation und/oder Anammox zu ermöglichen. Dies führt zu erhöhten oberflächennahen $\delta^{15}\text{N}_{\text{NO}_3^-}$ -Werten in den Wassermassen, die den küstennahen Auftrieb speisen. Verschiedene Sediment-Proxies der Produktivität deuten auf eine nach Süden zunehmende PP hin, was sich durch eine Nord-Süd Zunahme im $\delta^{15}\text{N}_{\text{sed}}$ -Signal zeigt, welche einen nach Süden zunehmenden oberflächennahen N-Verlust widerspiegelt. Zusätzlich nehmen die $\delta^{15}\text{N}$ -Werte, die in den core-top Sedimenten und in den Wassersäulenproben gemessen wurden, senkrecht zur Küste hin zu und zeigen damit eine Intensivierung des küstennahen Auftriebs entlang der Küstenlinie an, wobei die Oxykline und Nitrakline näher an die Oberfläche wandern. Die Kartierung zeigt, dass sowohl der Grad des N-Verlustes, welcher die unter-oberflächennahen $\delta^{15}\text{N}_{\text{NO}_3^-}$ -Werte beeinflusst, als auch die Stratifizierung der Ozeanoberfläche und der Grad der oberflächennahen Nitrat-Nutzung bei der Interpretation von $\delta^{15}\text{N}_{\text{sed}}$ -Daten aus Sedimentkernen zur Rekonstruktion der raum-zeitlichen Variabilität der peruanischen OMZ herangezogen werden sollten.

Demzufolge wurden zurückliegende Veränderungen der Ausdehnung der OMZ auf der Basis von vier Kolbenlot-Sedimentkernen, die außerhalb, an der Grenze und innerhalb der heutigen OMZ entlang eines meridionalen Transektes (von $3,5$ bis 15°S) ausgewählt wurden, rekonstruiert. In allen Sedimentkernen decken die gemessenen $\delta^{15}\text{N}$ -Werte das gesamte Holozän und das letzte Deglazial ab. Im nördlichen Teil entlang des nördlichen Teil des peruanische Kontinentalrands sind die Werte niedrig, von 4 bis 6‰ , mit einer beobachteten Amplitude von $\sim 1\text{‰}$ während des Holozäns und des Deglazials. Dies ist wahrscheinlich dadurch begründet, dass es in dieser Region keine OMZ Bedingungen gab. Im Gegensatz dazu weisen die im Süden erhaltenen Sedimentkerne mit bis zu $\sim 10\text{‰}$ und einer Amplitude von $\sim 4\text{‰}$ höhere Werte für den Zeitraum des Deglazials bis heute auf. Zurückzuführen ist dies wahrscheinlich auf die N-Abbauprozesse in der Wassersäule an den positionen des Sedimentkerne, die innerhalb der OMZ liegen. An allen untersuchten Sedimentkernen wurde ein abnehmender Trend der $\delta^{15}\text{N}$ -Werte während des Deglazials festgestellt, gefolgt von relativ stabilen $\delta^{15}\text{N}$ -Signaturen während des mittleren Holozäns. Interessant ist, dass alle untersuchten Sedimentkerne während des mittleren Holozäns durch geringe $\delta^{15}\text{N}$ -Werte ($\sim 5,5\text{‰}$) gekennzeichnet sind, was zeigt, dass im Oberflächenwasser kein schweres Nitrat

vorhanden war, welches durch Phytoplankton hätte aufgenommen werden können. Da Proxies für die Export-Produktion keine direkte Korrelation mit den $\delta^{15}\text{N}$ -Werte während des mittleren Holozäns anzeigen, ist eher anzunehmen, dass die Veränderungen der $\delta^{15}\text{N}$ -Werte aus Zirkulationsänderungen der unteren Oberflächenwasser resultieren. Ein Anstieg der Auftriebsintensität während des mittleren Holozäns hat möglicherweise eine effizientere Ventilation der oberen Wassersäule ermöglicht und somit N-Verlust-Prozesse verhindert und gleichzeitig für einen höheren Eintrag von Nitrat mit niedriger $\delta^{15}\text{N}$ Signatur in die photische Zone gesorgt.

Analog zu der heute durch Südhemisphären-Winter und La Niña Ereignisse hervorgerufene erhöhte Auftriebssintensität sollten deshalb in den Holozänen Sedimenten ins die für diese Klima-zustände typischen regionalen Verschiebungen der atmosphärischen Zirkulation, wie beispielsweise die über dem nordwestlichen Südamerika stattfinden den Verschiebungen der ITCZ, reflektiert werden. Deshalb wurde untersucht, wie sich die Niederschläge in den letzten 18 ka entwickelt haben. Um die Veränderungen des Guayas-River Abflusses untersuchen zu können, wurden hochaufgelöste XRF-Aufnahmen zur Elementverteilung in zwei Sedimentkernen untersucht. Hierbei sollte aus den Schwankungen des Ti-gehaltes Informationen über eine Verschiebung der Palöo-Niederschläge entlang der westlichen Flanke der äquatorialen Anden rekonstruiert werden. Im Vergleich zu anderen Niederschlagsuntersuchungen entlang des tropischen südamerikanischen Kontinents im Zeitraum der letzten Enteisungsperiode bis zum Holozän wurden unterschiedliche Ausprägungen von Variabilität ersichtlich. Die Aufzeichnungen der Niederschlagsvariabilität implizieren, dass sich Veränderungen im hydrologischen Kreislauf auf orbitalen und sub-orbitalen Zeitskalen von West- nach Ost-Südamerika unterscheiden. Orbitale Einflüsse verursachten ein gegenläufiges Verhalten der Niederschlagstrends zwischen Ost- und Westäquatorial Südamerika. Im Gegensatz dazu sind die 1000-jährigen Veränderungen der Niederschläge stark mit den nordatlantischen Klimavariabilitäten korreliert, was zu gleichmäßig feuchteren Bedingungen über Ost- und Westäquatorial Südamerika während der nordatlantischen Kälteperioden führte. Diese Ergebnisse können hilfreiche Daten zum Test der Sensitivität von Klimamodellen bezüglich regionaler Niederschläge liefern und helfen Niederschlagssimulationen in Südamerika für das nächste Jahrhundert zu verbessern. Auch können diese Daten sowie die Zunahme der Auftriebsaktivität im mittleren Holozän bestätigen, da die südöstlichen Passatwinde wahrscheinlich für die Verschiebung der ITCZ nördlich des peruanischen Kontinentalrandes verantwortlich sind.

Acknowledgements

Thanks Philippe, who was always available, taking time for me, help me, even at 2000 km from Kiel and Quelqu'un qui sait respecter les autres, plein d'humanité, merci. I would like to thank as well all the team of Bordeaux.

Ralph: The unavailable "Big Boss", never here, always busy but when you finally reach him, after you already burn your brain 10 times about an unsolvable problem, he just burn it a 11 time. At the end you are brain-less, exhausted, need 2 coffees to come back to life but you looked at every single problems, he asked you the right questions and solved your problem. Impressive! Just a little bit frustrating sometimes.

Thanks as well to all the team of the Geosciences institute, with special thanks for Thomas B. and Silvia Koch who was so patient with me, repeated every time what I forgot, brought a good mood in the lab and who is a deeply nice person.

I was given a warm welcome by all the French team at the University, Tim, Johan, Nabil, and Guillaume L., who support me for my arriving in the "Grand Nord". Special thanks to Nabil who accepted my hyper activity in the office and shown me the first steps of the PhD.

Thanks as well to my two working partners in SFB754, Claudia Ehlert and Patricia Grasse, was always nice to talk about science, as well as to drink a bier.

Herr The Duck: Save my life so many times that I don't have enough fingers to count them (yes, during a PhD you don't learn how to count except the weeks you spend doing useless work...). Always available, even if he is over busy with some other stuff and already spend half of the day helping other persons. I think that I am not the only one to who is save the life, and I always feel a bit ashamed to disturb him, again. I also should thank him for all the time with spend together in front of the computer working on the XRF paper, talking about science, him telling me all the history of science, saying jokes, laughing, etc. I also have to add that he is a king of a "Pot au feu", with half fat, half meat, and 2 pieces of carrot (I know the fan of statistics will scream that it is more than a 100%, that is new science, ask all the economists). You are the antipode of your/our boss, what he knows, and thanks 1000 times to give around your passion for science, to share your "undémorable" French music, Brassens for ever as well as your full heart for the Canard enchainé. Merci à toute la family aussi...

Merci Cécile qui m'a toujours redonné le moral dans les moments difficiles, même quand tu étais super occupée, qui a relu mes écritures calamiteuses. Et puis et surtout pour les bons moments passés.

Rüdiger: the mascot of the Geosciences institute, know everything about the German administration and a lot more, always nice to spend some time with you, merci "Opi".

Sarntein: Which show me what a hard life could be, showing me the long hours he spend with Nabil, side to side, talking for hours about half a sentence. It is also somebody who always passes by my office, said hello and asked me how I was going. He certainly asked more than my own supervisor. He also motivated me to start writing: "It is the most powerful and the single moment of such creativity in your whole life. It is imagination and creation" (cf. M. Sarntein)

Steffy, Steffy, that's a pity que tu ne fume plus, congratulations. Nothing and much too much to say.

Thanks Birgit R., for your help in the administration paper and your particularly good mood. Thanks Emma for your help and your patience and to feed me when I was writing.

Andrea/Vincent: That I met when I arrived in Kiel and with who I discovered the pleasure of learning German, but also all our trip around the city, the successions of good foods and nice moments. Et surtout Vincent, qui a toujours essayer de me montrer le côté "clair" de la science. M'a toujours motiver avec sa bonne humeur et son très bon sens satirique de l'humour. Bon, sauf peut-être quand il finissait sa propre thèse...

Exer WG: Welcomed me in Deutschland, showed me the city and the life in Kiel, super nice people, merci Üwe, Martin, Sven, Amélie,... all the others around that I cannot cite because the list would be too long.

A thanks as well to these frenchs who became "Kielers" Guillaume J., Nico (for your help as well), Bob, Andrea (who are not French but became kieler): for the super good mood that they always gave me, Claire, Philou.

Lunatic: Who host me many times for several hours, accepting that I stayed ages squatting their café to work, for 2 or 3 cups of caffeine and a smile.

Didier Vigouroux: Qui m'a "sauvé la vie" à longue distance. Merci beaucoup encore.

And all the people who support me but that I cannot cite, otherwise it will be longer than my own PhD.

Ich muss auch die Leute von Hansa⁴⁸ danken mit ein special Danke für Betty für dein Hilfe, immer, und Corinna, für die ganze Motivation und positive Energie. Du warst immer

da für meine läste "ligne droite" mit die gute Worten und der Smile. Vielen dank für dein "support", immer hier, egal der Tag und deine Stimmung, wann ich habe gefragt aber auch wann ich habe nicht, danke.

Bedankt Jeroen voor mijn slechte gevoel voor humor hebben gedoogd van het einde van proefschrift (anagram).

Et Nath bien sur, toujours, pour tout. Bien sur ma famille qui m'a toujours soutenue, aidée, encouragé et j'en passe bien d'autres, et depuis longue date déjà.

The “Deutsche Forschungsgemeinschaft, (DFG)” provided funding through SFB 754
“Climate- Biogeochemistry Interactions in the Tropical Ocean.”

List of abbreviations

AAIW: Antarctic Intermediate Water

ACC: Antarctic Circumpolar Current

ACR: Antarctic Cold Reversal

AMOC: Atlantic Meridional Overturning Circulation

BP: Before Present, before AD 1950

CC: California Current

CH₄: Methane

CO₂: Carbon Dioxide

C_{org}: Organic Carbon

$\delta^{15}\text{N}_{\text{NO}_3^-}$: Nitrogen isotopes measured on the nitrate

$\delta^{15}\text{N}_{\text{NO}_x}$: Nitrogen isotopes measured on the nitrate and nitrite ($\text{NO}_3^- + \text{NO}_2^-$)

$\delta^{15}\text{N}_{\text{sed}}$: Nitrogen isotopes measured on the sediment

EBUE: Eastern Boundary Upwelling Ecosystems

ENP: Eastern North Pacific

ENSO: El Niño Southern Oscillation

ESP: Eastern South Pacific

ETNP: Eastern Tropical North Pacific

ETSP: Eastern Tropical South Pacific

EUC: Equatorial Under Current

Fe: Iron

GU: Gunther Undercurrent

H1: Heinrich event 1

HC: Humboldt Current

HCl: Hydrogen Chloride

HNLC: High Nutrient Low Chlorophyll

IMARPE: Instituto Del Mar del Perú, Lima

IPCC: Intergovernmental Panel on Climate Change

ITCZ: Intertropical Convergence Zone

LGM: Last Glacial Maximum

MAR: Mass Accumulation Rate

NaCl: Sodium Chloride
NEC: North Equatorial Current
NECC: North Equatorial Counter Current
N-loss: Nitrogen Loss Processes
N: Nitrogen
N₂: Nitrogen gas
N₂O: Nitrous Oxide
NO₃⁻: Dissolved Nitrate
O₂: Oxygen
OM: Organic Matter
OMZ: Oxygen Minimum Zone
P: Phosphorus
PIC: Particulate Inorganic Carbon
PCC: Peru-Chile Current
PCCC: Peru-Chile Countercurrent
PCCoastalC: Peru-Chile Coastal Current
PCU: Peru Chile Upwelling
PCUC: Peru Chile Under Current
PP: Primary Production
SEC: South Equatorial Current
SiO₂: Biogenic Opal
SSCC: Southern Subsurface Counter Current
SST: Sea Surface Temperature
SST_{alk}: Sea Surface Temperature derived from alkenone unsaturation ratios
SST_{WOA09}: Sea Surface Temperature from the World Ocean Atlas 2009 dataset
THC: Thermohaline Circulation
TN: Total Nitrogen
WOA09: World Ocean Atlas 2009
WPWP: Western Pacific Warm Pool
YD: Younger Dryas

List of figures

Figure I.1. Atmospheric cells	34
Figure I.2. Seasonal variation in the ITCZ position.....	35
Figure I.3. ENSO and Walker circulation	36
Figure I.4. Global thermohaline circulation.....	36
Figure I.5. Oceanography of the Pacific basin.....	38
Figure I.6. North-South coastal section of water masses along South America.....	38
Figure I.7. Oxygen concentration in the world ocean.....	41
Figure III.1. Sample locations	56
Figure III.2. Schematic representation of the gas chromatograph system	60
Figure III.3. Schematic representation of the Elemental Analyser and Mass Spectrometer...	61
Figure IV.1. SST _{alk} along the Peruvian margin	64
Figure IV.2. Oceanographic pattern of the Peruvian margin	65
Figure IV.3. SST _{alk} and SST _{WOAco} comparison	67
Figure IV.4. U ^K ₃₇ against SST _{alk} and SST _{WOAco}	68
Figure V.1. Maps of oceanographic parameters of the Peru-Ecuador margin.....	73
Figure V.2. Samples locations along the Peru-Ecuador margin.....	75
Figure V.3. δ ¹⁵ N _{sed} and water column measurements	77
Figure V.4. Sedimentary results.....	78
Figure V.5. δ ¹⁵ N in the water column and surface sediment	79
Figure V.6. Relative nitrate utilization as a function of latitude	84
Figure V.7. Hypothetical scheme of the Peruvian upwelling system	88
Figure VI.1. Salinity distribution and nitrate utilization along the western margin of South America	94

Figure VI.2. Oxygen distribution, nitrogen isotopes and nitrate utilization along the western margin of South America	95
Figure VI.3. Compilation of $\delta^{15}\text{N}$ sediment mapped on the calculated nitrate utilization	97
Figure VI.4. Correlation between nitrogen isotopes corrected from mixing and nitrate utilization.....	99
Figure VII.1. Map of oxygen concentration off Peru and core location	105
Figure VII.2. Sedimentary results of the studied cores.....	108
Figure VII.3. Age model applied to the studied cores	109
Figure VII.4. MAR and sedimentation rate for the studied cores.....	114
Figure VII.5. $\delta^{15}\text{N}$ values off Peru and northern Chile.....	116
Figure VII.6. SST_{alk} from the studied cores	118
Figure VII.7. SST_{alk} and $\delta^{15}\text{N}$ values differences between the two cores M772-059 and -003	119
Figure VII.8. Schematic estimation of the Peruvian OMZ extent at different time intervals	120
Figure VIII.1. Seasonal changes in mean precipitation over South America	124
Figure VIII.2. Regional bathymetry and sediment core locations	129
Figure VIII.3. XRF counts for core M772-059.....	130
Figure VIII.4. Sedimentary records and age model for the studied cores.....	132
Figure VIII.5. Records for past changes in precipitation over South America	136

List of tables

Table 1. Difference between initial $\delta^{15}\text{N}$ of the upwelled nitrate and sedimentary $\delta^{15}\text{N}$	83
Table 2. Surface sediment data used for this study	159
Table 3. Radiocarbon dates (^{14}C -AMS) used for the studied cores.....	160
Table 4. Data of core M772-056-5	162
Table 5. Data of core M772-059-1	166
Table 6. Data of core M772-029-3	172
Table 7. Data of core M772-003-2	177

Chapter I. Introduction

I-1. Motivation for this study

During the 21st century, the interest and awareness for climate change becomes a major concern, mainly because of the observation of an increase in global temperature due to an increase in the atmospheric concentration of greenhouse gases (e.g. CO₂, CH₄ and water vapor) [Revelle, 1957; Intergovernmental Panel on Climate Change *IPCC*, 2007]. Direct consequences are observed on various compartments of the Earth system (melting of the ice sheets, increased occurrence of the warm phase (El Niño) of El Niño Southern Oscillation (ENSO), and increased frequency of natural disasters such as hurricanes, tornadoes, floods and droughts [IPCC, 2007]. Climate change is also reported to have a large impact on the ocean thermohaline circulation (THC) [Bond *et al.*, 1997; McManus *et al.*, 2004; Jouzel *et al.*, 2007], which plays an important role in main biogeochemical cycles (e.g. storage of CO₂ in the deep ocean, nutrient supply to the organisms, oxygen distribution) and in heat redistribution (Figure I.1; [Broecker, 1987; Rahmstorf, 2006; Kuhlbrodt *et al.*, 2007]).

This work is part of the interdisciplinary project: Collaborative Research Centre (SFB) 754 “Climate-Biogeochemistry Interactions in the Tropical Ocean“. As a concern about climate change, the SFB 754 aims to investigate changes in supply of oxygen to the tropical oxygen-depleted oceanic areas during past, present and future climates. Oxygen distribution in the global ocean is controlled by a close interplay of climate dynamics (e.g. atmospheric exchanges, oceanic ventilation) and oceanic biochemistry (e.g. PP and organic matter degradation due to bacterial activity). Along the Peruvian margin, changes in the surface hydrology originate from either local wind-driven upwelling or from the Pacific basin-scale circulation changes. The PP at the sea surface is directly linked to the upwelling-driven nutrient input. Off Peru, PP is one of the largest in the global ocean leading to a large amount of sinking particles through the water column to the sediment. Remineralisation (grazing and bacterial degradation), which occurs during the sinking of particles consumes large amounts of oxygen in subsurface. The combination of the large remineralisation of PP and slight ventilation in the subsurface drives the system to extremely oxygen-depleted conditions.

Under such low oxygen conditions, the importance of anaerobic microbial processes on organic matter (OM) leads to consumption of nitrate in the subsurface and thus a net loss of available nitrate from the global ocean, the so called N-loss processes [*Codispoti and Christensen, 1985*]. Ultimately, the N-loss processes produce nitrous oxide (N₂O) gas [further described in Chapter II-4], which is a strong greenhouse gas. OMZs therefore play a crucial role for the changes in nutrient cycles in the global ocean.

In addition, OMZs vary in response to climate fluctuations on different timescales, from seasonal, subdecadal (such as ENSO), decadal to millennial and orbital. As part of the SFB754 subproject A6, this study aims at reconstructing the spatial and temporal variability of the Peruvian OMZ, being the largest in the World, in response to changes in export PP and stratification-circulation of the upper-ocean, at centennial to millennial timescales during the last 18 ka BP.

Whereas it has been recently demonstrated that OMZs have been expanding during the last 50 years and that the oxygen distribution in the present-day ocean seems to be tightly linked to the actual climate change [*Stramma et al., 2008*], this overview of the long-term variability of the OMZ may enable to disentangle the human impact on global-change from the natural variability of the OMZ.

It may also help to better constrain the occurrence of widespread anoxic events that were associated with warmer climate and higher atmospheric CO₂ level like during the Mesozoic, especially during the Jurassic and Cretaceous periods with the occurrence of the so-called Oceanic Anoxic Events or OAEs [*Schlanger and Jenkyns, 1976; Takashima et al., 2006*]. Modeling studies also suggested an increase in surface temperature and CO₂ atmospheric concentration resulting from anthropogenic influences [*IPCC, 2007*]. It is therefore necessary to better understand OMZs sensitivity to climate change to assess their feedbacks on the future ocean.

The SFB 754 project addresses the following questions:

- How does subsurface dissolved oxygen in the tropical ocean respond to changes in ocean circulation and ventilation?
- What are the sensitivities and feedbacks linking low oxygen levels and key nutrient source and sink mechanisms?
- What are the magnitudes, timescales and controlling factors of past, present and likely future variations in oceanic oxygen and nutrient levels?

The present study focuses on:

- Improving our knowledge of the nitrogen isotope signal from the water column to the sediment under the influence of OMZ conditions.
- Understanding past changes of ETSP ocean dynamics, as well as its corresponding regional climate.
- Reconstructing the variability in the extent of the OMZ during the last 18 ka using nitrogen isotopes and paleo proxies for surface circulation and export production.

I-2. Outline

In addition to introduce this work and its main motivations, Chapter I gives a description of the modern hydrology and regional climate of the Eastern South Pacific (ESP).

A description of the proxies used in this study is presented in Chapter II.

The sample locations, methods, and age models used for the surface sediment samples and the 4 studied piston cores are given in Chapter III.

The following Chapters are the core of the thesis. Chapters IV, V, VI, VII, VIII report the five most significant outcomes of the analyses performed during this work. Chapters V, VII, VIII are presented in the shape of an article. Chapter IV presents a mapping effort of the sea surface temperature (SST) reconstruction, using alkenones unsaturation measurements (U_{37}^K) on surface sediment samples. A regional calibration between reconstructed SST using U_{37}^K and measured SST will be presented as a manuscript in preparation. Then we present a mapping of stable nitrogen isotopic measurements ($^{14}\text{N}/^{15}\text{N}$ ratio, $\delta^{15}\text{N}$) performed on bulk sediment along the Peruvian and Ecuadorian margins in the Chapter V. It allows describing and commenting on the processes controlling the spatial regional $\delta^{15}\text{N}$ gradients recorded in this area, in particular the role of nutrient availability and N-loss processes and finally gives paths for reflection and interpretation of $\delta^{15}\text{N}$ from marine sediment in paleo-records. The main outcome of this study is the observation of a latitudinal increase in surface sediment $\delta^{15}\text{N}$, in line with the $\delta^{15}\text{N}$ increase measured in the water column along the Ecuadorian-Peruvian coast. This is interpreted as a reflection of increase in the upwelling intensity and PP, which consequently influence 1) the extent of the underlying OMZ and 2) the availability of isotopically heavy nitrate to the surface. These results are presented as a manuscript published in Deep-Sea Research [*Mollier-Vogel et al.*, 2012]. The Chapter VI is the extension of this

work to the entire South American margin, comparing our $\delta^{15}\text{N}$ results with those obtained earlier off Chile [Hebbeln *et al.*, 2000; De Pol-Holz *et al.*, 2009].

Chapter VII is the direct application of the results presented in Chapter V to down-core $\delta^{15}\text{N}$ measurements. We reconstructed the variability of biogeochemical cycling during the last 18 ka BP from a latitudinal transect constituted of 4 cores along the Peruvian and Ecuadorian margins. As for the surface sediment, the southern cores show higher $\delta^{15}\text{N}$ values reflecting the record of the OMZ signal within the sediment. The most outstanding issue of this study is the collapse of the Peruvian OMZ in the upper 200 m of the water column, during the middle Holocene (8-5 ka BP) certainly in phase with a prolonged period of La Niña-like conditions.

In an attempt to put the OMZ variability into a broader climatic context, Chapter VIII presents comparison of a record of past changes in the dynamics of the ITCZ over the Eastern Equatorial Pacific (EEP) and its corresponding monsoon activity over South America with previous studies. This has been done by using a record of riverine runoff from a core collected in front of the Gulf of Guayaquil (Ecuador). At orbital timescales, the timing of rainfall maxima is characterized by an East-West antiphase along the equator, which is not obvious during the abrupt cold events of the deglaciation, when rainfall increases are recorded simultaneously east and west of equatorial South America.

The last Chapter IX presents the main conclusions of this study, and draws broader perspectives on the climate effects on the OMZ and nutrient cycle variability over the past and the present-day Peruvian upwelling system, which may help identifying how the Peruvian ecosystem will likely evolve under anthropogenic climate change.

I-3. Study Area

The Peruvian upwelling system variability and regional rainfall is closely related to regional atmospheric circulation, which results from the interplay between the ITCZ and the Walker circulation. Changes in the atmospheric circulation are mainly driven by seasonality and interannual variability associated with the ENSO. As the regional settings will be described in more detail in the following chapters, I will mainly focus here on presenting an overview on the atmospheric and oceanic circulation of the ETSP and on nutrient cycling within the Peruvian OMZ system.

I-3.1. Atmospheric circulation and variability of the system

I-1.3.1. The ITCZ

The low-level equatorward branches of the Hadley cell - the southeast and northeast trade winds (Figure I.1) - compose maximum convergence of the winds near the equator, defining the so-called Intertropical Convergence Zone (ITCZ) (Figure I.2). The convergence of warm air masses dominates the tropical troposphere and is associated with an intense rainfall belt following the ITCZ [Lutgens and Tarbuck, 2001]. Over the ocean, where thermal inertia is high, the ITCZ remains near 5°N year-round because of local air-sea interactions (Figure I.2). The seasonality of the ITCZ dynamics strongly influences the intensity of upwelling and determines the dry-wet cyclicality on land. However, at the seasonal timescale, rainfall patterns migrate latitudinally following the annual cycle of insolation over the adjacent South American continent. Furthermore due to the smaller thermal inertia of continents as compared to oceans, the South American monsoon bears rainfall latitudinal shifts by up to 20°S (Figure I.2).

The Peruvian desert located along the coast is subject to very low amount of rainfall during the austral summer (Dec-Jan-Feb). At the same time the eastern part of the Andes receives moisture from the Atlantic during austral summer associated with the southern displacement of the South American monsoon. The northern position of the ITCZ during austral winter (Jul-Aug-Sep) leads to periods without any significant precipitation on the Peruvian lowlands, resulting in a very intense aridity over this coastal region (Developed in Chap. VI). Over the South Pacific, the Westerlies are deflected by the Andes orographic barrier and deviates the atmospheric flow northward, feeding the tradewinds. The latter oscillate seasonally and interannually in synchrony with the ITCZ via the Hadley circulation. The presence of the Andes along the Western side of the South American continent prevents most of the atmospheric exchanges between the Atlantic and the Pacific basins [Bookhagen and Strecker, 2008].

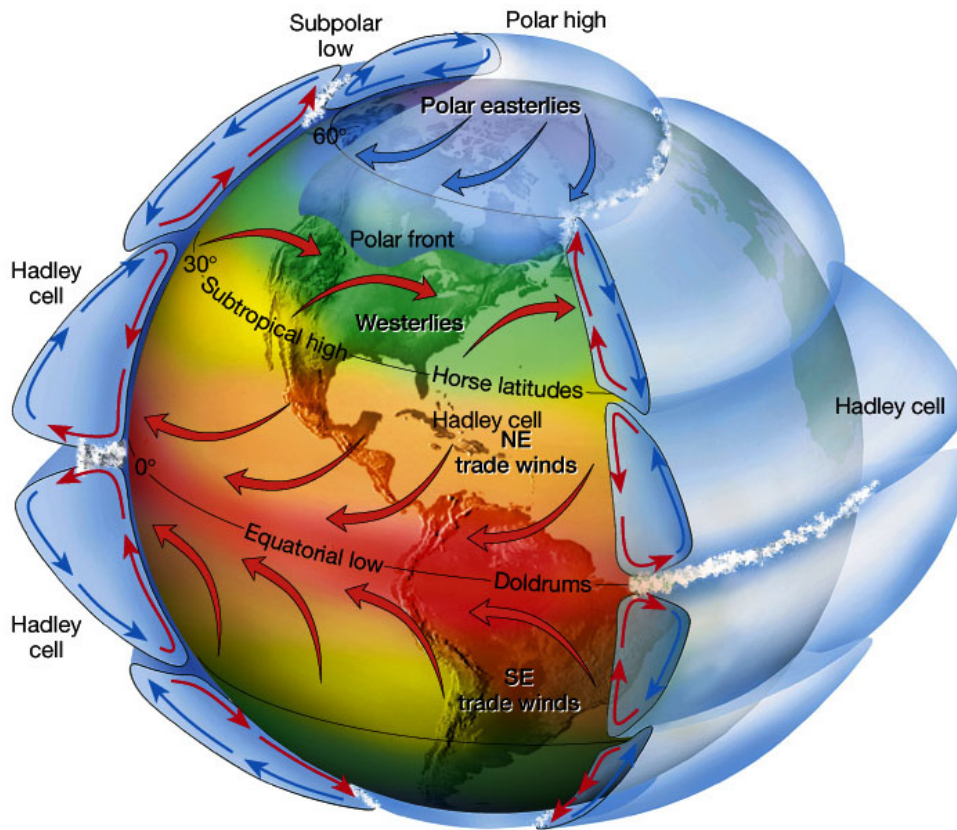
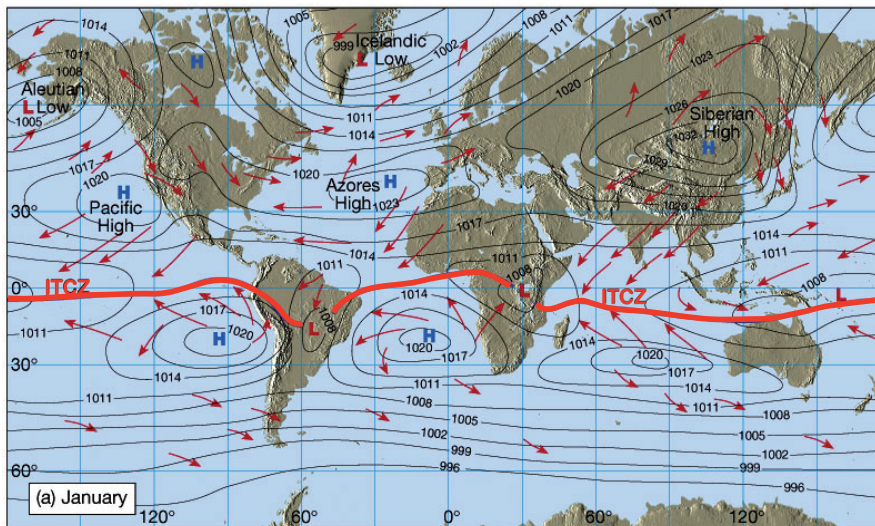


Figure I.1. Atmospheric cells

Idealized, atmospheric cell convection in a rotating Earth. The deflection of the winds within each cell is caused by the Coriolis force. [Figure 7.5 in *The Atmosphere*, 8th edition, *Lutgens and Tarbuck*, 2001].



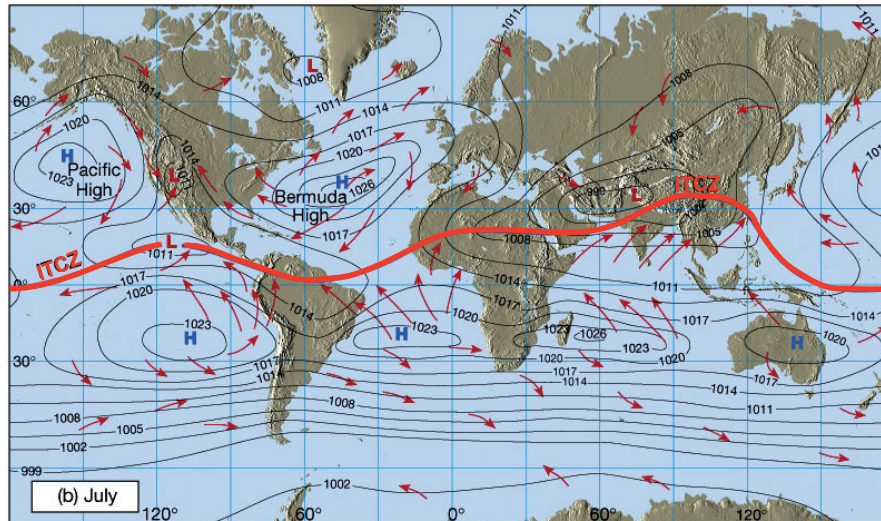


Figure I.2. Seasonal variation in the ITCZ position

The isobars show atmospheric pressure. a) Southern shift of ITCZ in January. b) Northern shift of ITCZ in July. (Figure 7.9 in *The Atmosphere*, 8th edition, *Lutgens and Tarbuck*, 2001).

I-2.3.1. The Walker circulation

The Walker circulation results from ocean-atmosphere interactions creating an East-West atmospheric zonal cell of which the lower limb is defined by the trade winds [*Walker*, 1923; 1924]. This cell creates a zonal SST gradient with cold temperatures in the East, defining the so-called Eastern Pacific Cold Tongue, and an accumulation of heat in the Western Pacific Warm Pool (WPWP), sustained by a zonal tilt of the equatorial Pacific thermocline. As a consequence of this East-West temperature gradient, the warm air is rising above the WPWP, diverging in every direction at the top of the troposphere for later converging and subsiding over the Cold Tongue. This East-West interplay of air convection and subsidence creates the Walker cell above the equatorial Pacific (Figure I.3, middle).

This atmospheric circulation is also strongly affected by ENSO [*Cane*, 2005]. During the warm phase of ENSO (El Niño), the weakening of the trade winds leads to a displacement of the warm air and surface water masses from the WPWP to the central Pacific and during strong events, the air masses even reach the ETSP coast. This warm phase of the oscillation provokes intense precipitation on land leading to coastal flooding. During the cold phase (La Niña) the trade winds strengthen, leading to an increase in the temperature and moisture at the WPWP, and to an expansion of the Cold Tongue to the central Pacific, coupled with even more arid conditions along the Peruvian coast.

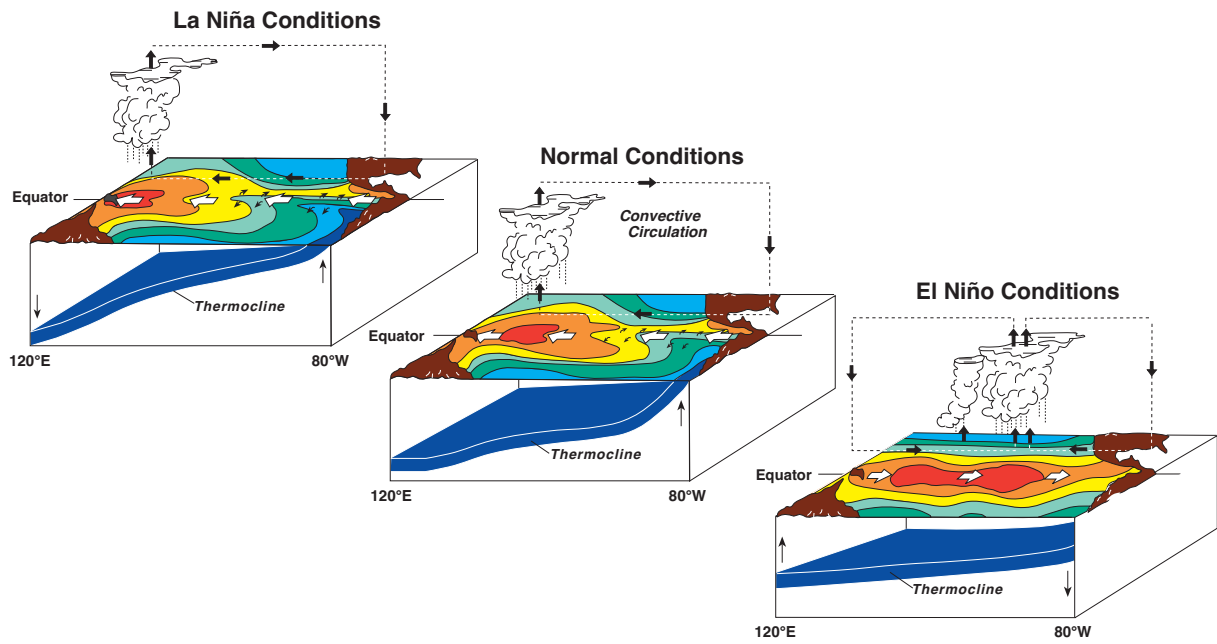


Figure I.3. ENSO and Walker circulation

Schematic illustration of the Walker circulation above the EEP, under normal condition (middle), for la Niña years (left) and for El Niño years (right), [Cane, 2005].

I-3.2. Regional oceanic circulation

At a global scale, the oceanic circulation is regulated by the Thermo-Haline Circulation (THC), which transports heat from the low to the higher latitudes by surface currents (Figure I.4; [Broecker, 1987; Rahmstorf, 2006]). The surface flow itself is balanced by deep-ocean currents, mainly driven by large-scale density fields defined by water mass temperature and salinity.

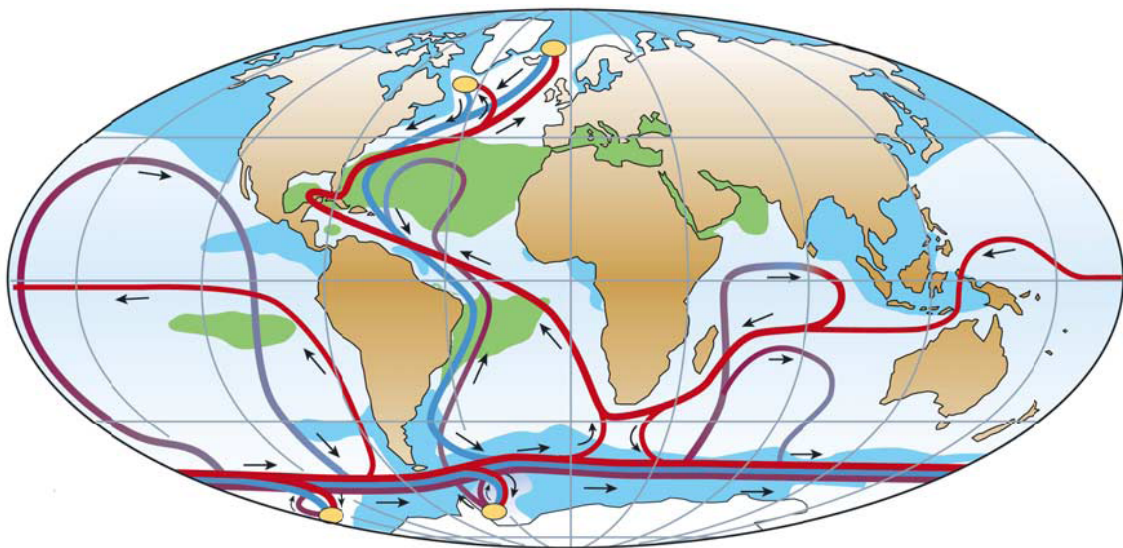


Figure I.4. Global thermohaline circulation

Highly simplified representation of the global thermohaline circulation. Surface currents are shown in red, deep waters in light blue and bottom waters in dark blue. The main deep-water formation sites are shown in orange. Green and blue shading show high, $>36\text{‰}$ and low, $<34\text{‰}$, salinity respectively, [Kuhlbrodt et al., 2007].

The oceanography of the tropical Eastern Pacific depends on the THC for intermediate to deep water circulation and is affected by the Hadley and the Walker circulations. The Antarctic Circumpolar Current (ACC) in line with the South Equatorial Current (SEC) interacts strongly with the South Pacific gyre (Figure I.5). At the eastern flank of the gyre the surface current, the so-called Humboldt Current (HC), flows equatorward along the South American margin. This cold and nutrient depleted current turns offshore off the Peruvian margin and gets influenced by the western Southern Subsurface Counter Current (SSCC; Figure I.5 & Chapter V, Figure V.1).

The Walker circulation stacks warm water in the WPWP, largely driven by the influence of the South Equatorial Current (SEC) (Figure I.5; [Walker, 1923; 1924]). In contrast, the divergence of the southeast and northeast trade winds along the equator provokes a poleward Ekman transport of the surface water mass locally, and is compensated by the subsurface Equatorial UnderCurrent (EUC) flowing eastward (Figure I.5). The upper waters of the EUC reach the surface near the Galapagos Island, while the deeper part of the EUC flows along the Peruvian coast, where it is upwelled ([Wyrtki, 1981; Kessler, 2006]; Figure I.5). This water transport leads to a progressive shoaling of the thermocline from the WPWP to the EEP (Figure I.3).

The subsurface currents of the ETSP are subdivided in two main regions: 1. The Northern ETSP, where the EUC and SSCC feed the Peru Chile Under Current (PCUC) flowing southward and 2. The Southern part, where the South Antarctic Mode Water (SAMW) originating from the ACC, reaches the southern Peruvian margin at $\sim 23^{\circ}\text{S}$ (Figure I.5 & 6; [Fiedler and Talley, 2006; Kessler, 2006; Czeschel et al., 2011]). From $\sim 23^{\circ}\text{S}$ on, the SAMW feeds the HC, which is going more offshore (details in the following Chapter V, Figure V.1).

The westerly surface water mass transport by the SEC and the North Equatorial Current (NEC) results in a thermocline tilt, which oscillates with the ENSO. During the normal and La Niña conditions, the thermocline is as deep as 150 m in the WPWP, while it nearly reaches the surface in the ETSP (Figure I.3). However, during El Niño events, the easterly displacement of the water masses deepens the thermocline in the ETSP (Figure I.3).

This strong oscillation also leads to intense upwelling along the Peruvian coast during La Niña conditions (More details are given in the following paragraph, Chapter 1.2.3).

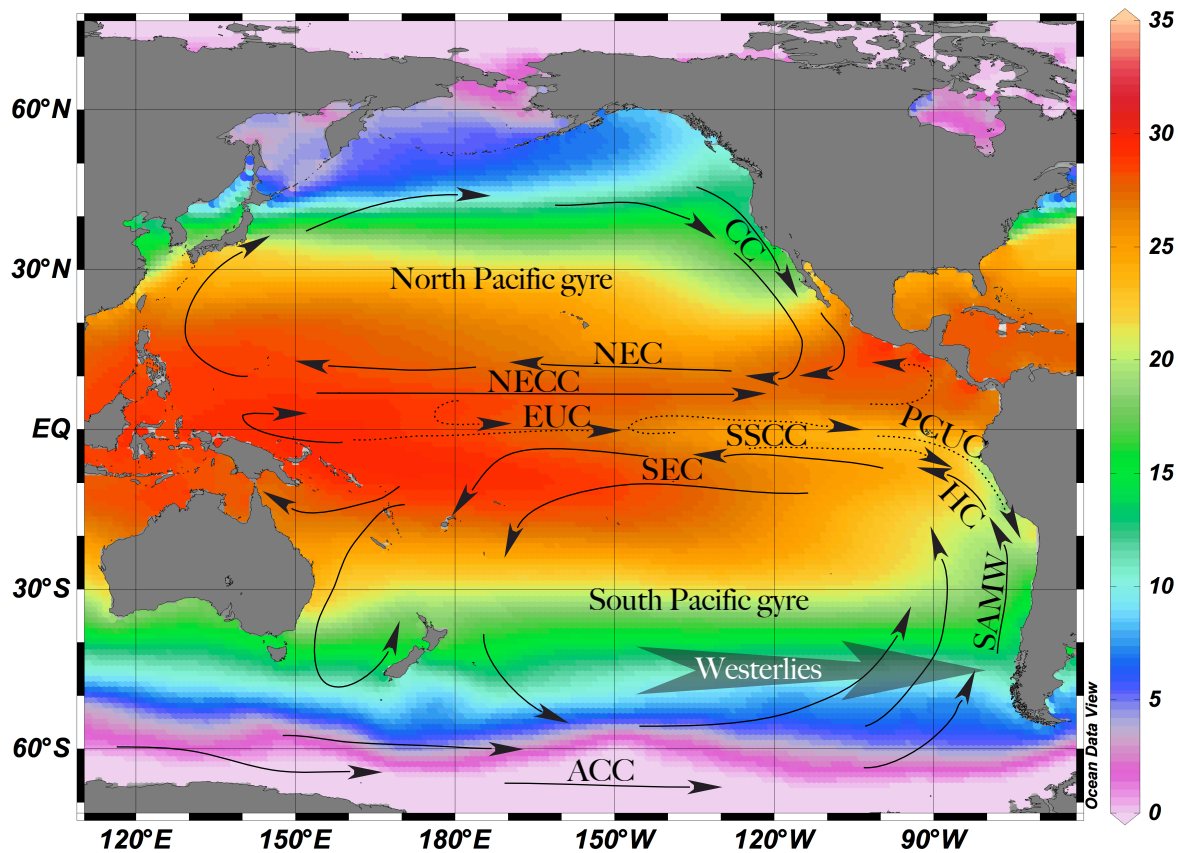


Figure I.5. Oceanography of the Pacific basin

Oceanography of the Pacific basin, composed by the main surface currents (solid lines): South Equatorial Current SEC, Antarctic Circumpolar Current ACC, Humboldt Current HC, North Equatorial Current NEC, North Equatorial Counter Current NECC, and subsurface currents (dashed lines): Equatorial Under Current EUC, Southern Subsurface Counter Current SSCC, Peru Chile Undercurrent PCUC [Fiedler and Talley, 2006; Kessler, 2006; Czeschel et al., 2011]. The background shading shows the SST dataset extracted from World Ocean Atlas 2009, WOA09.

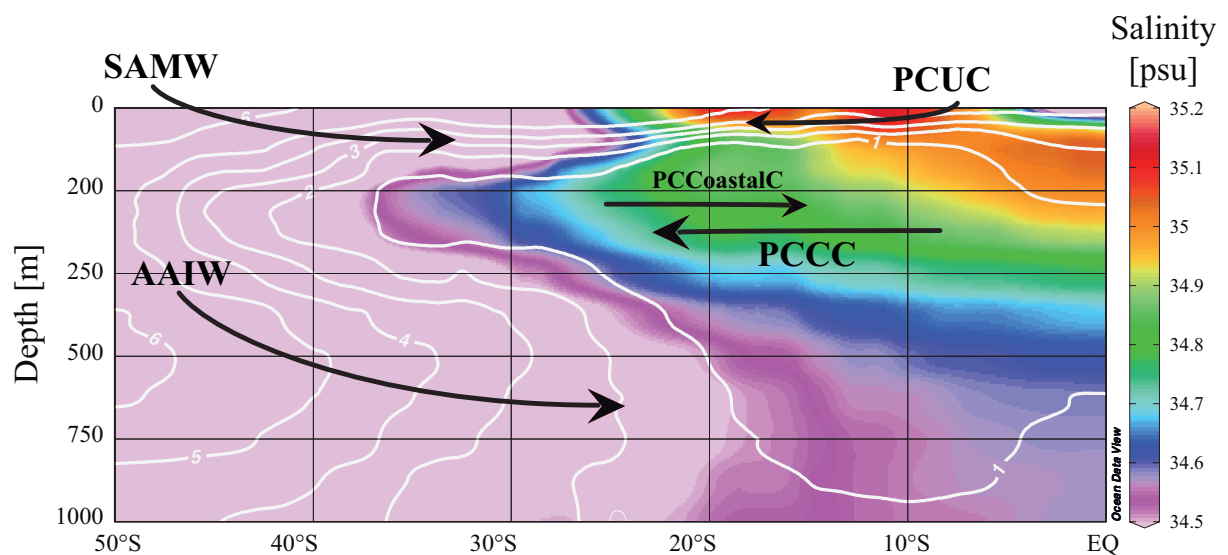


Figure I.6. North-South coastal section of water masses along South America

Hydrology along the South American margin, presented as a North-South section from the equator to 50°S with a width of ~100 km from the coast. The colour shading represents the salinity and the white isoline the oxygen concentrations from 1 to 6 ml L⁻¹. The abbreviations show the main current of the East Pacific: Peru-Chile Coastal Current PCCoastalC, Peru-Chile Counter Current PCCC, Sub Antarctic Mode Water SAMW and Antarctic Intermediate Water AAIW, [Fiedler and Talley, 2006].

I-3.3. Upwelling and productivity

Near shore (between 25 and 150 km away from the coastline) the interaction between the wind and the presence of the continental shelf produces seaward surface flow due to Ekman transport [Ekman, 1905; Price *et al.*, 1987], which in turn brings cool and nutrient-rich subsurface waters to the surface. Such coastal upwelling mixes and shallows the thermocline, which decreases local SST and enhances PP through nutrient supply to the euphotic zone [Pennington *et al.*, 2006]. During the austral winter, the northern position of the ITCZ leads to intense upwelling along the Peruvian coast, while a decrease in trade wind weakens the upwelling during the austral summer [Pennington *et al.*, 2006]. During the seasonal cycle, the peak of chlorophyll *a* occurs a few months after the maxima of upwelling intensity, i.e. during the summer and fall [Echevin *et al.*, 2008; Chavez and Messié, 2009]. According to Pennington *et al.*, [2006], this seasonal time lag may result from a deeper surface mixed layer restricting light availability or strong turbulent mixing of surface waters hindering phytoplankton growth. In the Peruvian Coastal Upwelling (PCU), the dominant primary producers are diatoms, of which the distribution may be related to prevailing climatic and oceanographic features [Abrantes *et al.*, 2007].

During La Niña, trade winds enhance upwelling, and the opposite occurs during El Niño. During El Niño events, physico-chemical processes as well as biogeochemical ones are strongly modified and a collapse of the upwelling leads to a dramatic decrease in PP, a strong increase in regional rainfall, and a reduction of the OMZ extent via a deepening of the thermocline and oxycline [Huyer *et al.*, 1987; Barber *et al.*, 1996]. At the same time, fisheries are largely reduced by the shutdown of the nutrient input from the upwelling [Philander, 1983; McPhaden *et al.*, 1998].

I-3.4. Nutrient cycles and OMZ

The PCU system is characterized by large exchanges of heat and CO₂ between the ocean and the atmosphere, due to the upwelling of cold, nutrient rich and CO₂ saturated subsurface

waters [Friederich *et al.*, 2008]. Due to the nutrient rich waters transported to the surface, which strongly increases biological PP, this area is one of the most productive ecosystems in the world ocean [Pennington *et al.*, 2006; Chavez *et al.*, 2008]. Additionally, the upwelled water releases large amounts of CO₂ in the atmosphere, due to a decrease of its solubility during their warming toward the surface [Friederich *et al.*, 2008]. However, the large surface PP consumes carbon for OM production, thus the balance between the CO₂ consumption by the biota and the release by the upwelling is difficult to disentangle [Wanninkhof and McGillies, 1999; Takahashi *et al.*, 2002]. The impact of the upwelling on the total carbon cycle is still under debate [Keeling *et al.*, 1996]. The seasonal time lag between the most intense upwelling and the PP maximum may lead to HNLC conditions, such as the one observed in the EEP [Cullen *et al.*, 1992], which has been proposed to be led by either grazing, iron or silicate limitation [Martin *et al.*, 1989; Fiedler *et al.*, 1991; Hutchins *et al.*, 2002; Bruland *et al.*, 2005].

Associated with the PCU, an intense OMZ underlays the current system and extends far offshore (Figure I.7), as a result of the interplay between the sinking of surface-derived high PP, leading to strong oxygen consumption due to OM remineralisation, and a weak ventilation by subsurface circulation [Fiedler and Talley, 2006]. Among the three OMZs in the World Ocean (Eastern South Pacific ESP, Eastern North Pacific ENP, and Arabian Sea AS), the Peruvian OMZ remains the shallowest and largest in regard of the volume (Figure I.7; [Kessler, 2006]). Off southern Peru where the OMZ is most intense and shallowest, the oxygen content ranges from saturated values at the surface to values <10 ml L⁻¹ at very shallow water depths (<50 m), while values <1 ml L⁻¹ are reached within the core of the OMZ (Figure I.6; [Karstensen *et al.*, 2008; Paulmier and Ruiz-Pino, 2009]). On average, the Peruvian OMZ ranges between 30-70 m and 300-500 m water depth. The OMZ spatial extent varies in function of the PP and the subsurface ventilation according, which makes it very sensitive to climate variability.

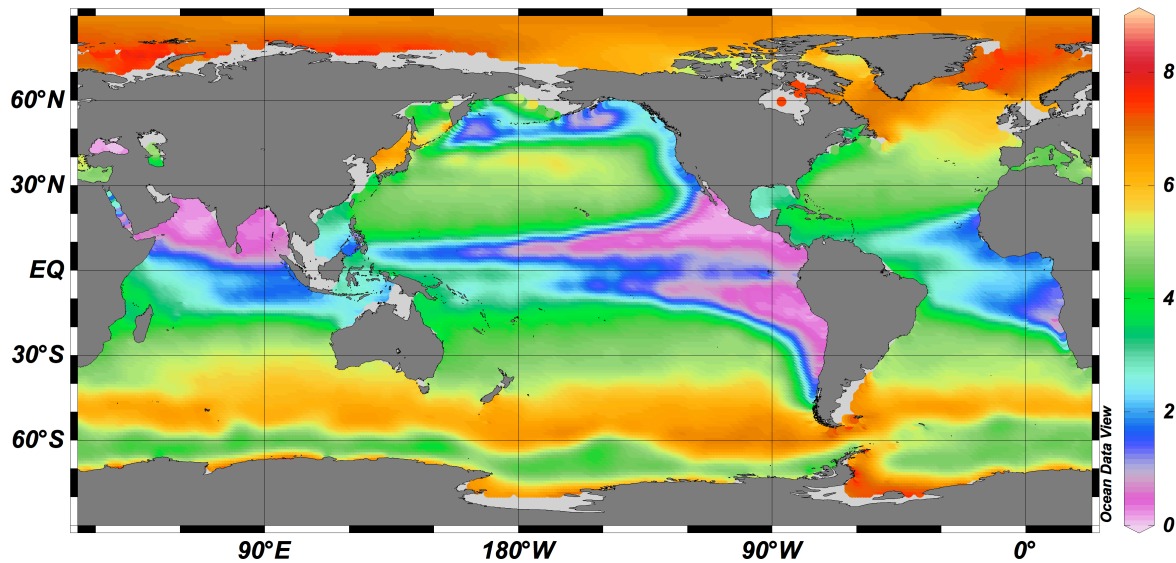


Figure I.7. Oxygen concentration in the world ocean

Oceanic dissolved oxygen concentrations distribution, in ml L^{-1} , at 250 m water depth. Dataset extracted from WOA09.

I-3.5. Past variability of the ETSP

Numerous evidence from paleoclimatic archives indicates that the ITCZ dynamics were affected on a longer term by global climate changes such as during the last deglaciation, which was globally characterized by a northward shift in the ITCZ position during this period, from ~ 19 ka BP to the early Holocene [Wang *et al.*, 2004; Gasse *et al.*, 2008]. During the abrupt climatic events which punctuated the last deglaciation such as the Heinrich 1 (H1, 19-17 ka BP) or the Younger Dryas (YD, 12.5-11.5 ka BP) cold events [McManus *et al.*, 2004; Rahmstorf, 2006] a southward shift in maximum rainfall was also recorded over northern South America [Peterson *et al.*, 2000; Haug *et al.*, 2001; Cruz *et al.*, 2009]. During the middle Holocene, an increase in interannual climate variability was attributed to the onset of ENSO at ~ 5 ka BP [Moy *et al.*, 2002].

The intensity of the Peruvian upwelling is known to strongly vary on annual and interannual timescales, but is also supposed to have been sensitive to climate changes on millennial to orbital timescale variations [Chazen *et al.*, 2009]. However the distinction between variability in ENSO and seasonality remains difficult to disentangle in the sediment, as well as the timing of its initial onset [Martin *et al.*, 1993; Rodbell *et al.*, 1999; Clement *et al.*, 2000; Rein *et al.*, 2005; Marchitto *et al.*, 2010].

It is also well known that the OMZ's extension has varied over the past [Altabet *et al.*, 1995; Ganeshram *et al.*, 1995; Martinez *et al.*, 2006; Pichevin *et al.*, 2007; Robinson *et al.*, 2007; Guitierrez *et al.*, 2009], parallel with changes in subsurface ventilation, surface ocean circulation and regional PP. Studies have been conducted in OMZ areas with different approaches to quantify oxygen content in the water column. Benthic foraminifera assemblages have been used to reconstruct past changes in oxygen content in the ETNP and ETSP [Cannariato and Kennett, 1999; Mallon, Thesis, 2011], as well as redox-sensitive trace metals in the sediment underlying the Peruvian OMZ (e.g. U, Mo, Cd, Re), which respond in specific manner to short-term oxygen fluctuations in the water column [Scholz *et al.*, 2011]. However, the quantitative reconstruction of past O₂ concentration in the oceanic water column still remains a challenge in paleoceanography.

Even though OMZ's are usually considered as dead zones, microbial processes taking place within the core of the OMZ, -i.e. where O₂ concentrations are below 2-10 μmol L⁻¹- allow tracing of N-loss by anaerobic bacteria through measurements of nitrogen isotopes. Specialized microbes use nitrate as an oxidant during the degradation of the OM and reduce nitrate into nitrous oxide (N₂O), and later on into nitrogen gas (N₂) [Codispoti, 2007; Lam *et al.*, 2009]. These so called N-loss processes, denitrification and/or anammox (developed in the following Chapter 11.4), represent a loss of bio-available nitrogen from the global ocean and produce N₂O gas, which is a strong greenhouse gas [Nevison *et al.*, 1995].

During these reduction steps, organisms preferentially use ¹⁴N instead of ¹⁵N, which makes the remaining nitrate pool enriched in ¹⁵N. Via upwelling, high ¹⁵N nitrate is then brought to the surface and assimilated by the biota, which may be ultimately recorded in the sediment after sinking of the OM [Cline and Kaplan, 1975; Brandes *et al.*, 2007; Granger *et al.*, 2008; Sigman *et al.*, 2009]. Following on these findings, a number of studies have used bulk sediment δ¹⁵N to reconstruct past changes in water column N-loss. They evidenced large changes in tropical OMZ's in response to climate fluctuations on orbital and millennial time-scales [e.g., Ganeshram *et al.*, 2000; Liu *et al.*, 2005; Pichevin *et al.*, 2007; Martinez and Robinson, 2010]. Some of these studies reported that cold climatic intervals were in general characterized by OMZ's contraction, while warm climatic intervals experienced expansion with corresponding changes in the ocean's nitrogen budget. Several mechanisms have been proposed as candidates for explaining the inferred variability, such as local PP variations which may trigger changes in local oxygen demand [Altabet *et al.*, 2002], or remote forcing of O₂ supply from intermediate water mass sources [Galbraith *et al.*, 2004; Meissner *et al.*, 2005;

Hendy and Pedersen, 2006]. Along the Peruvian margin, several studies have focused on the Holocene [*Agnihotri et al., 2006; Chazen et al., 2009*] and on the last few centuries [*Gutiérrez et al., 2009*]. Few modeling studies have been generated to better understand the factors influencing the OMZ extent and the subsequent implications for $\delta^{15}\text{N}$ measured in the water column and in the sediment [*Somes et al., 2010a; Somes et al., 2010b*].

Studies of the Peruvian OMZ during the Holocene time period mainly focused on the perennial upwelling location ($\sim 12^\circ\text{S}$) [see e.g. *Higginson et al., 2004; Agnihotri et al., 2006; Chazen et al., 2009; Gutiérrez et al., 2009*] and only few cover the last deglaciation [*Rein et al., 2005; Altabet et al., 2005*] (See following Chapter II.5). The present study completes the previous studies by mapping both biogeochemical and hydrological indicators along the entire Peruvian margin and comparing different cores located all along the Peruvian margin, within and outside the core of the OMZ.

Chapter II. Paleoproxies

The main goal of this study is to reconstruct past changes in the OMZ extent during the last 18 ka BP. Within the SFB 754 framework, inter-laboratory collaborations permitted a regional calibration of paleoproxies based on proxy measurements performed on the water column and on core tops, in an attempt to better understand the significance of paleoproxy measurements performed downcore on marine sediment cores. This calibration gave confidence in our interpretation of subsequent paleoproxy measurements performed in an attempt to reconstruct changes in surface and subsurface circulation regimes; this including variations in oxygen content and nutrient cycling, as well as changes in local upwelling intensity and PP.

Exported primary productivity, the first-order factor responsible for oxygen consumption through degradation of OM within the sinking particles, was reconstructed using measurements performed on dry bulk sediments such as the organic carbon content (C_{org}) as well as total nitrogen (mostly organic nitrogen, TN) and its isotopic signature ($\delta^{15}N$). In addition, the sedimentary content of biogenic opal (SiO_2) was also used to reconstruct the PP of diatoms and radiolaria, the former being often the most abundant primary producers thriving in nutrient-rich areas.

In upwelling regions, the supply of nutrients into the surface ocean is the main factor influencing the PP, and hence indirectly the OMZ extent. At the same time, the cold subsurface waters being upwelled act to reduce SST prior the PP peaks, so that past ocean SST reconstructions can provide valuable information on the status of past upwelling activity. Along the Peruvian margin, marine sediments contain relatively few planktonic foraminifera. Therefore, biologically-mediated calcium carbonate dissolution makes it difficult to accurately reconstruct paleotemperatures by measuring planktonic foraminifera Mg/Ca. We hence used alkenone-derived paleothermometry in order to estimate past changes in SST. Since alkenones are synthesized by certain species of coccolithophorids, which are primary producers, the high level of PP found in the Peruvian upwelling ecosystem ensures alkenone abundances high enough to estimate SST all along the studied cores.

$\delta^{15}N$ measurements are used to estimate regional nutrient cycling in association with the OMZ extent. However, the largely complex nitrogen cycle within such a dynamical oceanic region makes it difficult to utilize it as a straightforward proxy for nitrate utilization and/or N-

loss processes. For this reason, a multi-proxy approach was used to characterize which water column processes can be traced with $\delta^{15}\text{N}$ measurements performed on marine bulk sediments in relation with past climatic and oceanic changes.

II-1. Paleoproductivity

Several proxies were used to reconstruct past changes in export PP, such as sedimentary content of biogenic opal (SiO_2), organic carbon (C_{org}), total nitrogen (TN) and alkenone concentration [see review by *Henderson*, 2002].

Diatoms are unicellular siliceous phytoplanktonic organisms, and widely spread over the world ocean with particularly high abundances above coastal upwelling regions due to the affinity of diatoms to silica and N, P rich environment [*Abrantes et al.*, 2007]. Along the Peruvian margin, diatoms are the primary source of biogenic SiO_2 recorded in the sediment, with radiolarians and sponges not being a significant fraction of biogenic opal at our studied sites [*De Vries and Schrader*, 1981]. Along the PCU, several species of *Chaetoceros* comprise the most abundant diatom genus, and are especially abundant during austral spring when upwelling is still strong but waters are relatively clear to allow photosynthesis [*Strub et al.*, 1998]. The biogenic SiO_2 recorded in the sediment is also dependent on the availability of dissolved silica in the surface waters, as well as the silicic acid saturation within the subsurface water, which affects the preservation of SiO_2 [*Ragueneau et al.*, 2000]. It has also been observed that the thickness of diatom tests and consequently the SiO_2 preservation can be altered by iron availability [*Hutchins et al.*, 2002].

Downcore variability of sedimentary content of organic carbon (C_{org}), total nitrogen (TN) as well as alkenone concentration is also considered to reflect past changes in the overall biological production. In many highly productive regions, C_{org} is closely associated with annual SiO_2 production [*Pennington et al.*, 2006]. As for other coastal upwelling systems [*Müller*, 1977], it is reasonable to assume that the contribution of inorganic nitrogen, clay-bound or otherwise, is negligible as compared to organic nitrogen in the OM-rich sediments characterizing the sediments underneath the Peruvian upwelling system [*Müller*, 1977; *Martinez et al.*, 2006]. Therefore, TN is considered here as being almost entirely related to nitrogen originating from organic tissues reaching the seafloor ultimately derived from planktonic organisms. The alkenone concentration is an indicator of past changes in coccolithophorid productivity, which is one of the main calcium carbonate producers in the

open ocean. Even if it has been shown that within the oxygenated water, only ~1% of the phytoplankton production is buried in the sediment, the alkenones are well preserved in the sediment and provide some estimation for past changes in surface PP imputable to some species of coccolithophorids [Prahl *et al.*, 1989].

Paleoproductivity estimations from these above-mentioned sedimentary proxies are also affected by a complex set of oceanic processes unrelated to PP [Ragueneau *et al.*, 2000], such as dissolution, transport by current, diagenesis, etc. However, even if each proxy bears its own strengths and weaknesses, and in particular in regard of the difficulty to distinguish between preservation and productivity signals, a multi-proxy approach might allow to differentiate between proxy-dependent effects and changes in PP.

C/N ratio and $\delta^{13}\text{C}$ measurements performed on the C_{org} are often used to disentangle the terrestrial origin of OM from the marine one. Terrestrial OM is characterized by relatively low $\delta^{13}\text{C}_{\text{org}}$ values of -27 to -33‰, and high C/N ratios >20. In contrast, marine OM has typical $\delta^{13}\text{C}_{\text{org}}$ signatures varying between -19 and -22‰ and C/N ratios close to the Redfield ratio of 6 to 7 [Emerson and Hedges, 1988; Jasper and Gagosian, 1989; Hebbeln, 1992].

II-2. Terrigenous input

XRF scanner measurements allow the reconstruction of the elemental composition of the sediments. We use the Ti element intensity (in counts per seconds) relative to the Ca intensity to monitor past changes in terrigenous detrital content relative to marine carbonates, and consider it as a proxy for riverine runoff as in previous studies [Arz *et al.*, 1998; Haug *et al.*, 2001; Jaeschke *et al.*, 2007]. On the Peruvian margin, where the rainfall depends on the seasonal position of the ITCZ and on the ENSO variability, an estimation of the riverine runoff variability allows the reconstruction of regional rainfall changes over time which can be used to reconstruct past changes in the ITCZ dynamics and/or in the ENSO variability. As the ITCZ dynamics are closely related to the upwelling intensity along the Peruvian coast, it can be used as an indirect indicator of coastal Peruvian upwelling. We also used Bromine (Br) counts as well as Br/Ti to infer past changes in export production of OM [Ziegler *et al.*, 2008]. Downcore XRF scanner profiles may therefore be useful to disentangle the complexity of the multi-proxy reconstruction of the upwelling variability.

II-3. Alkenone/SST

SST has been estimated by using the alkenone unsaturation index (U_{37}^K) measured on the multicores and piston cores. In the modern ocean, C_{37} alkenones, long-chain unsaturated ketones ($C_{37:2}$ and $C_{37:3}$) are synthesized mainly by some species of coccolithophorids, (mainly *Emiliania huxleyi* and *Gephyrocapsa oceanica*), which live in the uppermost meters of the euphotic zone [Marlowe et al., 1990; Conte et al., 1992; Conte and Eglinton, 1993]. Alkenones are widely used to reconstruct SST, as the relative concentration of $C_{37:2}$ and $C_{37:3}$ varies in response to SST where the organism grew [Brassell et al., 1986; Ternois et al., 1997; Müller et al., 1998; Prahl et al., 2000; Conte et al., 2006]. The U_{37}^K index is calculated as follows (Equation 1):

$$U_{37}^K = (C_{37:2}) / (C_{37:2} + C_{37:3}) \quad (1)$$

Several calibrations exist to estimate SST; most of them are based on the following type of the equation (2):

$$SST = (U_{37}^K - a) / b \quad (2)$$

Calibrations based on surface sediments throughout the world ocean indicate that the alkenone-derived paleothermometry reflects mean-annual SST [Sonzogni et al., 1997; Müller et al., 1998]. However, recent studies point out a decoupling of the alkenone-based SST estimation and the mean-annual SST for coastal upwelling systems, suggesting that other processes may bias the SST estimation in the Peruvian upwelling area [Prahl et al., 2010; Kienast et al., 2012]. Additionally, a comparison between SST from alkenones and Magnesium/calcium (Mg/Ca) on foraminifera shows a diverging trend during the Holocene in this area. Alkenones show an increase in SST; while SST derived from planktonic foraminifera Mg/Ca rather suggests that SST have decreased slightly over the Holocene [Leduc et al., 2010]. A seasonal effect has been proposed to explain the difference in the paleo-SST signal of different organisms. However, the real origin of this divergence is not well understood yet, and complex interplay between coccolithophorids and diatoms [Schneider et al., 2010] and/or a problem in the calibration of the proxies cannot be excluded. Mg/Ca ratios of planktonic and benthic foraminifera have been measured in the northern part of the Peruvian margin and will be published elsewhere within the framework of the SFB754, subproject A6 [Böschen in prep].

Within this study, a comparison of the SST measured in the surface sediment and a map of satellite SST suggest that alkenone-based SST may be skewed toward the warm season or that the satellite data are not representing the cooling over the last 100 years.

II-4. Nitrogen isotopes

Paleo-changes of the OMZ extent may have strongly influenced the regional nitrogen cycle, either by changes in the relative nitrate utilization by the phytoplankton in surface waters, or by nitrate consumption within the OMZ core by N-loss processes. For these reasons, several studies have been using $\delta^{15}\text{N}$ in sediments to track changes in the subsurface O_2 concentrations across the past [Altabet *et al.*, 1995; Ganeshram *et al.*, 1995; Ganeshram *et al.*, 2000; Galbraith *et al.*, 2004; Altabet, 2006; Pichevin *et al.*, 2007; Martinez and Robinson, 2010; Sigman *et al.*, 2009]. Under suboxic conditions [$\text{O}_2 < 0.5 \text{ mg L}^{-1}$], heterotrophic bacteria reduce NO_3^- to N_2 through the so-called N-loss processes [Codispoti, 2007]. During these processes, light nitrate ($^{14}\text{N}_{\text{NO}_3^-}$) is preferentially removed from the water, leaving the remaining nitrate pool enriched in heavy nitrate ($^{15}\text{N}_{\text{NO}_3^-}$). Dissimilatory NO_3^- reduction, the first step in N-loss, causes pronounced isotopic fractionation (fractionation factor of $\sim 30\%$), producing isotopically light products (N_2 and N_2O), and isotopically heavier residual nitrate [Cline and Kaplan, 1975; Granger *et al.*, 2008]. The supply of nitrate to surface waters by upwelling and its utilization by plankton results in particulates OM isotopically enriched in ^{15}N that is ultimately buried in the sediments [Ganeshram *et al.*, 1995; Altabet *et al.*, 1999; Altabet, 2006]. The relative importance of denitrification, the stepwise reduction process involving a number of intermediates ($\text{NO}_3^- \rightarrow \text{NO}_2^- \rightarrow \text{NO} \rightarrow \text{N}_2\text{O} \rightarrow \text{N}_2$), compared to anammox (a more direct process, $\text{NO}_2^- + \text{NH}_4^+ \rightarrow \text{N}_2$) is strongly debated for the Peruvian OMZ and upwelling system [Lam *et al.*, 2009]. However, the dissimilatory reduction of nitrate to nitrite is the first step required for both processes. It follows that the isotopic fractionation during nitrate reduction is independent of which process ultimately leads to N_2 production and reflects net NO_3^- removal from the system. This isotopically high nitrate remaining within the OMZ core is then upwelled to the surface where it is used by the biota and might be finally buried in the underlying sediment.

Even if $\delta^{15}\text{N}$ is often used as an indicator of changes in subsurface O_2 concentrations in highly productive environments [Ganeshram *et al.*, 2000; Agnihotri *et al.*, 2006;], many other factors can generate nitrogen isotopic fluctuations such as relative nitrate utilization and the initial isotopic signature of the water mass [Mariotti *et al.*, 1981; Altabet and Francois, 1994; Martinez *et al.*, 2000]. Although the observed fractionation factor for this process (5 to 10%) is significantly lower than during N-loss processes (20-30%), it still can produce significant

isotopic enrichment of the remaining pool [*Holmes et al.*, 1998; *Waser et al.*, 1998; *Granger et al.*, 2004; *Horn et al.*, 2011]. Indeed, phytoplankton preferentially takes up NO_3^- containing the lighter nitrogen isotope (^{14}N) during photosynthesis and thus becomes depleted in ^{15}N with respect to the isotopic composition of the initial NO_3^- substrate [*Wada and Hattori*, 1978; *Waser et al.*, 1998; *Granger et al.*, 2004]. Thus, a low relative utilization of NO_3^- will tend to drive the $\delta^{15}\text{N}$ signal in particulate OM lower than the upwelled $\delta^{15}\text{N}_{\text{NO}_3^-}$ values. The corollary is that a complete NO_3^- utilization would result in a sedimentary $\delta^{15}\text{N}$ very close to the initial $\delta^{15}\text{N}_{\text{NO}_3^-}$ [*Altabet and Francois*, 1994, 2001; *Freudenthal et al.*, 2001].

A $\delta^{15}\text{N}$ signal of partial NO_3^- utilization in the sediment [*Francois et al.*, 1992; *Farrell et al.*, 1995; *Sigman et al.*, 1999] is typically observed in HNLC regions such as the Southern Ocean or the EEP [*Cullen et al.*, 1992], where persistent Fe limitation [*Martin et al.*, 1989] allows only partial NO_3^- utilization in surface waters even on a seasonal basis. Previous OMZ paleo-studies have been done only for areas not being considered as HNLC regions (Arabian Sea and ETNP OMZs). In the Peruvian OMZ, the intense perennial upwelling and moderate Fe limitation [*Bruland et al.*, 2005] on portions of the margin may produce a local HNLC-like effect. Hence $\delta^{15}\text{N}_{\text{sed}}$ in this region may reflect both water-column N-loss affecting the $\delta^{15}\text{N}$ of upwelled NO_3^- as well as its subsequent partial utilization in surface waters affecting the $\delta^{15}\text{N}$ of OM. Hence, both contributors to $\delta^{15}\text{N}_{\text{sed}}$ in the studied region are also expected to vary spatially with a) surface gradients in the relative nitrate utilization (which may also have a seasonal component) and b) subsurface OMZ intensity, respectively.

For nitrate utilization as well as N-loss processes, the initial isotopic signature of the water mass is important to take into account, as it sets up the isotopic values of the nitrogen substrate original values, so that an already isotopically heavy water mass will become even heavier. Even though the Peruvian margin hosts the biggest and shallowest OMZ in the World, the $\delta^{15}\text{N}$ recorded in the sediment are still very low as compared to what would intuitively be expected from such a high fertile environment. Indeed, south of the Peruvian OMZ the $\delta^{15}\text{N}$ values from the Chilean margin are much higher than the Peruvian ones, although the OMZ already disappears [*De Pol-Holz et al.*, 2009].

II-5. Paleo-studies of the region

It has been shown that OMZ in equatorial waters expand over the last century [*Stramma et al.*, 2010], thus we assume that in addition to be sensitive to seasonality and ENSO events,

OMZs extent was also influenced by longer-term climate variability. However past variations in OMZs are difficult to assess because paleoceanographic proxies do not directly relate to oxygen concentrations. Therefore surface and subsurface circulation related to climate changes, influencing variation in oxygen and nitrate available in the system, as well as changes in local upwelling intensity and export PP have been studied to estimate past fluctuation of OMZ conditions.

Along the Peruvian margin, core-top and piston core samples have been studied by *Wolf* [Thesis, 2002] and show an increase of export PP flux within the zone of the perennial upwelling, which is consistent with the modern data [<http://oceancolor.gsfc.nasa.gov/cgi/l3>]. However, paleo-reconstructions are more difficult to assign straightforward to the amount of export production as the terrigenous input play a major role in the dilution of the previously mentioned fraction.

Intense upwelling occurring in the southern part of the Peruvian margin generates a large sedimentation rate above the continental shelf, which had also varied over time [*Skilbeck and Fink, 2006*]. However, the active continental margin off Peru and Ecuador strongly disturbs the sedimentation of this area and makes it difficult to retrieve long and continuous records with high resolution on this shelf. Additionally, the northern part of the continental shelf remains shallow far offshore (up to ~100 km from the coast) but becomes narrow in the South with strong subsurface currents along the shelf break, reducing the sedimentation rate at this location. The shallow shelf makes the sampling of long term paleo-records harder in this area, due to a large impact of the sea-level transgression onto the shelf during the deglaciation [*Wolf, 2002*].

Therefore, many studies have been focused on the EEP, along the Pacific Cold Tongue, e.g., the Galapagos area and the Nazca Ridge [*Feldberg and Mix, 2003; Kienast et al., 2007; Koutavas and Sachs, 2008; Pichevin et al., 2009; Dubois et al., 2011*], which play a big role on the Peruvian hydrology or are influenced by the Peruvian upwelling system and associated processes [*Fiedler and Talley, 2006; Kessler, 2006*].

At the most southern limb of the Hadley cell, changes in the Westerlies position and intensity have been investigated along the Chilean margin as link to the ITCZ movements [*Kim et al., 2002; Kaiser et al., 2008; Lamy et al., 2010*]. These studies reconstructed paleo-SST addressing changes in circulation of the southern Peru-Chile Current system and possible impacts of the melting of the Patagonian ice sheets and southern ocean climate change.

Paleo-SST reconstructions for changes in ocean circulation and upwelling intensity cannot be addressed by foraminiferal oxygen isotope records and/or Mg/Ca ratios, as planktonic foraminifera are rare along the Peruvian margin, restricting as well carbon-14 (^{14}C) dating based on planktonic foraminifera. However, benthic foraminifera have been used to reconstruct nitrate concentrations [Glock *et al.*, 2011] and species assemblages for oxygen concentration [Mallon, 2011] along the Peruvian margin.

As a matter of fact, paleo-SST reconstructions were based on alkenones measurements (SST_{alk}) to better estimate changes in upwelling intensity along the Peruvian margin. Most of the studies are located at the perennial upwelling zone ($\sim 12^\circ\text{S}$) and mainly concentrate on last few centuries [Sifeddine *et al.*, 2008; Gutiérrez *et al.*, 2011], on the Holocene time period [Chazen *et al.*, 2009] and only one is covering the last deglaciation [Rein *et al.*, 2005]. Calibration of alkenone unsaturation ratios in the sediment with local and seasonal SST have not been done along the Peruvian margin but at the global scale, however showing some problems at this specific area, as discussed in Chapter IV.1. [Prah *et al.*, 2010; Kienast *et al.*, 2012].

During the mid-Holocene, Rein *et al.*, [2005] interpreted a decrease of sedimentation rate contemporary to a SST_{alk} decrease as a weakening of El Niño events. Several studies have also been done on sedimentological characteristics forced by the regional currentology [Wells, 1990; Skilbeck and Fink, 2006; Gutiérrez *et al.*, 2009].

As cited before, interannual ENSO related climate variability plays a large role in the hydrographic dynamics of the tropical Pacific [Cane, 2005]. Past changes of such events have been for long time studied on land using different methods at several sites, such as laminated sediments from Andean lake in Ecuador [Rodbell *et al.*, 1999; Moy *et al.*, 2002], Andean glaciers [Thompson *et al.*, 1998; Jomelli *et al.*, 2011] as well as archeological excavations along the Peruvian coast [Sandweiss *et al.*, 2009 and references therein].

$\delta^{15}\text{N}$ measurements in the sediment allow an estimation of the OMZ extent via an estimation of the N-loss processes taking place in the water column and being recorded in the sediment, as presented in the previous chapter [Chapter II-4]. Several studies have been done off the Chilean margin [De Pol-Holz *et al.*, 2006; Martinez *et al.*, 2006; Robinson *et al.*, 2007] and few off Peru located at the perennial upwelling area at a low resolution [Ganeshram *et al.*, 2000] or focused on the Holocene time period [Agnihotri *et al.*, 2006; Chazen *et al.*, 2009] and covering the last deglaciation [Higginson *et al.*, 2004]. However, calibration between the

modern data $\delta^{15}\text{N}$ within the water column and in the surface sediment has been only done along the Chilean margin [*De Pol-Holz et al.*, 2009].

The high resolution sedimentary records in this present study are the first covering the Holocene and the deglaciation along a North-South transect off the Peruvian margin.

Chapter III. Methodology

III-1. Sampling area

Surface sediments were collected during two cruises on board the German research vessel Meteor (cruises M77-1 and -2, 2008, [Pfannkuche *et al.*, 2008; Schneider *et al.*, 2008]). The sampling area extends from 1°N to 17°S and covers the Ecuadorian and Peruvian margins by 81 stations between 60 m and 2080 m depth along the coast (Figure III.1). This sampling covers the northern part and the core of the Peruvian OMZ from North to South and some cross-shelf transects at several latitudes (Chapter V; Figure V.1 and Figure V.2). The large distribution of the sampling allows a good reconstruction of how the processes link to the OMZ system later recorded in the sediment. At each of these stations, 6 multicorer tubes (30-60 cm each) were retrieved. An additional set of 13 samples from IMARPE (Instituto Del Mar del Perú, Lima), located between 5°S and 14°S, was also analyzed and included into this study.

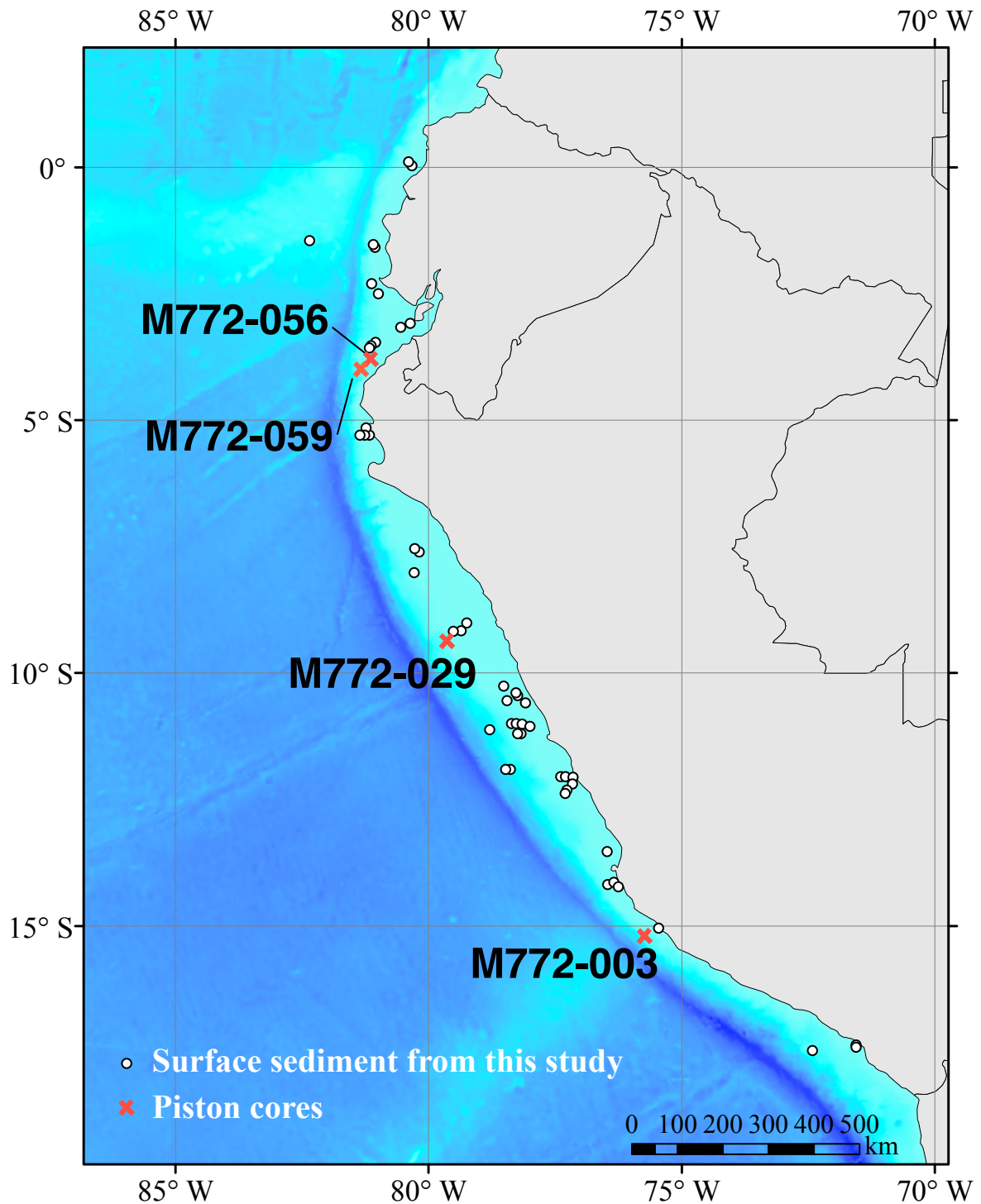


Figure III.1. Sample locations

Sample locations: white circles represent the surface sediment and the red crosses the piston core. The blue shading represents the marine topography (GEBCO One Minute Grid, version 2.0, <http://www.gebco.net>, courtesy from B. Willi e).

The four long piston-cores (10 to 15 m) studied here were collected from three key locations along the Peruvian margin (Figure III.1). The two northern cores, M772-056 and -

059 are located at the same latitude, 3.5°S, at the northern edge of the OMZ but at two different distances from the coast and different water depths (355 m and 997 m), respectively. Here sediments consist of fine homogenous green mud, and the high oxygen concentrations prevent the formation of laminations. The core descriptions of each core are reported in the cruise report from the cruise M772 on the following website: http://www.dfg-ozean.de/de/berichte/fs_meteor]. The two southern cores M772-029 and -003 are located at shallow depths, at the rim and within the core of the modern OMZ (433 m, 9°S and 271 m, 15°S, respectively). At these depths and latitudes, the combination of high biological export production and large oxygen deficiency result in high sedimentation rates, the absence of bioturbation and thus in the formation of millimeter scale green to yellow laminations that dominate the whole sedimentary sequences [http://www.dfg-ozean.de/de/berichte/fs_meteor]. Most of the cores are composed by sediment deposits from the last Deglaciation and the Holocene, which allowed biogeochemical reconstructions outside, at the edge and within the core of the OMZ during the last 18 ka BP.

III-2. Methods

For all the sediment samples, the two first centimeters of the multicores and each 5 cm from the piston cores, were freeze-dried, ground and homogenized using an agate mortar prior to all chemical analyses.

III-2.1. Analysis of export production-related proxies

The biogenic opal (SiO₂) measurements done at GEOMAR (Kiel, Germany) were carried out on 20 mg of freeze-dried and homogenized bulk sediment by using an automated extraction method and wet chemical leaching as described in *Müller and Schneider* [1993]. Standard deviation based on repeated measurements is $\pm 0.5\%$.

Organic carbon (C_{org}, wt %) was measured at the University of Bordeaux 1 (France), on the same samples used for SiO₂ measurements. A LECO C-S 125 analyzer was used after treatment of ~80-100 mg of sediment with hydrochloric acid (1N) to remove calcium carbonate. The precision on repeated measurements was better than $\pm 0.5\%$.

Total nitrogen was measured at the University of Bordeaux 1 with a Carlo-Erba CN elemental analyzer 2500 at the same time as the $\delta^{15}\text{N}$ measurements (see Chapter, III-2.4).

When analyzing U_{37}^K , it is also possible to determine the alkenone concentrations (the sum of $C_{37:2}$ and $C_{37:3}$ concentrations) which can be roughly used as a proxy for coccolith paleoproduction. The concentration of these long-chain ketones is determined according to the equation below (3):

$$(C_{37}) = (\text{Area } C_{37}) * [C_{36}] * (\text{Dilution}) / ((\text{Injected vol}) / (\text{Area } C_{36} * \text{Sample weight})) \quad (3)$$

(C_{37}) : respective concentration for either ($C_{37:2}$) or ($C_{37:3}$) in ng g^{-1} ; $[C_{36}]$: concentration of standard (ng g); the dilution (Dilution) and volume (Injected volume) of the sample used for the GC measurement, both expressed in μl ; the Sample weight is expressed in g.

III-2.2. XRF measurements

The X-ray fluorescence (XRF) core scanning instrument of Avaatech provides non-destructive bulk-sediment chemistry data measured on the surface of a split sediment core. The chemical composition is given as element intensities in counts per second (cps). For this work, the three northern cores M772-059 and -056 were measured with a 1 cm resolution using the XRF core scanner, at Kiel University. The split core halves were covered with a 4 μm thick ultralene film to avoid contamination of the XRF measurement unit and desiccation of the sediment. Geochemical data was obtained at two different tube voltages, 10kV for Al, Si, S, Cl, K, Ti, Mn, Fe and 30kV for Zn, Br, Sr, Rb, and Zr [see *Richter et al.*, 2006].

III-2.3. Alkenone analyses

Alkenones have been measured at the Institute of Geosciences at the CAU (Christian Albrecht University of Kiel). All samples were extracted by Accelerator Solvent Extraction (Dionex ASE200) from 0.5 g to 1 g freeze-dried and homogenized sediment samples. The surface sediment samples and the core M772-056 were measured using a solution of dichloromethane (100%) as a solvent at a pressure of 80 mbar and a temperature of 75°C. However after improvement of the extracting method, alkenones of cores M772-029, -003 and -059 were extracted using a mixture of dichloromethane and methanol (9:1) as solvents at a pressure of 100 mbar and a temperature of 100°C. This new method allows a better extraction of the alkenones, which is observed by an increase of the variability. This new method has been tested on one of the cores located at the same latitude (M772-059), and it shows very different SST variability to M772-056, which was measured with the old setup. Different

genus of alkenone concentrations may induce this difference in the SST datasets, however it is unlikely regarding the others proxies showing very similar trends in both cores.

For the extraction of the alkenones, 1 cm layer of silica gel and modified diatomaceous (Isolute HM-N, extraction grade) was poured at the bottom of the extraction cell, then 0.5 to 1 g of sediment was added and the rest of the upper part of the cell was filled by diatomaceous again. The extracts were purified later and analyzed by a double column multidimensional gas chromatograph (Agilent 6890N) system with two flame ionization detectors using hydrogen as a carrier gas (Figure III.2). Alkenone concentrations (C_{37} di- and triunsaturated ketone mass/grams of dry sediment) were calculated by normalizing to two internal standards (Skagerrak and Standard $C_{27}C_{36}$: composed of $10 \mu\text{g L}^{-1}$ of C_{27} and C_{36} $10 \mu\text{g L}^{-1}$), adding $C_{37:2}$ and $C_{37:3}$ in ng g^{-1} (see [Blanz *et al.*, 2005], for a complete description of the method).

The U_{37}^K used to estimate the SST was calculated with the following equations (4):

$$U_{37}^K = (C_{37:2}) / (C_{37:3} + C_{37:2}) \quad (4)$$

As the calibration of Müller *et al.* [1998] is the largest study over the world and thus the more robust, it is the one that has been used for this study (5):

$$\text{SST} = (U_{37}^K - 0.044) / 0.033 \quad (5)$$

Analytical precision, calculated on replicate analyses and repeated extractions of internal standard, is $\pm 0.05 U_{37}^K$ units or $\pm 1.5 \text{ }^\circ\text{C}$.

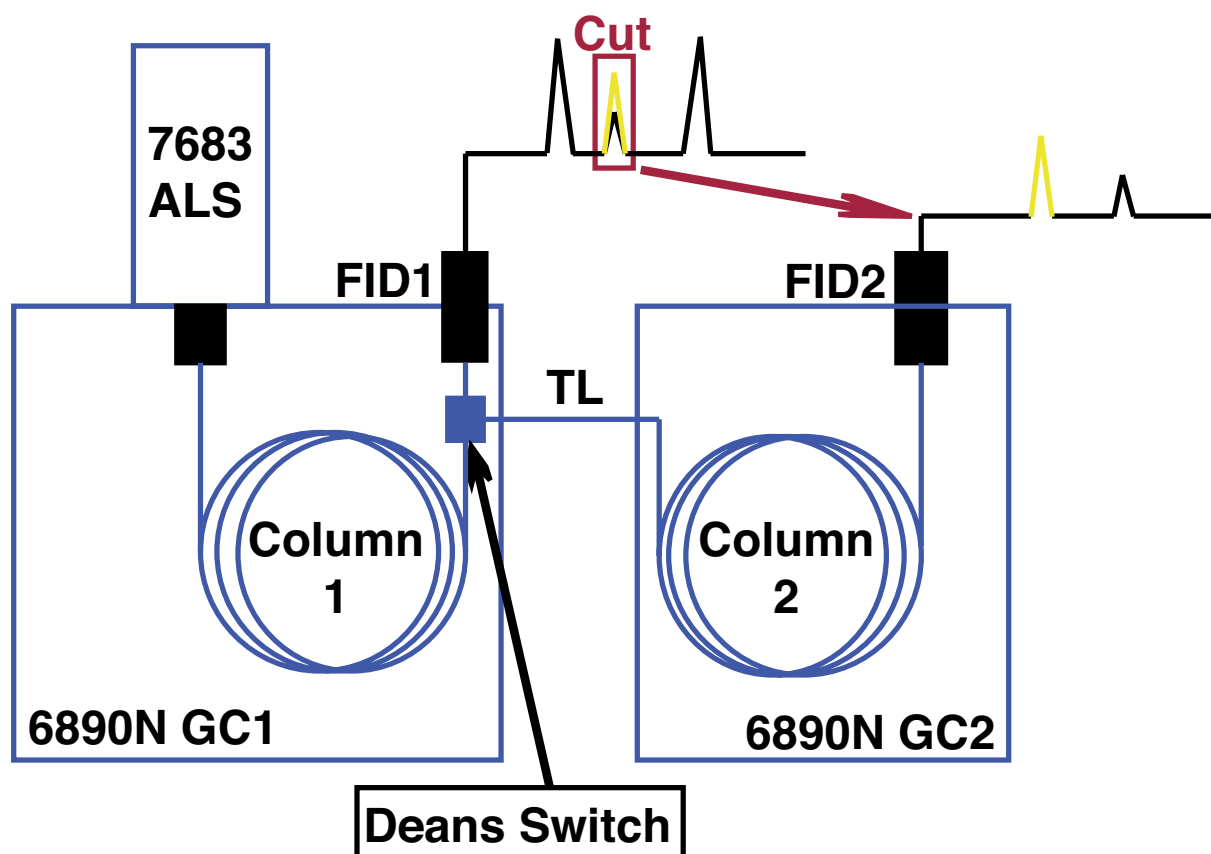


Figure III.2. Schematic representation of the gas chromatograph system

Schematic representation of the gas chromatograph system, using the second column for a better measurement precision of the peaks corresponding to the alkenone concentrations, TL: Transfer Line. Courtesy of T. Blanz.

III-2.4. Nitrogen isotope analyses

Nitrogen isotope ratios ($\delta^{15}\text{N}_{\text{sed}}$) and total nitrogen contents (TN) were measured at the University of Bordeaux I (EPOC, UMR CNRS 5805, France), on 5 to 60 mg of homogenized and freeze-dried bulk sediment. Samples were encapsulated in tin cups and then injected into a Carlo-Erba CN analyser 2500 coupled directly to a Micromass-Isoprime mass spectrometer, using He as the carrier gas (Figure III.3). The isotopic ratio is expressed in the delta notation (6):

$$\delta^{15}\text{N} = \left[\frac{(^{15}\text{N}/^{14}\text{N})_{\text{sample}} - (^{15}\text{N}/^{14}\text{N})_{\text{standard}}}{(^{15}\text{N}/^{14}\text{N})_{\text{standard}}} \right] * 1000 \quad (6)$$

with air N_2 as standard.

The precision of the isotopic analyses and nitrogen concentration were based on repeated measurements of selected sediment samples, in addition with routine international standards, such as Acetanilide for nitrogen concentration, Caseine, Glycine and in-house standards (Bassin) for isotopic measurements. The precision of the analyses based on standards and

samples replicates is ~ 0.23 ‰ and ~ 0.2 ‰ for nitrogen content and nitrogen isotopes respectively.

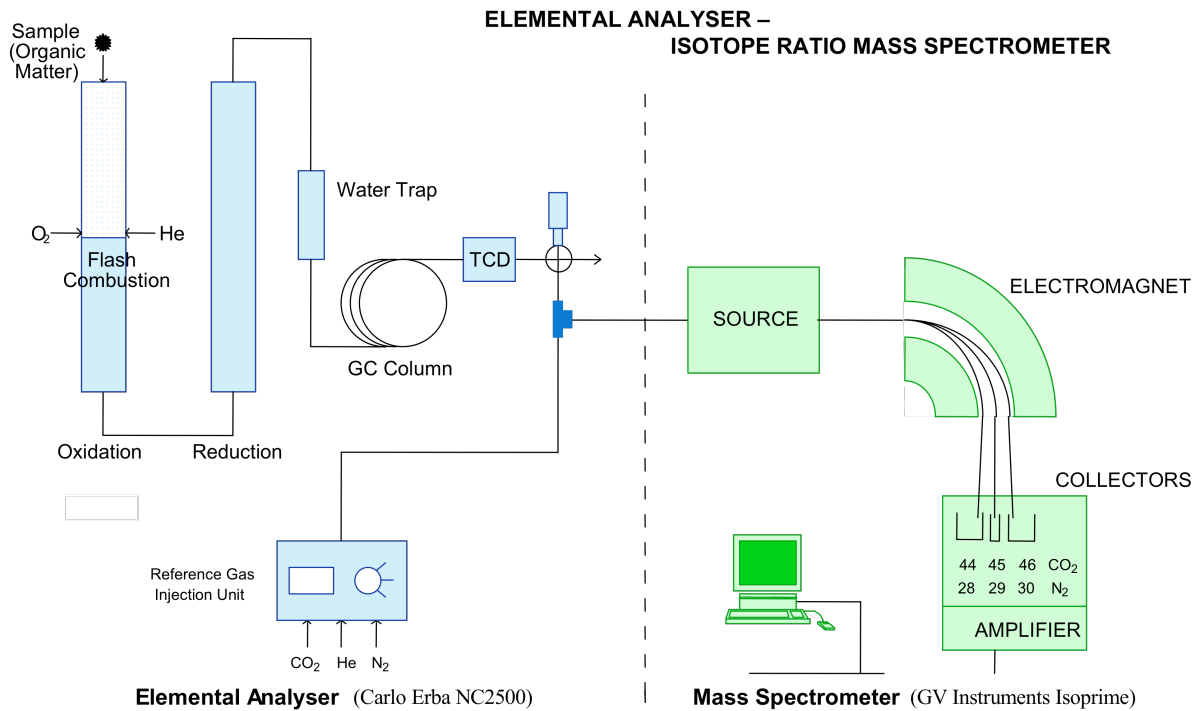


Figure III.3. Schematic representation of the Elemental Analyser and Mass Spectrometer

Schematic representation of the Elemental Analyser (Carlo ERba NC 2500) coupled to a Mass Spectrometer (GV). Reference Gas (CO_2 , He, N_2). Courtesy of Karine Charlier, University of Bordeaux I.

III-2.5. Radiocarbon and core chronology

The age models for the four piston cores are based on 61 radiocarbon measurements (Table 3) performed on the planktonic foraminifer species *Neogloboquadrina dutertrei* for the northern cores and on the humic fraction of OM in the sediments from the southern cores, where planktonic foraminifera were absent or rare. To verify the robustness of the datings on the humic fraction, we applied the two methods on the same samples on the northern core M772-056 (Table 3). For the humic fraction measurements, the sediment was checked under the microscope and an appropriate amount of organic material was selected for dating. The selected material was then extracted with 1% HCl, 1% NaOH, each at 60°C, and again with 1% HCl (alkali residue). The combustion to CO_2 of all fractions was performed in a closed quartz tube together with copper oxide (CuO) and silver wool at 900°C. Subsequently, each

sample gas was sealed again into a quartz tube together with CuO and silver wool and combusted a second time at 900°C in order to remove any contamination inhibiting the reduction of the sample CO₂ to graphite (e.g. sulphur). The sample CO₂ was reduced with H₂ over about 2 mg of Fe powder as catalyst, and the resulting carbon/iron mixture was pressed into a pellet in the target holder. For quality assurance, two portions of the humic acid fraction were sealed, combusted and reduced.

The organic fraction ages (soluble humic fraction) are on average ~800 years older than the calcite ages for the same depth horizon (Table 3). The age difference between the calcite and humic fractions is yet not completely understood, as it was found off Chile, that radiocarbon ages of alkenones also tend to be significantly older than those of foraminifera in coastal upwelling areas [Mollenhauer *et al.*, 2005]. For the time being, we assume that the humic fraction provides radiocarbon dates of mainly marine OM, as shown by C/N ratio and δ¹³C measured on OM, which is closest to that of marine calcite in the same setting. Accordingly, we use the humic fraction dates in the southern cores for chronological control. The MARINE09 calibration curve [Reimer *et al.*, 2009] has been used for all the age calibrations with a ΔR varying between 200 ± 50 years for the northern cores (M772-056 and -059) and up to 511 ± 278 years for the southern cores (M772-029 and -003) because of the intense upwelling taking place in this area [Ortlieb *et al.*, 2011]. The resulting age models imply sedimentation rates varying between ~30 in core -056 and 390 cm per ka in core -029 depending on the more or less coastal location of the core. The higher sampling resolution used for the XRF measurement (each cm), provides a time resolution ranging from ~167 years per cm during the mid-Holocene down to ~13 year per cm for the Heinrich 1 time interval. The two northern cores cover the Holocene (M772-056 and -059), however only the core -059 goes back to the deglaciation. Previous studies have shown that the sedimentation along the Peruvian margin suffers from major gaps [see Reinhardt *et al.*, 2002]. It seems to be particularly the case for the middle part of the Peruvian shelf, around 10-12°S, where many records present especially incomplete Holocene sedimentation [Higginson *et al.*, 2004; Chazen *et al.*, 2009]. In addition, unfortunately, the first 4000 years are also missing at site M772-029. Both of the southern cores (M772-029 and -003) cover the deglaciation and only the M772-003 covers the entire Holocene time period (Table 3).

The results and discussion are presented in the following chapters in the form of articles. Nevertheless, the unpublished data concerning the alkenones measurements on the surface sediment is presented at first, as a small subchapter.

Chapter IV. Alkenones in surface sediments

In organic rich sediments, the alkenone index U_{37}^K is commonly used to reconstruct the mean annual SST, as the Prymnesiophytes synthesize alkenones in relation to the temperature of the water where they grow (more detail in Chapter II-3). However, few recent studies show that it seems to be regionally more complicated than thought before, and a direct relation between U_{37}^K and the mean annual SST may be not totally straightforward [Prah1 *et al.*, 2010; Kienast *et al.*, 2012]. Indeed, seasonality leads to changes in SST, regional upwelling intensity and regional hydrology, which may affect either the timing when the coccolithophores bloom or biogeographical processes over the time. We present here new results of alkenone measurements on core-top samples retrieved during the Meteor cruise (December 2008) along the Ecuadorian-Peruvian margin between 0.5°N and 17°S (Figure IV.1). As described in Chapter II, the robust calibration derived from a world dataset, from Müller *et al.*, [1998] has been used to calculate the Paleo-SST derived from alkenone unsaturation ratios (SST_{alk}).

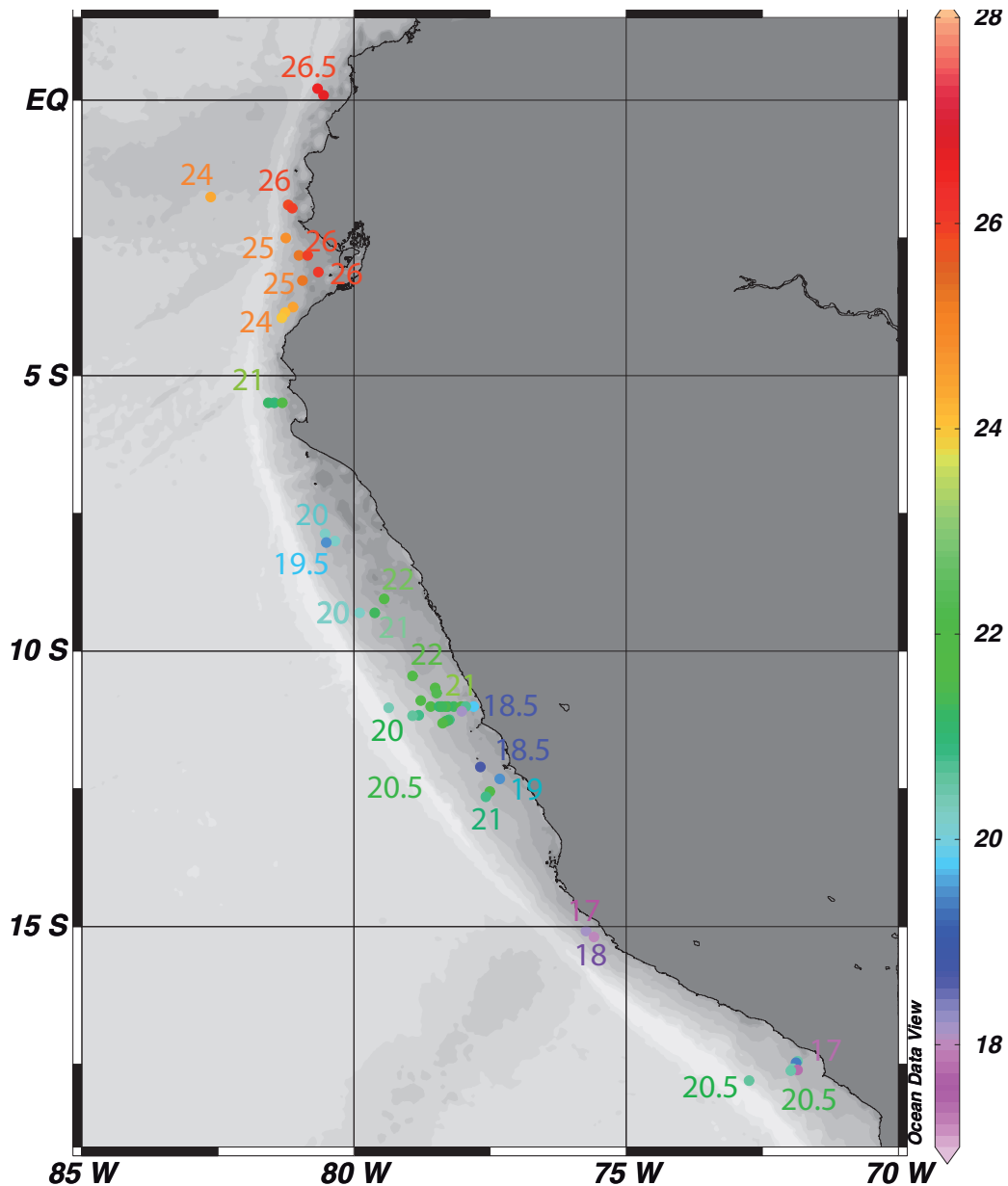


Figure IV.1. SST_{alk} along the Peruvian margin

SST derived from alkenone unsaturation ratios along the Peruvian margin. The gray shading shows the bathymetry of the area.

The Peruvian coast undergoes three different systems from North to South. The seasonality and PP increase southward at the same time that SST decreases due to upwelling:

1. North of 5°S, the Peruvian-Ecuadorian margin is located outside the perennial upwelling area, thus SST are consistently warm.
2. From 5°S to 10°S, the area is influenced by strong seasonality leading to a northward advection of colder surface waters from the more southern perennial upwelling but only during the austral winter (Jul-Aug-Sep).
3. Off central and southern Peru, 10°S to 15°S, the perennial upwelling cells occur during the entire year and

with a stronger intensity during the austral winter (Figure IV.2).

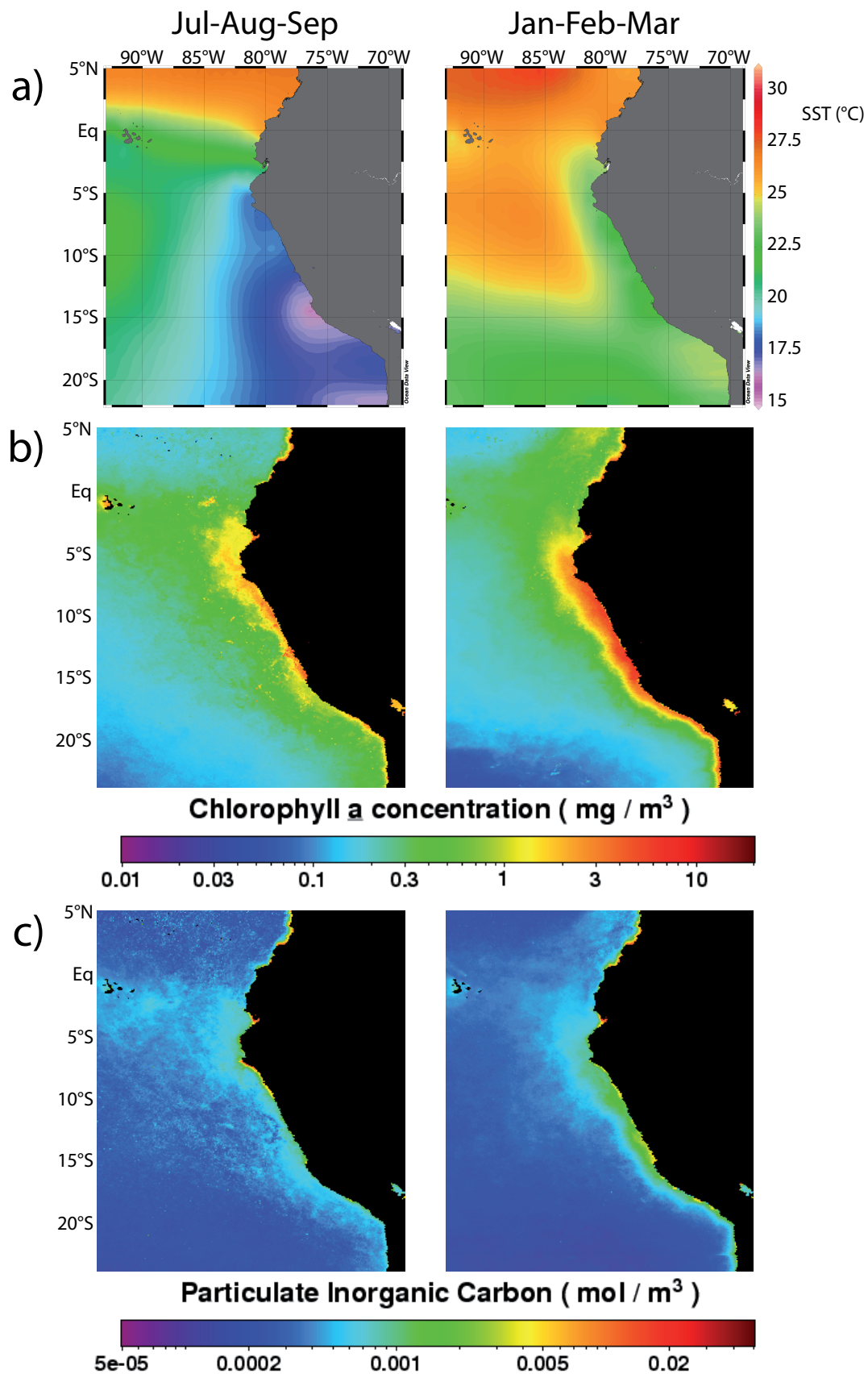


Figure IV.2. Oceanographic pattern of the Peruvian margin

This figure shows the oceanographic pattern of the Peruvian margin. The left and right panels represent the austral winter (Jul-Aug-Sep) and the summer (Dec-Jan-Feb), respectively. a) SST, b) Chlorophyll *a* concentration c) Particulate inorganic carbon. a) was extracted from the WOA₀₉, b) and c) from SeaWiFS dataset (<http://oceancolor.gsfc.nasa.gov/cgi/l3>).

The warmest SST_{alk} prevail off Southern Ecuador-Northern Peru (Figure IV.1) and represent the typical stable and warm SST of the equatorial region (Figure IV.2.a). Further south, SST_{alk} values progressively decrease due to their locations getting closer to the perennial Peruvian coastal upwelling. In addition, some contrasting colder values are located close to the coast at the perennial upwelling zone (11-12°S), leading to an increase of the SST_{alk} seaward, which the opposite trend is observed in the northern part of the Peruvian-Ecuadorian margin (Figure IV.1).

The intensity of the upwelling strongly oscillates with the seasonality of the system. Indeed, the peak of chlorophyll *a* occurs few months after the most intense upwelling [Chavez and Messié, 2009], due to the strong turbulence of the surface waters. The peak of Particulate Inorganic Carbon (PIC), which is directly linked to the production of calcareous organisms at the sea-surface, occurs at the same time of the chlorophyll *a* maximum, i.e. during the austral summer (Figure IV.2a-c). The maximum abundance of diatoms, which represent the major phytoplankton group in the Peruvian upwelling, also occurs at the same period of the year [Abrantes *et al.*, 2007]. Thus, the great seasonality of the Peruvian upwelling may lead to a main occurrence of the coccolithophorid, being calcareous organisms, only during the austral summer and consequently not allow recording mean annual SST off Peru.

We first made a comparison between the SST_{alk} and the annual mean and seasonal (austral summer and winter) SST from WOA₀₉ (SST_{WOA09}) data set (Figure IV.3). The SST_{alk} of this study have been averaged for each degree latitude, allowing a better correlation with the SST_{WOA09} along the Peruvian margin (Figure IV.3). At first glance, the SST_{alk} values are better correlated with the austral summer in the northern part of the margin. However, south of 5°S, the location of samples are closer to the perennial upwelling and the SST_{alk} seem to be better correlated to the mean annual SST_{WOA09} (Figure IV.3).

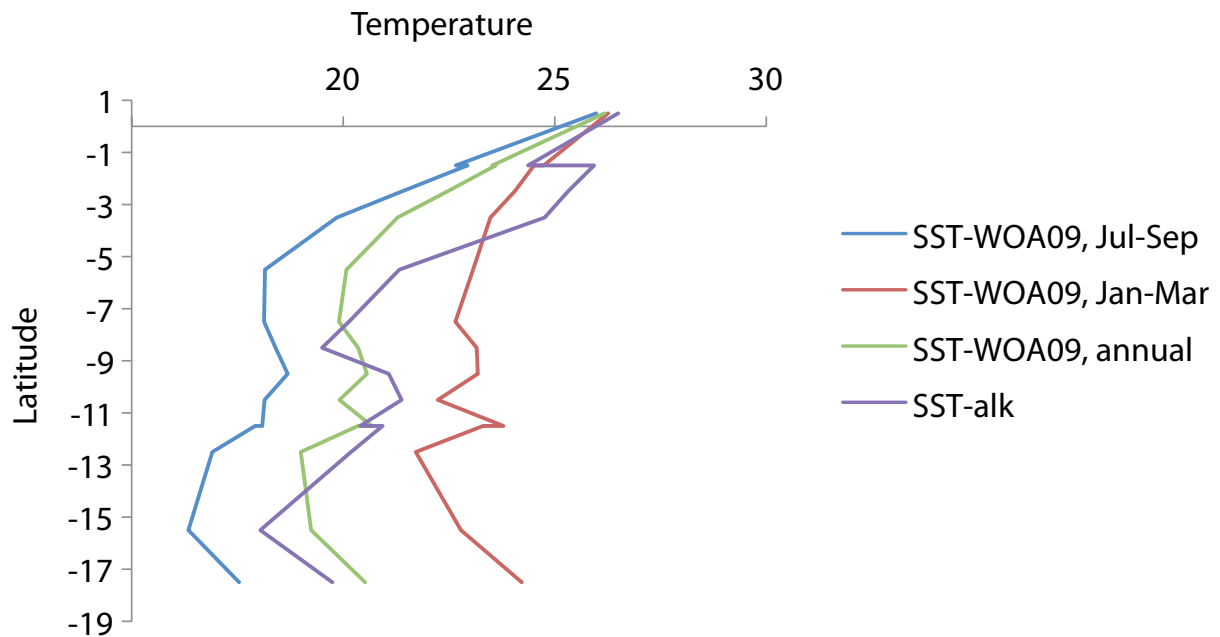


Figure IV.3. SST_{alk} and SST_{WOA09} comparison

The SST_{alk} of this study using Müller *et al.*, [1998] calibration (purple cross) and SST_{WOA09} from mean annual SST (green triangle), austral summer (red square) and austral winter (blue diamond) are plotted against latitude.

In order to estimate whether the annual mean SST can be reconstructed using alkenone unsaturated ratios, we made a regional comparison between the U_{37}^K values of this study and the SST extracted from the WOA09 dataset. Another picture emerges from the comparison between the U_{37}^K values plotted against the SST of the two seasons identified (Figure IV.4). Surprisingly, the SST_{alk} obtained with the calibration from Müller *et al.*, [1998] show a regression curve nearly parallel to the regression curve resulting from the calibration of U_{37}^K values versus austral winter. The shift between the two curves is $\sim 3^\circ\text{C}$, but the gradient of the regression curve are quite similar (~ 0.03). For the austral summer and mean annual SST_{WOA09}, the gradient of the regression is much higher than the gradient from the calibration from Müller *et al.*, [1998] (Figure IV.4), indicating that the organisms may synthesize alkenones in a different manner in function of their habitat. Thus, the Müller calibration may overestimate the SST derived from alkenones in the northern part of the Peruvian margin (Figure IV.3). These results are still surprising considering the increase of surface PP during the austral summer compared to the small PP and PIC during the winter (Figure IV.2). Thus it would be expected that the SST_{alk} would better correlated to the summer SST. However, the very low coastal resolution of the WOA09 may potentially involve some mismatch when calculating the calibration between U_{37}^K and the corresponding SST_{WOA09}. In addition, the

U_{37}^K values have been averaged to fit to the SST_{WOA09} , and then important information originally contained in the U_{37}^K values may be lost.

Until now, the calibration from Müller *et al.*, [1998] seems to be the best calibration to be used for past-SST reconstructions derived from alkenone concentrations, as it takes into account U_{37}^K values and the SST on a global scale.

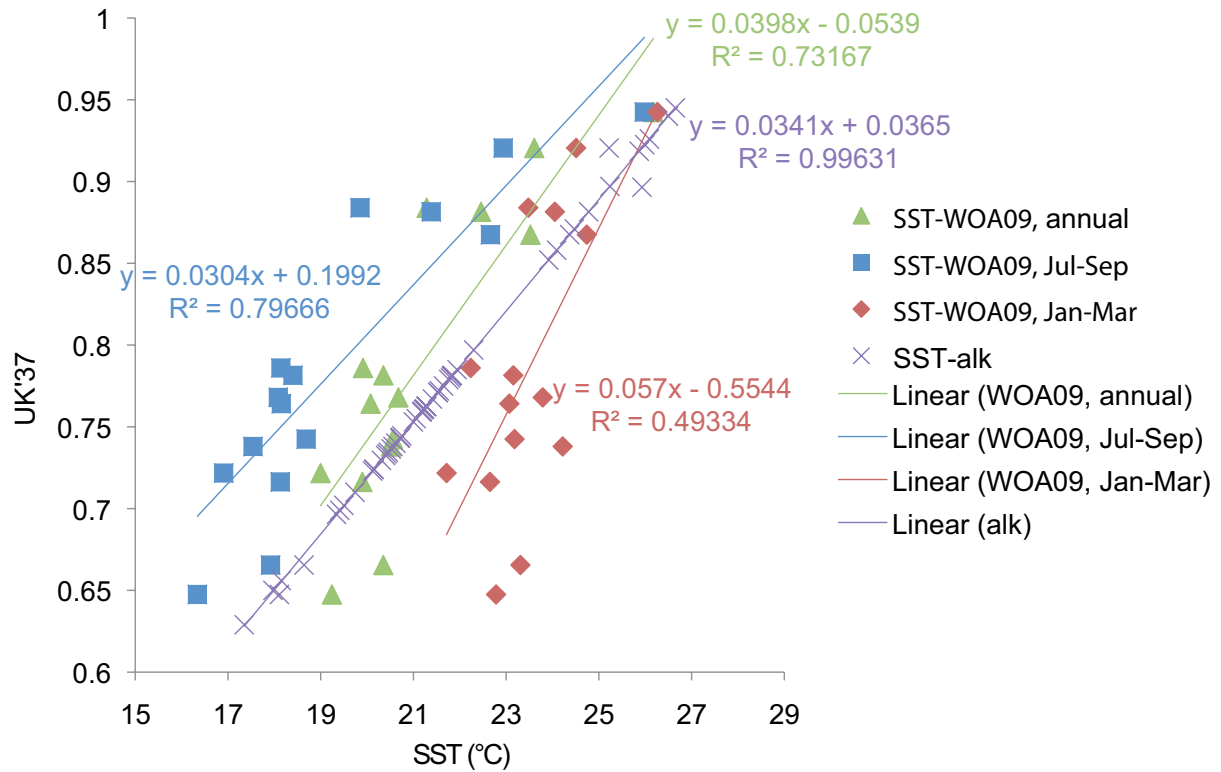


Figure IV.4. U_{37}^K against SST_{alk} and SST_{WOA09}

U_{37}^K values averaged by each degree latitude plotted against SST_{alk} dataset from this study and SST_{WOA09} for annual mean and for each seasons. The legend is the same as the previous figure.

Chapter V. Nitrogen isotope gradients off Peru and Ecuador related to upwelling, productivity, nutrient uptake and oxygen deficiency

Elfi **Mollier-Vogel**¹, Evgenia **Ryabenko**², Philippe **Martinez**³, Douglas **Wallace**⁴, Mark A. **Altabet**⁵, Ralph **Schneider**¹

¹ Institute of Geosciences, University of Kiel, Germany.

² Helmholtz Centre for Ocean Research (GEOMAR), Germany.

³ Université Bordeaux 1, UMR CNRS 5805 EPOC, France.

⁴ Halifax Marine Research Institute, Dalhousie University, Canada.

⁵ School for Marine Science and Technology, U Massachusetts Dartmouth, USA.

V-I. Abstract

We present new nitrogen isotope data from the water column and surface sediments for paleo-proxy validation collected along the Peruvian and Ecuadorian margins between 1°N and 18°S. Productivity proxies in the bulk sediment (organic carbon, total nitrogen, biogenic opal, C₃₇ alkenone concentrations) and ¹⁵N/¹⁴N ratios were measured at more than 80 locations within and outside the present-day Peruvian oxygen minimum zone (OMZ). Microbial N-loss to N₂ in subsurface waters under O₂ deficient conditions leaves a characteristic ¹⁵N-enriched signal in underlying sediments. We find that phytoplankton nutrient uptake in surface waters within the high nutrient, low chlorophyll (HNLC) regions of the Peruvian upwelling system influences the sedimentary signal as well. How the δ¹⁵N_{sed} signal is linked to these processes is studied by comparing core-top values to the ¹⁵N/¹⁴N of nitrate and nitrite (δ¹⁵N_{NOx}) in the upper 200 m of the water column. Between 1°N-10°S, subsurface O₂ is still high enough to suppress N-loss keeping δ¹⁵N_{NOx} values relatively low in the subsurface waters. However δ¹⁵N_{NOx} values increase toward the surface due to partial nitrate utilization in the photic zone in this HNLC portion of the system. δ¹⁵N_{sed} is consistently lower than the isotopic signature of upwelled NO₃⁻, likely due to the corresponding production of ¹⁵N depleted organic matter. Between 10°S and 15°S, the current position of perennial upwelling cells, HNLC conditions are relaxed and biological production and near-surface phytoplankton uptake of upwelled NO₃⁻ are most intense. In addition, subsurface O₂ concentration decreases to levels sufficient for N-loss by

denitrification and/or anammox, resulting in elevated subsurface $\delta^{15}\text{N}_{\text{NOx}}$ values in the source waters for coastal upwelling. Increasingly higher production southward is reflected by various productivity proxies in the sediments, while the north-south gradient towards stronger surface NO_3^- utilization and subsurface N-loss is reflected in the surface sediment $^{15}\text{N}/^{14}\text{N}$ ratios. South of 10°S , $\delta^{15}\text{N}_{\text{sed}}$ is lower than maximum water column $\delta^{15}\text{N}_{\text{NOx}}$ values most likely because only a portion of the upwelled water originates from the depths where highest $\delta^{15}\text{N}_{\text{NOx}}$ values prevail. Though the enrichment of $\delta^{15}\text{N}_{\text{NOx}}$ in the subsurface waters is unambiguously reflected in $\delta^{15}\text{N}_{\text{sed}}$ values, the magnitude of $\delta^{15}\text{N}_{\text{sed}}$ enrichment depends on both the depth of upwelled waters and high subsurface $\delta^{15}\text{N}_{\text{NOx}}$ values produce by N-loss. Overall, the degree of N-loss influencing subsurface $\delta^{15}\text{N}_{\text{NOx}}$ values, the depth origin of upwelled waters, and the degree of near-surface nitrate utilization under HNLC conditions should be considered for the interpretation of paleo $\delta^{15}\text{N}_{\text{sed}}$ records from the Peruvian oxygen minimum zone.

Keywords: water column, surface sediments, nitrogen isotopes, denitrification, OMZ, South America, Eastern Tropical Pacific

V-2. Introduction

The Humboldt Current System in the Eastern South Pacific is one of the most productive ecosystems in the world ocean, with permanent or seasonal upwelling cells along the coasts of Peru and Chile [Pennington *et al.*, 2006]. It is also very sensitive to El Niño Southern Oscillation (ENSO) events, which cause significant changes in the physical, chemical and biogeochemical conditions on interannual timescales [Huyer *et al.*, 1987; Barber *et al.*, 1996]. Large exchanges of heat and CO_2 between the ocean and the atmosphere result from the upwelling of cold, nutrient rich and CO_2 saturated subsurface waters and thus influences global biogeochemical cycles of carbon and coupled elements such as nitrogen. Associated with this current system, an intense oxygen minimum zone (OMZ) extends far offshore that results from the interplay between high export production, strong oxygen consumption due to organic matter (OM) remineralization, and weak ventilation by subsurface circulation. Off southern Peru where the OMZ is most intense and shallowest, the oxygen concentration ranges from saturated values at the surface to values $<10 \mu\text{mol L}^{-1}$ at very shallow water depths ($<50 \text{ m}$), while $<1 \mu\text{mol L}^{-1}$ are reached within its core [Karstensen

et al., 2008; *Paulmier and Ruiz-Pino*, 2009]. On average, the Peruvian OMZ ranges between 30-70 m and 300-500 m water depth.

Water column O₂ concentrations below 2-10 μmol L⁻¹ in the water column are associated with N-loss processes, e.g. denitrification and anammox [*Codispoti*, 2007; *Lam et al.*, 2009]. Under such conditions, nitrate is used as an oxidant during the degradation of the OM and its conversion to N₂ gas represents a loss of bio-available nitrogen from the global ocean. Dissimilatory NO₃⁻ reduction, the first step in N-loss, causes pronounced isotopic fractionation, producing isotopically light products (N₂ and N₂O), and isotopically heavier residual nitrate [*Cline and Kaplan*, 1975; *Liu and I. R. Kaplan*, 1989; *Brandes et al.*, 2007; *Granger et al.*, 2008; *Sigman et al.*, 2009]. Supply of this nitrate to surface waters by upwelling and its utilization by plankton isotopically enriches the particulate OM in ¹⁵N that is ultimately buried in the sediments [*Altabet et al.*, 1995; *Ganeshram et al.*, 1995; *Altabet*, 2006]. In these systems, good preservation of sediment OM leaves the isotopic signal in OM unaltered.

Following these findings, a number of studies have used bulk sediment δ¹⁵N (δ¹⁵N_{sed}) to reconstruct past changes in water-column N-loss. They have shown large variations for tropical OMZs in response to climate fluctuations on millennial to million year time-scales [*Altabet et al.*, 1995; *Ganeshram et al.*, 2000; *Altabet et al.*, 2002; *Liu et al.*, 2005; *Agnihotri et al.*, 2006; *De Pol-Holz et al.*, 2007; *Pichevin et al.*, 2007; *Martinez and Robinson*, 2010]. All these studies report that cold climatic intervals were generally characterized by contraction of the OMZs, while warm climatic intervals experienced expansion with corresponding changes in the ocean's nitrogen budget. Several mechanisms have been proposed as candidates for explaining the inferred variability, such as local productivity variations changing local oxygen demand [*Altabet et al.*, 2002] or remote forcing of the O₂ supply in intermediate source waters [*Galbraith et al.*, 2004; *Meissner et al.*, 2005; *Hendy and Pedersen*, 2006].

In addition to N-loss processes driven by intense OMZ conditions, other factors may influence the δ¹⁵N of OM reaching the sediments, the most notable of which is partial surface nitrate utilization by phytoplankton. Phytoplankton preferentially takes up NO₃⁻ containing the lighter nitrogen isotope (¹⁴N) during photosynthesis and thus OM is depleted in ¹⁵N relative to the NO₃⁻ substrate [*Wada and Hattori*, 1978; *Waser et al.*, 1998; *Granger et al.*, 2004]. Thus, a low relative utilization of NO₃⁻ will tend to drive the δ¹⁵N signal in particulate OM lower than for upwelled δ¹⁵N_{NO₃⁻} values, whereas complete NO₃⁻ utilization would result in an equivalence between the two [*Altabet and Francois*, 1994; *Altabet* 2001; *Freudenthal et*

al., 2001]. A sedimentary $\delta^{15}\text{N}$ signal typical for partial NO_3^- utilization [Francois *et al.*, 1992; Farrell *et al.*, 1995; Sigman *et al.*, 1999] is typically observed in high nutrient low chlorophyll (HNLC) regions such as the Southern Ocean and eastern Equatorial Pacific, where persistent Fe limitation [Martin *et al.*, 1989] allows for only partial NO_3^- utilization in surface waters even on a seasonal basis while previous OMZ paleo-studies were for areas far removed from HNLC regions (Arabian Sea and Mexican OMZ's). However, the Peru OMZ is adjacent to and perhaps overlapping with the eastern Equatorial Pacific HNLC region. Moreover, intense perennial upwelling and moderate Fe limitation [Bruland *et al.*, 2005] along parts of the margin may produce a local HNLC-like effect. Hence $\delta^{15}\text{N}_{\text{sed}}$ in this region may reflect both, water-column N-loss increasing the $\delta^{15}\text{N}$ of upwelled NO_3^- as well as its subsequent partial utilization in surface waters causing $\delta^{15}\text{N}$ in OM to be lower than upwelled $\delta^{15}\text{N}_{\text{NO}_3^-}$ values. In the Peru region, both contributors to $\delta^{15}\text{N}_{\text{sed}}$ are also expected to vary spatially and temporally with a) subsurface OMZ intensity and b) surface gradients in the relative nitrate utilization, respectively.

To further understand the contributions of subsurface N-loss and relative nutrient utilization to the Peruvian margin $\delta^{15}\text{N}_{\text{sed}}$ signal, this study investigates spatial changes in $\delta^{15}\text{N}_{\text{sed}}$ in core-top sediments with respect to the modern OMZ and surface distributions of NO_3^- utilization, associated with primary productivity. We present $\delta^{15}\text{N}$ data for both NO_3^- from the upper 200 m of the water column and bulk surface sediment, along with several other proxies related to export production (C_{org} , TN, Opal and alkenone concentrations), along the Peruvian margin.

V-3. Regional setting

Water masses and currents in the study area (1°N to 18°S, along the Ecuadorian-Peruvian margin) are well described [Fiedler and Talley, 2006]. Strong equatorial winds drag surface waters from the south along shore as part of the Peru-Chile Current (PCC) and Peru-Chile Coastal Current (PCCoastalC). Subsurface and offshore flow is in the opposite direction with the Equatorial Under Current (EUC) and Southern Subsurface Countercurrent (SSCC) forming the Peru-Chile Undercurrent (PCUC) and Peru-Chile Countercurrent (PCCC). These two currents are the main sources of the coastal upwelling cells [Wyrski, 1981; Silva *et al.*, 2009; Czeschel *et al.*, 2011]. The intermediate water source for the Peru OMZ is delivered by these currents from equatorial '13° water' characterized by high salinity, low O_2 ,

and high nutrients. Between 0°S and 10°S and down to 500 m depth, further O_2 depletion in this southward flow drives the system nearly anoxic south of 10°S (Figure V.1).

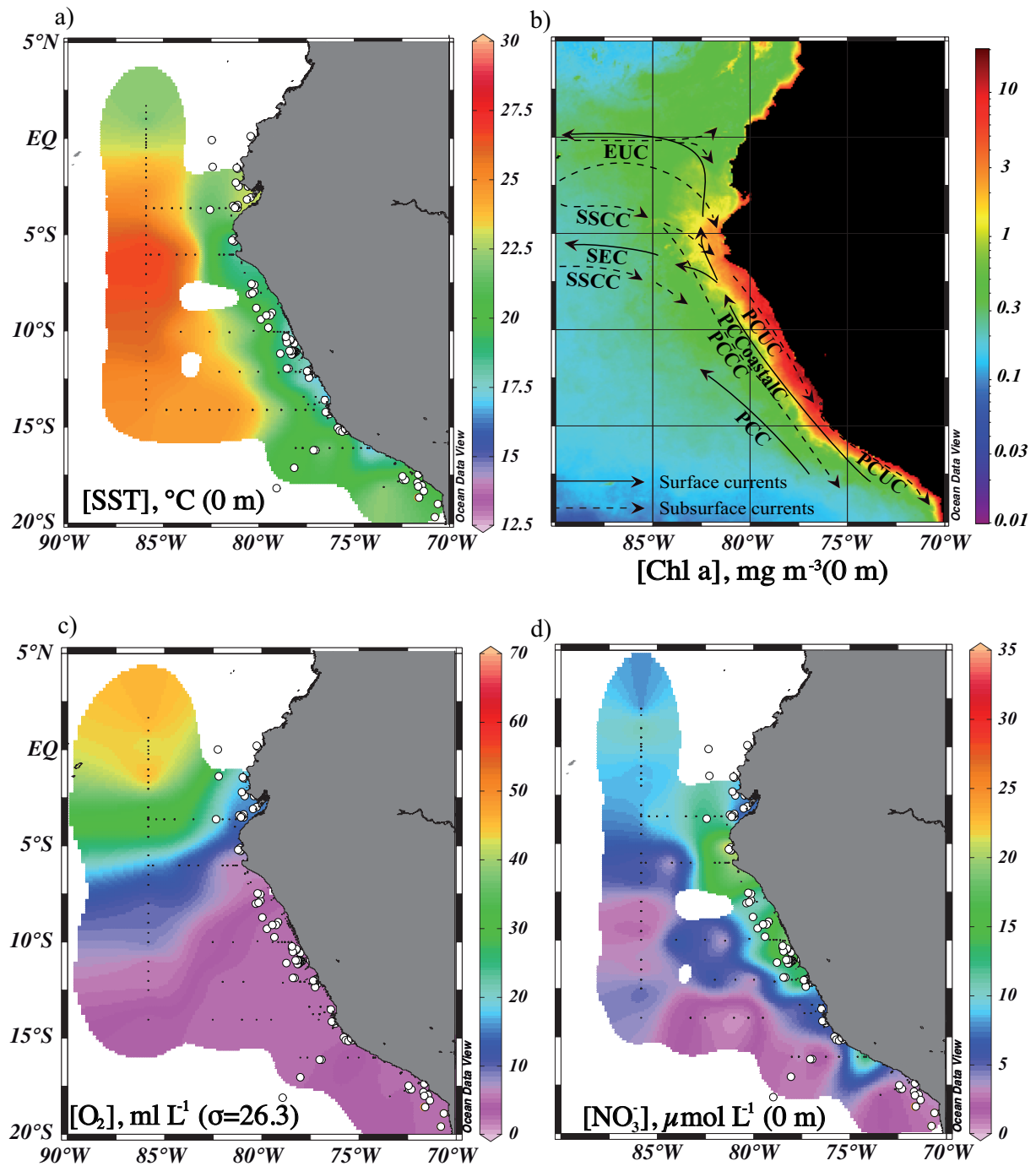


Figure V.1. Maps of oceanographic parameters of the Peru-Ecuador margin

Maps of oceanographic parameters used for comparison with proxy data from the Peru-Ecuador margin. **a)** Sea Surface Temperature (SST), **b)** Chlorophyll a concentrations from SeaWiFS averaged for boreal winters from 1997 until 2010 (<http://oceancolor.gsfc.nasa.gov/cgi/l3>, seasonal climatology). Surface currents are marked by solid lines: Peru Chile Current PCC, Peru Chile Coastal Current PCCoastalC, South Equatorial Current SEC, and subsurface currents by dash lines: Equatorial Undercurrent EUC, Southern Subsurface Counter Current SSCC, Peru Chile Counter Current PCCC, Peru Chile Undercurrent PCUC (adapted from [Penven et al, 2005; Kessler, 2006; Czeschel et al., 2011]). **c)** Oxygen concentrations along the $\sigma = 26.3$ contour. **d)** Nitrate concentrations at the surface. All water column data stem from CTD casts of the METEOR-2008

cruises gridded with the ocean data view software (*Schlitzer, R., Ocean Data View*, <http://odv.awi.de>, 2011). The white dots show the locations of the surface sediment samples used for this study.

The PCU is most intense between 5°S and 15°S and reaches as far as 100 km offshore. This coastal upwelling system is by far the richest in the world in terms of chlorophyll *a* concentration and biomass [*Chavez and Barber* 1987; *Chavez and Messié* 2009]. Upwelled waters are derived from about 50 m and 200 m water depth respectively during periods of moderate and strong upwelling [*Strub et al.*, 1998]. Between 10°S and 15°S, where the shelf becomes narrow, the strongest upwelling occurs in individual active cells that spread near shore along the margin (Figure V.1) [*Strub et al.*, 1998; *Echevin et al.*, 2004]. Some of the upwelling cells are perennial and are located around 11°-12°S and 14°-16°S [*Suess et al.*, 1987; *Strub et al.*, 1998]. Most of the PCU is strongly seasonal and reaches its maximum intensity during austral winter (Jun-Jul-Aug) [*Pennington et al.*, 2006; *Messié et al.*, 2009]. However, highest levels of chlorophyll *a* occur in austral summer, in antiphase to the upwelling season [*Chavez et al.*, 1996; *Pennington et al.*, 2006; *Echevin et al.*, 2008]. According to *Pennington et al.* [2006], this seasonal time lag between the maximum in biological production and upwelling might result from a deeper surface mixed layer restricting light availability and phytoplankton growth during austral winter. HNLC conditions in which Fe limitation prevents complete NO₃⁻ depletion at the surface are well known in the Eastern Eq. Pacific and along portions of the Peru Margin [*Fiedler et al.*, 1992; *Hutchins et al.*, 2002; *Bruland et al.*, 2005]. However, where upwelled waters have been in contact with sediments, Fe limitation is relieved [*Bruland et al.*, 2005] and sharp biogeochemical boundaries can occur between productive coastal waters and offshore HNLC waters.

V-4. Sampling and analytical methods

The physical, chemical, and biological dynamics in the water column as well as sediment and pore water geochemistry associated with the Peru OMZ were studied in a series of cruises carried out as part of the German collaborative research program *Climate - Biogeochemistry Interactions in the Tropical Ocean* (www.sfb754.de). Surface sediments were collected during cruises aboard the German research vessel Meteor (cruises M77-1 and -2, 2008, [*Pfannkuche et al.*, 2008; *Schneider et al.*, 2008]). The sampling area extends from 1°N to 17°S and covers the Ecuadorian and Peruvian margins by 81 stations between 60 m and 2080 m depth along the coast (Figure V.2).

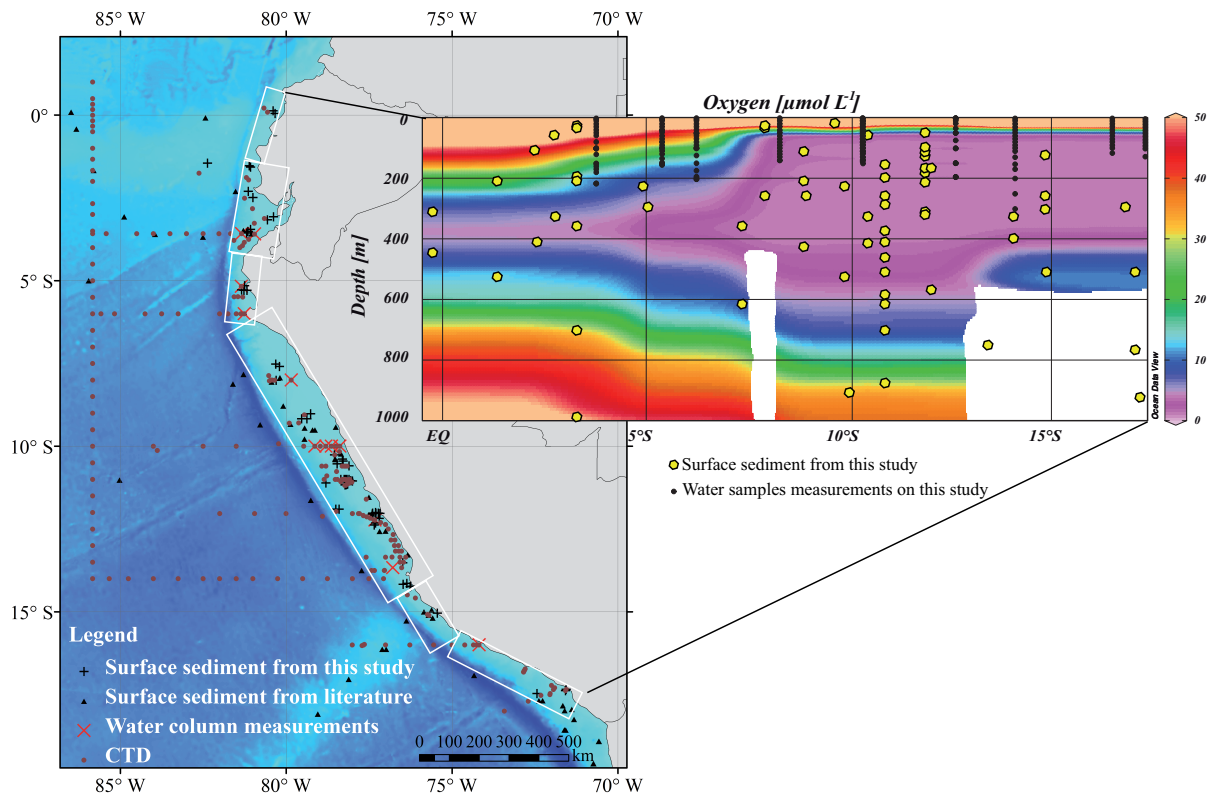


Figure V.2. Samples locations along the Peru-Ecuador margin

Map of the Peru-Ecuador margin showing surface sediment samples (small black crosses), rosette water sample stations (red crosses) and the CTD casts (red dots) used for this study. Surface sediment ^{15}N data from the literature [Farrell *et al.*, 1995; Wolf, 2002; Niggemann, 2005] is indicated by black triangles. The blue shading represents the marine topography (GEBCO One Minute Grid, version 2.0, <http://www.gebco.net>). The cross section shows positions of surface sediment (yellow dots) and water samples (black dots) with respect to the extension of the Peruvian OMZ as measured with the CTD casts collected during METEOR-2008 cruises (M77).

At each of these stations, 6 multicorer tubes (1m each) were retrieved. An additional set of 13 samples from IMARPE (Instituto Del Mar del Perú, Lima), located between 5°S and 14°S, were also analyzed and included into this study. Locations and data of all sampling sites are compiled in the PANGAEA database (<http://www.pangaea.de>). Water samples were collected on 77 stations during the 3rd and 4th Leg of M77 cruise onboard the R/V Meteor (Figure V.2, [Franck *et al.*, 2009; Stramma *et al.*, 2009]), using 12 L Niskin bottles on a CTD rosette system equipped with oxygen sensors. Nutrients and oxygen concentrations were determined according to the method of Grasshoff *et al.*, [1983]. Samples for the measurement of $\delta^{15}\text{N}$ of nitrate (NO_3^-) and nitrite (NO_2^-) ($\delta^{15}\text{N}_{\text{NO}_x}$) were collected in 120 ml plastic bottles. Samples containing nitrite concentration below $0.1 \mu\text{mol L}^{-1}$ were acidified with 0.5 ml of 25% HCl, otherwise samples were kept frozen until analysis. For these samples, pre-existing NO_2^-

was removed in the laboratory by addition of sulfanilic acid. The isotopic composition of dissolved nitrate ($\delta^{15}\text{N}_{\text{NO}_3^-}$) was measured using the Cd-reduction method [McIlvin and Altabet, 2005] with NaCl addition as described by [Ryabenko et al, 2009]. In this method, NO_3^- is reduced to NO_2^- using Cd powder after addition of 5 M NaCl, and NO_2^- is reduced to N_2O using acid. The samples were analyzed in Germany (IFM-GEOMAR) and in USA (SMAST), with a detection limit of $0.2 \mu\text{mol L}^{-1}$ for the nitrate and nitrite with the precision of the $\delta^{15}\text{N}$ measurements being $\pm 0.2\text{‰}$.

Surface sediment nitrogen isotope ratios ($\delta^{15}\text{N}_{\text{sed}}$) and total nitrogen contents (TN) were measured on ~5 to 60 mg of homogenized and freeze-dried bulk sediment, using a Carlo-Erba CN analyser 2500 interfaced directly to a Micromass-Isoprime mass spectrometer at Bordeaux University. The precision of the isotopic analyses was based on repeated measurements of selected surface sediment samples as well as routine international and in-house standards measurements is $\pm 0.2\text{‰}$ [Martinez and Robinson, 2010]. Organic carbon (C_{org} , wt %) measurements were carried out using a LECO C-S 125 analyzer after treatment of ~80-100 mg of sediment with hydrochloric acid to remove calcium carbonate, where precision on repeated measurements was better than $\pm 0.5\%$. Alkenone content was determined by accelerator solvent extraction (Dionex ASE) from 0.5 g freeze-dried and homogenized sediment samples, prior to C_{37} group analysis using a double column multidimensional gas chromatograph (Agilent 6890N) system [Blanz et al., 2005]. Biogenic opal was measured on 20 mg of freeze-dried and homogenized bulk sediment by using an automated extraction method and wet chemical leaching as described in Müller and Schneider, [1993]. Standard deviation based on repeated measurements is $\pm 0.5\%$.

V-5. Results

V-5.1. Surface sediments: $\delta^{15}\text{N}_{\text{sed}}$ and export production proxies

The surface sediment $\delta^{15}\text{N}_{\text{sed}}$ data along the margin can be separated into a northern (1°N to 8°S) and southern (8°S to 18°S) group (Figure V.3).

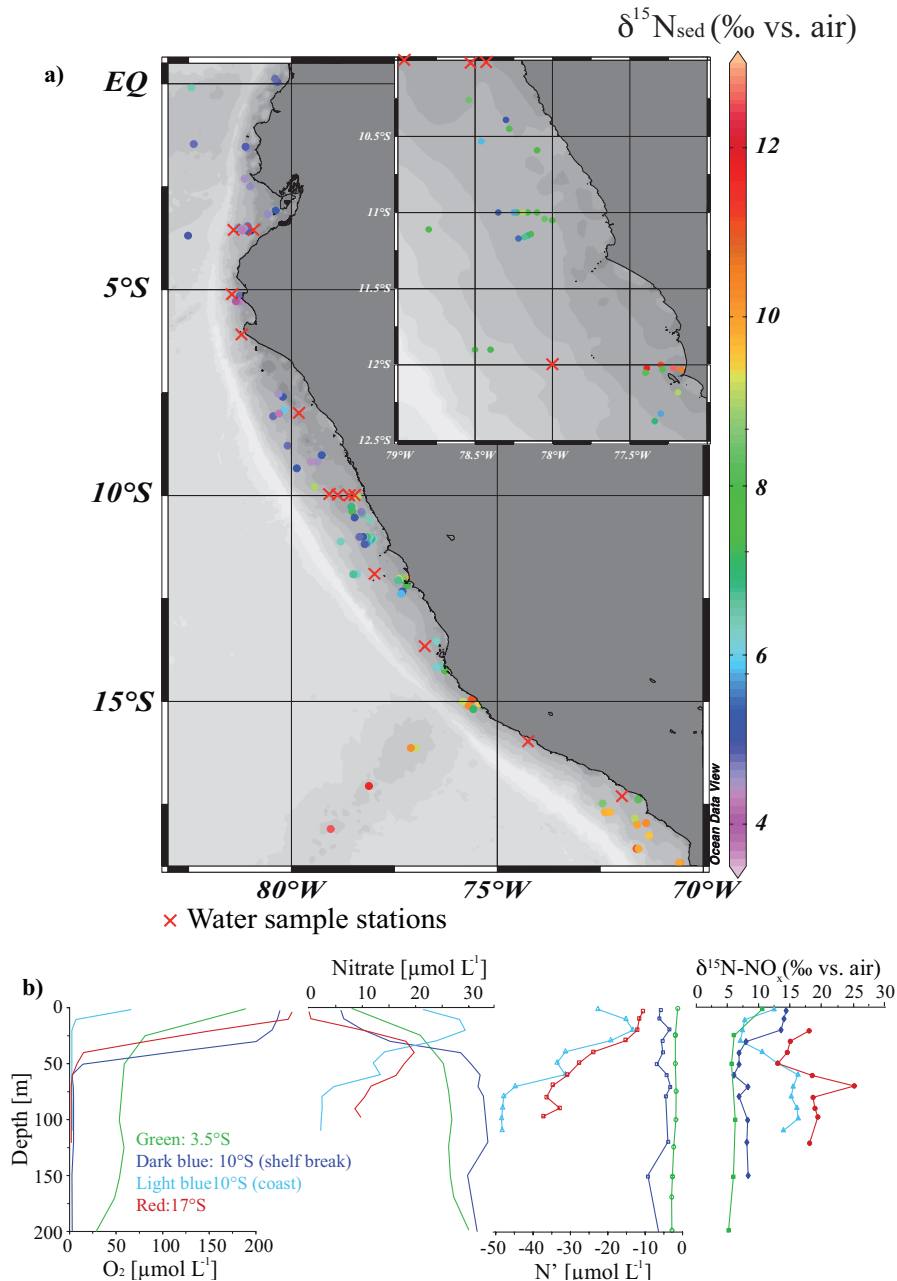


Figure V.3. $\delta^{15}\text{N}_{\text{sed}}$ and water column measurements

a) $\delta^{15}\text{N}_{\text{sed}}$ values in surface sediments (colored dots) and positions of water sample stations (red crosses) sampled during METEOR cruise (2008) along the Ecuador-Peru Margin. Gray shading delineates the bathymetric contours. Zoom in highlights occurrence of highest $\delta^{15}\text{N}_{\text{sed}}$ values close to the coast. b) 0 to 200 m water sample profiles for oxygen concentration, NO_3^- , N-deficit (or N^*) and $\delta^{15}\text{N-NO}_x$ at selected stations at 3.5°S (green curves), 10°S close to the coast (light blue curves) and on the continental slope (dark blue curves) as well as 17°S (red curves).

In the north, $\delta^{15}\text{N}_{\text{sed}}$ values are relatively low and uniform, ranging only between 4 to 5‰. In the southern part, values generally increase southward but reveal a larger range between 4.5 and 13‰. This north-south gradient is not a simple monotonic function of latitude since highest values are also located shoreward decreasing offshore by several ‰ within 100 km

distance of the perennial upwelling centers (Figure V.3). Only far offshore (>100 km from the coast) along the Nazca Rise do $\delta^{15}\text{N}_{\text{sed}}$ values increase again to higher values (see discussion).

Proxy data related to export production and composition of OM show the same latitudinal and cross-shelf trends as $\delta^{15}\text{N}_{\text{sed}}$ (Figure V.4).

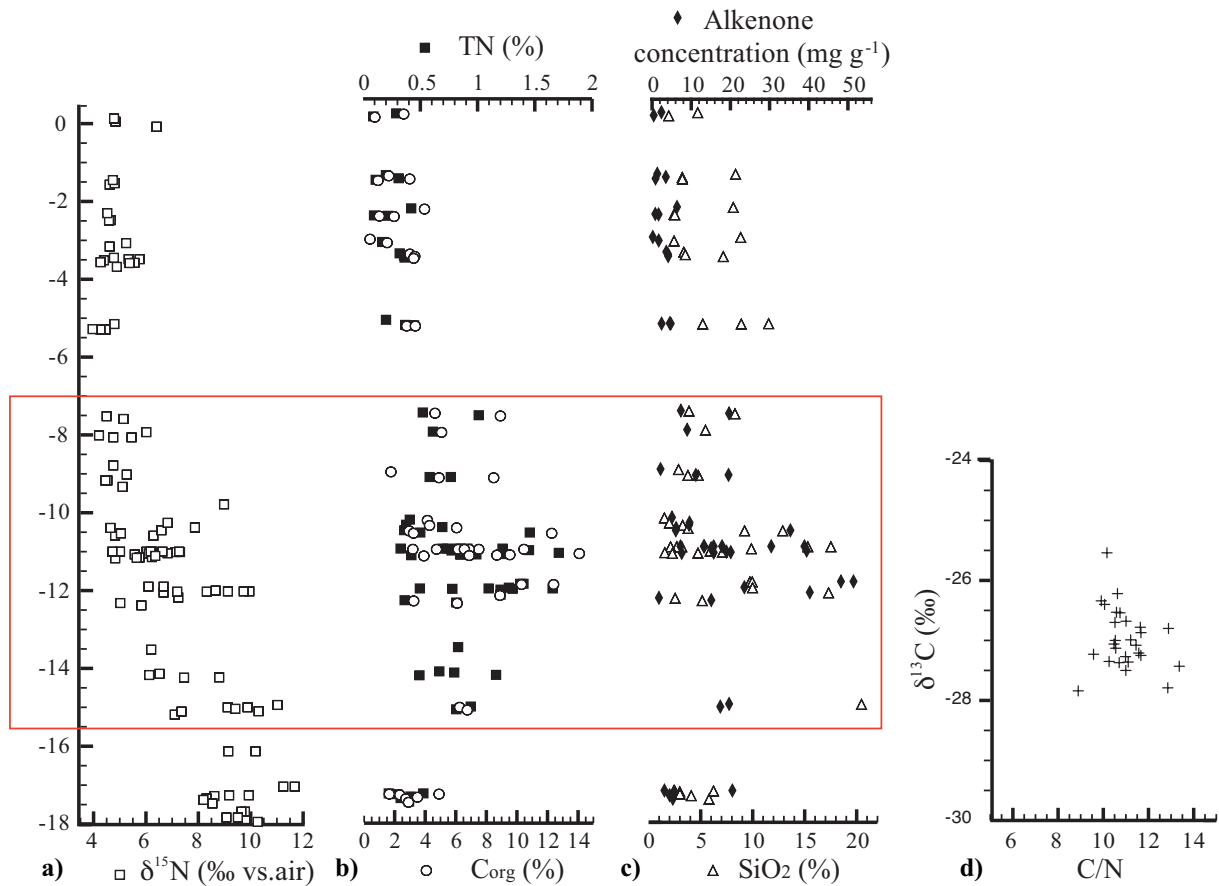


Figure V.4. Sedimentary results

a) $\delta^{15}\text{N}_{\text{sed}}$ values (‰) **b)** Total nitrogen (TN) and organic carbon C_{org} contents in (%), **c)** biogenic SiO_2 (%) and alkenone (mg.g^{-1}) contents versus latitude off Peru and Ecuador, **d)** C/N ratios versus $\delta^{13}\text{C}$ values (‰) of organic matter in surface sediments.

Organic carbon (C_{org}) values vary between 0.3% and 3% in the northern and between 2% and 16% in the southern part. Other productivity proxies reveal a very similar pattern with highest contents between 10 and 15°S. Total nitrogen content (TN) varies between 0.2% to 2%, biogenic opal (SiO_2) between 1% to 21%, and alkenone content (alk) between 1 ng to 50 ng per gram bulk sediment. Organic matter $\delta^{13}\text{C}$ and C/N ratio overall vary little between -20‰ and -23‰ and between 6 and 11, respectively (Figure V.4).

V-5.2. Water column oxygen, nitrate, and $\delta^{15}\text{N}$ distribution

The water column was sampled during the austral summer, the season of weak upwelling intensity but highest primary production, conditions that should be most representative of the sedimentary signal. O_2 concentrations show a transition from a relatively weak OMZ in the Equatorial region ($[\text{O}_2] > 20 \mu\text{mol L}^{-1}$) to an intense and broad OMZ south of 8°S ($[\text{O}_2] < 5 \mu\text{mol L}^{-1}$; Figure V.1 & Figure V.2). North of 8°S , subsurface $\delta^{15}\text{N}_{\text{NO}_x}$ is about 6‰ and close to the oceanic average, consistent with a lack of N-loss in the northern portion of the study region (Figure V.3b). South of 8°S , decreasing oxygen concentrations trigger N-loss processes, which are reflected in decreasing dissolved NO_3^- , a more negative N deficit ($\text{N}^- = [\text{NO}_3^-] + [\text{NO}_2^-] - 16 \times [\text{PO}_4^{3-}]$) and increasing $\delta^{15}\text{N}_{\text{NO}_x}$ values between 6 to 20‰ (Figure V.3b).

A comparison of all sediment $\delta^{15}\text{N}_{\text{sed}}$ sampled on the continental shelf and upper slope with overlying $\delta^{15}\text{N}_{\text{NO}_x}$ values in the upper 200 m of water column is presented in Figure V.5.

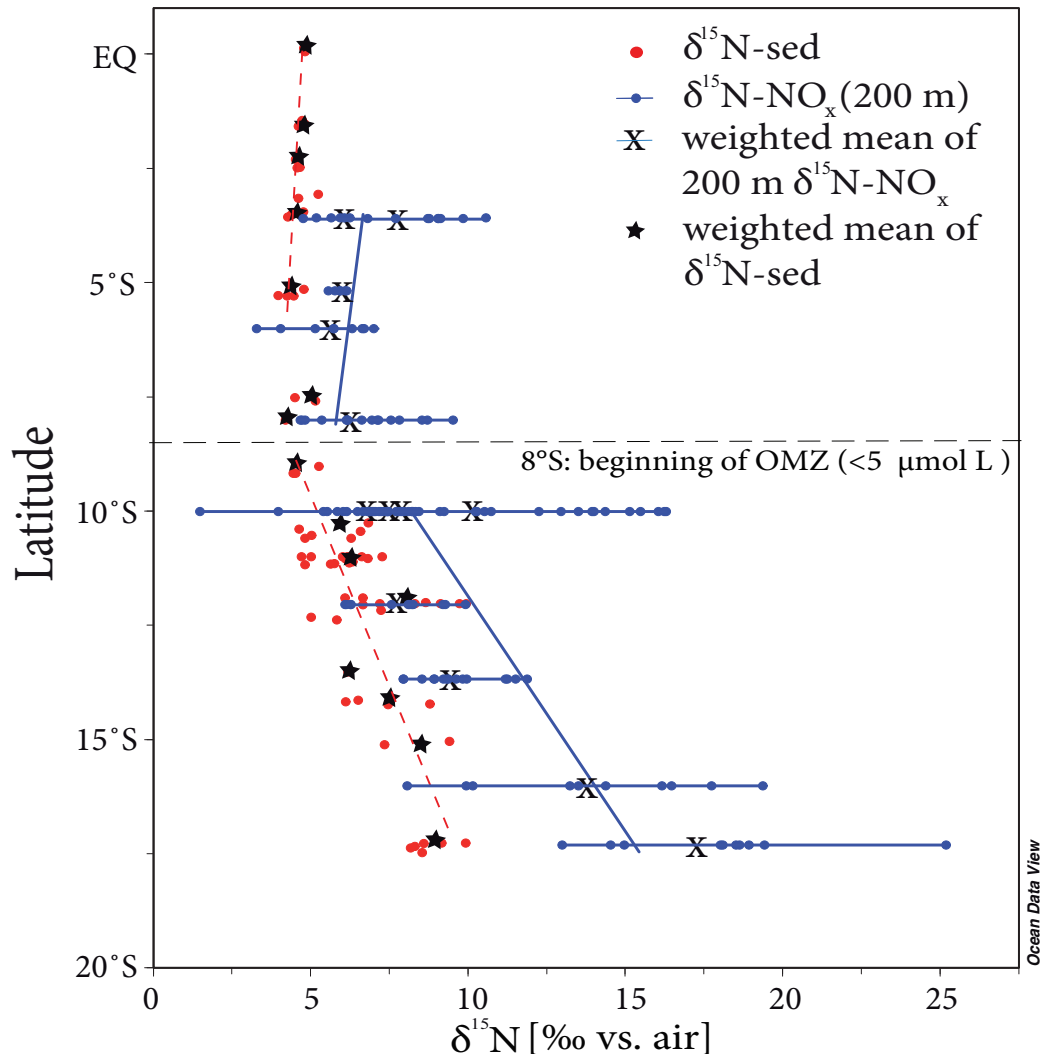


Figure V.5. $\delta^{15}\text{N}$ in the water column and surface sediment

Latitudinal distribution of $\delta^{15}\text{N}_{\text{sed}}$ (red dots) in surface sediments on the continental shelf and slope plotted against $\delta^{15}\text{N}_{\text{NOx}}$ (blue dots) in the upper 200 m water depth. The weighted mean values are marked by black crosses for the upper 200 m of the water column and black stars for the sediment. The equations used for the calculation of both weighted mean values are shown in the text. The red dashed line and the blue solid line represent linear regressions for the sediment and the water column mean values, respectively.

The distribution plots showing also weighted mean values for $\delta^{15}\text{N}_{\text{sed}}$ and the $\delta^{15}\text{N}_{\text{NOx}}$ in the upper 200 m calculated using the two following equations:

$$(\text{TN}_1 * \delta^{15}\text{N}_{\text{sed1}} + \text{TN}_2 * \delta^{15}\text{N}_{\text{sed2}} + \dots + \text{TN}_x * \delta^{15}\text{N}_{\text{sedx}}) / (\text{TN}_1 + \text{TN}_2 + \dots + \text{TN}_x) \quad (7)$$

$$([\text{NO}_3^-]_1 * \delta^{15}\text{N}_{\text{NOx1}} + \dots + [\text{NO}_3^-]_{200\text{m}} * \delta^{15}\text{N}_{\text{NOx200m}}) / ([\text{NO}_3^-]_1 + \dots + [\text{NO}_3^-]_{200\text{m}}) \quad (8)$$

highlight the general trends in variability as well as the degree of similarity between water and sediment values.

North of 8°S , the $\delta^{15}\text{N}_{\text{sed}}$ data have both a low mean value and low variance with respect to the weighted mean. Subsurface $\delta^{15}\text{N}_{\text{NOx}}$ data also have low scatter and are fairly constant with latitude due to the absence of depleted oxygen conditions (Figure V.3b). At the surface, $\delta^{15}\text{N}_{\text{NOx}}$ increases according to the magnitude of partial nitrate/nitrite utilization causing a larger variance in local values at a given latitude (Figure V.3b & Figure V.5). In general, weighted mean $\delta^{15}\text{N}_{\text{NOx}}$ values are 1 to 2‰ higher than sediment values. This offset can be explained by the partial nutrient utilization in surface waters, leading to higher $\delta^{15}\text{N}_{\text{NOx}}$ values and lower $\delta^{15}\text{N}$ in the OM produced. Our observations show elevated surface NO_3^- concentrations extending well offshore of the upwelling centers indicative of HNLC conditions (Figure V.1d).

South of $\sim 8^\circ\text{S}$, the sedimentary and water column $\delta^{15}\text{N}$ values, as well as the latitudinal variability increase southward (Figure V.5). N-loss processes cause the increase of $\delta^{15}\text{N}_{\text{NOx}}$ values within the OMZ, the likely cause also for the increase in $\delta^{15}\text{N}_{\text{sed}}$ values. However, the influence of other processes on $\delta^{15}\text{N}_{\text{sed}}$ needs to be considered as discussed below.

V-6. Discussion

V-6.1. Possible sedimentary influences on $\delta^{15}\text{N}_{\text{sed}}$

In order to explain the North to South gradient of $\delta^{15}\text{N}$ values observed along the Peruvian margin; we assume that $\delta^{15}\text{N}_{\text{sed}}$ principally reflects the isotopic composition of marine organic matter (OM) excluding inorganic nitrogen, such as ammonium, or terrestrially derived nitrogen as an important component of the sediments studied. As for other coastal

upwelling systems [Müller, 1977], it is reasonable to assume that the contribution of inorganic nitrogen, clay-bound or otherwise, is negligible compared to organic nitrogen in the OM rich sediments characteristic for the Peruvian upwelling system (Figure V.4b). On the other hand, fluvial sediment transport, particularly by the Guayas River at the northern Peruvian and Ecuadorian margin, may contribute a significant amount of terrestrial OM that could influence the $\delta^{15}\text{N}_{\text{sed}}$ values. To the south, the coastal region is hyper-arid with minimal input from rivers draining the western slopes of the Andes. In general, terrestrial OM is characterized by low $\delta^{15}\text{N}$ values of the order 2 to 3‰, low $\delta^{13}\text{C}_{\text{org}}$ values of -27 to -33‰ particularly in the tropical rainforest catchments relevant here, and high C/N ratios >20. In contrast, marine OM has typical $\delta^{13}\text{C}_{\text{org}}$ values between -19 and -22‰ and C/N ratios close to the Redfield ratio of 6 to 7 [Emerson and Hedges, 1988; Jasper and Gagosian, 1989; Hebbeln, 1992]. Along the Peruvian and Ecuadorian margins, C/N ratios range between 6 and 11 and $\delta^{13}\text{C}_{\text{org}}$ values between -20 and -23‰ with no correlation between them, indicating that sediment OM is predominantly of marine origin (Figure V.4d). Therefore any influence by terrestrial input on the $\delta^{15}\text{N}_{\text{sed}}$ signal can be neglected and the observed north to south gradient in $\delta^{15}\text{N}_{\text{sed}}$ interpreted as reflecting purely marine processes.

Another consideration is whether remineralization of OM during its settling in the water column and subsequent burial within the sediment may affect the preserved $\delta^{15}\text{N}_{\text{sed}}$ signal. First, we rule out any post-burial diagenetic effects. They have only been found to be significant when the OM is poorly preserved in the sediments leading to an increase in $\delta^{15}\text{N}$ by several ‰ [Altabet, 1988; Altabet, 2001]. This is clearly not an issue for the high OM sediments of the Peru margin (Figure V.4). Moreover, the environmental setting in the Peruvian upwelling is very similar to the ones off North-West Africa and Mexico, where no change in downcore $\delta^{15}\text{N}$ in the first 10 cm of sediment was observed [Ganeshram et al., 1995; Martinez et al., 2000].

Regarding remineralization in the water column, small particles have been found to increase in $\delta^{15}\text{N}$ with depth below the euphotic zone but large fast sinking particles generally not [Holmes et al, 1998; Altabet et al, 1999]. As a result, particles with longer settling times could be prone to greater remineralization leading to elevated $\delta^{15}\text{N}$ value. Such would be the case with increasing bottom depth, as it is observed for the sites on the Nazca Rise (Figure V.3a). On the shelf, however, we observed the opposite trend: $\delta^{15}\text{N}_{\text{sed}}$ values decrease from the coast to the outer shelf (Figure V.3a and Figure V.7b). Decreasing values with increasing depth on the shelf are difficult to explain by OM degradation, particularly in an environment

with very high productivity and fluxes into the organic-rich sediments off Peru. Therefore this trend on the shelf requires an alternative explanation as discussed below.

V-6.2. Influence of N-loss processes and nutrient uptake in the water column on $\delta^{15}\text{N}_{\text{sed}}$ gradients

The relative importance of denitrification, the stepwise reduction process involving a number of intermediates ($\text{NO}_3^- \rightarrow \text{NO}_2^- \rightarrow \text{NO} \rightarrow \text{N}_2\text{O} \rightarrow \text{N}_2$), compared to anammox ($\text{NO}_2^- + \text{NH}_4^+ \rightarrow \text{N}_2$) is strongly debated for the Peruvian OMZ. This makes it difficult also to assign variations in the nitrogen isotope signal in the water column and sediments off Peru to one of these processes only. However, the dissimilatory reduction of nitrate to nitrite is a first required step for both processes [Lam *et al.*, 2009]. It follows that the isotopic fractionation during nitrate reduction is independent of which process ultimately leads to N_2 production and reflects net NO_3^- removal from the system. Within the OMZ south of 8°S , the latitudinal increase of $\delta^{15}\text{N}_{\text{NOx}}$ in water depths below 50 m is thus well correlated with the onset of near anoxic conditions and development of the N-deficit (N') (Figure V.3b) due to intensification of N-loss processes. When upwelled, the NO_3^- will carry an enriched ^{15}N signal into surface waters that, if nitrate is completely utilized on relevant time/space scales, will be reflected in OM produced in the euphotic zone and finally recorded in the sediments.

For comparison with sedimentary $\delta^{15}\text{N}_{\text{sed}}$ values, we first consider weighted mean $\delta^{15}\text{N}_{\text{NOx}}$ values measured in the upper 200 m with weighted mean values representing all surface sediment sites along the different cross shelf transects (Figure V.5). Weighted mean $\delta^{15}\text{N}_{\text{NOx}}$ values shift from $\sim 6.8\text{‰}$ at 3.5°S to $\sim 17.5\text{‰}$ at 17°S . Complete water column profiles for the entire 200 m water depth (Figure V.3b) suggest that the southward increase in $\delta^{15}\text{N}_{\text{NOx}}$ values above the nitracline between 8° and 17°S (Table I and Figure V.5) derives from the upwelling of subsurface nitrate enriched in ^{15}N by N-loss processes.

Latitude	Initial $\delta^{15}\text{N}_{\text{NOx}}$ value at the nitracline	$\delta^{15}\text{N}_{\text{sed}}$ at the corresponding location	Difference
3.6	5.7	4.3	1.4
8	4.7	4.2	0.5
10	6	6	0.02
12	6.2	6.2	0.04
13.7	8.9	8.6	0.3
17	14.5	8.9	5.6

Table 1. Difference between initial $\delta^{15}\text{N}$ of the upwelled nitrate and sedimentary $\delta^{15}\text{N}$

Calculated difference between the initial $\delta^{15}\text{N}_{\text{NOx}}$ at the nitracline and $\delta^{15}\text{N}_{\text{sed}}$ values for the corresponding location.

Nonetheless, $\delta^{15}\text{N}_{\text{sed}}$ values are consistently lower than weighted mean $\delta^{15}\text{N}_{\text{NOx}}$ values above the nitracline. Therefore alteration of isotopic composition during downward transport of OM and subsequent burial into shelf sediments seems not to be the case, as remineralization and diagenesis tend to increase the $\delta^{15}\text{N}$ values of OM. Moreover, the latitudinal $\delta^{15}\text{N}_{\text{sed}}$ increase is only about half of that measured in the water column, with weighted mean $\delta^{15}\text{N}_{\text{sed}}$ values of $\sim 4.5\text{‰}$ from 3.5° to 8°S shifting to $\sim 9\text{‰}$ at 17°S (Figure V.5). Accordingly, the difference between weighted mean $\delta^{15}\text{N}_{\text{NOx}}$ and $\delta^{15}\text{N}_{\text{sed}}$ values increases progressively from less than 1.0‰ at 10°S and reach $\sim 9\text{‰}$ at 17°S (Figure V.5). Between 10° and 12°S the difference between weighted mean $\delta^{15}\text{N}_{\text{NOx}}$ and $\delta^{15}\text{N}_{\text{sed}}$ values is close to 0 (Figure V.5), indicating that the sedimentary signal is likely to record complete nutrient utilization over the year. The larger difference between weighted mean $\delta^{15}\text{N}_{\text{NOx}}$ and $\delta^{15}\text{N}_{\text{sed}}$ values may imply that the sedimentary signal in the southernmost region is not fully recording the increase of ^{15}N enrichment due to N-loss processes in the water column within the OMZ.

Enhanced $\delta^{15}\text{N}_{\text{NOx}}$ values in surface waters shallower than 30 m (Figure V.3b) not reflected in the sedimentary signal, can partly be the result of incomplete phytoplankton nutrient utilization and fractionation during nitrate assimilation [Altabet, 2001; Granger et al., 2004]. Although the observed fractionation factor for this process ($5\text{-}10\text{‰}$) is significantly less than that for denitrification ($20\text{-}30\text{‰}$), it can produce significant isotopic enrichment of the remaining nitrogen pool in surface waters due to Rayleigh fractionation [Altabet and Francois, 1994; Holmes et al., 1998; Waser et al, 1998; Horn et al., 2011]. Consequently the

vertical gradient of nutrient utilization toward the photic zone causes an increase in the near-surface $\delta^{15}\text{N}_{\text{NO}_x}$ (Figure V.3b) and a corresponding decrease in the $\delta^{15}\text{N}$ of the OM produced in the photic zone and subsequently buried in the sediment. Thus, the combination of the isotopic effects associated with subsurface N-loss and surface partial nutrient utilization can be preserved in the $\delta^{15}\text{N}_{\text{sed}}$ signal along the Peru margin. To better estimate the impact of nutrient utilization on the latitudinal $\delta^{15}\text{N}_{\text{sed}}$ gradient along the Peruvian margin, we correlated $\delta^{15}\text{N}_{\text{NO}_3}$ values between the surface and the nitracline, defined as the depth of highest nitrate concentration close to the photic zone, to the corresponding relative utilization (remaining fraction: equation 8) for three different areas at 3-8°S, 10°S, and 17°S (Figure V.6).

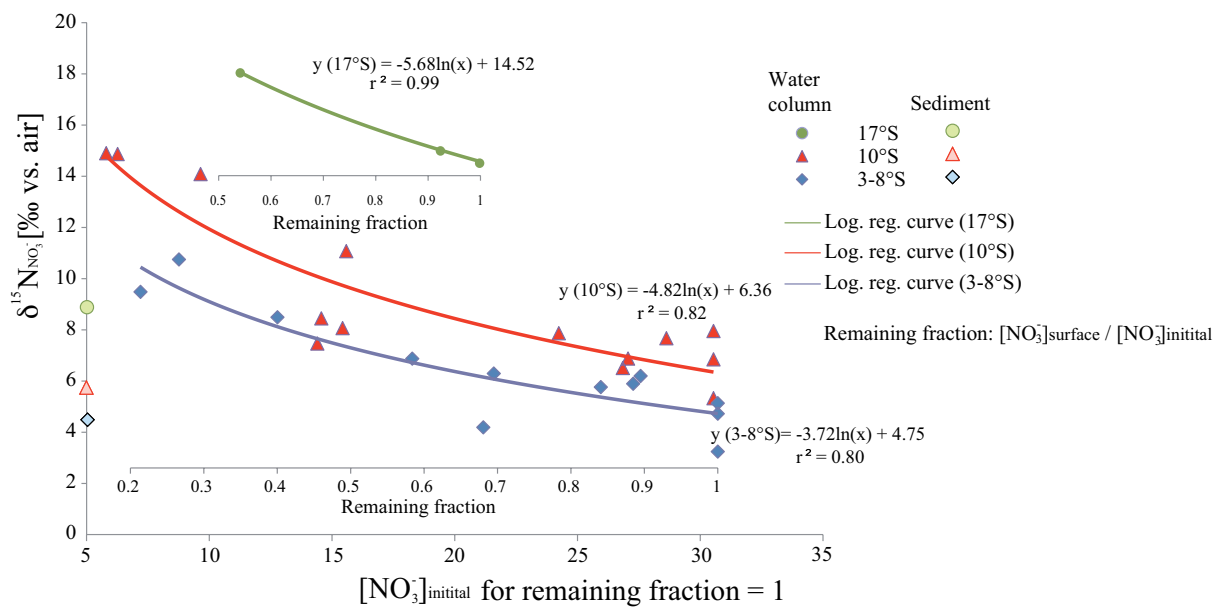


Figure V.6. Relative nitrate utilization as a function of latitude

Correlations between $\delta^{15}\text{N}_{\text{NO}_3}$ and the remaining fraction of nitrate in surface waters, calculated as the ratio of nitrate concentrations between surface and nitracline depths: with blue diamonds for 3° to 8°S, red triangles at 10°S and green circles at 17°S. The lines show respective logarithmic regression curves for each area. Equations show the southward change in fractionation factor (ϵ_u) and in the resulting initial $\delta^{15}\text{N}_{\text{NO}_3}$, for details see the text.

It was shown in culture studies that nitrate reductase comprises the major fractionating step in nitrate assimilation via reduction to nitrite [Granger *et al.*, 2004]. Isotope fractionation by nitrite reductase is rather different than that of nitrate and is either small or even not expressed because transport across the membrane is rate limiting [Waser *et al.*, 1998]. Thus, we considered only $\delta^{15}\text{N}_{\text{NO}_3}$ values for calculation of an apparent fractionation factor of nitrate utilization in the euphotic zone using equation (9) [Altabet and Francois, 1994]:

$$f = [\text{NO}_3^-]_{\text{surface}} / [\text{NO}_3^-]_{\text{initial}} \quad (9)$$

$$\delta^{15}\text{N}_{\text{NO}_3} = \delta^{15}\text{N}_{\text{NO}_3\text{-initial}} - \epsilon_u \times \ln(f), \quad (10)$$

where $\delta^{15}\text{N}_{\text{NO}_3\text{-initial}}$ and $\delta^{15}\text{N}_{\text{NO}_3}$ represent the initial isotopic signature of nitrate supplied to the surface and the isotopic signature of the nitrate after utilization, respectively; ϵ_u is the apparent fractionation factor of nitrate uptake. $[\text{NO}_3^-]_{\text{initial}}$ is the nitrate concentration of newly upwelled water estimated from the nitracline, corresponding to the highest $[\text{NO}_3^-]$ near or within the photic zone. ϵ_u can be directly estimated from the logarithmic regression of the Rayleigh plot of $\delta^{15}\text{N}_{\text{NO}_3}$ versus f (remaining fraction).

Values of the fractionation factor of apparent utilization along a vertical gradient, through the upper water column for each station, range from 3.7‰ in the northern stations to 5.7‰ at 17°S (Figure V.6). This modest range in ϵ_u , as well as its average over the Peruvian margin (4.7‰) is well within the range of prior field observations [Holmes *et al.*, 1998; Waser *et al.*, 1998; Altabet, 2001; Altabet and Francois, 2001; Horn *et al.*, 2011]. The slight increase in the observed fractionation factor from 3-8°S to 17°S could be associated with more favorable conditions for phytoplankton growth in the southern region, which corresponds very well with observed modern chlorophyll *a* concentrations perhaps due to relaxation of HNLC conditions (Figure V.1b). Indeed, between 12°S and 15°S, the strong perennial upwelling brings iron to the surface all along the year, increasing primary production and thus relative nitrate utilization [Bruland *et al.*, 2005].

The apparent fractionation factor ϵ_u may also vary due to changes in the diversity of nitrogen utilizing organisms [Waser *et al.*, 1998]. It was previously shown that, due to specific conditions like upwelling intensity, different specific diatom assemblages are found along the Peruvian margin [Abrantes *et al.*, 2007]. These changes in the population may influence the fractionation factor as each species might fractionate at different rates. However, it remains uncertain what the magnitude of such an effect on the small latitudinal difference in ϵ_u could be and we do not consider it further.

Furthermore, horizontal mixing may skew the calculation of the vertical fractionation factor above the nitracline, bringing an isotopically enriched signal into the system. However, this is unlikely as the main surface to subsurface current feeding the coastal upwelling, the PCCoastalC is equatorward (Figure V.1b). Therefore any horizontal mixing would increase the $\delta^{15}\text{N}_{\text{NO}_3}$ values to the North, which is in contradiction to the observations.

For the northern region the initial $\delta^{15}\text{N}_{\text{NO}_x}$ values between 3.5°S and 10°S obtained for the water column station at a given latitude are close to the $\delta^{15}\text{N}_{\text{sed}}$ values (Table 1). This is also true for the y-intercepts of the logarithmic regressions representing an average for the initial

$\delta^{15}\text{N}_{\text{NO}_3}$ in each region ($f=1$: no utilization, Figure V.6). This implies little net effect of surface partial nitrate utilization on the $\delta^{15}\text{N}_{\text{sed}}$ in the northern region.

At 17°S nitrate concentration was close to 0 at shallowest water depths during the sampling (Figure V.3b), implying complete nitrate utilization at that time. Due to the lack of nitrate it was not possible to measure water column $\delta^{15}\text{N}$, restricting the correlation between of $\delta^{15}\text{N}_{\text{NO}_3}$ and f at 17°S (Figure V.6) to f values of about 0.5. Theoretically, complete nitrate utilization should lead to $\delta^{15}\text{N}_{\text{sed}}$ values more similar to the initial $\delta^{15}\text{N}_{\text{NO}_3}$, as it is observed in the northern stations (Figure V.6, Table 1). Therefore other reasons must be considered to explain the large difference between the $\delta^{15}\text{N}_{\text{sed}}$ and initial $\delta^{15}\text{N}_{\text{NO}_3}$ (Figure V.6, Table 1) or weighted $\delta^{15}\text{N}_{\text{NO}_x}$ values (Figure V.5).

The explanation could be that the initial $\delta^{15}\text{N}_{\text{NO}_3}$ measured may only represent an seasonally very high value for the nitracline, but would be much lower than the measured one in the water column at 17°S (Figure V.3b). Since we have only water column measurements available for one day during the season of less intense upwelling but highest productivity (December to January; [Pennington *et al.*, 2006]), our water column data is probably not representative of the full spread of seasonal variations in nitrate and its isotopic properties, in contrast to the northern regions where either perennial ($12\text{-}15^\circ\text{S}$) or weaker and less permanent upwelling ($3\text{-}8^\circ\text{S}$) conditions prevail. For the moment we assume that the $\delta^{15}\text{N}_{\text{sed}}$ value of $\sim 9\text{‰}$ at 17°S is the multi-annual integration of the intra- and interannual variability of the isotopic signature of upwelled nitrate. More water column measurements will be needed to confirm this assumption since the sedimentary signal is integrating the signal of particulate OM produced throughout the euphotic zone as well as across seasonal timescale and spatial scales associate with the width of the shelf/upper slope.

As a feasibility test, we calculated the theoretical $\delta^{15}\text{N}$ of the particles produced above the nitracline (accumulated product: $\delta^{15}\text{N}_{\text{PN}}$), observed at each station ignoring temporal or spatial effects. As in previous work for the Equatorial Pacific [Altabet and Francois, 1994], $\delta^{15}\text{N}_{\text{PN}}$ can be estimated using the Rayleigh equation for the accumulated product (II), using the $\delta^{15}\text{N}_{\text{NO}_3\text{-initial}}$ in Figure V.6 and Table 1 [Mariotti *et al.*, 1981]:

$$\delta^{15}\text{N}_{\text{PN}} = \delta^{15}\text{N}_{\text{NO}_3\text{-initial}} + f / (1 - f) \times \epsilon_u \times \ln(f) \quad (\text{II})$$

From the equation (II), we found that $\delta^{15}\text{N}_{\text{PN}}$ values increase from 3.7‰ at 3.5°S to 14.2‰ at 17°S , which is broadly in agreement with the southward increase of measured $\delta^{15}\text{N}_{\text{sed}}$ (Figure V.5). These calculated values underestimate $\delta^{15}\text{N}_{\text{sed}}$ by $\sim 1\text{‰}$ in the North, but overestimates the sedimentary by $\sim 5\text{‰}$ in the South, as is reflected in the comparison between

$\delta^{15}\text{N}_{\text{sed}}$ and $\delta^{15}\text{N}_{\text{NO}_x}$ (Figure V.5), as well as in the difference between the $\delta^{15}\text{N}_{\text{NO}_3\text{-initial}}$ and the $\delta^{15}\text{N}_{\text{sed}}$ values (Figure V.6). Although the few water column data available in this area do not allow us to explain this discrepancy properly it is difficult to assume that during the unsampled season initial $\delta^{15}\text{N}_{\text{NO}_3}$ will become as low as the $\delta^{15}\text{N}_{\text{sed}}$ values at 17°S are indicating. This would be only possible if subsurface currents above the OMZ transport nitrate depleted in ^{15}N at least seasonally into the southern Peruvian upwelling region. To verify this assumption will need more water column measurements for the full annual cycle.

Alternatively, although we are confident that all our core-top values are from the latest Holocene, we cannot completely rule out small differences in surface age of few hundreds of years. From palaeo-studies it is known that centennial variations in the $\delta^{15}\text{N}_{\text{sed}}$ can have a magnitude of several ‰ in this region [Agnihotri *et al.*, 2006; Chazen *et al.*, 2009]. Then slight variations in core-top age at a given site could account for some deviation between $\delta^{15}\text{N}_{\text{sed}}$ and modern $\delta^{15}\text{N}_{\text{NO}_3\text{-initial}}$ values. However, all core top values on the shelf at about 17°S scatter between 8 and 11‰ and do not reach water values within the nitracline, which makes this explanation for the larger difference between the sediment and water values unlikely.

Another noteworthy finding of this study are increasing $\delta^{15}\text{N}_{\text{sed}}$ values towards the coast along cross shelf transects. Under progressive NO_3^- utilization with increasing distance from shore, $\delta^{15}\text{N}_{\text{sed}}$ values should increase correspondingly [Holmes *et al.*, 1998; Hebbeln *et al.*, 2000; Pichevin *et al.*, 2005] opposite to what is observed in most of our surface sediment $\delta^{15}\text{N}$ data on the shelf. The only increasing trend with increasing distance from the coast is observed for the deeper sites on the Nazca Rise, where we cannot exclude a $\delta^{15}\text{N}_{\text{sed}}$ increase as a result of diagenetic ^{15}N enrichment. In shallow waters between 11°S and 15°S instead, we observe a cross-shelf $\delta^{15}\text{N}_{\text{sed}}$ gradient decreasing seaward, particularly at the perennial upwelling centers [Suess *et al.*, 1987; Strub *et al.*, 1998; Echevin *et al.*, 2008]. The $\delta^{15}\text{N}_{\text{sed}}$ and $\delta^{15}\text{N}_{\text{NO}_x}$ values reach their minima at about 100 km from the coast at shelf break and increase again with increasing distance offshore (Figure V.7).

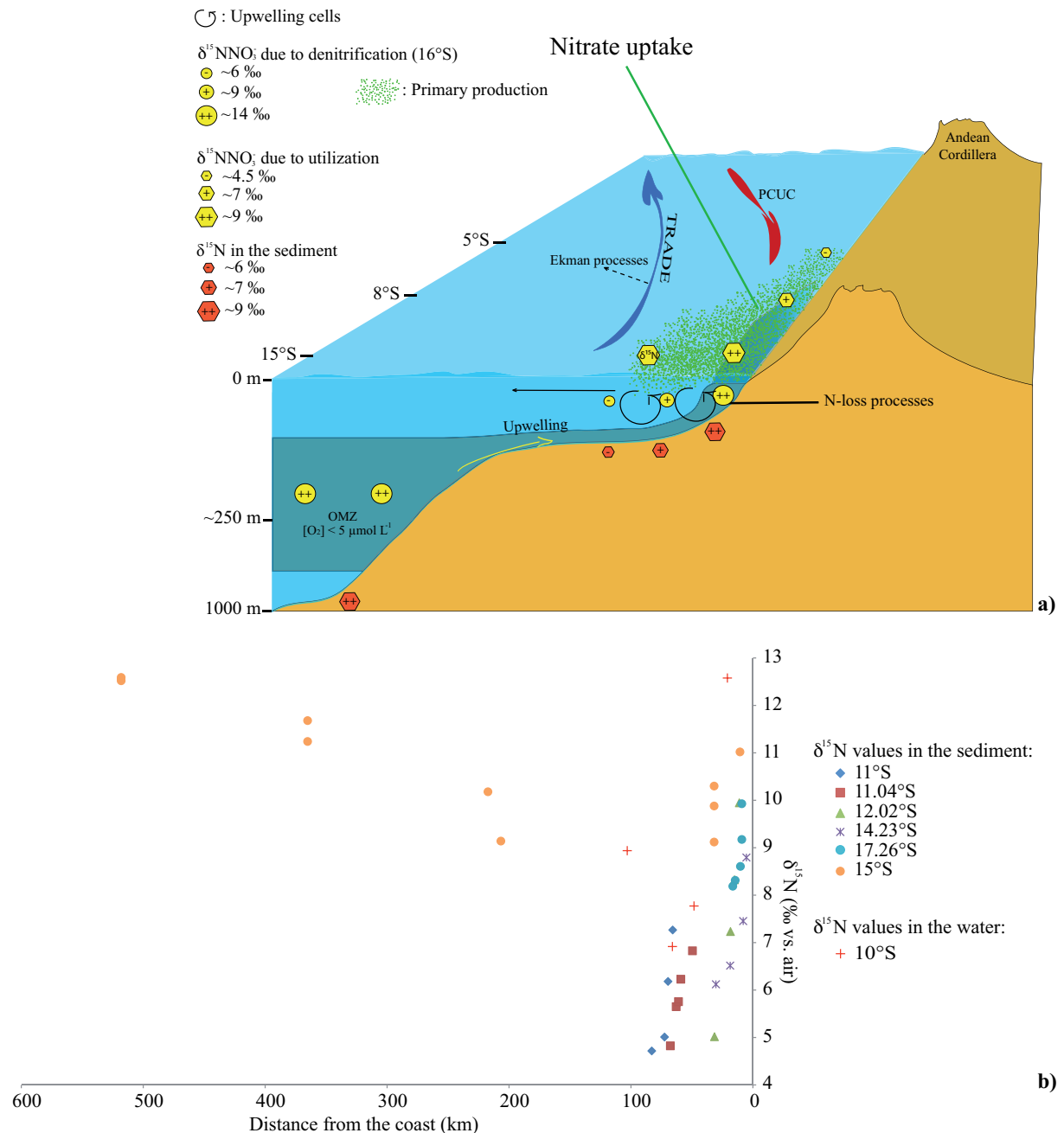


Figure V.7. Hypothetical scheme of the Peruvian upwelling system

a) Hypothetical scheme of nitrate utilization and N-loss processes taking into account $\delta^{15}\text{N}$ values of nitrate in the water column and later recorded in sediment organic matter. **b)** Plots showing $\delta^{15}\text{N}_{\text{sed}}$ and $\delta^{15}\text{N}_{\text{NO}_x}$ values as a function of the distance from the coast, in the perennial upwelling areas. Note the increase of values toward the coast within the 100 km distance, reflecting upwelling of high $\delta^{15}\text{N}$ nitrate inshore, either due to shoaling of the OMZ on the shelf or deeper reaching upwelling.

A likely explanation for decreasing trends in the sedimentary signal and thus in initial $\delta^{15}\text{N}_{\text{NO}_3}$ values with distance from the coast is that intense perennial upwelling inshore brings the oxycline as well as heavy $\delta^{15}\text{N}_{\text{NO}_x}$ values to much shallower water depth of 30 to 50 meters (Figure V.3b and Figure V.7). In addition, the deepening of the oxycline seaward leads to lower $\delta^{15}\text{N}_{\text{NO}_x}$ in the subsurface between 50 and 120 m (Figure V.3b: profile 10°S). Better

ventilation and low $\delta^{15}\text{N}_{\text{NO}_x}$ observed further offshore, probably result from the PCCoastalC, preventing high $\delta^{15}\text{N}_{\text{NO}_x}$ from the core of the OMZ to reach the photic zone. Unfortunately, no data on nutrient and oxygen conditions are available from the regional oceanography presented by *Czeschel et al.*, [2011] and thus this hypothesis needs further verification. In sum, heavy $\delta^{15}\text{N}_{\text{NO}_x}$ resulting from N-loss processes does not penetrate the euphotic zone and cannot be taken up by primary producers. Consequently, the cross-shelf trend of lower sediment $\delta^{15}\text{N}$ offshore is only observed in the OMZ south of 8°S (Figure V.7).

Alternatively, the decrease of $\delta^{15}\text{N}_{\text{NO}_x}$ and $\delta^{15}\text{N}_{\text{sed}}$ values from the coast towards the shelf break may be explained by nitrogen fixation [*Dalsgaard et al.*, 2003; *Kuypers et al.*, 2005; *Lehmann et al.*, 2007; *Gruber and Galloway*, 2008; *Galan et al.*, 2009; *Fernandez et al.*, 2011; *Sohm et al.*, 2011]. However this is unlikely considering the large nitrate pool in the upwelling area and low fixation rates ($23.8 \mu\text{mol N m}^{-2} \text{d}^{-1}$; [*Sohm et al.*, 2011]) as compared to 35 times higher N-loss rates ($679 \mu\text{mol N m}^{-2} \text{d}^{-1}$; [*Lam et al.*, 2009]). Thus this will not significantly change the system from an isotopic perspective.

Finally, it should be highlighted that $\delta^{15}\text{N}_{\text{NO}_x}$ values measured only during one single season is compared to the sedimentary $\delta^{15}\text{N}$, which integrates few dozens years. Thus, this comparison can only be taken as an approximation of the latitudinal and cross-shelf gradients that already fit very well in general but need further improvement by enhancing the spatial and temporal resolution. Particularly, it may be very helpful to further investigate the impact of seasonality on biogeochemical dynamics and coastal ecosystem response. Particular emphasis should be given to the nitrogen isotope signature of particulate matter as a function of water depth, which may allow disentangling the fractionation processes taking place above, within and below the OMZ. Studies on the interface between sediments and bottom water may unravel the complex issue of coastal nutrient limitation, particularly the role of iron release to the water column [*Scholz et al.*, 2011].

Overall, our new data provides strong evidence that the large scale gradients in $\delta^{15}\text{N}_{\text{sed}}$ along the Peruvian margin are dominated by N-loss processes within the OMZ with a modest overprint from partial NO_3^- utilization in surface waters particularly north of 8°S . Due to strong upwelling, $\delta^{15}\text{N}_{\text{NO}_3\text{-initial}}$ enriched in ^{15}N by N-loss processes in subsurface waters is incorporated into OM and ultimately preserved in the underlying $\delta^{15}\text{N}_{\text{sed}}$. This is reflected in both, zonal and latitudinal $\delta^{15}\text{N}_{\text{sed}}$ pattern. For the Peruvian margin any interpretation of $\delta^{15}\text{N}_{\text{sed}}$ records should thus primarily consider N-loss processes in subsurface waters when strongly enriched $\delta^{15}\text{N}_{\text{sed}}$ values are found.

V-6.3. Comparison to N. Chile

Comparable studies have been performed along the Chilean margin [De Pol-Holz et al., 2009], which reveal significant differences between both regions. Along the Peruvian margin, average $\delta^{15}\text{N}_{\text{sed}}$ values increase southward from 4‰ (5°S) to 10‰ (18°S) while along the Chilean margin $\delta^{15}\text{N}_{\text{sed}}$ values are generally higher and increase northward from 9‰ (45°S) to 15‰ (23°S). Highest $\delta^{15}\text{N}_{\text{sed}}$ values are not located within the core of the OMZ along the Peruvian margin (8-20°S), but off Chile between 23°S and 27°S. This is found even though oxygen minimum conditions in this region are limited to a narrow poleward coastal current. A likely scenario could be that the southward flowing PCUC, with an initial isotopic signature of 4-5‰ becomes both progressively enriched in $^{15}\text{N}_{\text{NO}_3^-}$ and shoals to the surface. Thus, south of the Peruvian OMZ, the narrow subsurface current carrying high $\delta^{15}\text{N}_{\text{NO}_3^-}$ signal poleward along the margin may be the source of upwelled waters off northern Chile. Together with local subsurface N-loss processes and coastal upwelling, the current transport results in very high initial $\delta^{15}\text{N}_{\text{NO}_3^-}$ values near the surface off northern Chile leading to very high $\delta^{15}\text{N}_{\text{sed}}$ values (>14‰) in the underlying sediments. However, this hypothesis for the moment does not consider northward transport mechanisms and supply of preformed nutrients with a southern $\delta^{15}\text{N}_{\text{NO}_3^-}$ signature. This will require further investigations of all data available for the South America margin.

V-7. Conclusions

A strong similarity between $\delta^{15}\text{N}_{\text{NO}_x}$ and $\delta^{15}\text{N}_{\text{sed}}$ gradients along the Peruvian margin indicates that the sedimentary signal reflects well latitudinal and cross-shelf changes in the isotopic composition of nitrate in Peruvian waters due to nitrogen cycling processes governed by oxygen minimum conditions and upwelling intensity. $\delta^{15}\text{N}_{\text{sed}}$ values show a strong increase towards the South with progressively higher $\delta^{15}\text{N}$ values in the water column. Enrichment in ^{15}N is associated with N-loss processes taking place within the OMZ, particularly south of 8°S. The N-loss signal is recorded in the sediment when heavy $\delta^{15}\text{N}_{\text{NO}_3^-}$ is brought to the surface by upwelling and consumed completely by phytoplankton. Thus the $\delta^{15}\text{N}_{\text{sed}}$ values observed are sensitive to depth origin of upwelled water, which is not necessarily at the nitracline, where NO_3^- concentrations are the highest. Sediment $\delta^{15}\text{N}$ values are by $\sim 1.5\text{‰}$ lower than upwelled $\delta^{15}\text{N}_{\text{NO}_x}$ due to partial NO_3^- utilization in surface waters all along the Peruvian margin, except for the perennial upwelling region where the difference between the

sedimentary signal and enhanced $\delta^{15}\text{N}_{\text{NO}_x}$ values is close to zero. In this region it also appears that nitrate enriched in ^{15}N is particularly upwelled on the inner shelf close to coast. This would explain the observed decrease in sedimentary $\delta^{15}\text{N}$ from the coast to the outer shelf because at the outer rim of upwelling centers, less intense upwelling is bringing up water from shallower depths above the core of the OMZ and why we observe a cross-shelf gradient with a seaward decrease of the $\delta^{15}\text{N}$ values within the water column and in the sediment. In contrast, much higher $\delta^{15}\text{N}$ sediment values are found off N. Chile likely due to shoaling of the subsurface layer with very $\delta^{15}\text{N}_{\text{NO}_3}$ in the narrow poleward undercurrent originating from the Peru OMZ.

V-8. Acknowledgements

We would like to thank Karine Charlier for assistance with sedimentary nitrogen isotopes, T. Bösch and D. Gutiérrez for providing biogenic opal data and additional nitrogen isotope data respectively. J. Karstensen is thanked for discussing the oceanography of the region and B. Willié to provide the basic map of the Figure V.2. This work is a contribution of Sonderforschungsbereich 754 "Climate—Biogeochemistry interactions in the tropical ocean" (<http://www.sfb754.de>), which is supported by the Deutsche Forschungsgemeinschaft. Financial support was partly provided by French research program LEFE-EVE (INSU CNRS) to P.M. The manuscript benefited from the constructive and very helpful comments of two anonymous reviewers.

Chapter VI. Nitrogen isotope evolution through water mass transport along the Eastern South American margin

VI-1. Introduction

Following the previous chapter, and in order to apply the calibration performed along the Peruvian margin, we present here a compilation of $\delta^{15}\text{N}$ measurement on surface sediments along the western margin of South America. From 0.5°N to 45°S , the coastal sample collection covers the surface area underlying the modern OMZ. In the world ocean, $\delta^{15}\text{N}$ values are known to vary consistently with several processes, such as the N-loss processes and relative nitrate utilization [Chapter V]. Previous studies of the three OMZs (North Pacific, South Pacific, and Arabian Sea) have assumed that the variability of the $\delta^{15}\text{N}$ values within the OMZ is driven primarily by the N-loss process [*Pride et al.*, 1999; *Agnihotri et al.*, 2006; *Pichevin et al.*, 2007; *Galbraith et al.*, 2008]. Some studies have also demonstrated that $\delta^{15}\text{N}$ values may vary due to changes in the relative utilization of the nitrates, either by changes in the PP or in the nitrate availability [*Francois et al.*, 1992; *Voss et al.*, 1996; *Holmes et al.*, 1998; *Hebbeln et al.*, 2000; *Pichevin et al.*, 2005]. In addition to the multiple processes fractionating the nitrate signal, upwelling enables the transfer of isotopically heavy nitrate from the subsurface to the surface. The high isotopic signal from the core of the OMZ is thus assimilated by the biota via nitrate uptake and, further more, integrated in the sinking particulate matter [*Altabet et al.*, 1999]. High $\delta^{15}\text{N}$ values originating from either the N-loss process or relative nitrate utilization increases the general isotopic signature of a water mass. This implies that a water mass with an initially heavy isotopic signature may result in high $\delta^{15}\text{N}$ values recorded in the sediment, even in absence of the N-loss process within the upper water column. Indeed, the origin of the nitrate available at the surface for organisms may be considered as one of the most important factors influencing the variability of the $\delta^{15}\text{N}$ values recorded in the underlying sediment.

VI-2. Oceanography along the western South American coast

The western margin of South America is composed of two main systems: 1. To the South, the Peru-Chile Undercurrent (PCUC) and the Peru-Chile Countercurrent (PCCC), which

are the main sources of the upwelling cells ([Wyrski, 1981; Silva et al., 2009; Czeschel et al., 2011] Figure VI.1.a).

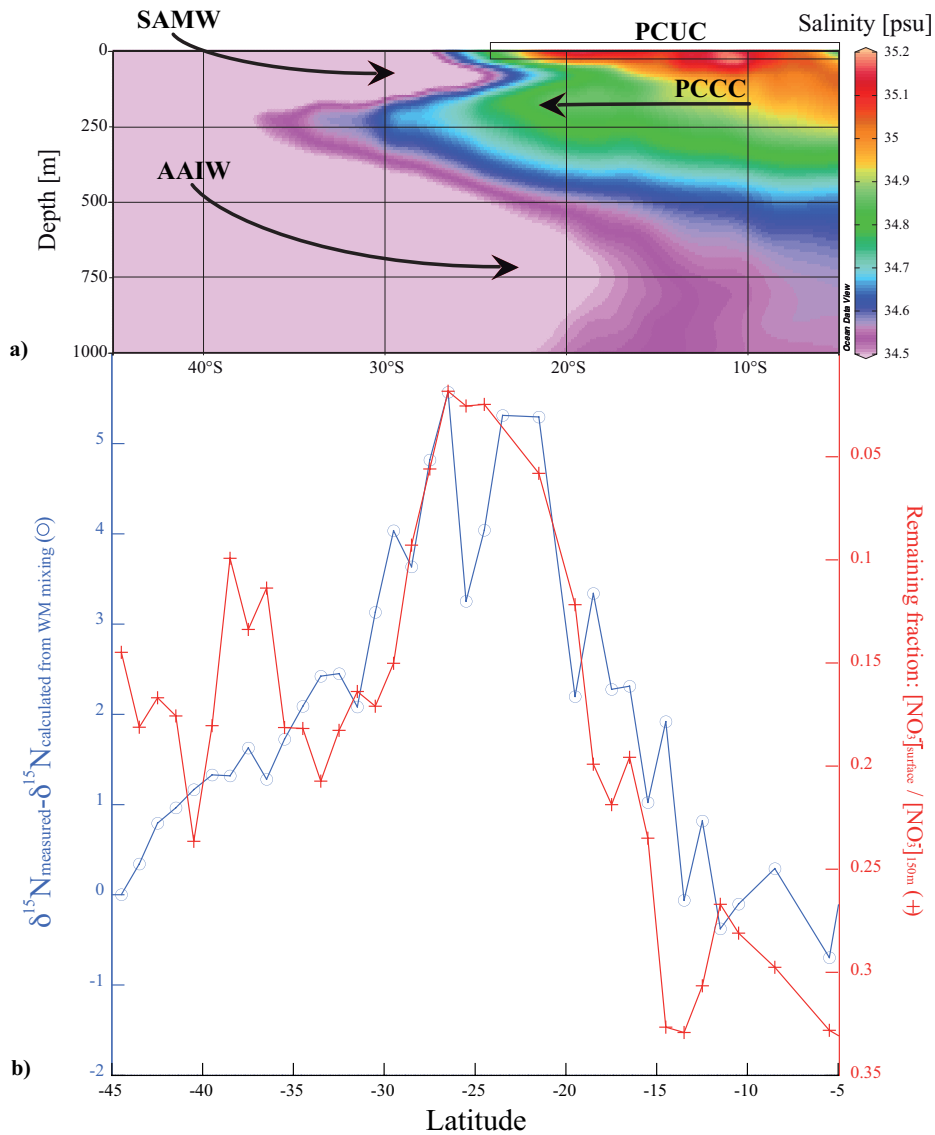


Figure VI.1. Salinity distribution and nitrate utilization along the western margin of South America

a) Salinity distribution as a function of depth and latitude from ~ 100 km along the coast, extracted from WOA09; **b)** Latitudinal distribution of nitrate utilization calculated with the equation (14) out of WOA09 data set (red curve with crosses) and difference between $\delta^{15}N_{sed}$ and $\delta^{15}N$ calculated from water mass mixing (blue curve with open circles).

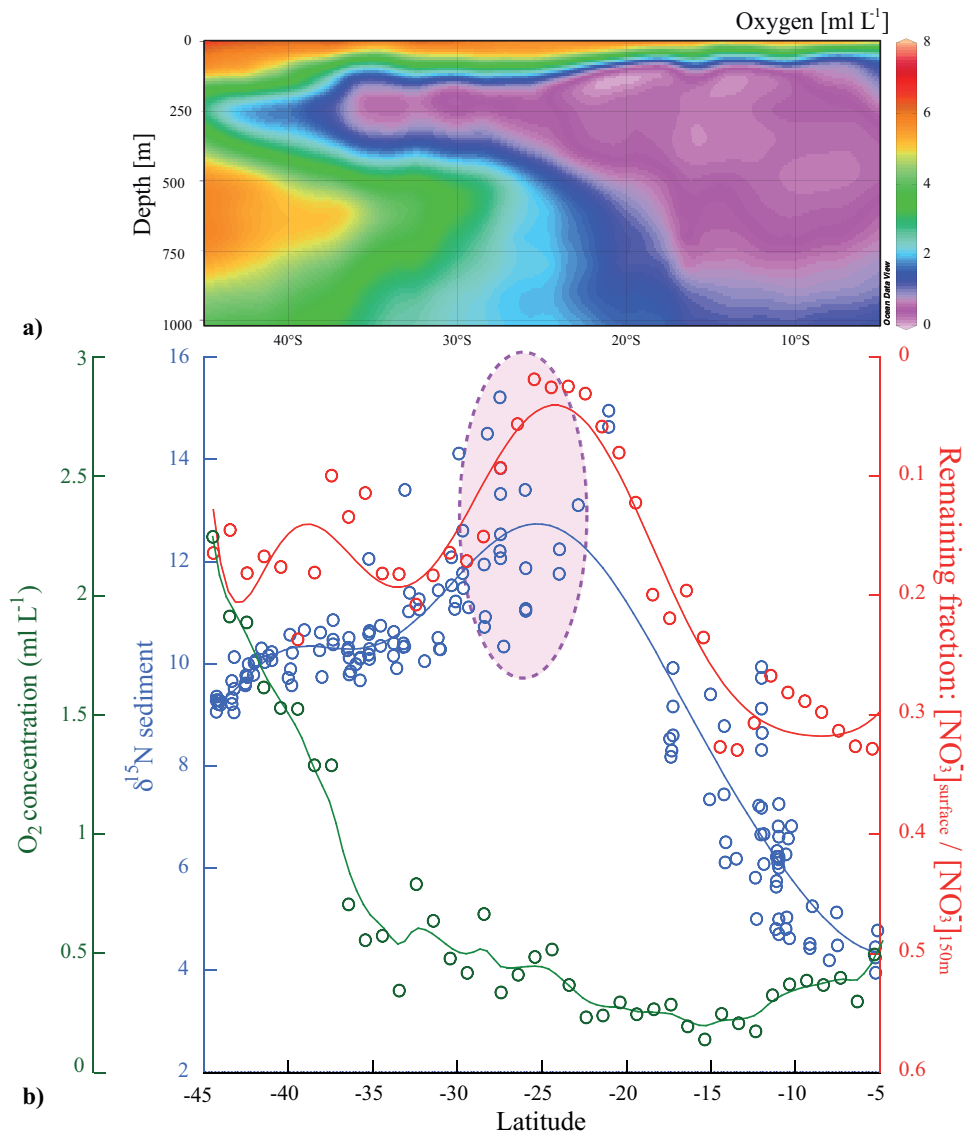


Figure VI.2. Oxygen distribution, nitrogen isotopes and nitrate utilization along the western margin of South America

a) Coastal distribution of annual mean oxygen concentration as a function of depth and latitude, extracted from WOA09; b) Plot showing $\delta^{15}\text{N}_{\text{sed}}$ values (blue curve), oxygen concentration at 250 m water depth (green curve) and nitrate utilization (red curve) between 5°S and 45°S, both extracted from WOA09.

The intermediate water source for the Peru OMZ is characterized by high salinity, low O₂, and high nutrients. Between 0°S and 10°S and down to 500 m depth, further O₂ depletion in this southward flow results in near anoxia south of 10°S (Figure IV.2.a). The eastern South Pacific OMZ develops from 5°S to 30°S, with maximum expansion of the OMZ core (< 0.5 ml L⁻¹) between 8°S and 20°S and reaching up to 30 m below the surface off Peru. The PCU is found between 5°S and 15°S; the strongest upwelling occurs in individual active cells, with some perennial cells located around 11-12°S and 14-16°S [Suess *et al.*, 1987; Strub *et al.*, 1998].

2. To the North, the flow is driven by SubAntarctic Mode water (SAMW) from the surface

down to 250 m, coming from the Antarctic Circumpolar Current (ACC) and reaching 25°S (Figure VI.1.a). Underlying SAMW, Antarctic Intermediate Water (AAIW) extends from 250 m to below 1000 m and reaches to the equatorial area. These two currents are characterized by low salinity, high O₂ content, but are relatively nutrient deficient [De Pol-Holz *et al.*, 2009]. Thus the OMZ is ventilated from below by AAIW and at the surface by SAMW, reaching very low oxygen concentrations between 10°S and 23°S, from the surface down to ~450 m (Figure VI.2.a). Consequently, in between the AAIW and the SAMW, a thin water tongue remains oxygen depleted (Gunther Undercurrent, GU, 200-300 m water depth), and the core of the OMZ possessing the lowest O₂ concentrations becomes absent. Most of the upwelling along the Chilean coast is located around 35-38°S, however surface waters only contain GU derived components during times of strong upwelling [Strub *et al.*, 1998].

Additionally, the western South American margin is well known to possess high PP, however differently distributed along the coast. Highest levels of chlorophyll *a*, associated with PP, are located along the Peruvian margin and occur in austral summer, in antiphase with the strongest upwelling season [Chavez *et al.*, 1996; Echevin *et al.*, 2008]. The large amount of nitrate occurring during the austral winter leads to seasonal HNLC conditions [Pennington *et al.*, 2006]. In contrast, the northern and central Chilean margin is characterized by much lower nitrate concentration and a quasi-total consumption of the nitrate is observed in the surface water (Figure VI.3).

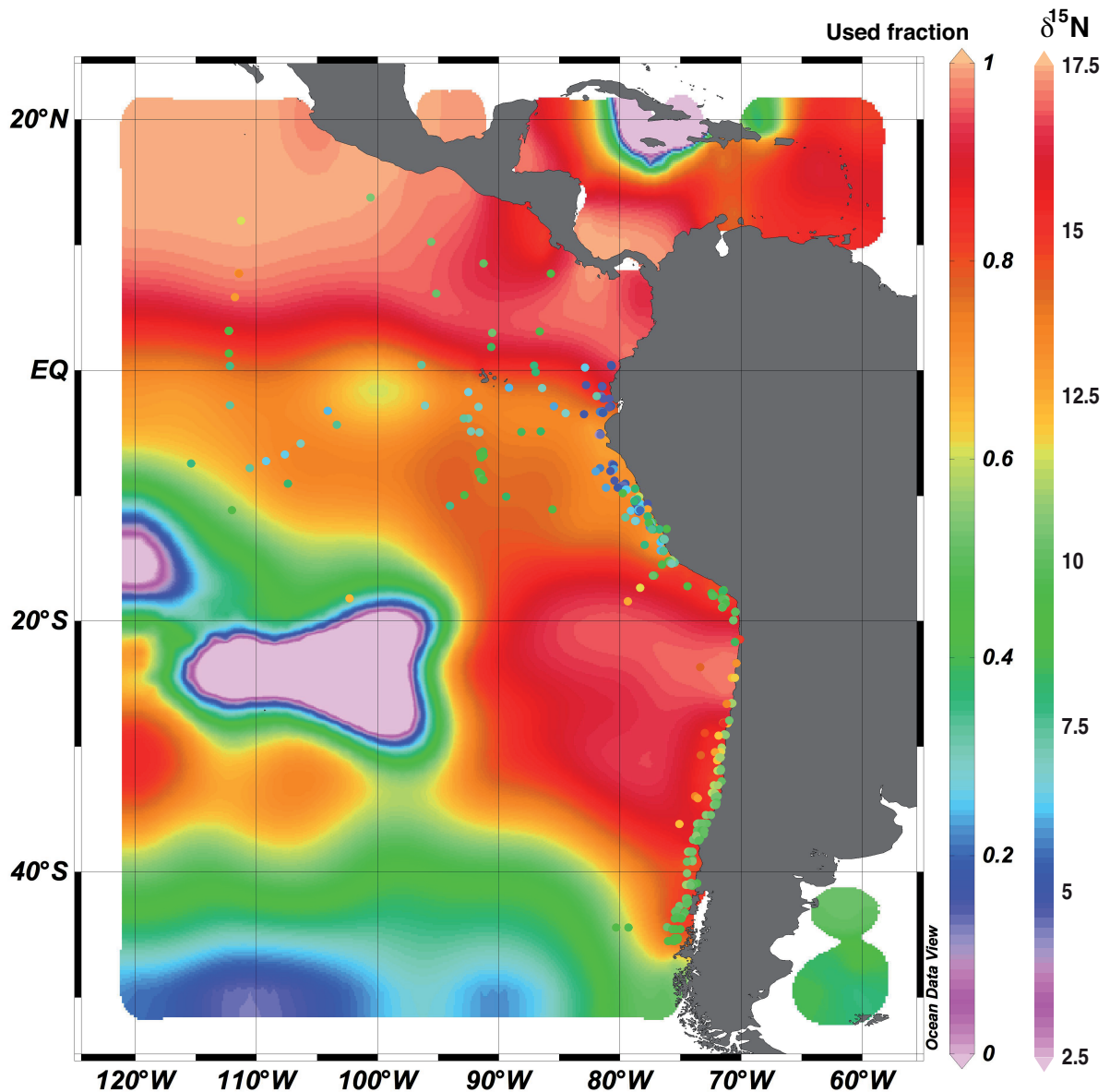


Figure VI.3. Compilation of $\delta^{15}\text{N}$ sediment mapped on the calculated nitrate utilization

Compilation of $\delta^{15}\text{N}$ sediment from this study and from the literature [Farrell *et al.*, 1995; Hebbeln *et al.*, 2000; De Pol-Holz *et al.*, 2009].

VI-3. Results and discussion

A compilation of data from the present study and previous literature from the Chilean margin allowed an assessment of the processes influencing the $\delta^{15}\text{N}$ signal for the entire western South American margin.

Along the Peruvian margin $\delta^{15}\text{N}_{\text{sed}}$ average values increase from 4‰ (5°S) to 10‰ (18°S), which is in agreement with the PCUC flowing southward along the coast (Figure VI.3).

Along the Chilean margin $\delta^{15}\text{N}_{\text{sed}}$ values are generally higher and increase northward from 9‰ (45°S) to 15‰ (23°S). Surprisingly, higher $\delta^{15}\text{N}_{\text{sed}}$ values are not located within the core of the OMZ along the Peruvian margin (10-20°S), but off Chile between 23°S and 27°S (Figure VI.2.b), even though they are located in well-oxygenated surface and subsurface waters ($[\text{O}_2] > 0.5 \text{ ml L}^{-1}$). This observation questions previous paleoceanographic reconstructions that have explained highest $\delta^{15}\text{N}_{\text{sed}}$ values by strongest denitrification during Glacial/Interglacial cycles [Pride *et al.*, 1999; Agnihotri *et al.*, 2006; Pichevin *et al.*, 2007; Galbraith *et al.*, 2008].

The two water masses that compose the coastal oceanography along South America, the PCUC flowing southward and the SAMW flowing northward, meet at ~25°S. The SAMW is better oxygenated than the PCUC, therefore strong N-loss processes are not observed within the water sample stations south of 21°S [Hebbeln *et al.*, 2000; De Pol-Holz *et al.*, 2009]. These two water masses flow in opposite directions, which causes chemical and physical mixing around ~25°S (Figure VI.1.a); this may explain the $\delta^{15}\text{N}$ variability along the South American coast. To test this hypothesis we considered the two water masses as 2 end-members in regard to their salinity and temperature characteristics, and calculated a theoretical mixing of the water masses. From the WOA09 [Garcia *et al.*, 2010], we extracted salinity and temperature at the average depth of the two water masses (500 m), with a resolution of 1° latitude and 1° longitude from the coast. To calculate the percentage for each water mass contribution for a specific latitude, we used equation (13) and (14) derived from equation (12) (see below). The calculation has been performed for each degree of latitude and independently for the salinity and the temperature.

$$\text{Sal} = x_1 \cdot s_{5^\circ\text{S}} + x_2 \cdot s_{45^\circ\text{S}} \quad (12)$$

$$x_1 = (s - s_{5^\circ\text{S}}) / (s_{5^\circ\text{S}} - s_{45^\circ\text{S}}) \quad (13)$$

$$x_2 = 1 - x_1 \quad (14)$$

In these equations, x_1 and x_2 represent the percentages of mixing respectively for the PCUC and the SAMW, and t the salinity at each degree latitude for the two parameters. $s_{5^\circ\text{S}}$ and $s_{45^\circ\text{S}}$ are considered the two end-members.

To test the robustness of this approach, we calculated the theoretical temperature variability due to mixing, based on the salinity equation, and vice versa. The comparison of the theoretical temperature and the temperature from WOA09 at 500 m water depth shows a significant correlation, with $r^2 = 0.97$. Additionally, the temperature-based equation was applied to calculate the theoretical salinity, and a significant correlation was obtained. The last step was to apply this mixing equation to the $\delta^{15}\text{N}_{\text{sed}}$ values.

After using the process described above, we obtained the theoretical $\delta^{15}\text{N}$ variability due to the mixing of the two water masses, considering the two $\delta^{15}\text{N}_{\text{sed}}$ end members of 4‰ at 5°S and 9‰ at 45°S. This theoretical $\delta^{15}\text{N}$ was subtracted from the $\delta^{15}\text{N}_{\text{sed}}$ measured, which gives us the $\delta^{15}\text{N}_{\text{sed}}$ change due to nitrate utilization and/or the N-loss process, excluding the mixing of the different water mass $\delta^{15}\text{N}$ signatures.

The $\delta^{15}\text{N}_{\text{sed}}$ corrected for mixing ($\delta^{15}\text{N}_{\text{corrected}}$) still follows the general trend of nitrate utilization (Figure VI.1), with a higher correlation between $\delta^{15}\text{N}_{\text{corrected}}$ and nitrate utilization for the SAMW than for the PCUC, showing the influence of N-loss process along the Peruvian margin ($r^2 = 0.7$ and $r^2 = 0.4$ respectively; Figure VI.4).

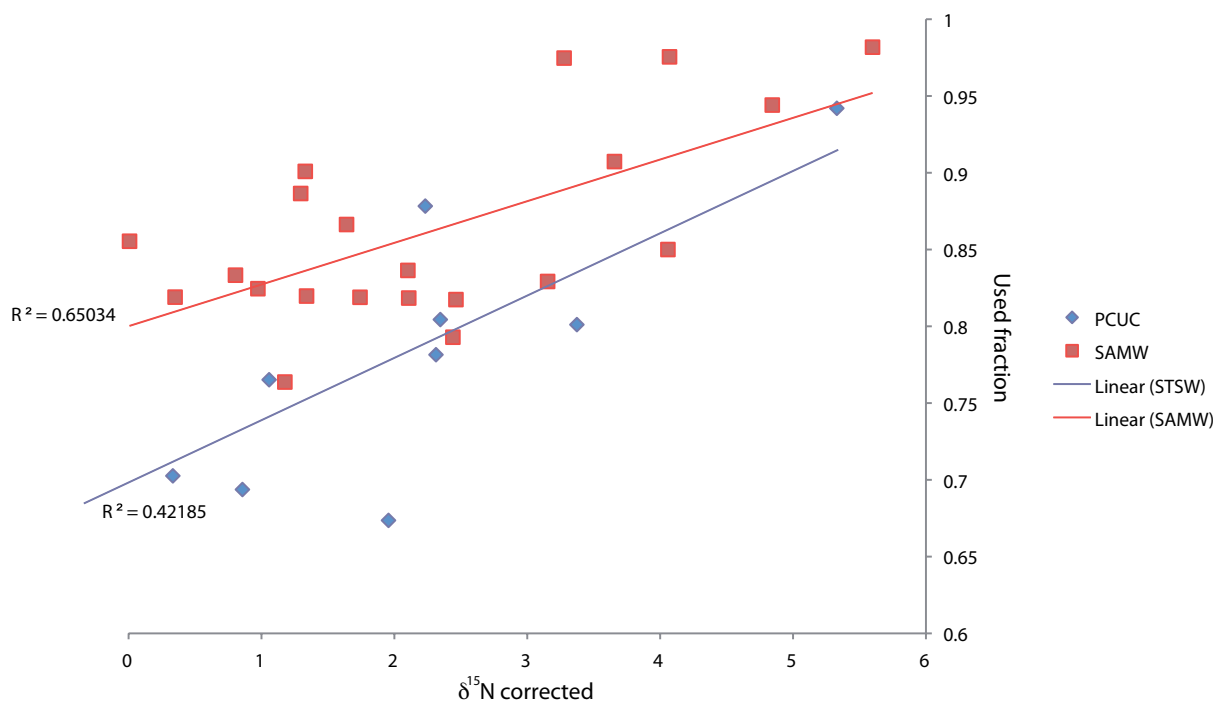


Figure VI.4. Correlation between nitrogen isotopes corrected from mixing and nitrate utilization

This plot shows the correlation between the $\delta^{15}\text{N}_{\text{corrected}}$ and the used fraction calculated from the WOA09. The blue diamonds correspond to the Peru-Chile Under Current (PCUC) from 5°S to 24.5°S, and the red squares to the South Antarctic Mode Water (SAMW) from 24.5°S to 45°S.

In addition, the OMZ core stopped at $\sim 23^\circ\text{S}$ and O_2 concentration values increased to the South due to well-oxygenating SAMW off Chile. As is observed along the Peruvian margin, N-loss processes do not take place in the photic zone once the oxycline ($[\text{O}_2] < 0.5 \text{ ml L}^{-1}$) is deeper than $\sim 100 \text{ m}$ water depth (Figure VI.2.a). [De Pol-Holz et al., 2009] also show the absence of N-loss processes evidence in the water column south of 21°S. Consequently, the N-loss process does not explain the $\delta^{15}\text{N}_{\text{sed}}$ variability along the Chilean margin.

Although the sampling resolution of the $\delta^{15}\text{N}_{\text{NO}_3^-}$ values over the upper surface water (200 m) off the Chilean margin is lower than from the Peruvian margin, we are still able to distinguish generally higher $\delta^{15}\text{N}_{\text{NO}_3^-}$ values (11‰ to 18‰) [Fig. 5d in *De Pol-Holz et al.*, 2009] than the ones shown off Peru (5‰ to 17‰) (Chapter V, Figure V.5). Consequently the initial isotopic signature of the SAMW is already higher than that of the PCUC. The confluence of the two water masses, located at $\sim 25^\circ\text{S}$, is consistent with the highest $\delta^{15}\text{N}$ values observed in the water column as well as in the sediment. Around 27°S , SAMW sinks below the PCUC down to 500 m water depth. As SAMW waters are no longer upwelled to the surface, the high $\delta^{15}\text{N}_{\text{NO}_3^-}$ signature is not assimilated by the phytoplankton and thus is not recorded in the sediment.

To better interpret the impact of nitrate utilization on $\delta^{15}\text{N}_{\text{sed}}$ values, we calculated an estimation of nitrate utilization based on annual nitrate concentrations from WOA09 dataset along the entire South American margin (5°S to 45°S , Figure VI.1.b) from equation (15):

$$\frac{[\text{NO}_3^-]_{\text{surface}}}{[\text{NO}_3^-]_{150\text{ m}}} \quad (15)$$

Highest nitrate utilization is concomitant to highest $\delta^{15}\text{N}_{\text{sed}}$ values between 23°S and 25°S , and the statistical correlation between $\delta^{15}\text{N}_{\text{sed}}$ and nitrate utilization along the entire South American margin is significant with an $r^2 = 0.7$. Thus, we can conclude that the SAMW possesses a higher initial $\delta^{15}\text{N}$ signature of $\sim 14\%$ in the water column and $\sim 9\%$ in the sediment at 45°S , and becomes impoverished in $^{14}\text{NO}_3^-$ due to nitrate utilization from the phytoplankton on its way to the North. As far as can be observed within our dataset, $\delta^{15}\text{N}_{\text{sed}}$ from the Peruvian margin and from the Chilean margin increases respectively towards the South and the North until the confluence of the two water masses at $\sim 25^\circ\text{S}$.

In conclusion, PCUC with an initial isotopic signature of $4\text{--}5\%$ flows southward becomes enriched in ^{15}N , and the $\delta^{15}\text{N}_{\text{sed}}$ increases up to 10% . The SAMW possesses a higher initial $\delta^{15}\text{N}_{\text{sed}}$ signature of 9% , increasing towards the North to 15% , which may result from the accumulation of isotopically heavy nitrate in the water mass. Paleoceanographic reconstructions should take into account the initial signature of the water mass before making further interpretations. Furthermore, our study shows that both nitrate utilization and the N-loss process affects the $\delta^{15}\text{N}$ recorded in the sediment along the South American margin.

Chapter VII. Mid-Holocene collapse of the Peruvian oxygen minimum zone

Elfi Mollier-Vogel^{1*}, Philippe Martinez², Ralph R. Schneider

¹Institute of Geosciences, University of Kiel, Germany

²Université Bordeaux 1, UMR CNRS 5805 EPOC, avenue des facultés, 33405 Talence cedex, France

This chapter is going to be submitted to Paleocyanography

VII-1. Abstract

This study presents new high resolution $\delta^{15}\text{N}$ records from piston cores collected within and outside the present-day OMZ along a latitudinal transect from 3.5°S to 15°S . Under suboxic to anoxic conditions in the subsurface waters, microbial N-loss to N_2 , e.g. denitrification and/or anammox, leaves a characteristic ^{15}N -enriched signal in underlying sediments. Thus, we interpret $\delta^{15}\text{N}$ values as mostly representative to changes in N-loss processes, although HNLC conditions prevail in the region of the study area and may shift a little the $\delta^{15}\text{N}$ values. Radiocarbon dating of foraminifera and organic matter reveals that the cores cover the Holocene and the last deglaciation with high sedimentation rate allowing interpretations at millennial to centennial timescale. High $\delta^{15}\text{N}$ values, reaching 10‰ and large amplitude changes, with a magnitude of $\sim 4\text{‰}$ are observed in the southern part of the studied area during the last 18 ka BP. In contrast the northern cores, off Peru, show low $\delta^{15}\text{N}$ values varying from 4 to 6‰ with amplitude of only 1‰, during the same time period. Interestingly, the $\delta^{15}\text{N}$ decreases in all the studied cores from the last deglaciation to the early Holocene (17 to 8.5 ka BP) and reaches minimum value during the mid-Holocene. Surprisingly, $\delta^{15}\text{N}$ values from cores located within the OMZ show similar values as the more northern cores located outside the OMZ. This minimum is not related to local changes in sedimentary proxies related to export production, such as organic carbon, total nitrogen or bromine, considered as an indirect proxy for primary productivity and appears to be controlled by changes in the ventilation of the area. The low $\delta^{15}\text{N}$ values recorded between 8.5 to 5 ka BP are well correlated with more arid conditions developed along the Peruvian margin and an increase of the sea surface temperature gradient between the West and East Pacific along the equator, implying a climate similar to more La Niña-like conditions.

Consequently, an strong intensification of the upwelling during the mid-Holocene may have led to greater ventilation of the surface and subsurface waters, deepening the oxycline and revealing similar conditions that observed today in the northern part of the study area.

VII-2. Introduction

The ETSP is one of the most productive areas in the world ocean due to permanent or seasonal upwelling cells along the coasts. This area also hosts the most intense and shallowest OMZ in the open ocean. Off Peru, the dissolved oxygen content ranges from saturated values at the surface to values lower than 0.25 ml L^{-1} within the euphotic zone (20 to 50 m), and reaches values of less than 0.02 ml L^{-1} at greater depths of 100 to 450 m within the core of the OMZ [Thamdrup *et al.*, 2012]. Strong oxygen minimum conditions results from the interplay of a weak advection of oxygen by the subsurface circulation of poleward undercurrents and a high oxygen demand related to the remineralization of large amounts of sinking organic matter (OM) at sub-surface depths. The OMZ is also characterized by N-loss processes, i.e. the bacterial reduction of nitrate (e.g., denitrification and/or anammox) under suboxic to anoxic conditions ($[\text{O}_2] < 0.5 \text{ ml L}^{-1}$; [Codispoti and Christensen, 1985]). The relative importance of denitrification ($\text{NO}_3^- \rightarrow \text{NO}_2^- \rightarrow \text{NO} \rightarrow \text{N}_2\text{O} \rightarrow \text{N}_2$), compared to anammox ($\text{NO}_2^- + \text{NH}_4^+ \rightarrow \text{N}_2$) is strongly debated for the Peruvian OMZ [Lam *et al.*, 2009] but both processes can be considered as the main sink of oceanic N and thus as one major biogeochemical process that controls the inventory of nitrate in the global ocean, the oceanic biological production and CO_2 fluxes between the ocean and the atmosphere. Along with ongoing global warming, OMZs seem to intensify and also expand spatially [Stramma *et al.*, 2008; Stramma *et al.*, 2010], incurring drastic changes from the combined impact of both rapidly declining O_2 concentrations and increasing CO_2 levels due to reduced solubility of both gases. In the core of OMZ, N-loss processes occurring during the degradation of OM possess a large isotopic fractionation and lead to the accumulation of ^{15}N -enriched nitrate in the remaining pool [Wada and Hattori, 1978; Altabet and Francois, 1994]. Supply of these heavy nitrates to the surface waters by upwelling and its utilization by plankton will then enrich the particulate OM in the heavy isotope [Altabet *et al.*, 1999; Mollier-Vogel *et al.*, 2012]. A good preservation of the isotopic signals generated in the water column, as is observed in areas characterized by high fluxes and accumulation rates of OM, enables the use of sedimentary $\delta^{15}\text{N}$ records to reconstruct changes in the extent of intermediate-water suboxia

and related N-loss processes that varied significantly with climate on orbital, millennial and decadal time-scales [Altabet *et al.*, 1995; Ganeshram *et al.*, 1995; Agnihotri *et al.*, 2006; Martinez *et al.*, 2006; Pichevin *et al.*, 2007; Robinson *et al.*, 2009; Gutiérrez *et al.*, 2009]. Sedimentary nitrogen isotope records from the ETSP margins off Chile and Peru indicate that the extent of N-loss in the water column was lower during the last glacial period than during modern times, then ventilation strongly decreased at the beginning of the deglaciation and slowly recovered again into the early Holocene [Higginson *et al.*, 2004; De Pol-Holz *et al.*, 2006; Robinson *et al.*, 2007]. Increased ventilation of intermediate waters during glacial intervals has been attributed to both enhanced oxygen supply by subsurface water masses and decreased oxygen demand in the subsurface due to lower export production.

In addition to glacial-interglacial variations, more recent studies have demonstrated that the extent of the Peruvian OMZ may also change abruptly at very short time-scales, i.e., decadal over the last few hundred years [Gutierrez *et al.*, 2006; Sifeddine *et al.*, 2008] to centennial over the last 10 ka BP [Agnihotri *et al.*, 2008; Chazen *et al.*, 2009]. Several forcing mechanisms play an important role in the dynamic of these large OMZs, which can vary with the time-scale considered. Based on sedimentary records located in the centre of the modern Peruvian upwelling area and the OMZ between 12 and 14°S, Gutierrez *et al.* [2009] showed that conditions characteristic for the modern system with low surface productivity and higher sub-surface oxygenation develop in phase with the end of the Little Ice Age. This development was driven by a change in the local atmospheric circulation associated to a weakening in Walker circulation strength and a more southern position of the ITCZ, which is in opposition to the modern conditions. On the other hand, for instance, Chazen *et al.* [2009] proposed that surface productivity and sub-surface ventilation off Peru were remotely driven through processes originating from outside the southeastern Pacific, such as changes in the global nutrient cycle. Thus, that may explain the lack of a positive relationship between local indicators of higher export production and the expected high $\delta^{15}\text{N}$ in sediments, especially over the late Holocene. This brief examination of the literature suggest that there is no consensus on the mechanisms, atmospheric and/or oceanic, behind the export production and OMZ fluctuations recorded on the Peruvian margin, and that major processes affecting the system during recent multidecadal variations may be different from centennial- to millennial-scale changes.

The most recent studies dedicated to the dynamics of the Peruvian OMZ over the last 20 ka BP [Higginson *et al.*, 2004; Agnihotri *et al.*, 2006, 2008; Chazen *et al.*, 2009; Gutierrez *et*

al., 2009; *Sifeddine et al.*, 2008] all focused on the central part of the margin between ~ 10 and $\sim 15^{\circ}\text{S}$ where the sediments over the platform intersect the OMZ and constitute a well-preserved depositional center of laminated organic-carbon-rich mud facies [*Reinhardt et al.*, 2002], where the geochemical and climatic signals are particularly well preserved. Although the OMZ and the productive area are most intense in the central part of the Peruvian margin between 10 and 15°S , their influence on coastal and offshore surface waters over the shelf and upper margin extends far beyond these limits [*Pennington et al.*, 2006; *De Pol-Holz et al.*, 2007]. Therefore the aim of this study is to reconstruct changes in surface water biological productivity and export fluxes and compare these with the variability of oxygen deficiency in subsurface waters, using a set of four shallow sediment cores recovered along a latitudinal transect between 3° and 14° S. These 4 cores cover the northern rim of the OMZ off Ecuador as well as its centre part off central and southern Peru, enabling a mesoscale spatial view on the climatic and paleoceanographic fluctuations within the coastal upwelling and OMZ in the ETSP.

VII-3. Material and methods

VII-3.1. Core locations

We present new data obtained from four long piston-cores (10 to 15 m) collected at three locations along the Peruvian and Ecuadorian margins (Figure VII.1). The two southern cores M772-003 and -029 are located at shallow depths in the centre and the northern extension of the modern OMZ, at 15°S in water depth of 271 m and at 9°S in 433 m, respectively. At these depths and latitudes, the combination of high biological export production and large oxygen deficiency results in high sedimentation rates of biogenic OM and opal, the absence of bioturbation and thus in the formation of millimeter scale green to yellow laminations that dominate the whole sedimentary sequences. The two northern cores, M772-056 and -059 are located at the northern edge of the OMZ at 3.5°S but at two different water depths, 355 m and 997 m, respectively. Here sediments consist of fine homogenous green, hemipelagic mud, and high oxygen concentration, allowing substantial benthic population at the sea floor, prevent the preservation of laminations even for the shallow site which is still located at the northern rim of the OMZ (Figure VII.1).

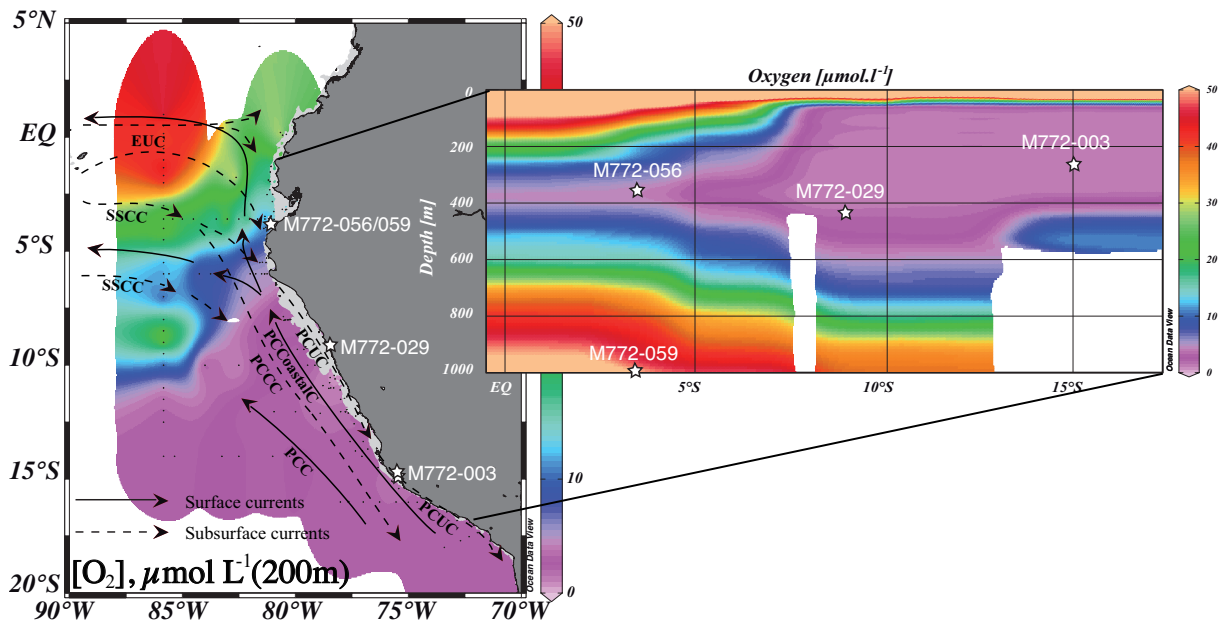


Figure VII.1. Map of oxygen concentration off Peru and core location

Map of the Peru-Ecuador margin showing oxygen concentrations at 200 m water depth, from CTD casts of the METEOR-2008 cruises gridded with the ocean data view software [Schlitzer, R., *Ocean Data View*, <http://odv.awi.de>, 2011]. White and black crosses show the locations of the studied cores. Surface currents are marked by solid lines: PCC - Peru Chile Current, PCCoastalC - Peru Chile Coastal Current, SEC - South Equatorial Current, and subsurface currents by dash lines: EUC - Equatorial Undercurrent, SSCC - Southern Subsurface Counter Current, PCCC - Peru Chile Counter Current, PCUC - Peru Chile Undercurrent [adapted from *Penven et al.*, 2005; *Kessler*, 2006; *Czeschel et al.*, 2011]. As for the map, the cross section shows the extent of the Peruvian OMZ as measured with the CTD casts.

Previous studies have shown that Holocene paleoclimatic records along the Peruvian margin can suffer from large gaps in sedimentation [see *Reinhardt et al.*, 2002]. This seems to be particularly the case for the middle part of the Peruvian shelf, around 10-12°S, where many records reveal incomplete Holocene sections [*Higginson et al.*, 2004; *Rein et al.*, 2005; *Chazen et al.*, 2009]. Accordingly, at site M772-029, due to a very low sedimentation rate or a major hiatus, the last 6000 years are covered by the uppermost 50 cm of sediment only (Table 3; Figure VII.3). For the other sites complete deglaciation to latest Holocene sediment sequences could be recovered.

VII-3.2. Geochemical analyses

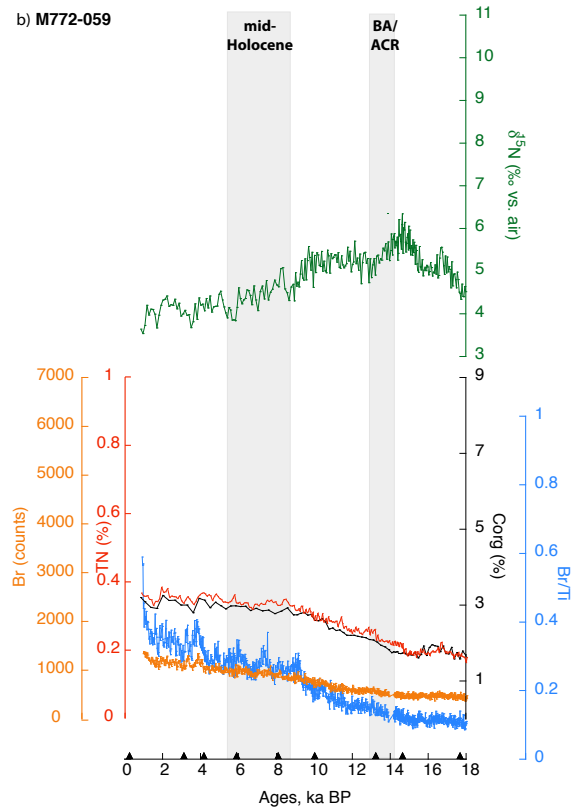
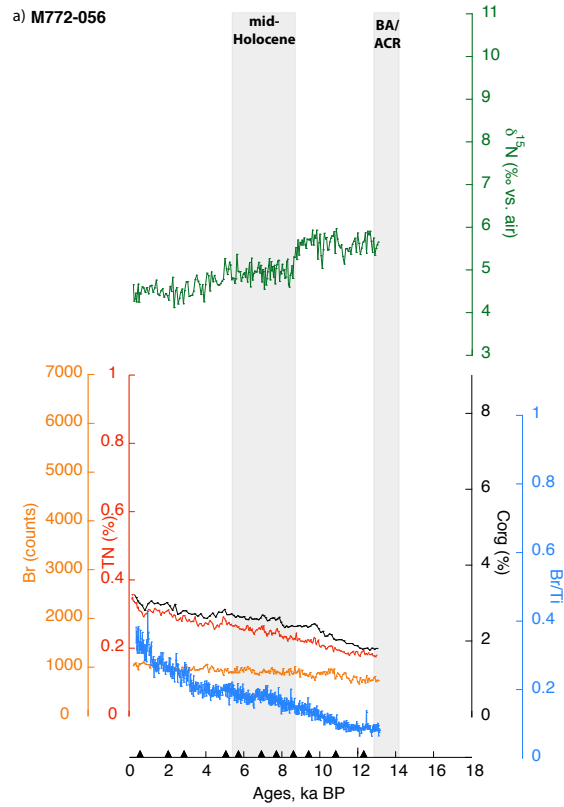
Sedimentary $\delta^{15}\text{N}$ and total nitrogen contents (TN, wt %) were measured on ~5 to 60 mg of homogenized and freeze-dried bulk sediment, using a Carlo-Erba CN analyser 2500 interfaced directly to a Micromass-Isoprime mass spectrometer at Bordeaux University,

France. The precision of the isotopic analyses, based on repeated measurements of selected surface sediment samples as well as routine international and in house standards measurements is $\pm 0.23\%$ [Martinez and Robinson, 2010]. Nitrogen isotope values are reported in delta (δ) notation where: $\delta^{15}\text{N} = ((^{15}\text{N}/^{14}\text{N}_{\text{sample}}/^{15}\text{N}/^{14}\text{N}_{\text{standard}}) - 1) / 1000$, and the standard is atmospheric N_2 .

Organic carbon contents (C_{org} , wt %) were measured with a LECO C-S 125 analyzer after treatment of $\sim 80\text{-}100$ mg of sediment with hydrochloric acid to remove calcium carbonate. The precision of repeated measurements was better than ± 0.5 wt %.

Alkenone content was determined at Kiel University, Germany, by accelerator solvent extraction (Dionex ASE) from 0.5 g freeze-dried and homogenized sediment samples, in combination with the C_{37} ketone unsaturation index analysis using a double column multidimensional gas chromatograph (Agilent 6890N) system [Blanz et al., 2005]. Values are reported as the sum of total C_{37} ketones per dry weight total sediment (ng/g).

Elemental composition of sediments was analyzed using an Avaatech X-ray fluorescence (XRF) Core Scanner at 1 cm distance following the procedure described in Tjallingii et al., [2010] XRF scanner measurements provide a semi-quantitative estimate for changes in the relative proportions of major and minor elements, indicative of variations for terrigenous or marine particles, e.g. Ti, Fe, Al, or Ca, Br, respectively. In addition, fluctuations in Br mimic well changes in productivity-related components such as C_{org} , TN [Ziegler et al., 2008; Cartapanis et al., 2011; Figure VII.2]. Consequently, we normalized the Br element intensity (in counts per seconds) to the Ti intensity (Br/Ti) to monitor past changes in PP relative to that of terrigenous detrital supply, and consider it as an indirect approximation (proxy) for export productivity as in previous studies [Cartapanis et al., 2011].



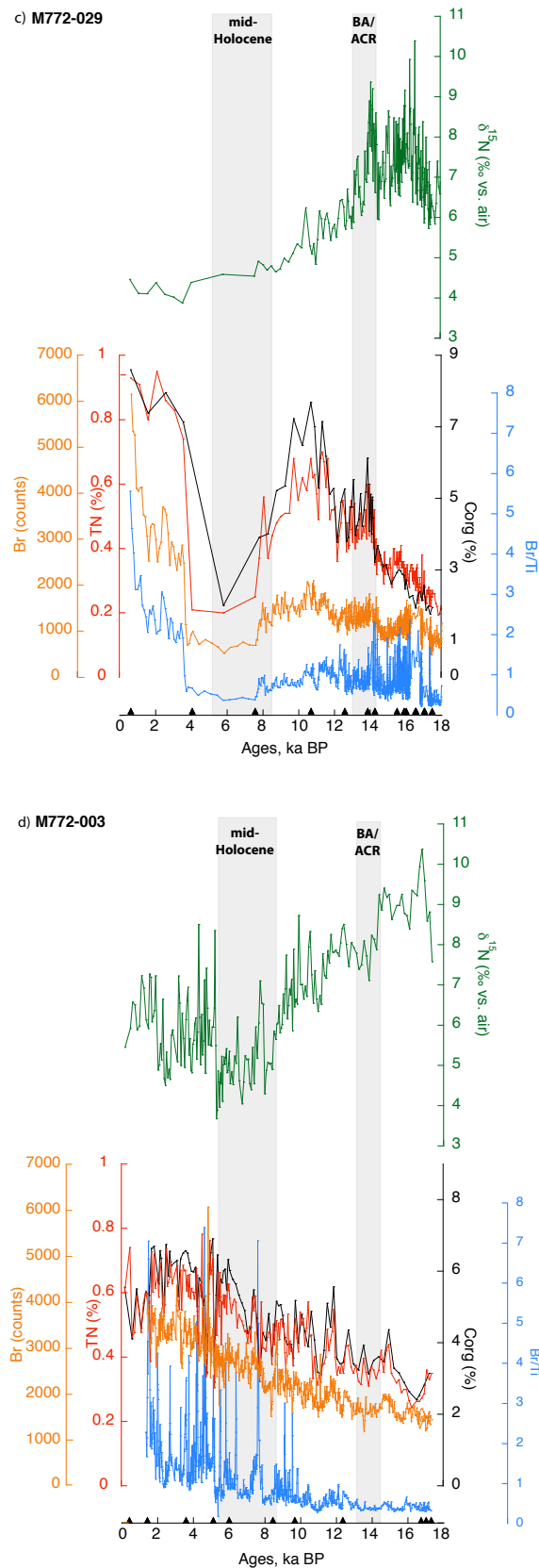


Figure VII.2. Sedimentary results of the studied cores

Sedimentary results: organic carbon (C_{org} ; black curve), nitrogen content (TN; grey curve), Bromine XRF measurements (Br; orange curve), Br/Ti ratio (Br/Ti; blue curve) and nitrogen isotopes ($\delta^{15}N$; green curve) shown for each studied core: a) M772-056, b) M772-059, c) M772-029 and d) M772-003.

VII-3.3. Age Model

For this study, the age model was based on 56 radiocarbon measurements (Table 3) performed on the planktonic foraminifer species *Neogloboquadrina dutertrei* for the northern cores and on the humic fractions of organic matter in the sediment for the southern cores, where amounts of planktonic foraminifera in 2 cm thick core sections were not high enough for radiocarbon measurements with the conventional AMS system operated at the Leibniz Laboratory at Kiel University. To test to which degree ^{14}C -ages of foraminifer calcite differ from those obtained from OM, we applied the two methods of dating on foraminifera and on OM from selected samples of the northern core M772-056 (Table 3; Figure VII.3).

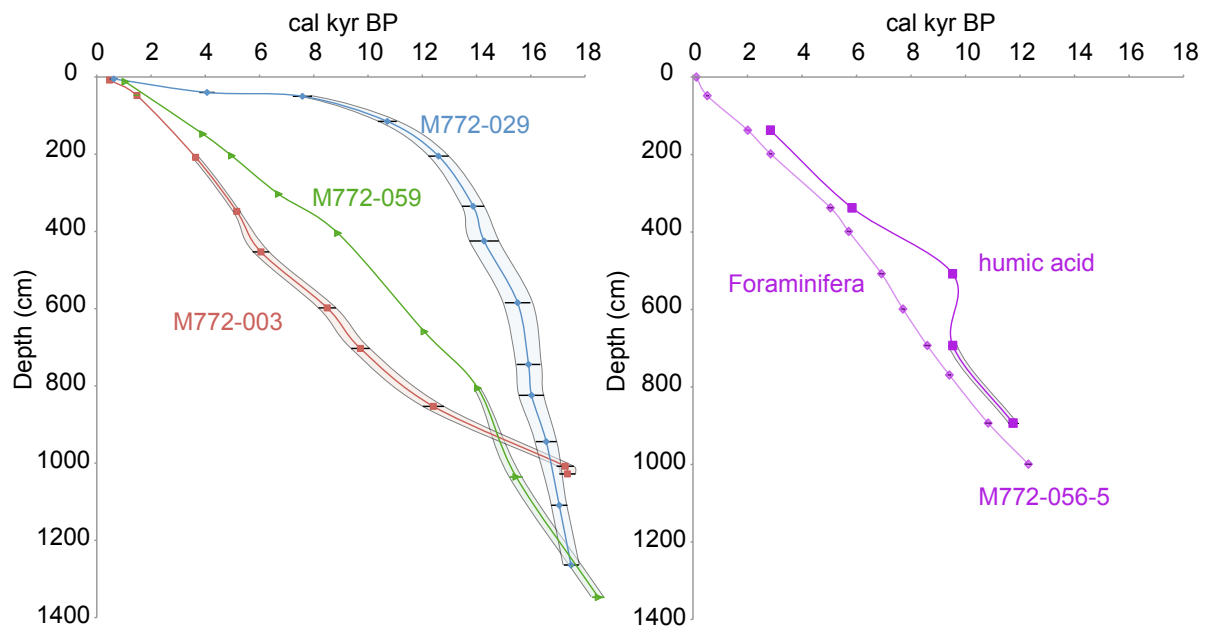


Figure VII.3. Age model applied to the studied cores

Radiocarbon dates (^{14}C -AMS) plotted against depth for each studied core. The right panel shows the difference between ^{14}C -AMS measured on the humic acid fraction of the OM and ^{14}C -AMS measured on planktonic foraminifera (*N. dutertrei*), from the core M772-056. The left panel shows the ^{14}C -AMS measured on the humic acid fraction vs depth for core M772-029 and -003. The ^{14}C -AMS dates of core M772-059 have been measured on planktonic foraminifera (*N. dutertrei*). However, in order to better correlate the studied cores to each other we estimated the age based on humic acid fraction for the core M772-059, by adding 800 years, corresponding to the average difference between the two ^{14}C -AMS dates of core M772-056.

After conversion into calendar years, the ages of the soluble humic fraction are systematically ~ 800 years older than those from calcite ages for the same depth horizons (Table 3; Figure VII.3). We assume that the soluble humic fraction extracted from total OM primarily represents the more recently (freshly) produced marine OM instead of old refractory organic carbon that may bias the dating towards much older values than observed between the calcite and the soluble humic fraction. The age difference between the calcite and humic fraction, although not yet completely understood, is coherent with previous results from the Namibian and Chilean upwelling systems [Mollenhauer *et al.*, 2004] where differences between 500 and 2000 years were found to exist between foraminiferal calcite and alkenones. We thus assume that the soluble humic fraction provides radiocarbon dates of mainly marine OM, which is closest to that of marine calcite in the Peruvian setting with very high marine OM production, export and deposition rates. Accordingly, we use absolute dates of the soluble humic fraction in the southern cores for age control. For all radiocarbon dates the MARINE09 calibration curve [Reimer *et al.*, 2009] has been used for conversion into calendar ages, with a ΔR varying between 200 ± 50 years for the northern cores (M772-056 and -059) and up to 511 ± 278 years for the southern cores (M772-029 and -003). The large range of local reservoir age and standard error result from the changes in the upwelling intensity taking place in this area, estimated by comparison between ^{14}C -ages measured on marine and continental shelves [Ortlieb *et al.*, 2011].

The resulting age models imply sedimentation rates varying between ~ 30 and 390 cm ka depending on the position of the core site more or less distal from coastal upwelling centers or from fluvial sediment supply. Each studied core being sampled every 5 cm, the temporal resolution of the results ranges between a minimum of ~ 167 years during the mid-Holocene (site M772-059) and a maximum of ~ 13 years for the Heinrich 1 time interval (site M772-029). One of the northern cores only covers the Holocene (M772-056), while all the other ones (M772-059, -029 and -003, Figure VII.3) go back in time until the deglaciation. However, at the rim of the modern OMZ the upper part of the core M772-029 is marked by discontinuities, which do not allow a sufficient record of the last 8 ka BP and only the M772-003 covers the entire Holocene time period (Figure VII.3).

VII-4. Results and discussion

We report new high resolution records of $\delta^{15}\text{N}$, total nitrogen (TN), organic carbon (C_{org}) and XRF measurements measured on four sediment cores from the Peruvian margin. The two southern cores M772-029 and -003 are located underneath the northern extension and within the core of the modern OMZ, respectively. The two cores in the North, M772-056 and -059, are located at the northernmost edge of the OMZ and were retrieved along the same latitude but at different water depths (Figure VII.1). Focusing on the last 18 ka BP, the new $\delta^{15}\text{N}$ records are compared with previously published records from the same area in order to establish a more comprehensive spatial and temporal picture of centennial and millennial scale variations and regional differences in the $\delta^{15}\text{N}$ signal off Peru. This should allow to better assess how the supply of nutrients and associated productivity as well as the extent of the OMZ within the Peruvian upwelling system have varied during the Deglaciation period and the Holocene.

The two northern cores reveal continuously low bulk sediment $\delta^{15}\text{N}$ values during the last 18 ka BP, varying between 4 and 6‰, which is in the range of the typical mean value of dissolved nitrate in the ocean (Figure VII.2a,b). Despite the small range of variations, the $\delta^{15}\text{N}$ record at site M772-059 reveals a slight increase from 18 ka BP to a maximum centered at about 14 ka BP. Afterwards a long-term decrease toward the Present is expressed in both cores from northernmost part of the Peruvian upwelling area. In contrast, the $\delta^{15}\text{N}$ records from the Peruvian upwelling center, which corresponds also to the core of the OMZ, are characterized by much larger variations of about 4 to 5‰ in magnitude during the Deglaciation to the mid-Holocene (17 to 8.5 ka BP) and during the last 6 ka BP (Figure VII.2c,d). Here lowest values of 4 to 6‰, similar to those in the northern cores are apparent only for the Mid- to Late Holocene, while deglaciation to Early Holocene values range between 6 and 10.5‰, much higher than observed in the North for this period. The most striking feature in all four $\delta^{15}\text{N}$ records along this transect is the similarity and low variance at very low values of ~ 4.5 ‰ that is reached during the mid-Holocene from ~ 5.5 to 7.5 ka BP, following a general decrease in $\delta^{15}\text{N}$ values along the Peruvian margin since 14 ka BP (Figure VII.2).

First, the observed $\delta^{15}\text{N}$ fluctuations could result from local changes in nutrient (nitrate) demand due to varying primary productivity. Field studies have shown that preferential uptake of ^{14}N by plankton occurs during photosynthesis, resulting in OM that is enriched in the light isotope and a residual dissolved nitrate pool that is correspondingly

enriched in the heavy isotope ^{15}N [Wada and Hattori, 1976; Altabet and François, 1994]. Thus, an increase in the relative nitrate utilization, either due to more biological export production for the same amount of nitrate or less nitrate available for the same biological export production must result in an increase in $\delta^{15}\text{N}$.

A suite of organic proxies (C_{org} , TN and Br counts) related to export production was measured at each site. At the two northern sites, TN, C_{org} and Br follow the same pattern with a continuous rise from the last Deglaciation period toward the Late Holocene (Figure VII.2) implying a general increase in productivity over this period. However, these trends may reflect dilution by siliciclastic material, which represents the major fraction of the bulk sediment close to the Gulf of Guayaquil. Normalization of Br counts over Ti counts, which is a siliciclastic component, may correct for the dilution effect. As is shown by the Br/Ti records (Figure VII.2.a-d) the two northern sites probably experienced a gradual increase in export production at sites M772-056 and -059 over the last 18 ka. This increase must certainly result from an increase in upwelling-driven delivery of nutrients to the surface toward the late Holocene because the gradual decrease in $\delta^{15}\text{N}$ apparent in both records over the last 14 ka BP implies a relaxation in nutrient utilization with a nutrient supply exceeding the biological demand (Figure VII.2.a,b). Although $\delta^{15}\text{N}$ values remained quite low over the last 18 ka BP, and much lower than those observed at the southern sites where N-loss processes are known to occur [Pride *et al.*, 1999], we cannot exclude an impact of water column denitrification as an explanation for the slight deglacial increase in sedimentary $\delta^{15}\text{N}$ in the North. Nowadays subsurface oxygen concentrations are too high to promote water column N-loss processes at position of the northern cores, and recent measurements of the isotopic composition of nitrate within the water column rules out any impact of N-loss processes on the nitrate isotopic signal in subsurface waters [Mollier-Vogel *et al.*, 2012]. However, deglacial to Holocene changes in the isotopic signature of nitrate delivered from the centre of the OMZ or a periodic extension of the OMZ may have influenced also the northern Peruvian sedimentary $\delta^{15}\text{N}$ records, particularly during the deglaciation, thus explaining the slight $\delta^{15}\text{N}$ increase between 18 and 14 ka at sites M772-056 and -059. During the deglaciation at ~ 14 -15 ka BP, an increase in sedimentary $\delta^{15}\text{N}$ off northern Peru is consistent with an intensification of inventory-altering fractionation, like water-column N-loss processes within low-latitude eastern boundary currents [Jaccard and Galbraith, 2012]. Accordingly, we propose that the expansion of the eastern tropical south Pacific OMZ at the time of the deglaciation contributed to the small deglacial $\delta^{15}\text{N}$ increase observed at the two northern sites.

A different picture emerges from the results obtained on the two southern sites, at present located in the heart of the oxygen minimum depth, with oxygen concentrations being close to zero at the water depth of the core sites [Thamdrup *et al.*, 2012]. This region coincides also with the highest biological production (<http://oceancolor.gsfc.nasa.gov/cgi/13>). Not surprisingly, $\delta^{15}\text{N}$ values are heavier, and export production indicators (TN, C_{org} and $\log(\text{Br}/\text{Ti})$) show also much higher values than for the northern cores (Figure VII.2a-d). Located at the rim of the OMZ core, $\delta^{15}\text{N}$ values from the core M772-029 increase from 6 to 10‰ at the beginning of the deglaciation (18-16 ka BP) directly followed by a decrease until 14 ka BP, back to the values observed prior to the deglaciation (Figure VII.2.c). During the beginning of the deglaciation, this large oscillation is also marked by a strong variability, of $\sim 2\%$ (Figure VII.2.c). Before the slow decrease of $\delta^{15}\text{N}$ values until the mid-Holocene (8 ka BP), a significant peak occurred between 14 and 13 ka BP, with a magnitude of $\sim 3\%$. From 8 ka BP to the present, core M772-029 (9°S) was interrupted by large hiatus (Figure VII.2.c), thus the full variability of the mid to Late Holocene is missing at this location, while the most southern core M772-003 (at 15°S) provides an uninterrupted archive of the OMZ since the last glacial period (Figure VII.2d). The highest $\delta^{15}\text{N}$ values are found during the oldest interval ~ 14 -18 ka BP at the two core sites. At site M772-003, this maximum is followed by a short interval, from 14 to 13 ka BP, characterized by a slight decrease of 1 to 1.5‰, which may correspond to the Antarctic Cold Reversal/Boelling/Alleroed, as previously shown off southern Chile [McManus *et al.*, 2004; De Pol-Holz *et al.*, 2006; Martinez *et al.*, 2006]. Then, the decrease of $\delta^{15}\text{N}$ values occurred earlier (~ 12 ka BP) and more abruptly at site M772-029 than at site -003. Nitrogen isotopic values of core M772-003 then reach their lowest values, being similar to those found at the northern cores, and ranging between 5 and 5.5‰, from ~ 8 ka BP until 5 ka BP (Figure VII.4). Finally, at 15°S, $\delta^{15}\text{N}$ values increase abruptly with large amplitude variations during the last 5 ka BP. Since a similar pattern was observed by Higginson and Altabet [2004] for the last 5 kyr of the Holocene on three cores recovered between 11 and 13°S, we assume that this is a general characteristic of the southern part of the Peruvian margin and an indication of large centennial-scale oscillations of the OMZ [Chazen *et al.*, 2009].

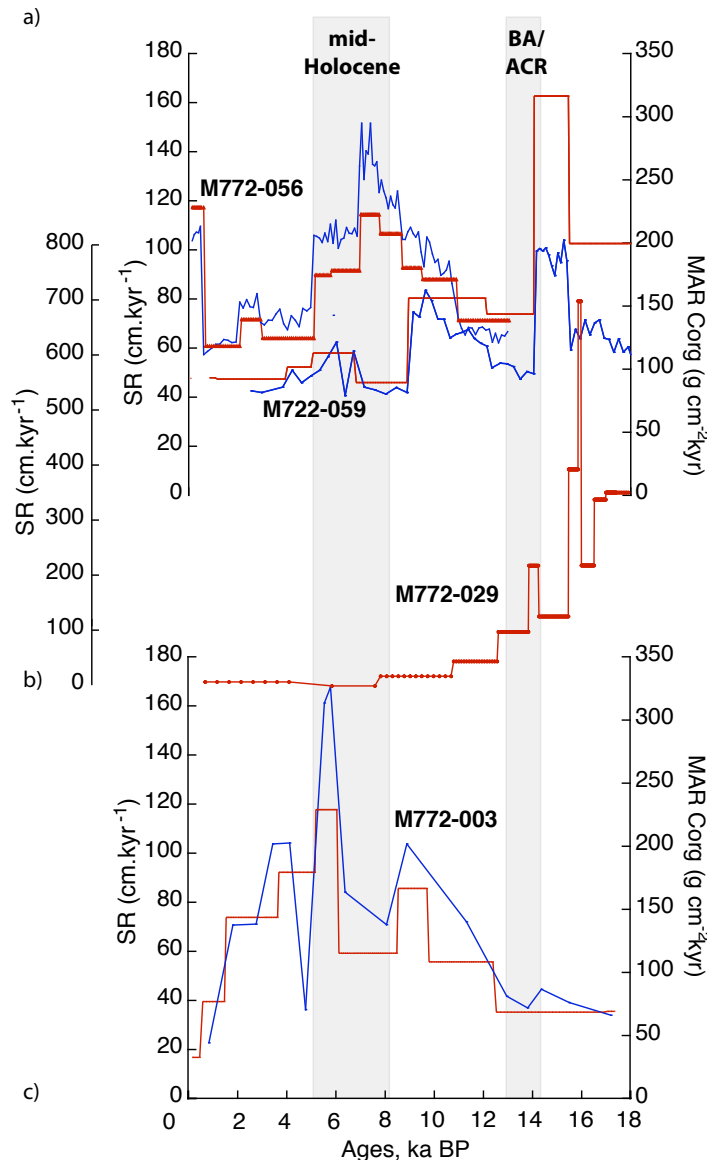


Figure VII.4. MAR and sedimentation rate for the studied cores

This figure shows the sedimentation rate (pink curve) and the Mass Accumulation Rate (MAR) for C_{org} content (details in the text; blue curve) of cores a) M772-056 and -059, b) -029 and c) -003. Unfortunately, the dry bulk density was not available for the core M772-029, located off central Peru.

Not surprisingly, our export production and $\delta^{15}N$ records at sites M772-003 and -029 share lots of similarities with those published by *Chazen et al.* [2009] and *Higginson and Altabet* [2004] on nearby cores, and all these observations converge necessarily to the same interpretation. The higher $\delta^{15}N$ values found in the southern part of the Peruvian upwelling, as well as the variations of about 4 to 5‰ in magnitude during the deglaciation, the early Holocene until 8 ka BP and even larger during the last 5-6 kyr have been interpreted as the result of variations in the extent of the OMZ causing periods of strong N-loss processes, driving the nitrogen isotopic values toward ^{15}N enriched values [see also *Higginson et*

Altabet, 2004; Agnihotri et al., 2006; Chazen et al., 2009]. These variations appear in great contrast with those observed for the northern cores where only slightly variable nutrient conditions are found as indicated by $\delta^{15}\text{N}$ values close to the average value of dissolved nitrate in the ocean.

Nevertheless, only for the mid-Holocene between 8 and 5 ka BP, all $\delta^{15}\text{N}$ records from the upwelling center show a pronounced trend towards low values identical to those typical for the northern part of the Peruvian margin. This feature implies a profound regime shift in the central Peruvian upwelling system during the global mid-Holocene climate optimum. This shift toward low $\delta^{15}\text{N}$ values within and outside the modern Peruvian OMZ could be induced by the increased influence of oxygen and nutrient-rich EUC subsurface waters that ventilate the Peruvian margin and would decrease the effects of strong nutrient utilization and N-loss processes on $\delta^{15}\text{N}$ at that time. Indeed, as previously demonstrated by *Chazen et al. [2009]*, the apparent lack of any co-variations in SST reconstruction, export production related indicators, and nitrogen isotopic variations is a clear indication that local changes in upwelling and associated biological production do not greatly impact the OMZ variability. Rather, a remote forcing like ventilation, through the circulation of subsurface water masses, exerted the most important influence on the oxygen deficiency. Determination of SST by alkenones concentrations is still under debate along the Peruvian margin [*Prahl et al., 2010; Kienast et al., 2012*] and regional calibration has not been done yet. However, SST-alk from core M772-003, representative either of the summer season or annual mean, shows constantly low values during the mid-Holocene (Figure VII.5). As for nowadays, if we consider that coccolithophores also bloomed during the austral summer at this time period, this may be interpreted as upwelling occurring during the entire year.

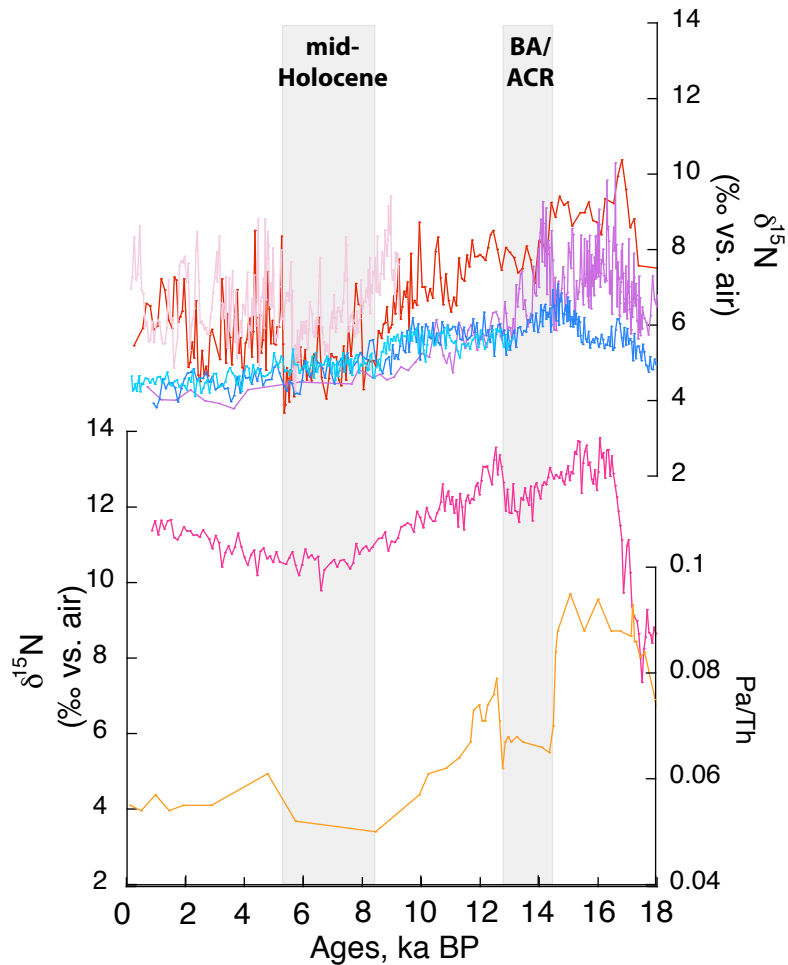


Figure VII.5. $\delta^{15}\text{N}$ values off Peru and northern Chile

Plot of the $\delta^{15}\text{N}$ values for the core GeoB 7139-2 (dark pink curve; [De Pol-Holz *et al.*, 2007]) and the core PC-2 (light pink; [Chazen *et al.*, 2009]) as well as each core of this study: M772-056 (light blue curve), M772-059 (dark blue curve), M772-029 (purple curve), M772-003 (red curve). The curve at the bottom of the graph (yellow curve) represents sedimentary $^{231}\text{Pa}/^{230}\text{Th}$ from GGC5, associated with the AMOC circulation intensity [McManus *et al.*, 2004].

A series of other climatic archives support the hypothesis of a large shift in the climatic and oceanographic state of the Peruvian upwelling system and the associated OMZ during the mid-Holocene. Terrestrial records have indicated that the Peruvian hinterland experienced large periods of droughts during the mid-Holocene period [Villagrán and Varela, 1990; Sandweiss *et al.*, 1996; Cross *et al.*, 2000; Moy *et al.*, 2002]. Nowadays, less precipitations on land is concomitant with a decrease in SST due to a large increase in upwelling intensity induced by stronger trade winds, which lead to a local increase in surface PP and a mixing of the surface waters as during La Niña like conditions. Besides, a study of

the siliciclastic sedimentation on cores from the Peruvian shelf [Rein *et al.*, 2005] as well as Peruvian hinterland floods records [Keefe *et al.*, 2003], lead to a very similar conclusion that fewer floods, associated with El Niño events, governed the sedimentation during the mid-Holocene time interval (5-8 ka BP). A general decrease of the sedimentation on the southern Peruvian margin [Rein *et al.*, 2005; Skilbeck and Fink, 2006], was interpreted as erosion due to an enhancement of the PCUC going southward (Figure VII.1). And yet, sedimentary archives from the centre of the Peruvian upwelling and OMZ do not show any evidence for an increase in export production, due to increase in local nitrate input, correlated with the decrease of $\delta^{15}\text{N}$ values during that period. This supports the interpretation that the OMZ is remotely controlled [Chazen *et al.*, 2009], or that local oxygen demand through the export of particulate OM is largely dominated by ventilation processes, associated with seasonality and/or ENSO variability observed in Ocean-Atmosphere model results for the tropical Pacific area during the mid-Holocene [Clement *et al.*, 2000].

Looking in a broader view, the mid-Holocene is also marked by an enhancement of the East-West gradient of equatorial SST [Koutavas *et al.*, 2006] and a northward displacement of the Westerlies [Lamy *et al.*, 2001; Kaiser *et al.*, 2008], which is in a good agreement with a assumption of more La Niña-like conditions at this time period.

For a better understanding of the spatial changes in the extent of the OMZ, we compared our study to a more southern sedimentary record located off northern Chile [De Pol-Holz *et al.*, 2006; Figure VII.1]. The variability of the $\delta^{15}\text{N}$ values of core M772-003 (15°S) and core GeoB 7139-2 [De Pol-Holz *et al.*, 2006], located at 30°S, show strong similarities during the last deglaciation and the Holocene (Figure VII.5). Surprisingly, increases in Atlantic Meridional Overturning Circulation (AMOC) described by Mc Manus *et al.*, [2004], are well correlated with decreases in $\delta^{15}\text{N}$ values along the South American margin (Figure VII.5), probably due to better ventilation of the surface waters. However, between 15-12.5 ka BP, a latitudinal decoupling is observed between an increase of the $\delta^{15}\text{N}$ values in the northern cores (M772-059/-029) compared to a decrease in the more Southern ones, M772-003 and GeoB 7139-2. Indeed, the more northern position of the ITCZ during the Bolling Allerød (BA) [Haug *et al.*, 2001; Wang *et al.*, 2007; Mollier-Vogel *under review in QSR*], leads to a shift of the OMZ northward. At the northern part of the Peruvian margin, where the core of the OMZ is very deep and the subsurface waters are well-ventilated, $\delta^{15}\text{N}$ values slightly increase by $\sim 1\text{‰}$. However, at the rim of the core of the OMZ, core M772-029 recorded a strong increase of the $\delta^{15}\text{N}$ values, $\sim 3\text{‰}$, during the BA. In the middle of the OMZ core, changes are

not so significant and at the core location M772-003, $\delta^{15}\text{N}$ values remain stable, at $\sim 7.5\text{‰}$, within their course to lower values through the deglaciation and then until the mid-Holocene. Last, core GeoB 7139-2 off northern Chile even recorded a small decrease of one per mil (Figure VII.5)

However, contemporary to the long term decrease of the AMOC intensity from 11.5 to 8 ka BP, a global decrease of $\delta^{15}\text{N}$ values is observed all along the South American margin (Figure VII.5). This may reflect better ventilation of the surface and subsurface waters following the same process previously observed across the Peruvian shelf [Mollier-Vogel et al., 2012]. Additionally, during the mid-Holocene period, SST_{alk} measured on sediment cores show low values, 20.5°C on average, for the core M772-003 and higher SST_{alk} , $\sim 22^\circ\text{C}$, for the northern core M772-059 (Figure VII.6). This observation may be associated to intense upwelling taking place in the upwelling centre at the southern Peruvian margin.

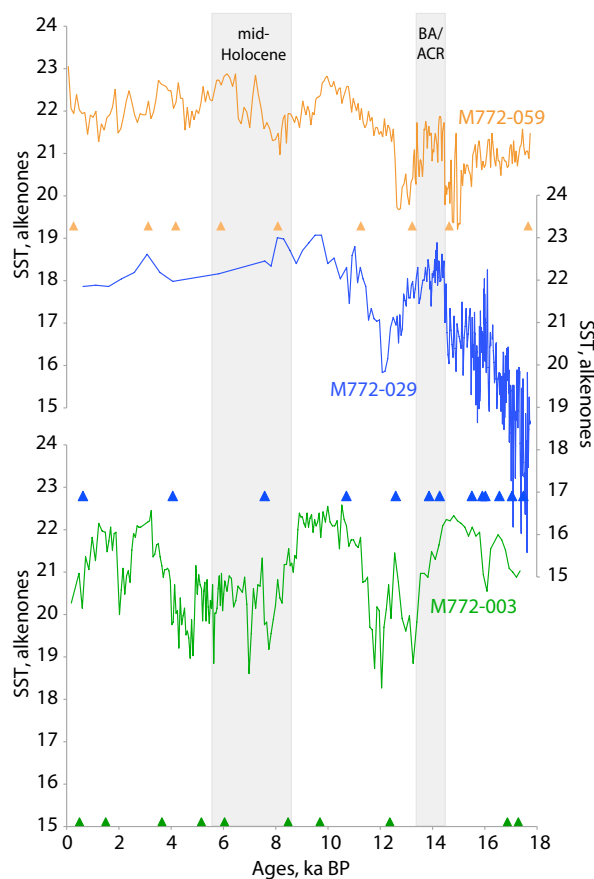


Figure VII.6. SST_{alk} from the studied cores

SST derived from alkenone unsaturated ratios for core M772-059 (orange curve), M772-029 (blue curve) and M772-003 (green curve).

The calculation of the difference between the SST_{alk} of the northern and southern cores shows the highest and longest lasting difference during this time period (Figure VII.7).

Indeed, strong upwelling occurring during the mid-Holocene may lead to enhance ventilation of the subsurface waters, leading to a deepening of the oxycline as well as the N-loss processes taking place within the core of the OMZ. Thus heavy nitrate resulting from these N-loss processes are no longer upwelled and consumed by biological productivity. Therefore, only light nitrate is used by the biota and recorded in the sediment [Mollier-Vogel *et al.*, 2012].

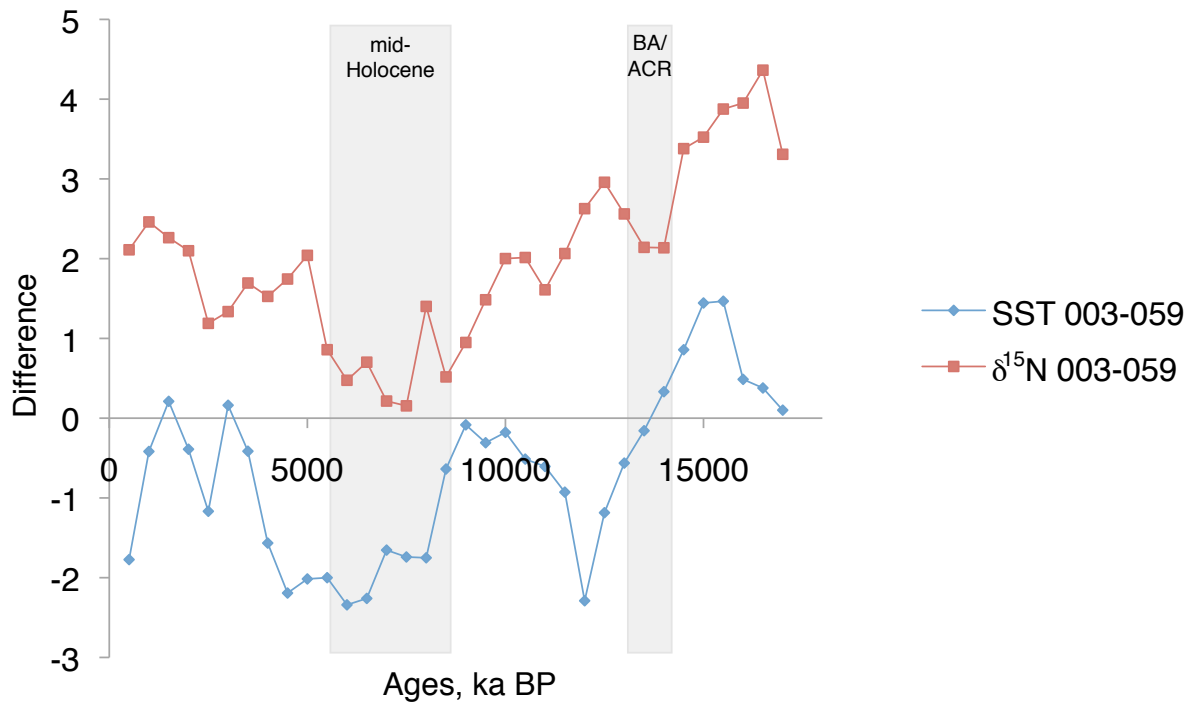


Figure VII.7. SST_{alk} and δ¹⁵N values differences between the two cores M772-059 and -003

Calculation of the difference between the two cores M772-059 and -003, for SST derived from alkenone unsaturated ratios (blue diamonds) and δ¹⁵N values every 500 years (red squares).

From the beginning of the deglaciation, we observe a general shrinkage of the ETSP OMZ from the North, as the Peruvian waters get ventilated before those at the northern Chilean margin (Figure VII.8). This shrinkage seems to have been intense enough to provoke a collapse of the OMZ conditions within the upper waters all along the South American margin, leading to records of only low δ¹⁵N values within the sediment (Figure VII.5). These general La Niña-like conditions led to a global shift of the entire Hadley cell, the ITCZ [Haug *et al.*, 2001; Mollier-Vogel *et al.*, submitted to QSR] and Westerlies [Lamy *et al.*, 2001; Kaiser *et al.*, 2008], and probably an enhancement of the circulation intensity/velocity. These conditions reached a sort of stable state during the entire mid-Holocene, ventilating the surface and subsurface waters, via the PCUC, southward until northern Chile [De Pol-Holz *et al.*, 2006]. Indeed, during the mid-Holocene, the low δ¹⁵N values observed by De Pol-Holz

et al., [2007] (Figure VII.5) are comparable to $\delta^{15}\text{N}$ values of the core-tops observed at the southern rim of the OMZ, at $\sim 45^\circ\text{S}$ [Hebbeln *et al.*, 2000; De Pol-Holz *et al.*, 2009].

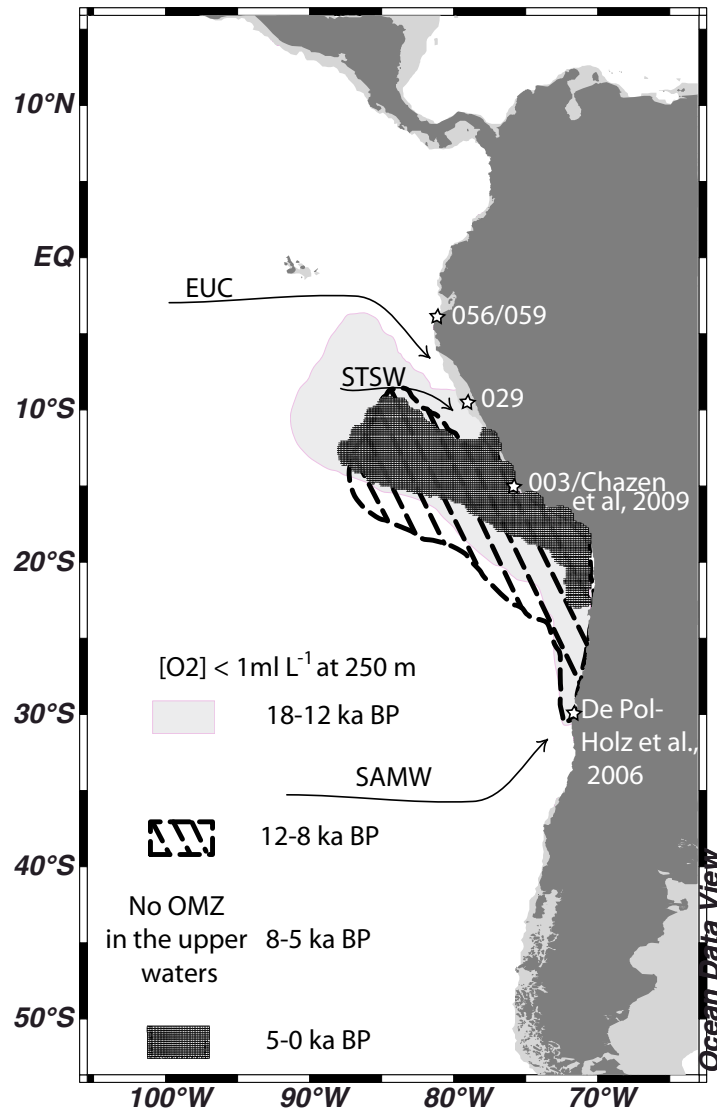


Figure VII.8. Schematic estimation of the Peruvian OMZ extent at different time intervals

Schematic representation of an estimation of the Peruvian OMZ extent within in the upper waters at characteristic time periods.

All together, the mid-Holocene was marked by several events such as an abrupt sea level rise before this time interval [Keefe *et al.*, 2003], a low marine sedimentation due to low riverine runoff, on the northern Peruvian margin, as well as La Niña like conditions prevailing between 8.5 and 5 ka BP, as suggested by Andean Lakes studies and Peruvian geoarcheological evidence [Sandweiss *et al.*, 1999; Cross *et al.*, 2000; Ekdahl *et al.*, 2008]. Consequently this intense and constant upwelling occurring during the mid-Holocene might involve a large ventilation of the upper part of the water column and avoid the extension of

OMZ in shallow subsurface, avoiding any heavy nitrate to reach the surface waters and being uptaken by the biota, leading to low $\delta^{15}\text{N}$ values recorded in the sediment all along the South American margin.

VII-5. Conclusions

This first continuous record covering the Holocene and the last Deglaciation reports on the displacement of the upwelling cell toward the shelf with the rise of the sea level shown by a large decrease in the $\delta^{15}\text{N}$ values between 17 to 8.5 ka BP. In this region, the stable climate of the mid-Holocene is marked by constant La Niña-like conditions, which intensively ventilate the subsurface waters. The vertical structure of the thermocline was different at that time and the core of the OMZ was deeper during the collapse period, thus preventing nitrate enriched in ^{15}N to be upwelled and assimilated by phytoplankton at the surface. This is quite similar to what we observe in the northern part of the modern Peruvian/Ecuadorian upwelling system [Mollier-Vogel *et al.*, 2012]. North of 10°S , the OMZ is still active and only slightly less intense than in the southern part of the system but much deeper (section Fig. 1) and sedimentary $\delta^{15}\text{N}$ values are low compared to the modern conditions and dominated by nutrient utilization processes rather than N-loss processes. As it is well mentioned in several studies based on diverse proxies over the Pacific basin, the late Holocene reveal a period of intense variable seasonality, which might also be associated with an enhance in the ENSO frequency.

VII-6. Acknowledgements

Thanks J. van der Lubbe and C. Blanchet for fruitful conversation. This work is a contribution of Sonderforschungsbereich 754 “Climate–Biogeochemistry interactions in the tropical ocean” (www.sfb754.de), which is supported by the Deutsche Forschungsgemeinschaft.

Chapter VIII. Rainfall response to orbital and millennial forcing in northern Peru over the last 18 ka

Elfi Mollier-Vogel^{1*}, Guillaume Leduc¹, Tebke Bösch², Ralph R. Schneider¹

¹Institute of Geosciences, University of Kiel, Germany

²Helmholtz Centre for Ocean Research Kiel (GEOMAR), Kiel, Germany

Submitted to Quaternary Science Reviews

VIII-1. Abstract

We present a high-resolution marine record of sediment input from the Guayas River, Ecuador, that reflects changes in precipitation along western equatorial South America during the last 18 ka. When compared to other Deglacial to Holocene rainfall records located across the tropical South American continent, different modes of variability become apparent. The records of rainfall variability imply that changes in the hydrological cycle at orbital and sub-orbital timescales were different from western to eastern South America. Orbital forcing caused an antiphase behavior in rainfall trends between eastern and western equatorial South America. In contrast, millennial-scale rainfall changes, remotely connected to the North Atlantic climate variability, led to homogeneously wetter conditions over eastern and western equatorial South America during North Atlantic cold spells. These results may provide helpful diagnostics for testing the regional rainfall sensitivity in climate models and help to refine rainfall projections in South America for the next century.

VIII-2. Introduction

Seasonal and interannual rainfall variability in western equatorial South America is driven by a multitude of climatic processes, with the complex regional patterns additionally shaped by orography. On the Amazonian side of the equatorial Andes, high precipitation rates are found throughout the year, with maxima occurring at the equinoxes (Figure VIII.1.a; [Poveda *et al.*, 2006; Garreaud *et al.*, 2009]).

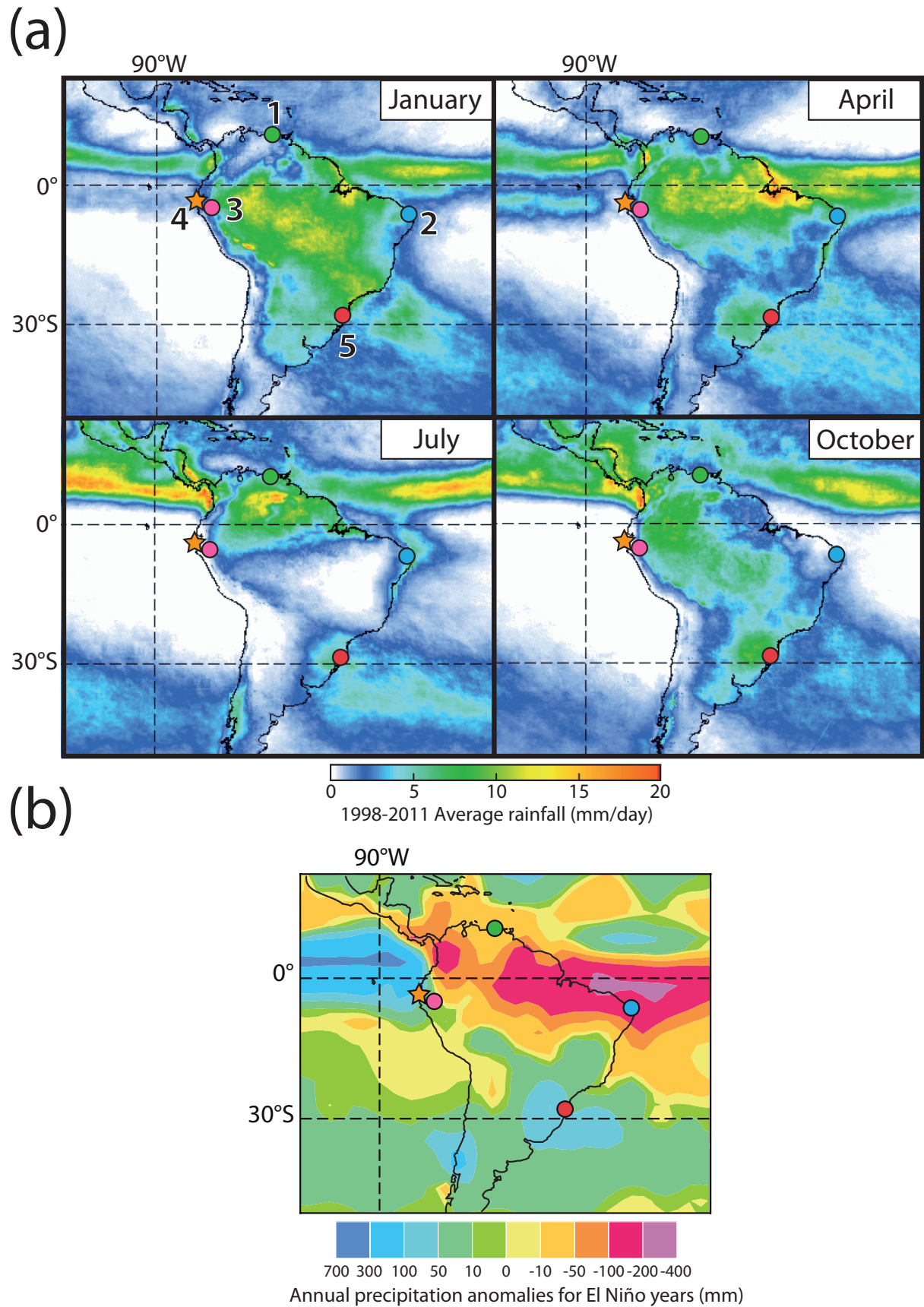


Figure VIII.1. Seasonal changes in mean precipitation over South America

(a) Seasonal changes in mean precipitation over South America derived from the Tropical Rainfall Measuring Mission (TRMM). Data extracted from the NASA/GSFC website available at

<http://trmm.gsfc.nasa.gov/>. Location of paleo-precipitation records displayed in Figure VIII.5 are numbered as following: (1) *Haug et al.* [2001]; (2) *Cruz et al.* [2009]; (3) *van Breukelen et al.* [2008]; (4) This study; (5) *Wang et al.* [2007]. (b) Annual precipitation anomalies over South America for typical El Niño (modified from *Dai and Wigley*, [2000]).

On the Pacific side, the orogenic barrier of the Andes blocks moisture transport from the Atlantic Ocean, making the Ecuadorian and Peruvian lowlands much drier than on the eastern side of the Andes. Still, there is a well defined subdivision between coastal regions located north and south of the equator which are affected by opposite seasonality in rainfall regimes (Figure VIII.1.a; [*Poveda et al.*, 2006; *Garreaud et al.*, 2009]). In addition, interannual rainfall variability associated with the El Niño-Southern Oscillation (ENSO) contributes to the rainfall pattern complexity over South America (Figure VIII.1.b; [*Dai and Wigley*, 2000]). Since the importance of these factors for regional rainfall patterns is difficult to assess, it remains problematic to understand the sensitivity of the hydrological cycle over South America to the climatic forcing at different timescales.

Beyond historical rainfall records, valuable information can be gained from paleoclimatic archives spanning time windows over which different forcings were at play. Past shifts in rainfall over South America since the Last Glacial Maximum (LGM) are thought to depend on, both, changes in orbital parameters and in the Atlantic Meridional Overturning Circulation (AMOC) intensity [*Cruz et al.*, 2005; *Wang et al.*, 2007]. Changes in summer rainfall intensity are characterized by a latitudinal antiphase behaviour between northern and southern tropics [*Haug et al.*, 2001; *Cruz et al.*, 2005; *Wang et al.*, 2007]. At the orbital timescale, a maximum in boreal summer insolation during the early Holocene triggered intense rainfall in northern South America, followed by a progressive aridification associated with the austral summer insolation increase during the mid- to late Holocene [*Haug et al.*, 2001]. In contrast, the southern tropics experienced drier conditions during the early to mid-Holocene, followed by wet conditions during the late Holocene as recorded in speleothems from southern Brazil [*Cruz et al.*, 2005; *Wang et al.*, 2007] and Andean lakes [*Baker et al.*, 2001; *Bird et al.*, 2011].

Closer to the equator, where the sun passes twice at zenith each year, the regional pattern of rainfall variability seems to be more complex than the simple antiphase behavior observed north and south of the equator where dry and wet seasons are well defined. Speleothem records collected close to the equator at the eastern and western edges of the Amazonian Basin indicate that Holocene changes in insolation have triggered an East-West antiphase in rainfall trends [*Cruz et al.*, 2009]. During the mid Holocene in particular, Northeastern Brazil

was associated with wetter conditions than nowadays South of the equator [*Cruz et al.*, 2009], while the western equatorial South America was marked by drier conditions [*van Breukelen et al.*, 2008].

At the millennial timescale, a slowdown in AMOC associated with North Atlantic cold spells such as the Heinrich event 1 (H1) and the Younger Dryas (YD) induced a southward shift in rainfall over northern South America [*Peterson et al.*, 2000; *Haug et al.*, 2001; *Leduc et al.*, 2007]. Similar to the case for orbital forcing, the southern tropical South America experienced an increase in rainfall opposite to the North. Clearly wetter conditions are revealed in speleothems from southern Brazil during the H1 and the YD [*Cruz et al.*, 2005]. The same pattern is observed for Brazilian rivers runoff situated closer to the equator in marine records [*Arz et al.*, 1998; *Jennerjahn et al.*, 2004; *Jaeschke et al.*, 2007]. However, no clear East-West antiphase in rainfall response to North Atlantic cold spells is apparent in existing continental speleothems records located close to the equator [*van Breukelen et al.*, 2008; *Cruz et al.*, 2009]. The available records rather suggest a moderate increase or no changes in equatorial rainfall at the east and west of the Amazonian Basin during the H1 and the YD. Therefore climate changes at orbital and millennial timescales tend to enhance or decrease rainfall amount over tropical South America in different ways. Yet we are lacking continuous paleoprecipitation records covering the full Deglacial and Holocene time periods for the eastern equatorial Pacific (EEP) and Peruvian coastal plains to decipher whether or not the rainfall anomalies observed above the Amazonian basin are mirrored on the Pacific side of the Andes.

Here we present two continuous Ti/Ca records close to the northern Peruvian coast, south to the Gulf of Guayaquil in the EEP, covering the last 18 ka. The studied site, situated midway from the hyperhumid Colombian margin to the North and the hyperarid Peruvian desert to the South, provides the opportunity to better understand how ocean-atmosphere interactions are set up under different climatic boundary conditions and may modulate regional rainfall regimes from oceanic areas to mountain tops. The records provide information on past changes in sediment discharge induced by regional rainfall changes with sub-centennial resolution. These Ti/Ca records compared with rainfall records from the other key regions of tropical South America (Figure VIII.1.) allow an improved assessment of regional rainfall response to orbital and millennial-scale climate forcing.

VIII-3. Regional settings

At the seasonal timescale, rainfall patterns over the South American continent migrate latitudinally following the annual cycle of insolation, but over the adjacent ocean the Intertropical Convergence Zone (ITCZ) remains near 5°N because of local air-sea interactions (Figure VIII.1.a). In addition, south of the equator, the Andes impede moisture transport to the Pacific Ocean, leaving the Pacific coastal plains within a rain shadow (Figure VIII.1.a). Consequently, a sharp regional contrast exists between the Pacific side of the Andean Cordillera and the Amazonian Basin at the equator, the latter receiving most of its rainfall from the Atlantic Ocean [Bookhagen and Strecker, 2008].

Rainfall patterns over the South American continent closely follow the South American Monsoon system. Rainfall maxima occur north of the equator during the boreal summer and vice-versa during the austral summer (Figure VIII.1.a). Along the equator, a broad precipitation maximum occurs in April (Figure VIII.1.a). On the other hand, October rainfall is reduced and tends to be confined above the western side of the Amazonian Basin (Figure VIII.1.a). These features result in a bimodal distribution of the annual cycle of rainfall, with maxima occurring at equinoxes above the Amazonian Basin [Poveda *et al.*, 2006].

Along the Pacific coast, regional rainfall also varies from region to region because local land-ocean-atmosphere interactions regulate precipitation distribution superimposed on the dynamics of the ITCZ (Figure VIII.1.a). North of the equator, the Pacific side of the Columbian Margin receives high amounts of rainfall from the low-level westerly Choco Jet, which transports moisture from the EEP to the western flank of the Andes during the boreal summer [Poveda and Mesa, 2000; Bookhagen and Strecker, 2008]. South of the equator, rainfall maxima occur during austral summer when the ITCZ prevails above the eastern equatorial Pacific in the southern hemisphere (Figure VIII.1.a; [Liu and Xie, 2002]). South of 5°S , the hyperarid Peruvian desert extends along the Pacific coastline and is sustained year-round by the cold Humboldt current and its associated upwelling system (Figure VIII.1.a; [Garreaud *et al.*, 2009]).

At the interannual timescale, warm ENSO anomalies in the EEP are marked by drier conditions in northern South America and along the equator above the Amazonian basin, while conditions over southeastern South America and the EEP are comparatively wetter (Figure VIII.1.b; [Dai and Wigley, 2000; Silvestri, 2004]). Along northern Peru and Ecuadorian coastlines, El Niño events provoke important increases in precipitation as compared to normal years (Figure VIII.1.b; [Dai and Wigley, 2000]). Little further to the

South, within the northern Peruvian desert located between 5 and 10°S, significant rainfall exclusively occurs during El Niño events [Wells, 1990].

Rainfall patterns occurring within the river catchments of interest for our study area are, unlike along the Amazonian flanks of the Andes, unimodal. A rainy season from January to March occurs both in Guayaquil (1°S) and Piura (5°S), but the amount of precipitation received in Guayaquil is about an order of magnitude larger than in Piura (<http://www.allmetsat.com>).

VIII-4. Material and methods

Piston cores M772-059 (3°57.01'S, 81°19.23'W, 997 m water depth) and M772-056 (3°44.99'S, 81°07.25'W, 350 m water depth) were collected south of the Gulf of Guayaquil (Figure VIII.1.). The Gulf of Guayaquil is composed of a sedimentary platform, with an outer shelf break into the continental margin situated at a water depth of ~100 m (Figure VIII.2; [Witt and Bourgois, 2010]).

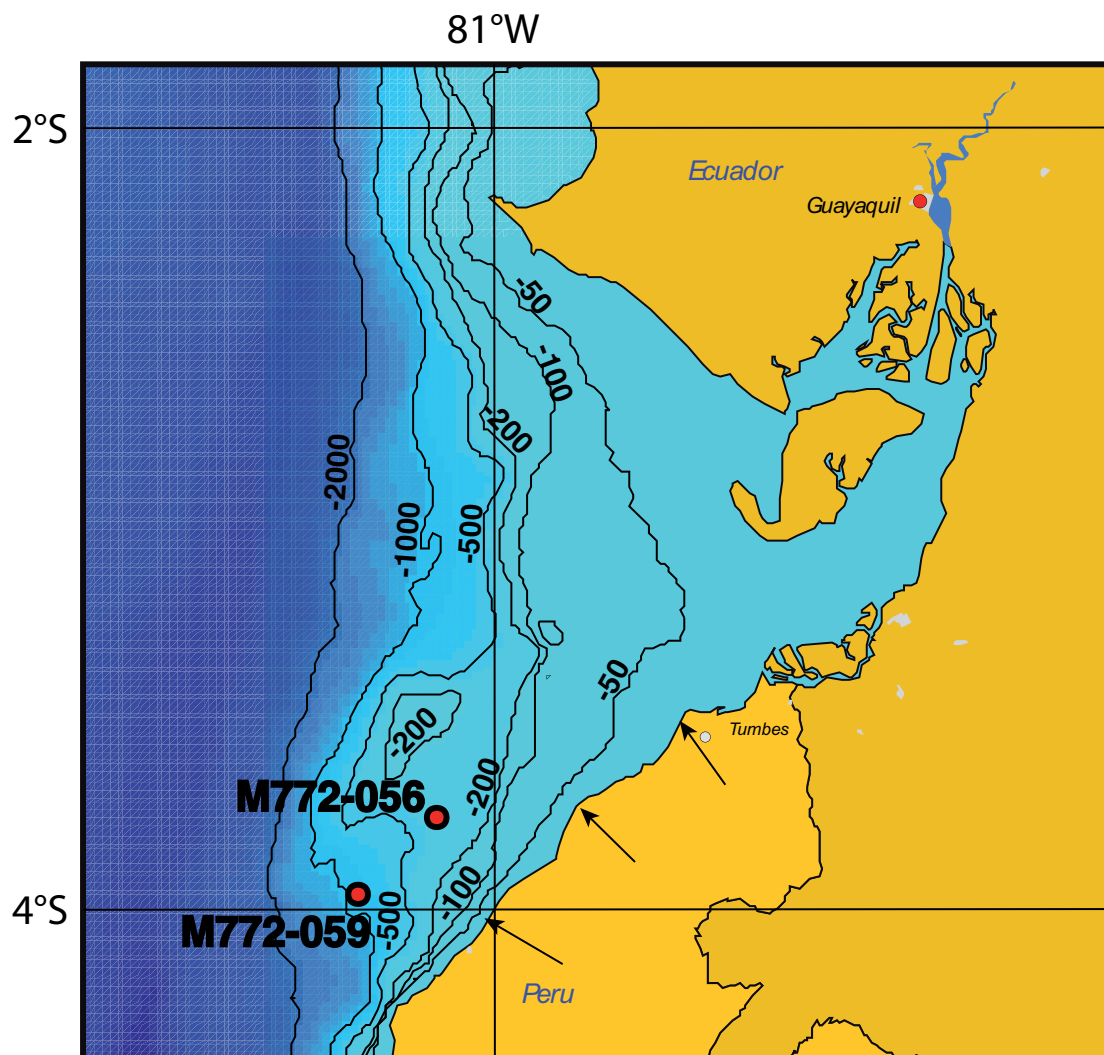


Figure VIII.2. Regional bathymetry and sediment core locations

Regional bathymetry (isobaths in meters) and sediment core locations. The Gulf of Guayaquil is typically marked by water depths shallower than 100 m. Assuming that regional relative sea level rise followed the eustatic sea level evolution, the 100 m and 50 m isobaths provide qualitative indications on how the coastline may have evolved in response to eustatic sea level, with the 100 m and 50 m isobaths representing coastlines at ~15 and 11 ka, respectively [Bard *et al.*, 1996]. The arrows locate small rivers mouths that may occasionally represent a significant source of terrigenous material to coring sites during El Niño events [Wells, 1990].

The sediments accumulating at the coring sites are dominated by terrigenous particle discharge associated with riverine runoff controlled by regional rainfall intensity, and contain as a secondary component marine biogenic carbonates. Sedimentary discharge into the Gulf of Guayaquil is mainly linked to the Guayas River runoff, which integrates rainfall from a narrow catchment located North of Guayaquil on the western flank of the Ecuadorian Andes [Twilley, 2001]. The Guayas River discharge closely tracks the integrated precipitation occurring on land within the basin catchment without any time lag [Twilley, 2001]. The northern Peruvian coast is subdivided by a mosaic of small coastal river catchments, which are much more sensitive to ENSO as compared to the Guayas River [Wells, 1990].

The age model of the combined full Deglacial to Late Holocene record is based on radiocarbon measurements from 10 and 11 different depth levels for cores M772-059 and M772-056, respectively (Table 3; Figure VIII.3).

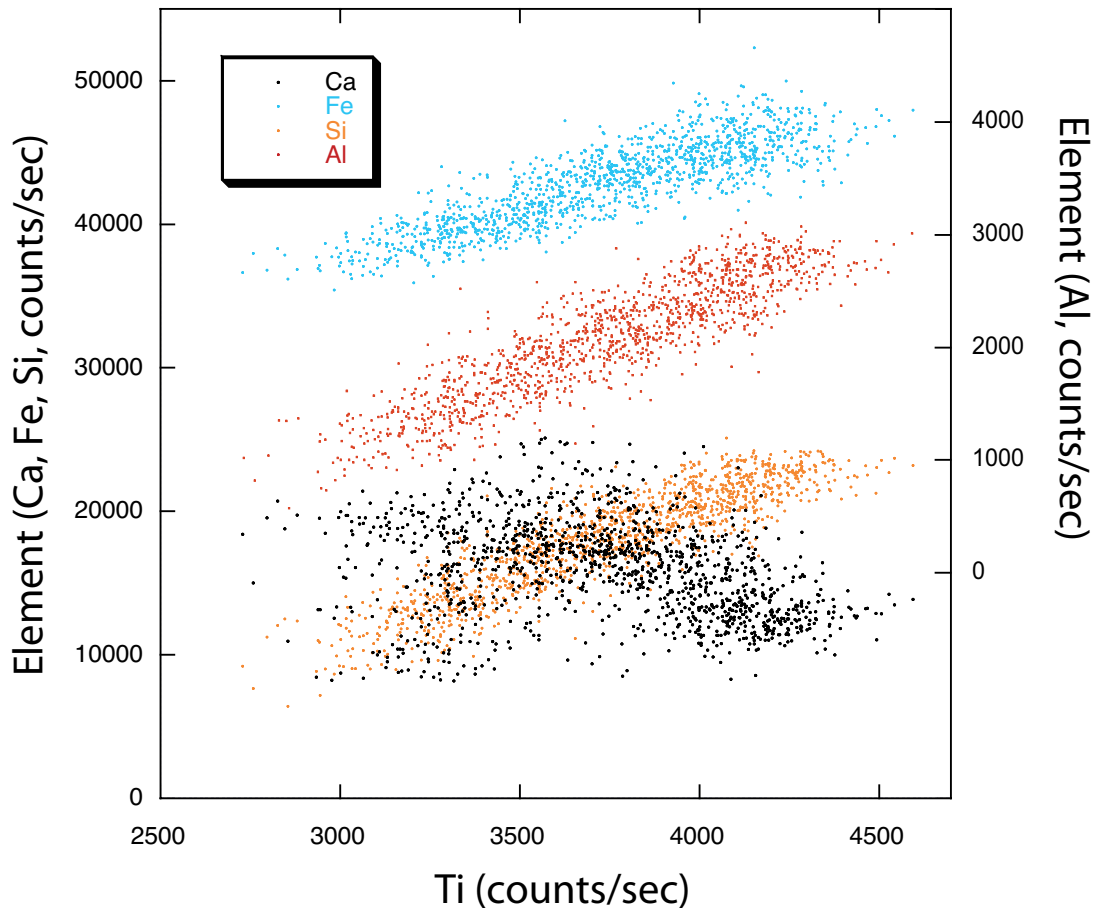


Figure VIII.3. XRF counts for core M772-059

XRF counts for Ca, Al, Si and Fe plotted as a function of Ti counts for core M772-059.

Radiocarbon measurements were performed on the planktonic foraminifera species *Neogloboquadrina dutertrei* at the Leibniz Laboratory for Radiometric Dating and Stable Isotope Research, University of Kiel (CAU). Radiocarbon ages were calibrated using MARINE09 [Reimer *et al.*, 2009], with a constant ΔR of 200 \pm 50 years based on sites with known reservoir ages situated closest to our core location in the marine Reservoir correction database (<http://calib.qub.ac.uk/marine/>). For core M772-059, the resulting age model implies sedimentation rates varying between \sim 50 and 170 $\text{cm} \cdot \text{kyr}^{-1}$, providing a time resolution ranging from \sim 22 $\text{years} \cdot \text{cm}^{-1}$ during the mid-Holocene down to \sim 6 $\text{years} \cdot \text{cm}^{-1}$ for the Heinrich 1 time interval. For core M772-056, the resulting age model implies sedimentation rates varying between \sim 63 and 117 $\text{cm} \cdot \text{kyr}^{-1}$, providing a time resolution ranging from \sim 16 $\text{years} \cdot \text{cm}^{-1}$ during the mid-Holocene down to \sim 8 $\text{years} \cdot \text{cm}^{-1}$ for the early Holocene time interval.

Contents of total carbon (TC) and organic carbon (C_{org}) were measured on core M772-059 from bulk and decalcified sediment, respectively, using an elemental analyzer. The carbonate content was then calculated using the equation $\% \text{CaCO}_3 = (\% \text{TC} - \% C_{\text{org}}) \cdot 8.33$.

The relative elemental composition of sediments was analysed using an Avaatech X-ray fluorescence (XRF) Core Scanner at 1 cm distance following the procedure described in [Tjallingii *et al.*, 2010]. We use the Ti element intensity (in counts per seconds) relative to the Ca intensity to monitor past changes in terrigenous detrital content relative to that of marine carbonates, and consider it as a proxy for riverine runoff as in previous studies [Arz *et al.*, 1998; Haug *et al.*, 2001; Jaeschke *et al.*, 2007]. We also check the log (Si/Al) to look for outstandingly high log (Si/Al) changes, which may indicate significant changes in biogenic opal fluxes, most likely reflecting productivity of diatoms and radiolaria.

VIII-5. Results

VIII-5.1. XRF data

We use log-ratios of Ti/Ca ($\log \text{Ti/Ca}$), which provide unbiased estimates for the relative concentration of Ti over Ca with respect to sedimentary heterogeneities and nonlinearities between the XRF intensity and its corresponding sedimentary concentration [Weltje and Tjallingii, 2008]. In marine sediments mainly composed of terrigenous material at tropical latitudes, as at our core sites, the $\log (\text{Ti/Ca})$ has been widely applied to reconstruct past changes in continental detritus accumulation as a qualitative indicator for rainfall variability occurring on the adjacent continent. Such assumption relates to the fact that Ti representing the dominating detrital fraction, once normalized to marine biogenic Ca, reflects the variable input of terrigenous material at coring sites. Variations of elemental XRF intensity of Si, Al, Ca and Fe are shown as a function of Ti intensity in Figure VIII.3. For clarity, we only consider the core M772-059 that covers the last 18 ka and for which carbonate content data are available for validating the interpretation of XRF data. Ti is positively correlated to Si, Al and Fe with near perfection (Figure VIII.3), and shows negative correlation to Ca at a confidence level of 95% ($r^2 = 0.066$, $n = 1327$, Figure VIII.3). The positive correlation between Ti and the other terrestrial elements is expected as those elements have the same origin. The negative statistical correlation between Ti and Ca (Figure VIII.3) suggests that the amount of Ca with respect to that of Ti was mainly affected by dilution with the terrigenous phase. The calcium carbonate content in the sediment core is only a minor component that varies between 2 and 8 % of dry bulk sediment (Figure VIII.4).

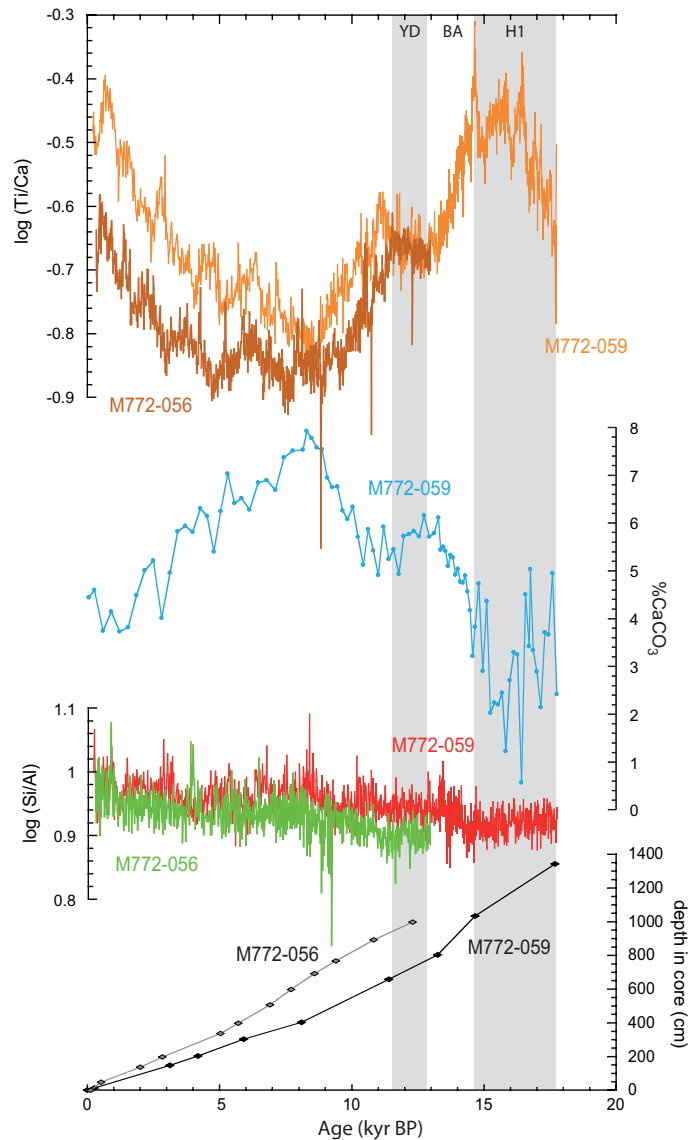


Figure VIII.4. Sedimentary records and age model for the studied cores

(a) Log (Ti/Ca) for cores M772-059 and M772-056. (b) Carbonate content in core M772-059. (c) Log (Si/Al) for cores M772-059 and M772-056. (d) Age / Depth relationships for cores M772-059 and M772-056.

Such low amount of carbonate content cannot be considered as the diluting factor for the overall terrigenous fraction indicated by changes in Ti, Al, Si and Fe. Rather, it is likely that coeval changes in the accumulation of the terrigenous fraction have been responsible for dilution of carbonates, which implies that the log (Ti/Ca) is a true reflection of varying terrigenous input.

Changes in carbonate supply to the seafloor due to the varying marine production probably did not occur. This is corroborated by a low-resolution biogenic opal record measured on core M772-056 varying between 0 and 4% of dry sediment without any distinguishable features (data not shown). Such low amounts of biogenic opal are well below

the analytical uncertainty associated with the opal measurement procedure [Wells, 1990], and thus cannot be used as a reliable indicator for varying diatoms productivity. We use the log (Si/Al) to track changes in biogenic Si that can reflect variations in opal content linked to changes in productivity of diatoms and radiolaria. Downcore changes in log (Si/Al) from both M772-059 and M772-056 (Figure VIII.4) suggest little if any significant changes in biogenic Si contribution from diatoms, further corroborating our assumption that primary productivity cannot explain the observed changes in the log (Ti/Ca) at our coring sites.

Ideally, changes in lithogenic fluxes should be derived from calculation of accumulation rates using sedimentation rates and dry bulk density values. The information contained in the computation of such fluxes would however be highly dependent on the number of age tie points [Rühlemann *et al.*, 1999], which cannot be obtained at a resolution sufficient enough to directly date both millennial and centennial scale changes as documented by the log (Ti/Ca) records. The advantage of XRF core scanning is to provide useful information on past changes in the proportion of elements of continental versus marine origin at very high temporal resolution. It has been successfully used to monitor rainfall variability from cores situated in the vicinity of river mouths all along the tropics [see e.g. Arz *et al.*, 1998; Haug *et al.*, 2001; Adegbe *et al.*, 2003; Jennerjahn *et al.*, 2004; Jaeschke *et al.*, 2007; Tachikawa *et al.*, 2011]

VIII-5.2. Variations in terrigenous input

The log (Ti/Ca) record of M772-059 tracks changes in supply of terrigenous material at our deeper coring site back to 18 ka, of which the likely main contributor is the Guayaquil River runoff over Ecuadorian and northern Peruvian Andes, in association with regional response of precipitation to long and short term climate changes (Figure VIII.4). The oldest part of the core is marked by a rapid increase in log (Ti/Ca) between ~18 and 17 ka, followed by a broad maximum of log (Ti/Ca) recorded between ~17 and 15 ka, corresponding to the H1 cold event. A sharp decrease in log (Ti/Ca) which, according to our age model, corresponds to the Boelling/Alleroed time period, indicates a rapid and substantial decrease in terrigenous input immediately following the H1. At the onset of the Younger Dryas chronozone, the log (Ti/Ca) is marked by a moderate increase, which reversed the deglacial decreasing trend in riverine runoff. The log (Ti/Ca) decreasing trend of the deglacial time interval resumes after the YD and reaches a minimum at ~8 ka BP. The mid- to late Holocene part of the sequence

is marked at first order by an increasing trend in lithogenic fluxes over the last 8 ka, on which rapid multi-centennial scale changes are superimposed.

VIII-6. Discussion

VIII-6.1. Sedimentary patterns

Despite the relative proximity of cores M772-059 and M772-056 to the Guayas River estuary, sediment delivery at the two core sites may have been affected also by oceanic transport processes. Core M772-056 is situated closer to the edge of the shelf platform of the Gulf of Guayaquil while core M772-059 was retrieved from the upper Peruvian slope (Figure VIII.2). Any change in subsurface to intermediate water mass movements could have modified the sedimentary pattern; however, these are not expected to alter the sedimentary signals in a similar way at the respective water depths. Therefore, the observation that cores M772-059 and M772-056 share similar changes at the multi-centennial and multi-millennial timescales suggests that mainly changes in regional rainfall and its associated river runoff with terrigenous delivery control the $\log(\text{Ti}/\text{Ca})$ variability at our core sites.

The $\log(\text{Ti}/\text{Ca})$ record of M772-056 covers the last 13 ka only, but the main patterns described for core M772-059 remain valid (Figure VIII.4). Small contrasts in the timing of submillennial-scale variations superimposed on the long-term trends in both cores indicate that adjustments in the age model may be needed to improve the one-to-one coupling of these events (Figure VIII.4). Changes in eustatic sea level cannot explain similar trends in the sedimentological composition of both cores. The differences in distance to the coast and in water depth between M772-059 and M772-056 would promote different time transgressive shifts in sediment accumulation rates and composition at both sites.

For the earlier part of the deglaciation, which is only recorded in M772-059, we cannot dismiss an impact of sea level rise on the $\log(\text{Ti}/\text{Ca})$. However, the earliest sharp increase in $\log(\text{Ti}/\text{Ca})$ recorded between ~18 to 16.5 ka corresponding to the onset of the H1 climatic chronozone occurred when the deglaciation and sea level rise already began [Arz *et al.*, 1998], moving depositional accommodation space shoreward. Therefore, the high sedimentary input at M772-059 site during the H1 was linked to a change in sediment delivery caused by increased riverine runoff and associated regional rainfall. Similar reasoning can be applied to the YD chronozone, during which the slight but significant increase in $\log(\text{Ti}/\text{Ca})$ cannot be attributed to the retraction of the shoreline linked to sea level rise. We thus assume that the

H1 and, to a lesser extent the YD, were influenced by increased sedimentary delivery from the surrounding hinterland during wetter conditions as compared to the time interval bracketing those events. On the other hand we cannot rule out that sea level rise contributed to the overall magnitude of the decreases in $\log(Ti/Ca)$, recorded between 14.5 and 13 ka as well as between 11 and 9 ka BP.

VIII-6.2. Review of precipitation changes around equatorial South America during the last 18 ka

Overall, our record confirms the equatorial East-West antiphasing in precipitation trends as previously found at the orbital timescale for the last 18 ka in speleothem records collected in equatorial South America (Figure VIII.5).

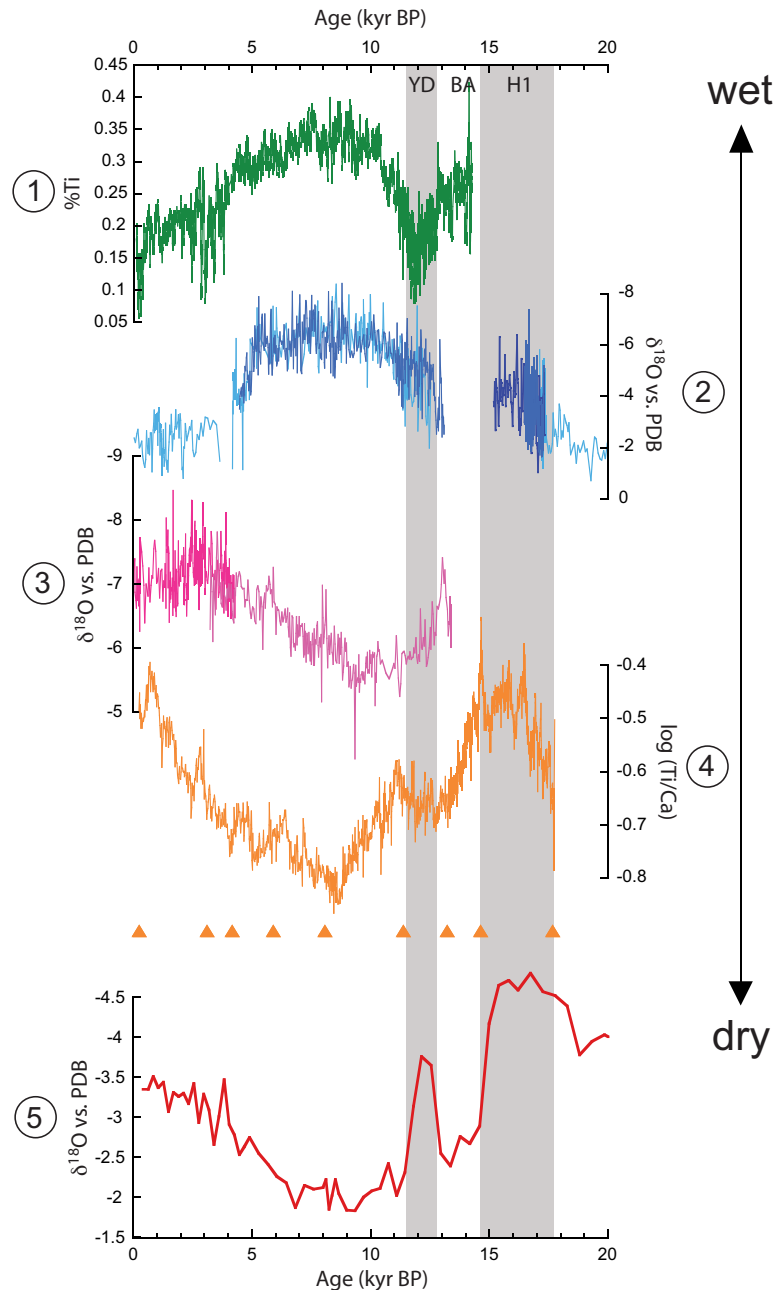


Figure VIII.5. Records for past changes in precipitation over South America

Records for past changes in precipitation over South America. (1) *Haug et al.* [2001]; (2) *Cruz et al.* [2009]; (3) *van Breukelen et al.* [2008]; (4) This study; (5) *Wang et al.* [2007]. The Younger Dryas (YD) and Bolling/Alleroed (BA) time intervals are reported at top of the panel according to the GISP2 timescale [*Grootes et al.*, 1993] while the timing of the Heinrich event 1 (H1) chronozone was chosen after *Bard et al.* [2000]. Orange triangles indicate radiocarbon ages used to compute the M772-059 age model.

Modeling experiments successfully reproduce the implied zonal antiphasing in precipitation trends recorded along the equator during the Holocene when they are forced by changes in orbital parameters, e.g. [*Cruz et al.*, 2009]. This feature can be explained by an atmospheric response to latent heat release in the upper troposphere, which caused stronger subsidence over northeastern Brazil to accommodate the enhanced convection and upward

motion during times of enhanced austral summer insolation and its associated increase in austral summer monsoon [*Cruz et al.*, 2009].

The rainfall increase recorded at our studied site during H₁ stands out as a prominent wet phase and co-occurred with wet conditions on the eastern side of the Amazonian Basin [*Arz et al.*, 1998; *Jennerjahn et al.*, 2004; *Jaeschke et al.*, 2007; *Cruz et al.*, 2009]. This strongly suggests in-phase rainfall anomalies at equatorial latitudes at millennial timescales (Figure VIII.5). Moreover, as indicated by the log (Ti/Ca) record, the H₁ event was probably experiencing large centennial scale variance in rainfall, highlighting the internal complexity of this event (see also; [*Álvarez-Solas et al.*, 2011]). A recent lacustrine record in the Lake Peten Itza provides evidence for such a multi-phased H₁ climate anomaly [*Escobar et al.*, 2012]. The authors assigned these centennial-scale shifts within the H₁ chronozone to multiple iceberg discharges in the North Atlantic during H₁ [*Bard et al.*, 2000]. A recent speleothem record from the central Peruvian Andes recorded similar high-frequency shifts in precipitation during Heinrich events 4 and 3 [*Kanner et al.*, 2012], which mimics sea surface temperature changes from the Bermuda Rise [*Sachs and Lehman*, 1999]. All this evidence reinforces the idea that Heinrich stadials contain complex internal climate variability, which needs to be further studied. An overall wet H₁ can be at least partly explained by a southward shift in the mean ITCZ latitudinal position over oceanic regions surrounding South America along with its associated monsoon variability over the continent in analogy to increases in precipitation recorded in speleothems from Southern Brazil (Figure VIII.5) [*Wang et al.*, 2004; *Cruz et al.*, 2005; *Wang et al.*, 2007] and in the Andean altiplano by ~20°S [*Blard et al.*, 2009].

At our studied site, the 18 to 8 ka time interval is marked by a general decrease in sediment discharge from the Ecuadorian Andes (Figure VIII.5). This suggests a long-term aridification co-occurring with the deglaciation phase from the Last Glacial to the Early Holocene, with potentially some superimposed sea level imprint (Figure VIII.5). Such a feature is in contrast with sites located north of the equator where the last deglaciation is marked by an overall increase in precipitation [*Pahnke et al.*, 2007]. Interestingly, a marine site located at the equator close to the northern Ecuadorian margin was also marked by pronounced increases in riverine runoff over the last five terminations [*Rincón-Martínez et al.*, 2010]. However, the temporal resolution of these records is not resolving millennial scale variations superimposed on the deglacial trend. Although our record is not covering the full glacial period, from the oldest part of the record it is apparent that the start of H₁ was associated with a strong increase in the log (Ti/Ca), which decreased back toward the

deglacial values observed before the H1. Overall, our riverine runoff record from northern Peru suggests that rainfall changes occurring during the deglaciation and the H1 were of opposite sign as compared to those recorded at marine sites located in northern Ecuador and along the Colombian margin [Escobar et al., 2012].

The only moderate increase in precipitation along the equator during the YD compared to the H1 probably reflects differences in the magnitude of these cold spells and/or in the regional climate response to AMOC perturbation under glacial and interglacial boundary conditions [Roche et al., 2011]. A muted YD anomaly compared to that associated with H1 was also recorded in Lake Peten Itza [Escobar et al., 2012], suggesting that these two events did not affect tropical rainfall with the same intensity.

For the mid- to late Holocene rapid rainfall fluctuations are detected, superimposed on the first-order increasing trend in precipitation. These are probably connected to analogous variations recorded in the southern tropics [Strikis et al., 2011], close to the equator [Moy et al., 2002] as well as in the northern tropics [Marchitto et al., 2010]. The phasing of these changes however cannot be satisfactorily resolved given the limitation in the existing age model of our sedimentary sequence. Thus it remains speculative to associate these centennial changes in regional rainfall to shorter Holocene fluctuations in AMOC [Bond et al., 2001].

VIII-7. Conclusions

We report a new, high-resolution record of riverine runoff covering the last 18 ka from the northern Peruvian margin at 3.5°S. We detect periods of high runoff during the H1, the YD and the late Holocene, while conditions of reduced runoff occurred during the Early and mid Holocene. These changes in runoff are considered as the expression of rainfall variability during the wet season at the western flanks of the Andes. Our record mimics rainfall variability reported from speleothem records of precipitation in southern Brazil, suggesting that both the southern tropical America and the Pacific coast situated much closer to the equator were affected in similar ways by orbital and millennial-scale climate forcing. This however contrasts with another speleothem record located in northeastern Brazil very close to the equator, which shows wetter conditions during the early Holocene and the H1.

The comparison of our record with other available high-resolution records from South America implies that shifts in rainfall pattern above South America were influenced in different ways by climate forcing at different timescales. The sediment cores as well as the

speleothems records show a North-South antiphase of the rainfall maxima occurring at both orbital and millennial timescales, likely triggered by changes in insolation and in AMOC intensity, respectively. This antiphase is observed all around the South American continent, except in a speleothem from northeastern Brazil which is located in the southern hemisphere, but where the trend in rainfall changes at the orbital timescale is in phase with the rainfall trends recorded in other archives from the northern hemisphere. Such feature was explained so far by a remote forcing of the South American monsoon triggered by changes in orbital parameters. Such mechanism is fully consistent with our new XRF results that testify to an interhemispheric seesaw in monsoon-driven precipitation changes above the South America continent at the orbital timescale.

Regardless whether changes in the annual cycle of rainfall and/or in the ENSO were also at play in shaping those rainfall trends, our results may help to better understand how regional rainfall may change over South America under anthropogenic climate forcing. However, given the complexity of the tropical South America rainfall response to climate changes that have occurred over the last 18 ka, further mapping efforts with high resolution time series are needed to draw a clearer picture of the spatial extent of regional rainfall shifts associated with ITCZ movements and monsoonal moist air transport onto the South American continent. Reductions of model-proxy data mismatches at the regional scale may be achieved when using modeling studies integrating a better spatial resolution of the Andean topography. This may contribute also to reduce the regional uncertainties on the future evolution of rainfall patterns associated with anthropogenic climate change.

VIII-8. Acknowledgements

We thank Rik Tjallingii for his help with XRF measurements and Francisco Cruz and Jeroen van der Lubbe for fruitful discussion. Two anonymous reviewers are thanked for their constructive comments on an earlier version of the manuscript that significantly improved its quality.

Chapter IX. General conclusions

IX-1. Conclusions

As part of the subproject A6 in the SFB754 project, the initial aim of this work was to reconstruct spatio-temporal changes in the OMZ extent over the last 18 ka. We have used a suite of sedimentary proxies such as organic carbon, opal and nitrogen content to estimate past variations in export production, which ultimately consumes oxygen during the degradation of the OM. In parallel, alkenone paleothermometry was applied downcore to estimate regional SST variability that potentially contains additional information on upwelling intensity.

A first synthesis of core-top analysis was conducted to assess how modern hydrological and geochemical characteristics affect the spatial distribution of the sedimentary signal in the studied area [Chapter V: *Mollier-Vogel et al.*, 2012]. It has been observed that, within the OMZ, N-loss processes taking place within the water column led the remaining nitrate pool of the water column to become strongly enriched in ^{15}N . Such process is reflected in surface sediments from which nitrogen isotope measurements can be used to reconstruct N-loss processes occurring in subsurface waters. An additional factor associated with nitrate utilization in surface waters was also identified in our compilation that deviates the nitrogen isotopic signatures towards lower isotopic values. Other external factors controlling the ventilation of subsurface waters however must be accounted for to estimate changes in OMZ extent.

We have investigated the relative impact of these processes in a suite of core-top sediments collected along the Peruvian and Ecuadorian margins. A comparison of sedimentary $\delta^{15}\text{N}_{\text{sed}}$ with $\delta^{15}\text{N}_{\text{NO}_x}$ in the water column shows strong similarities along the Peruvian margin transect, indicating that changes in isotopic composition of the nitrate in Peruvian waters are reflected in the sedimentary record [Chapter V: *Mollier-Vogel et al.*, 2012]. However, the $\delta^{15}\text{N}_{\text{sed}}$ remains, in most cases, lower than the $\delta^{15}\text{N}_{\text{NO}_x}$ values measured in the water column. This may be explained by incomplete utilization of nitrate probably resulting from iron and/or silicic acid limitation associated with HNLC conditions prevailing in the studied region. The present-day northernmost extent of the OMZ core within the upper waters reaches 8°S , and is concomitant with a regional shift in PP, as reflected by an increase in organic carbon, opal and nitrogen sedimentary content. Within the OMZ, the

nitrate is enriched in ^{15}N , a feature primarily mediated by N-loss processes taking place in subsurface waters that ultimately feed the surface waters through upwelling. Additionally, the incomplete nitrate utilization by phytoplankton triggers the overall increase of $\delta^{15}\text{N}_{\text{sed}}$ values toward the South and from the inner shelf to the coast, where the most intense upwelling takes place, to slightly lower values than the ones observed in the water column.

Interestingly, higher $\delta^{15}\text{N}_{\text{sed}}$ values are found off Northern Chile, where anoxic and/or suboxic waters do not prevail. This oceanic region is influenced by ventilation from the SAMW which is an old, nutrient-depleted water mass. Along its northern path, the SAMW, which transports isotopically heavy nitrate, gets gradually enriched in ^{15}N due to cumulative nitrate consumption along its path. That may explain the high $\delta^{15}\text{N}$ values observed at $\sim 21^\circ\text{S}$ in the sediment and water column (Chapter VI). Consequently, a multitude of processes such as N-loss processes, relative nitrate utilization, and regional oceanography have to be considered while attempting to interpret sedimentary $\delta^{15}\text{N}$ values.

4 pistons cores have been retrieved along a North-South transect along the Peruvian margin and cover the last 18 ka BP [Chapter VII: *Mollier-Vogel et al.*, in prep]. The deglaciation is marked by a decrease of $\delta^{15}\text{N}$ values, of $\sim 1\%$ for the northern cores and $\sim 5\%$ for the most southern core location, reaching a minimum during the mid-Holocene. Such a $\delta^{15}\text{N}$ minimum is consistently recorded in all the sedimentary records studied. The $\delta^{15}\text{N}$ minimum is recorded during the period when the ETSP was marked by an increase in the SST gradient between the West and East Pacific along the equator, by strong droughts recorded along the Peruvian hinterland, and by periods characterized by an overall northern shift of the Westerlies. All of these features are typical of La-Niña-like conditions – i.e. of a period during which ENSO activity was reduced. Alkenones indicate that relatively cold SST prevailed in the southernmost core during the mid-Holocene (8-5 ka), suggesting an intensification of upwelling activity during this period, likely additionally influencing the sedimentary $\delta^{15}\text{N}$ values through subsurface ventilation of the OMZ. Intensification of upwelling during the mid-Holocene may have strongly ventilated the upper meters of the water column and prevented N-loss processes to take place close to the surface. This may have lead to only light nitrate available in the surface for the organisms and explain the low $\delta^{15}\text{N}$ values recorded in the sediment.

Additional evidence for past evolution of the Peruvian upwelling and its associated atmospheric variability was obtained by studying the interactions between the ITCZ

latitudinal movements and the subsequent regional precipitation. We studied two cores collected offshore of the Guayas River mouth [Chapter VIII: *Mollier-Vogel et al.*, submitted to QSR]. We measured relative abundance of major and minor elements downcore using XRF to reconstruct past changes in riverine runoff, and interpreted it as being the expression of rainfall variability integrated over the Guayas River catchment, which is situated along the western flank of the Andes, during the wet season. The comparison of our record with other available high-resolution records of precipitation from South America, comprising speleothems as well as marine sediment cores, show a North-South antiphase of the rainfall maxima occurring at both orbital and millennial timescales, likely triggered by changes in insolation and in AMOC intensity, respectively. This antiphase is observed all around the South American continent, except in a speleothem from northeastern Brazil which is located in the southern hemisphere, but where the trend in rainfall changes at the orbital timescale is in phase with the rainfall trends recorded in other archives from the northern hemisphere. At our core site, we detect periods of high runoff during the HI, the YD and the late Holocene, while conditions of reduced runoff occurred during the Early and mid Holocene.

This reduction in riverine runoff, associated with a more northerly position of the ITCZ and South American monsoon, is in full agreement with the strong increase in upwelling intensity assumed to occur during the entire mid-Holocene. Indeed the strong correlation between the northern position of the ITCZ and the intensification of the upwelling may have resulted from a more northern position and a strengthening of the Hadley cell. This leads to greater ventilation of the surface water driving a deepening of the oxycline, which may prevent N-loss processes to take place in the upper hundred meters of the water column, as observed in the $\delta^{15}\text{N}_{\text{sed}}$ values during this time period.

IX-2. Outlook

The exchange of knowledge and the common work with other subprojects made being part of the SFB754 advantageous. Providing the first proxy calibration for the entire Peruvian margin, this study rose questions for the interpretation of the proxies themselves; as we have demonstrated for the sedimentary $\delta^{15}\text{N}$, which records the signal of several processes taking place within the water column. A comparison of the $\delta^{15}\text{N}$ with the work done on larger scale with benthic foraminifera: either using species assemblages to assess oxygen concentrations at a very high resolution [*Mallon, 2011*], or the measurements of pore density on benthic

foraminifera test, allowing estimation of nitrate concentration in the water [Glock, 2011], may help to disentangle the fractionation of sedimentary $\delta^{15}\text{N}$ directly induced by oxygen concentrations via N-loss processes. Supplementary work comparing SST_{alk} and SST from Mg/Ca ratio would permit better understanding the potential seasonal effects on SST derived from the alkenone unsaturation index.

The $\delta^{15}\text{N}$ calibration between water column and surface sediments demonstrates that the diversity of processes influencing the $\delta^{15}\text{N}$ within the OMZ, makes it difficult to disentangle them when they are integrated within the $\delta^{15}\text{N}$ signal of the bulk sediment. During the second phase of the SFB754 project, research will be focused on diatom records of nitrogen isotopes associated with silicon isotopes. The latter, driven by silicic acid utilization, will allow separation of the nitrogen fractionation from utilization by diatoms, which is the main primary producer of the area, to better constrain the initial signature of the nitrate.

A crucial issue in this study was the strong seasonality of the hydrological features occurring within the Peruvian upwelling system, which appears to be very sensitive to variations in the mean climatic background. A better understanding of the processes responsible for antiphase in the annual cycle of PP and nitrate supply to the surface, the latter being associated with changes in upwelling intensity, may be overcome via sediment traps deployed at different depths and recording changes in export productivity with a sub-annual time resolution. Additionally, a better knowledge of the coastal current systems would help to better identify the origin of the upwelled nitrate. Better temporal and spatial resolution would largely improve the knowledge of the Peruvian system, especially with better gridding at $\sim 20^\circ\text{S}$ where the two water masses merge.

In a broader context, these results may be integrated in modeling studies, such as the model from the subproject B1 in project SFB754 (C. Somes), which integrates oceanic biogeochemistry and isotopic signatures within a coupled ocean-atmosphere-biogeochemical model. The development of such fully interactive systems still poses a challenge, as complex physical and biogeochemical processes that often operate on small time and space scales need to be parameterized. Reductions of model-proxy data mismatches at the regional scale may be achieved when using modeling studies integrating a better spatial resolution of the Andean topography, in particular by using nested models that better resolve ocean circulation along continental margins. This may also reduce the regional uncertainties on the future evolution of the Peruvian OMZ as well as rainfall patterns associated with anthropogenic climate change.

Bibliography

- Abrantes, F., C. Lopes, A. Mix, and N. Pisiás (2007), Diatoms in Southeast Pacific surface sediments reflect environmental properties, *Quaternary Science Reviews*, 26(1-2), 155-169.
- Adegbe, A. T., R. R. Schneider, U. Röhl, and G. Wefer (2003), Glacial millennial-scale fluctuations in central African precipitation recorded in terrigenous sediment supply and freshwater signals offshore Cameroon, *Palaeogeography, Palaeoclimatology, Palaeoecology*, 197(3-4), 323-333.
- Agnihotri, R., M. A. Altabet, and T. D. Herbert (2006), Influence of marine denitrification on atmospheric N₂O variability during the Holocene, *Geophysical research letters*, 33.
- Agnihotri, R., M. A. Altabet, T. D. Herbert, and J. E. Tierney (2008), Subdecadally resolved paleoceanography of the Peru margin during the last two millennia, *Geochem. Geophys. Geosyst.*, 9(5), Q05013.
- Altabet, M. A. (1988), Variations in nitrogen isotopic composition between sinking and suspended particles: implications for nitrogen cycling and particle transformation in the open ocean, *Deep Sea Research Part A: Oceanographic Research Papers*, 35(4), 535-554.
- Altabet, M. A., and R. Francois (1994), Sedimentary nitrogen isotopic ratio as a recorder for surface ocean nitrate utilization, *Global Biogeochem. Cycles*, 8(1), 103-116.
- Altabet, M. A., R. Francois, D. W. Murray, and W. L. Prell (1995), Climate-related variations in denitrification in the Arabian Sea from sediment ¹⁵N/¹⁴N ratios, *Nature*, 373(6514), 506-509.
- Altabet, M. A., C. Pilskaln, R. Thunell, C. Pride, D. Sigman, F. Chavez, and R. Francois (1999), The nitrogen isotope biogeochemistry of sinking particles from the margin of the Eastern North Pacific, *Deep Sea Research Part I: Oceanographic Research Papers*, 46(4), 655-679.
- Altabet, M. A. (2001), Nitrogen isotopic evidence for micronutrient control of fractional NO₃-utilization in the equatorial Pacific, *Limnology and Oceanography*, 46(2), 368-380.
- Altabet, M. A., and Francois, R. (2001). Nitrogen isotope biogeochemistry of the Antarctic Polar Frontal Zone at 170°W. *Deep Sea Research Part II: Topical Studies in Oceanography* 48, 4247-4273.
- Altabet, M. A., M. J. Higginson, and D. W. Murray (2002), The effect of millennial-scale changes in Arabian Sea denitrification on atmospheric CO₂, *Nature*, 415(6868), 159-162.
- Altabet, M. A. (2006), Isotopic tracers of the marine nitrogen cycle. Marine Organic Matter: Chemical and Biological Markers, *Springer-Verlag. , J. Volkman. berlin Heidelberg*(2), 251-293.
- Álvarez-Solas, J., M. Montoya, C. Ritz, G. Ramstein, S. Charbit, C. Dumas, K. Nisancioglu, T. Dokken, and A. Ganopolski (2011), Heinrich event 1: an example of dynamical ice-sheet reaction to oceanic changes, *Clim. Past*, 7(4), 1297 - 1306.
- Arz, H. W., J. Pätzold, and G. Wefer (1998), Correlated Millennial-Scale Changes in Surface Hydrography and Terrigenous Sediment Yield Inferred from Last-Glacial Marine Deposits off Northeastern Brazil, *Quaternary Research*, 50(2), 157-166.
- Baker, P. A., Seltzer, G. O., Fritz, S. C., Dunbar, R. B., Grove, M. J., Tapia, P. M., Cross, S. L., Rowe, H. D., and Broda, J. P. (2001). The History of South American Tropical Precipitation for the Past 25,000 Years. *Science* 291, 640-643.
- Barber, R. T., M. P. Sanderson, S. T. Lindley, F. Chai, J. Newton, C. C. Trees, D. G. Foley, and F. P. Chavez (1996), Primary productivity and its regulation in the equatorial Pacific during and following the 1991-1992 El Niño, *Deep Sea Research Part II: Topical Studies in Oceanography*, 43(4-6), 933-969.
- Bard, E., B. Hamelin, M. Arnold, L. Montaggioni, G. Cabioch, G. Faure, and F. Rougerie (1996), Deglacial sea-level record from Tahiti corals and the timing of global meltwater discharge, *Nature*, 382(6588), 241-244.
- Bard, E., F. Rostek, J.-L. Turon, and S. Gendreau (2000), Hydrological Impact of Heinrich Events in the Subtropical Northeast Atlantic, *Science*, 289(5483), 1321-1324.

- Bird, B. W., Abbott, M. B., Rodbell, D. T., and Vuille, M. (2011). Holocene tropical South American hydroclimate revealed from a decadal resolved lake sediment $\delta^{18}\text{O}$ record. *Earth and Planetary Science Letters* **310**, 192-202.
- Blanz, T., K.-C. Emeis, and H. Siegel (2005), Controls on alkenone unsaturation ratios along the salinity gradient between the open ocean and the Baltic Sea, *Geochimica et Cosmochimica Acta*, **69**(14), 3589-3600.
- Blard, P. H., J. Lavé, K. A. Farley, M. Fornari, N. Jiménez, and V. Ramirez (2009), Late local glacial maximum in the Central Altiplano triggered by cold and locally-wet conditions during the paleolake Tauca episode (17-15 ka, Heinrich 1), *Quaternary Science Reviews*, **28**(27-28), 3414-3427.
- Bond, G., W. Showers, M. Cheseby, R. Lotti, P. Almasi, P. deMenocal, P. Priore, H. Cullen, I. Hajdas, and G. Bonani (1997), A Pervasive Millennial-Scale Cycle in North Atlantic Holocene and Glacial Climates, *Science*, **278**(5341), 1257-1266.
- Bond, G., Kromer, B., Beer, J., Muscheler, R., Evans, M. N., Showers, W., Hoffmann, S., Lotti-Bond, R., Hajdas, I., and Bonani, G. (2001). Persistent Solar Influence on North Atlantic Climate During the Holocene. *Science* **294**, 2130-2136.
- Bookhagen, B., and M. R. Strecker (2008), Orographic barriers, high-resolution TRMM rainfall, and relief variations along the eastern Andes, *Geophys. Res. Lett.*, **35**(6), L06403.
- Brandes, J. A., A. H. Devol, and C. Deutsch (2007), New Developments in the Marine Nitrogen Cycle, *Chemical Reviews*, **107**(2), 577-589.
- Brassell, S. C., G. Eglinton, I. T. Marlowe, U. Pflaumann, and M. Sarnthein (1986), Molecular stratigraphy: a new tool for climatic assessment, *Nature*, **320**(6058), 129-133.
- Broecker, W. S. (1987), Unpleasant surprises in the greenhouse?, *Nature*, **328**(6126), 123-126.
- Bruland, K. W., E. L. Rue, G. J. Smith, and G. R. DiTullio (2005), Iron, macronutrients and diatom blooms in the Peru upwelling regime: brown and blue waters of Peru, *Marine Chemistry*, **93**(2-4), 81-103.
- Cane, M. A. (2005), The evolution of El Niño, past and future, *Earth and Planetary Science Letters*, **230**(3-4), 227-240.
- Cannariato, K. G., and J. P. Kennett (1999), Climatically related millennial-scale fluctuations in strength of California margin oxygen-minimum zone during the past 60 k.y, *Geology*, **27**(11), 975-978.
- Cartapanis, O., K. Tachikawa, and E. Bard (2011), Northeastern Pacific oxygen minimum zone variability over the past 70 kyr: Impact of biological production and oceanic ventilation, *Paleoceanography*, **26**(4), PA4208.
- Chavez, F. P., and R. T. Barber (1987), An estimate of new production in the equatorial Pacific, *Deep Sea Research Part A. Oceanographic Research Papers*, **34**(7), 1229-1243.
- Chavez, F. P., K. R. Buck, S. K. Service, J. Newton, and R. T. Barber (1996), Phytoplankton variability in the central and eastern tropical Pacific, *Deep Sea Research Part II: Topical Studies in Oceanography*, **43**(4-6), 835-870.
- Chavez, F. P., A. Bertrand, R. Guevara-Carrasco, P. Soler, and J. Csirke (2008), The northern Humboldt Current System: Brief history, present status and a view towards the future, *Progress In Oceanography*, **70**(2-4), 95-105.
- Chavez, F. P., and M. Messié (2009), A comparison of Eastern Boundary Upwelling Ecosystems, *Progress In Oceanography*, **83**(1-4), 80-96.
- Chazen, C. R., M. A. Altabet, and T. D. Herbert (2009), Abrupt mid-Holocene onset of centennial-scale climate variability on the Peru-Chile Margin, *Geophys. Res. Lett.*, **36**(L18704).
- Clement, A. C., R. Seager, and M. A. Cane (2000), Suppression of El Niño during the Mid-Holocene by Changes in the Earth's Orbit, *Paleoceanography*, **15**(6), 731-737.
- Cline, J. D., and I. R. Kaplan (1975), Isotopic fractionation of dissolved nitrate during denitrification in the eastern tropical north pacific ocean, *Marine Chemistry*, **3**(4), 271-299.
- Codispoti, L. A., and J. P. Christensen (1985), Nitrification, denitrification and nitrous oxide cycling in the eastern tropical South Pacific ocean, *Marine Chemistry*, **16**(4), 277-300.

- Codispoti, L. A. (2007), An oceanic fixed nitrogen sink exceeding 400 Tg N a⁻¹ vs the concept of homeostasis in the fixed-nitrogen inventory, *Biogeosciences*, **4**(2), 233-253.
- Conte, M. H., Eglinton, G., and Madureira, L. A. S. (1992). Long-chain alkenones and alkyl alkenoates as palaeotemperature indicators: their production, flux and early sedimentary diagenesis in the Eastern North Atlantic. *Organic Geochemistry* **19**, 287-298.
- Conte, M. H., and Eglinton, G. (1993). Alkenone and alkenoate distributions within the euphotic zone of the eastern North Atlantic: correlation with production temperature. *Deep Sea Research Part I: Oceanographic Research Papers* **40**, 1935-1961.
- Conte, M. H., M.-A. Sicre, C. Rühlemann, J. C. Weber, S. Schulte, D. Schulz-Bull, and T. Blanz (2006), Global temperature calibration of the alkenone unsaturation index (U^K₃₇) in surface waters and comparison with surface sediments, *Geochem. Geophys. Geosyst.*, **7**.
- Cross, S. L., P. A. Baker, G. O. Seltzer, S. C. Fritz, and R. B. Dunbar (2000), A new estimate of the Holocene lowstand level of Lake Titicaca, central Andes, and implications for tropical palaeohydrology, *The Holocene*, **10**(1), 21-32.
- Cruz, F. W., S. J. Burns, I. Karmann, W. D. Sharp, M. Vuille, A. O. Cardoso, J. A. Ferrari, P. L. Silva Dias, and O. Viana (2005), Insolation-driven changes in atmospheric circulation over the past 116,000 years in subtropical Brazil, *Nature*, **434**(7029), 63-66.
- Cruz, F. W., M. Vuille, S. J. Burns, X. Wang, H. Cheng, M. Werner, R. Lawrence Edwards, I. Karmann, A. S. Auler, and H. Nguyen (2009), Orbitally driven east-west antiphasing of South American precipitation, *Nature Geosci.*, **2**(3), 210-214.
- Cullen, J. J., M. R. Lewis, C. O. Davis, and R. T. Barber (1992), Photosynthetic Characteristics and Estimated Growth Rates Indicate Grazing Is the Proximate Control of Primary Production in the Equatorial Pacific, *J. Geophys. Res.*, **97**(C1), 639-654.
- Czeschel, R., L. Stramma, F. U. Schwarzkopf, B. S. Giese, A. Funk, and J. Karstensen (2011), Middepth circulation of the eastern tropical South Pacific and its link to the oxygen minimum zone, *J. Geophys. Res.*, **116**(C1), C01015.
- Dai, A., and T. M. L. Wigley (2000), Global patterns of ENSO-induced precipitation, *Geophys. Res. Lett.*, **27**(9), 1283-1286.
- Dalsgaard, T., Canfield, D. E., Petersen, J., Thamdrup, B., and Acuna-Gonzalez, J. (2003). N₂ production by the anammox reaction in the anoxic water column of Golfo Dulce, Costa Rica. *Nature* **422**, 606-608.
- De Pol-Holz, R., Ulloa, O., Dezileau, L., Kaiser, J. r. m., Lamy, F., and Hebbeln, D. (2006). Melting of the Patagonian Ice Sheet and deglacial perturbations of the nitrogen cycle in the eastern South Pacific. *Geophys. Res. Lett.* **33**.
- De Pol-Holz, R., O. Ulloa, F. Lamy, L. Dezileau, P. Sabatier, and D. Hebbeln (2007), Late Quaternary variability of sedimentary nitrogen isotopes in the eastern South Pacific Ocean, *Paleoceanography*, **22**.
- De Pol-Holz, R., R. S. Robinson, D. Hebbeln, D. M. Sigman, and O. Ulloa (2009), Controls on sedimentary nitrogen isotopes along the Chile margin, *Deep Sea Research Part II: Topical Studies in Oceanography*, **56**(16), 1100-1112.
- De Vries, T. J., and H. Schrader (1981), Variation of upwelling/oceanic conditions during the latest Pleistocene through Holocene off the central Peruvian coast: A diatom record, *Marine Micropaleontology*, **6**(2), 157-167.
- Dubois, N., Kienast, M., Kienast, S., Normandeau, C., Calvert, S. E., Herbert, T. D., and Mix, A. (2011). Millennial-scale variations in hydrography and biogeochemistry in the Eastern Equatorial Pacific over the last 100 kyr. *Quaternary Science Reviews* **30**, 210-223.
- Echevin, V., I. Puillat, C. Grados, and B. Dewitte (2004), Seasonal and mesoscale variability in the Peru upwelling system from in situ data during the years 2000 to 2004, *Gayana (Concepción)*, **68**, 167-173.
- Echevin, V., O. Aumont, J. Ledesma, and G. Flores (2008), The seasonal cycle of surface chlorophyll in the Peruvian upwelling system: A modelling study, *Progress In Oceanography*, **79**(2-4), 167-176.

- Ekdahl, E. J., Fritz, S. C., Baker, P. A., Rigsby, C. A., and Coley, K. (2008). Holocene multidecadal-to millennial-scale hydrologic variability on the South American Altiplano. *The Holocene* **18**, 867-876.
- Ekman, V. W. (1905), On the influence of the Earth's rotation on ocean currents, *Arch. Math. Astron. Phys.*, **2**, 1-52.
- Emerson, S., and Hedges, J. I. (1988). Processes Controlling the Organic Carbon Content of Open Ocean Sediments. *Paleoceanography* **3**, 621-634.
- Escobar, J., D. A. Hodell, M. Brenner, J. H. Curtis, A. Gilli, A. D. Mueller, F. S. Anselmetti, D. Ariztegui, D. A. Grzesik, L. Pérez, A. Schwalb, and T. P. Guilderson (2012), A ~43 ka record of paleoenvironmental change in the Central American lowlands inferred from stable isotopes of lacustrine ostracods, *Quaternary Science Reviews*(0).
- Farrell, J. W., T. F. Pedersen, S. E. Calvert, and B. Nielsen (1995), Glacial-interglacial changes in nutrient utilization in the equatorial Pacific Ocean, *Nature*, **377**(6549), 514-517.
- Feldberg, M. J., and Mix, A. C. (2003). Planktonic foraminifera, sea surface temperatures, and mechanisms of oceanic change in the Peru and south equatorial currents, 0-150 ka BP. *Paleoceanography* **18**, 1016.
- Fernandez, C., Farías, L., and Ulloa, O. (2011). Nitrogen Fixation in Denitrified Marine Waters. *PLoS ONE* **6**, e20539.
- Fiedler, P. C., Philbrick, V., and Chavez, F. P. (1991). Oceanic upwelling and productivity in the eastern tropical Pacific. *Limnology and Oceanography* **36**, 1834-1850.
- Fiedler, P. C., F. P. Chavez, D. W. Behringer, and S. B. Reilly (1992), Physical and biological effects of Los Niños in the eastern tropical Pacific, 1986-1989, *Deep Sea Research Part A. Oceanographic Research Papers*, **39**(2), 199-219.
- Fiedler, P. C., and L. D. Talley (2006), Hydrography of the eastern tropical Pacific: A review, *Progress In Oceanography*, **69**(2-4), 143-180.
- Franck et al (2009), Cruise Report M77 Leg 3, 2009., <http://www.ifm.zmaw.de/control-station-meteormerian/meteor-cruises/>.
- Francois, R., Altabet, M. A., and Burckle, L. H. (1992). Glacial to Interglacial Changes in Surface Nitrate Utilization in the Indian Sector of the Southern Ocean as Recorded by Sediment $\delta^{15}\text{N}$. *Paleoceanography* **7**, 589-606.
- Freudenthal, T., Neuer, S., Meggers, H., Davenport, R., and Wefer, G. (2001). Influence of lateral particle advection and organic matter degradation on sediment accumulation and stable nitrogen isotope ratios along a productivity gradient in the Canary Islands region. *Marine Geology* **177**, 93-109.
- Friederich, G. E., J. Ledesma, O. Ulloa, and F. P. Chavez (2008), Air-sea carbon dioxide fluxes in the coastal southeastern tropical Pacific, *Progress In Oceanography*, **79**(2-4), 156-166.
- Galan, A., Molina, V., Thamdrup, B., Woebken, D., Lavik, G., Kuypers, M. M. M., and Ulloa, O. (2009). Anammox bacteria and the anaerobic oxidation of ammonium in the oxygen minimum zone off northern Chile. *Deep Sea Research Part II: Topical Studies in Oceanography* **56**, 1125-1135.
- Galbraith, E. D., M. Kienast, T. F. Pedersen, and S. E. Calvert (2004), Glacial-interglacial modulation of the marine nitrogen cycle by high-latitude O₂ supply to the global thermocline, *Paleoceanography*, **19**(4), PA4007.
- Galbraith, E. D., M. Kienast, S. L. Jaccard, T. F. Pedersen, B. G. Brunelle, D. M. Sigman, and T. Kiefer (2008), Consistent relationship between global climate and surface nitrate utilization in the western subarctic Pacific throughout the last 500 ka, *Paleoceanography*, **23**.
- Ganeshram, R. S., T. F. Pedersen, S. E. Calvert, and J. W. Murray (1995), Large changes in oceanic nutrient inventories from glacial to interglacial periods, *Nature*, **376**(6543), 755-758.
- Ganeshram, R. S., T. F. Pedersen, S. E. Calvert, G. W. McNeill, and M. R. Fontugne (2000), Glacial-Interglacial Variability in Denitrification in the World's Oceans: Causes and Consequences, *Paleoceanography*, **15**, pp361-376.
- Garcia, H. E., R. A. Locarnini, T. P. Boyer, J. I. Antonov, M. M. Zweng, O. K. Baranova, and D. R. Johnson (2010), World Ocean Atlas 2009, *S. Levitus, Ed. NOAA Atlas NESDIS 71, U.S.*

- Government Printing Office, Washington, D.C., Volume 4: Nutrients (phosphate, nitrate, silicate).
- Garreaud, R. D., M. Vuille, R. Compagnucci, and J. Marengo (2009), Present-day South American climate, *Palaeogeography, Palaeoclimatology, Palaeoecology*, 281(3-4), 180-195.
- Gasse, F., Chalié, F., Vincens, A., Williams, M. A. J., and Williamson, D. (2008). Climatic patterns in equatorial and southern Africa from 30,000 to 10,000 years ago reconstructed from terrestrial and near-shore proxy data. *Quaternary Science Reviews* 27, 2316-2340.
- Glock, N. (2011). Benthic foraminifera as geochemical and micropaleontological proxies for redox conditions in the Peruvian oxygen minimum zone. *University of Kiel, Germany Ph.D. Thesis*.
- Glock, N., Eisenhauer, A., Milker, Y., Liebetrau, V., Schönfeld, J., Mallon, J., Sommer, S., and Hensen, C. (2011). Environmental influences on the pore density of *Bolivina spissa* (Cushman). *The Journal of Foraminiferal Research* 41, 22-32.
- Granger, J., D. M. Sigman, J. A. Needoba, and P. J. Harrison (2004), Coupled Nitrogen and Oxygen Isotope Fractionation of Nitrate during Assimilation by Cultures of Marine Phytoplankton, *Limnology and Oceanography*, 49(5), 1763-1773.
- Granger, J., Sigman, D. M., Lehmann, M. F., and Tortell, P. D. (2008). "Nitrogen and oxygen isotope fractionation during dissimilatory nitrate reduction by denitrifying bacteria." *American Society of Limnology and Oceanography*, Waco, TX, Etats Unis.
- Grasshoff, K., M. Ehrhardt, and K. Kremling (1983), Methods of seawater analysis, (2nd edn.), *Verl. Chem., Weinheim*, 419 pp.
- Gruber, N., and Galloway, J. N. (2008). An Earth-system perspective of the global nitrogen cycle. *Nature* 451, 293-296.
- Gutiérrez, D., Sifeddine, A., Reyss, J. L., Vargas, G., Velasco, F., Salvatelli, R., Ferreira, V., Ortlieb, L., Field, D., Baumgartner, T., Boussafir, M., Boucher, H., Valdes, J., Marinovic, L., Soler, P., and Tapia, P. (2006). Anoxic sediments off Central Peru record interannual to multidecadal changes of climate and upwelling ecosystem during the last two centuries. HAL - CCSD.
- Gutiérrez, D., A. Sifeddine, D. B. Field, L. Ortlieb, G. Vargas Easton, F. P. Chávez, F. Velasco, V. Ferreira, P. Tapia, R. Salvatelli, H. Boucher, M. C. Morales, J. Valdés, J.-L. Reyss, A. Campusano, M. Boussafir, M. Mandeng-Yogo, M. García, and T. Baumgartner (2009), Rapid reorganization in ocean biogeochemistry off Peru towards the end of the Little Ice Age, *Biogeosciences*, 6(5).
- Gutiérrez, D., Bouloubassi, I., Sifeddine, A., Purca, S., Goubanova, K., Graco, M., Field, D., MÈjanelle, L., Velasco, F., Lorre, A., Salvatelli, R., Quispe, D., Vargas, G., Dewitte, B., and Ortlieb, L. (2011). Coastal cooling and increased productivity in the main upwelling zone off Peru since the mid-twentieth century. *Geophys. Res. Lett.* 38, L07603.
- Haug, G. H., K. A. Hughen, D. M. Sigman, L. C. Peterson, and U. Röhl (2001), Southward Migration of the Intertropical Convergence Zone Through the Holocene, *Science*, 293(5533), 1304-1308.
- Hebbeln, D. (1992). Weichselian glacial history of the Svalbard area: correlating the marine and terrestrial records. *Boreas* 21, 295-302.
- Hebbeln, D., M. Marchant, T. Freudenthal, and G. Wefer (2000), Surface sediment distribution along the Chilean continental slope related to upwelling and productivity, *Marine Geology*, 164(3-4), 119-137.
- Hendy, I. L., and T. F. Pedersen (2006), Oxygen minimum zone expansion in the eastern tropical North Pacific during deglaciation, *Geophys. Res. Lett.*, 33(20), L20602.
- Higginson, M., J., and Altabet, M., A. (2004). "Initial test of the silicic acid leakage hypothesis using sedimentary biomarkers." American Geophysical Union, Washington, DC, Etats Unis.
- Holmes, R. M., J. W. McClelland, D. M. Sigman, B. Fry, and B. J. Peterson (1998), Measuring $^{15}\text{N-NH}_4^+$ in marine, estuarine and fresh waters: An adaptation of the ammonia diffusion method for samples with low ammonium concentrations, *Marine Chemistry*, 60(3-4), 235-243.

- Horn, M. G., R. S. Robinson, T. A. Rynearson, and D. M. Sigman (2011), Nitrogen isotopic relationship between diatom-bound and bulk organic matter of cultured polar diatoms, *Paleoceanography*, *26*(3), PA3208.
- Hutchins, D. A., C. E. Hare, R. S. Weaver, Y. Zhang, G. F. Firme, G. R. DiTullio, M. B. Alm, S. F. Riseman, J. M. Maucher, M. E. Geesey, C. G. Trick, G. J. Smith, E. L. Rue, J. Conn, and K. W. Bruland (2002), Phytoplankton iron limitation in the Humboldt Current and Peru Upwelling, *Limnology and Oceanography*, *47*(4), 997-1011.
- Huyer, A., R. L. R. L. Smith, and T. Paluszkiwicz (1987), Coastal upwelling off Peru during normal and El Niño times, 1981-1984, *J. Geophys. Res.*, *92*(CO13), 14,297-214,230.
- IPCC (2007), Contribution of Working Groups I, II and III to the Fourth Assessment Report of the Intergovernmental Panel on Climate Change, in: *Climate Change 2007, Synthesis Report*, IPCC, Geneva, Switzerland, pp 104.
- Jaccard, S. L., and E. D. Galbraith (2011), Large climate-driven changes of oceanic oxygen concentrations during the last deglaciation, *Nature Geosci*, advance online publication.
- Jaeschke, A., Rühlemann, C., Arz, H., Heil, G., and Lohmann, G. (2007). Coupling of millennial-scale changes in sea surface temperature and precipitation off northeastern Brazil with high-latitude climate shifts during the last glacial period. *Paleoceanography* **22**, PA4206.
- Jasper, J. P., and Gagosian, R. B. (1989). Glacial-interglacial climatically forced $\delta^{13}\text{C}$ variations in sedimentary organic matter. *Nature* **342**, 60-62.
- Jennerjahn, T. C., Ittekkot, V., Arz, H. W., Behling, H., Pätzold, J., and Wefer, G. (2004). Asynchronous Terrestrial and Marine Signals of Climate Change During Heinrich Events. *Science* **306**, 2236-2239.
- Jomelli, V., Khodri, M., Favier, V., Brunstein, D., Ledru, M.-P., Wagnon, P., Blard, P.-H., Sicart, J.-E., Braucher, R., Grancher, D., Bourles, D. L., Braconnot, P., and Vuille, M. (2011). Irregular tropical glacier retreat over the Holocene epoch driven by progressive warming. *Nature* **474**, 196-199.
- Jouzel, J., V. Masson-Delmotte, O. Cattani, G. Dreyfus, S. Falourd, G. Hoffmann, B. Minster, J. Nouet, J. M. Barnola, J. Chappellaz, H. Fischer, J. C. Gallet, S. Johnsen, M. Leuenberger, L. Loulergue, D. Luethi, H. Oerter, F. Parrenin, G. Raisbeck, D. Raynaud, A. Schilt, J. Schwander, E. Selmo, R. Souchez, R. Spahni, B. Stauffer, J. P. Steffensen, B. Stenni, T. F. Stocker, J. L. Tison, M. Werner, and E. W. Wolff (2007), Orbital and Millennial Antarctic Climate Variability over the Past 800,000 Years, *Science*, *317*(5839), 793-796.
- Kaiser, J., Schefuß, E., Lamy, F., Mohtadi, M., and Hebbeln, D. (2008). Glacial to Holocene changes in sea surface temperature and coastal vegetation in north central Chile: high versus low latitude forcing. *Quaternary Science Reviews* **27**, 2064-2075.
- Kanner, L. C., S. J. Burns, H. Cheng, and R. L. Edwards (2012), High-Latitude Forcing of the South American Summer Monsoon During the Last Glacial, *Science*, *335*(6068), 570-573.
- Karstensen, J., L. Stramma, and M. Visbeck (2008), Oxygen minimum zones in the eastern tropical Atlantic and Pacific oceans, *Progress In Oceanography*, *77*(4), 331-350.
- Keefer, D. K., Moseley, M. E., and deFrance, S. D. (2003). A 38000-year record of floods and debris flows in the Ilo region of southern Peru and its relation to El Niño events and great earthquakes. *Palaeogeography, Palaeoclimatology, Palaeoecology* **194**, 41-77.
- Keeling, R. F., S. C. Piper, and M. Heimann (1996), Global and hemispheric CO₂ sinks deduced from changes in atmospheric O₂ concentration, *Nature*, *381*, 218 - 221.
- Kessler, W. S. (2006), The circulation of the eastern tropical Pacific: A review, *Progress In Oceanography*, *69*(2-4), 181-217.
- Kienast, S. S., Kienast, M., Mix, A. C., Calvert, S. E., and François, R. (2007). Thorium-230 normalized particle flux and sediment focusing in the Panama Basin region during the last 30,000 years. *Paleoceanography* **22**, PA2213.
- Kienast, M., G. MacIntyre, N. Dubois, S. Higginson, C. Normandeau, C. Chazen, and T. D. Herbert (2012), Alkenone unsaturation in surface sediments from the eastern equatorial Pacific: Implications for SST reconstructions, *Paleoceanography*, *27*(1), PA1210.

- Kim, J.-H., Schneider, R. R., Hebbeln, D., Møller, P. J., and Wefer, G. (2002). Last deglacial sea-surface temperature evolution in the Southeast Pacific compared to climate changes on the South American continent. *Quaternary Science Reviews* **21**, 2085-2097.
- Koutavas, A., P. B. deMenocal, G. C. Olive, and J. Lynch-Stieglitz (2006). Mid-Holocene El Niño-Southern Oscillation (ENSO) attenuation revealed by individual foraminifera in eastern tropical Pacific sediments, *Geology*, **34**(12), 993-996.
- Koutavas, A., and Sachs, J. P. (2008). Northern timing of deglaciation in the eastern equatorial Pacific from alkenone paleothermometry. *Paleoceanography* **23**, PA4205.
- Kuhlbrodt, T., A. Griesel, M. Montoya, A. Levermann, M. Hofmann, and S. Rahmstorf (2007). On the driving processes of the Atlantic meridional overturning circulation, *Rev. Geophys.*, **45**(2), RG2001.
- Kuypers, M. M. M., G. Lavik, D. Wobken, M. Schmid, B. M. Fuchs, R. Amann, B. B. Jørgensen, and Jetten, M. S. M. (2005). Massive nitrogen loss from the Benguela upwelling system through anaerobic ammonium oxidation. *PNAS* **102**, 6478-6483.
- Lam, P., G. Lavik, M. M. Jensen, J. van de Vossen, M. Schmid, D. Wobken, D. Gutiérrez, R. Amann, M. S. M. Jetten, and Kuypers, M. M. M. (2009). Revising the nitrogen cycle in the Peruvian oxygen minimum zone. *PNAS* **106**, 4752-4757.
- Lamy, F., Hebbeln, D., Röhl, U., and Wefer, G. (2001). Holocene rainfall variability in southern Chile: a marine record of latitudinal shifts of the Southern Westerlies. *Earth and Planetary Science Letters* **185**, 369-382.
- Lamy, F., Kilian, R., Arz, H. W., Francois, J.-P., Kaiser, J., Prange, M., and Steinke, T. (2010). Holocene changes in the position and intensity of the southern westerly wind belt. *Nature Geosci* **3**, 695-699.
- Leduc, G., Vidal, L., Tachikawa, K., Rostek, F., Sonzogni, C., Beaufort, L., and Bard, E. (2007). Moisture transport across Central America as a positive feedback on abrupt climatic changes. *Nature* **445**, 908-911.
- Leduc, G., R. Schneider, J. H. Kim, and G. Lohmann (2010), Holocene and Eemian sea surface temperature trends as revealed by alkenone and Mg/Ca paleothermometry, *Quaternary Science Reviews*, **29**(7-8), 989-1004.
- Lehmann, M. F., Sigman, D. M., McCorkle, D. C., Granger, J., Hoffmann, S., Cane, G., and Brunelle, B. G. (2007). The distribution of nitrate $^{15}\text{N}/^{14}\text{N}$ in marine sediments and the impact of benthic nitrogen loss on the isotopic composition of oceanic nitrate. *Geochimica et Cosmochimica Acta* **71**, 5384-5404.
- Liu, K.-K., and I. R. Kaplan (1989), The eastern tropical Pacific as a source of ^{15}N -enriched nitrate in seawater off southern California, *Limnol. Oceanogr.*, **34**, 820-830.
- Liu, W. T., and X. Xie (2002), Double intertropical convergence zones-a new look using scatterometer, *Geophys. Res. Lett.*, **29**(22), 2072.
- Liu, Z., M. A. Altabet, and T. D. Herbert (2005), Glacial-interglacial modulation of eastern tropical North Pacific denitrification over the last 1.8-Myr, *Geophys. Res. Lett.*, **32**(23), L23607.
- Lutgens and Tarbuck, *The Atmosphere*, 8th edition, (2001).
- Mallon, J. (2011), Benthic Foraminifera of the Peruvian & Ecuadorian Continental Margin, *University of Kiel, Germany, Ph.D. Thesis*.
- Marchitto, T. M., Muscheler, R., Ortiz, J. D., Carriquiry, J. D., and van Geen, A. (2010). Dynamical Response of the Tropical Pacific Ocean to Solar Forcing During the Early Holocene. *Science* **330**, 1378-1381.
- Mariotti, A., J. Germon, P. Hubert, P. Kaiser, R. Letolle, A. Tardieux, and P. Tardieux (1981), Experimental determination of nitrogen kinetic isotope fractionation: Some principles; illustration for the denitrification and nitrification processes, *Plant and Soil*, **62**(3), 413-430.
- Marlowe, I. T., Brassell, S. C., Eglinton, G., and Green, J. C. (1990). Long-chain alkenones and alkyl alkenoates and the fossil coccolith record of marine sediments. *Chemical Geology* **88**, 349-375.
- Martin, J. H., R. M. Gordon, S. Fitzwater, and W. W. Broenkow (1989), Vertex: phytoplankton/iron studies in the Gulf of Alaska, *Deep Sea Research Part A. Oceanographic Research Papers*, **36**(5), 649-680.

- Martin, L., Fournier, M., Mourguiart, P., Sifeddine, A., Turcq, B., Flexor, J.-M., and Absy, M. L. (1993). Southern Oscillation Signal in South American Palaeoclimatic Data of the Last 7000 Years. *Quaternary Research* **39**, 338-346.
- Martinez, P., P. Bertrand, S. Calvert, E., T. Pedersen, F., G. Shimmield, B., V. E. Lallier, and M. Fontugne, R (2000), Spatial variations in nutrient utilization, production and diagenesis in the sediments of a coastal upwelling regime (NW Africa): Implications for the paleoceanographic record, Sears Foundation for Marine Research, New Haven, CT, Etats Unis.
- Martinez, P., F. Lamy, R. R. Robinson, L. Pichevin, and I. Billy (2006), Atypical $\delta^{15}\text{N}$ variations at the southern boundary of the East Pacific oxygen minimum zone over the last 50 ka, *Quaternary Science Reviews*, **25**(21-22), 3017-3028.
- Martinez, P., and R. S. Robinson (2010), Increase in water column denitrification during the last deglaciation: the influence of oxygen demand in the eastern equatorial Pacific, *Biogeosciences*, **7**(1), 1-9.
- McIlvin, M. R., and M. A. Altabet (2005), Chemical Conversion of Nitrate and Nitrite to Nitrous Oxide for Nitrogen and Oxygen Isotopic Analysis in Freshwater and Seawater, *Anal. Chem.*, **77**, pp 5589 -5595.
- McManus, J. F., R. Francois, J.-M. Gherardi, L. D. Keigwin, and S. Brown-Leger (2004), Collapse and rapid resumption of Atlantic meridional circulation linked to deglacial climate changes, *Nature*, **428**(6985), 834 - 837.
- McPhaden, M. J., A. J. Busalacchi, R. Cheney, J.-R. Donguy, K. S. Gage, D. Halpern, M. Ji, P. Julian, G. Meyers, G. T. Mitchum, P. P. Niiler, J. Picaut, R. W. Reynolds, N. Smith, and K. Takeuchi (1998), The Tropical Ocean-Global Atmosphere observing system: A decade of progress, *J. Geophys. Res.*, **103**(C7), 14169-14240.
- Meissner, K. J., E. D. Galbraith, and C. Völker (2005), Denitrification under glacial and interglacial conditions: A physical approach, *Paleoceanography*, **20**(3), PA3001.
- Messié, M., Ledesma, J., Kolber, D. D., Michisaki, R. P., Foley, D. G., and Chavez, F. P. (2009). Potential new production estimates in four eastern boundary upwelling ecosystems. *Progress In Oceanography* **83**, 151-158.
- Mollenhauer, G., Eglinton, T. I., Ohkouchi, N., Schneider, R. R., Müller, P. J., Grootes, P. M., and Rullkötter, J. (2003). Asynchronous alkenone and foraminifera records from the Benguela Upwelling System. *Geochimica et Cosmochimica Acta* **67**, 2157-2171.
- Mollenhauer, G., Kienast, M., Lamy, F., Meggers, H., Schneider, R. R., Hayes, J. M., and Eglinton, T. I. (2005). An evaluation of ^{14}C age relationships between co-occurring foraminifera, alkenones, and total organic carbon in continental margin sediments. *Paleoceanography* **20**, PA1016.
- Mollenhauer, G., D. Montluçon, and T. I. Eglinton (2005), Radiocarbon dating of alkenones from marine sediments - II. Assessment of carbon process blanks, *Radiocarbon*, **47**(3), 413-424.
- Mollier-Vogel, E., Ryabenko, E., Martinez, P., Wallace, D., Altabet, M. A., and Schneider, R. (2012). Nitrogen isotope gradients off Peru and Ecuador related to upwelling, productivity, nutrient uptake and oxygen deficiency. *Deep Sea Research Part I: Oceanographic Research Papers* **70**, 14-25.
- Moy, C. M., G. O. Seltzer, D. T. Rodbell, and D. M. Anderson (2002), Variability of El Niño/Southern Oscillation activity at millennial timescales during the Holocene epoch, *Nature*, **420**(6912), 162-165.
- Müller, P. J. (1977), C/N ratios in Pacific deep-sea sediments: Effect of inorganic ammonium and organic nitrogen compounds sorbed by clays, *Geochimica et Cosmochimica Acta*, **41**(6), 765-776.
- Müller, P. J., and R. Schneider (1993), An automated leaching method for the determination of opal in sediments and particulate matter, *Deep Sea Research Part I: Oceanographic Research Papers*, **40**(3), 425-444.
- Müller, P. J., Kirst, G., Ruhland, G., von Storch, I., and Rosell-Melé, A. (1998). Calibration of the alkenone paleotemperature index U^{K}_{37} based on core-tops from the eastern South Atlantic and the global ocean (60°N-60°S). *Geochimica et Cosmochimica Acta* **62**, 1757-1772.

- Nevison, C. D., R. F. Weiss, and D. J. Erickson, III (1995), Global oceanic emissions of nitrous oxide, *J. Geophys. Res.*, 100(C8), 15809-15820.
- Niggemann, J. (2005). Composition and degradation of organic matter in sediments from the Peru-Chile upwelling region. *University of Bremen, Germany PhD-thesis*.
- Ortlieb, L., G. Vargas, and J. F. Saliège (2011), Marine radiocarbon reservoir effect along the northern Chile-southern Peru coast (14-24 degrees S) throughout the Holocene, *Quaternary Research*, 75, 91-103.
- Pahnke, K., J. P. Sachs, L. Keigwin, A. Timmermann, and S.-P. Xie (2007), Eastern tropical Pacific hydrologic changes during the past 27,000 years from D/H ratios in alkenones, *Paleoceanography*, 22(4), PA4214.
- Paulmier, A., and D. Ruiz-Pino (2009), Oxygen minimum zones (OMZs) in the modern ocean, *Progress In Oceanography*, 80(3-4), 113-128.
- Pennington, J. T., K. L. Mahoney, V. S. Kuwahara, D. D. Kolber, R. Calienes, and F. P. Chavez (2006), Primary production in the eastern tropical Pacific: A review, *Progress In Oceanography*, 69(2-4), 285-317.
- Penven, P., V. Echevin, J. Pasapera, F. Colas, and J. Tam (2005), Average circulation, seasonal cycle, and mesoscale dynamics of the Peru Current System: A modeling approach, *J. Geophys. Res.*, 110(C10), C10021.
- Peterson, L. C., Haug, G. H., Hughen, K. A., and Röhl, U. (2000). Rapid Changes in the Hydrologic Cycle of the Tropical Atlantic During the Last Glacial. *Science* 290, 1947-1951.
- Pfannkuche et al (2008), Cruise Report M77 Leg 1, 2008. , <http://www.ifm.zmaw.de/control-station-meteormerian/meteor-cruises/>.
- Philander, S. G. H. (1983), El Niño Southern Oscillation phenomena, *Nature*, 302(5906), 295-301.
- Pichevin, L., P. Martinez, P. Bertrand, R. Schneider, J. Giraudeau, and K. Emeis (2005), Nitrogen cycling on the Namibian shelf and slope over the last two climatic cycles: Local and global forcings, *Paleoceanography*, 20.
- Pichevin, L., E. Bard, P. Martinez, and I. Billy (2007), Evidence of ventilation changes in the Arabian Sea during the late Quaternary: Implication for denitrification and nitrous oxide emission, *Global Biogeochem. Cycles*, 21.
- Pichevin, L. E., Reynolds, B. C., Ganeshram, R. S., Cacho, I., Pena, L., Keefe, K., and Ellam, R. M. (2009). Enhanced carbon pump inferred from relaxation of nutrient limitation in the glacial ocean. *Nature* 459, 1114-1117.
- Poveda, G., and O. J. Mesa (2000), On the existence of Lloró (the rainiest locality on Earth): Enhanced ocean-land-atmosphere interaction by a low-level jet, *Geophys. Res. Lett.*, 27(11), 1675-1678.
- Poveda, G. n., P. R. Waylen, and R. S. Pulwarty (2006), Annual and inter-annual variability of the present climate in northern South America and southern Mesoamerica, *Palaeogeography, Palaeoclimatology, Palaeoecology*, 234(1), 3-27.
- Prahl, F. G., G. J. de Lange, M. Lyle, and M. A. Sparrow (1989), Post-depositional stability of long-chain alkenones under contrasting redox conditions, *Nature*, 341(6241), 434-437.
- Prahl, F., T. D. Herbert, S. Brassell, N. Ohkouchi, M. Pagani, A. Rosell-Melé, D. Repeta, and Sikes, E. (2000). Status of alkenone paleothermometer calibration: Report from Working Group 3, *Geochem. Geophys. Geosyst.* vol. 1.
- Prahl, F. G., J.-F. Rontani, N. Zabeti, S. E. Walinsky, and M. A. Sparrow (2010), Systematic pattern in U_{37}^K - Temperature residuals for surface sediments from high latitude and other oceanographic settings, 13 pp., Elsevier, Kidlington, Royaume-Uni.
- Price, J. F., R. A. Weller, and R. R. Schudlich (1987), Wind-Driven Ocean Currents and Ekman Transport, *Science*, 238(4833), 1534-1538.
- Pride, C., R. Thunell, D. Sigman, L. Keigwin, M. Altabet, and E. Tappa (1999), Nitrogen Isotopic Variations in the Gulf of California Since the Last Deglaciation: Response to Global Climate Change, *Paleoceanography*, 14(3), 397-409.
- Ragueneau, O., Tréguer, P., Leynaert, A., Anderson, R. F., Brzezinski, M. A., DeMaster, D. J., Dugdale, R. C., Dymond, J., Fischer, G., François, R., Heinze, C., Maier-Reimer, E.,

- Martin-Jézéquel, V., Nelson, D. M., and Quéguiner, B. (2000). A review of the Si cycle in the modern ocean: recent progress and missing gaps in the application of biogenic opal as a paleoproductivity proxy. *Global and Planetary Change* **26**, 317-365.
- Rahmstorf, S. (2006). Thermohaline Ocean Circulation. *Encyclopedia of Quaternary Sciences*.
- Rahmstorf, S. (2006). Thermohaline Ocean Circulation. *Encyclopedia of Quaternary Sciences*.
- Reimer, P. J., M. G. L. Baillie, E. Bard, A. Bayliss, J. W. Beck, P. G. Blackwell, C. B. Ramsey, C. E. Buck, G. S. Burr, R. L. Edwards, M. Friedrich, P. M. Grootes, T. P. Guilderson, I. Hajdas, T. J. Heaton, A. G. Hogg, K. A. Hughen, K. F. Kaiser, B. Kromer, F. G. McCormac, S. W. Manning, R. W. Reimer, D. A. Richards, J. R. Southon, S. Talamo, C. S. M. Turney, J. van der Plicht, and C. E. Weyhenmeyer (2009), IntCal09 and Marine09 radiocarbon age calibration curves, 0-50,000 years cal BP, *RADIOCARBON*, *51*(4), 1111-1150.
- Rein, B., A. Lückge, L. Reinhardt, F. Sirocko, A. Wolf, and W.-C. Dullo (2005), El Niño variability off Peru during the last 20,000 years, *Paleoceanography*, *20*(PA4003).
- Reinhardt, L., Kudrass, H. R., Lückge, A., Wiedicke, M., Wunderlich, J., and Wendt, G. (2002). High-resolution sediment echosounding off Peru: Late Quaternary depositional sequences and sedimentary structures of a current-dominated shelf. *Marine Geophysical Researches* **23**, 335-351.
- Revelle, R., Suess, H. E. (1957), Carbon Dioxide Exchange Between Atmosphere and Ocean and the Question of an Increase of Atmospheric CO₂ during the Past Decades, *Tellus*, *9*(1), 18-27.
- Richter, T. O., S. van der Gaast, B. Koster, A. Vaars, R. Gieles, H. C. de Stigter, H. De Haas, and T. C. E. van Weering (2006), The Avaatech XRF Core Scanner: technical description and applications to NE Atlantic sediments, *Geological Society, London, Special Publications*, *267*(1), 39-50.
- Rincón-Martínez, D., F. Lamy, S. Contreras, G. Leduc, E. Bard, C. Saukel, T. Blanz, A. Mackensen, and R. Tiedemann (2010), More humid interglacials in Ecuador during the past 500 kyr linked to latitudinal shifts of the equatorial front and the Intertropical Convergence Zone in the eastern tropical Pacific, *Paleoceanography*, *25*(2), PA2210.
- Robinson, R. S., Mix, A., and Martinez, P. (2007). Southern Ocean control on the extent of denitrification in the southeast Pacific over the last 70 ka. *Quaternary Science Reviews* **26**, 201-212.
- Robinson, R. S., Martinez, P., Pena, L. D., and Cacho, I. (2009). Nitrogen isotopic evidence for deglacial changes in nutrient supply in the eastern equatorial Pacific. *Paleoceanography* **24**, PA4213.
- Roche, D. M., H. Renssen, D. Paillard, and G. Levassasseur (2011), Deciphering the spatio-temporal complexity of climate change of the last deglaciation: a model analysis, *Clim. Past*, *7*(2), 591-602.
- Rodbell, D. T., G. O. Seltzer, D. M. Anderson, M. B. Abbott, D. B. Enfield, and J. H. Newman (1999), An ~15,000 Year Record of El Niño-Driven Alluviation in Southwestern Ecuador, *Science*, *283*(5401), 516-520.
- Rühlemann, C., P. J. Müller, and R. R. Schneider (1999), Organic carbon and carbonate as paleoproductivity proxies: Examples from high and low productivity areas of the tropical Atlantic, *Springer-Verlag Berlin Heidelberg, Fischer, G., and Wefer, G. (eds), Use in proxies of paleoceanography: Examples from the South Atlantic.*, pp 315-344.
- Ryabenko, E., Mark A. Altabet, and D. W. R. Wallace (2009), Effect of chloride on the chemical conversion of nitrate to nitrous oxide for d₁₅N analysis, *Limnol. Oceanogr.*, *7*, 545-552.
- Sachs, J. P., and S. J. Lehman (1999), Subtropical North Atlantic Temperatures 60,000 to 30,000 Years Ago, *Science*, *286*(5440), 756-759.
- Sandweiss, D. H., Richardson, J. B., Reitz, E. J., Rollins, H. B., and Maasch, K. A. (1996). Geoarchaeological Evidence from Peru for a 5000 Years B.P. Onset of El Niño. *Science* **273**, 1531-1533.
- Sandweiss, D. H., K. A. Maasch, and D. G. Anderson (1999), Transitions in the Mid-Holocene, *Science*, *283*(5401), 499-500.

- Sandweiss, D. H., R. S. Solís, M. E. Moseley, D. K. Keefer, and C. R. Ortloff (2009), Environmental change and economic development in coastal Peru between 5,800 and 3,600 years ago, *Proceedings of the National Academy of Sciences*, 106(5), 1359-1363.
- Schlanger, S. O., and H. C. Jenkyns (1976), Cretaceous anoxic events: causes and consequences, *Geologie en Mijnbouw*, 55(3-4), pp. 179-184.
- Schneider, B., G. Leduc, and W. Park (2010), Disentangling seasonal signals in Holocene climate trends by satellite-model-proxy integration, *Paleoceanography*, 25(4), PA4217.
- Schneider et al. (2008), Cruise Report M77 Leg 2, 2008., <http://www.ifm.zmaw.de/control-station-meteormerian/meteor-cruises/>.
- Scholz, F., C. Hensen, A. Noffke, A. Rohde, V. Liebetrau, and K. Wallmann (2011), Early diagenesis of redox-sensitive trace metals in the Peru upwelling area - response to ENSO-related oxygen fluctuations in the water column, *Geochimica et Cosmochimica Acta*, 75(22), 7257-7276.
- Sifeddine, A., Gutiérrez, D., Ortlieb, L., Boucher, H., Velazco, F., Field, D., Vargas, G., Boussafir, M., Salvatelli, R., Ferreira, V., García, M., Valdés, J., Caquineau, S., Mandeng Yogo, M., Cetin, F., Solis, J., Soler, P., and Baumgartner, T. (2008). Laminated sediments from the central Peruvian continental slope: A 500 year record of upwelling system productivity, terrestrial runoff and redox conditions. *Progress In Oceanography* 79, 190-197.
- Sigman, D. M., M. A. Altabet, R. Francois, D. C. McCorkle, and Gaillard, J.-F. (1999). The Isotopic Composition of Diatom-Bound Nitrogen in Southern Ocean Sediments. *Paleoceanography* 14, pp 118-134.
- Sigman, D. M., P. J. DiFiore, M. P. Hain, C. Deutsch, and D. M. Karl (2009), Sinking organic matter spreads the nitrogen isotope signal of pelagic denitrification in the North Pacific, *Geophys. Res. Lett.*, 36.
- Silva, N., N. Rojas, and A. Fedele (2009), Water masses in the Humboldt Current System: Properties, distribution, and the nitrate deficit as a chemical water mass tracer for Equatorial Subsurface Water off Chile, *Deep Sea Research Part II: Topical Studies in Oceanography*, 56(16), 992-1008.
- Silvestri, G. E. (2004). El Niño signal variability in the precipitation over southeastern South America during austral summer. *Geophys. Res. Lett.* 31, L18206.
- Skilbeck, C. G., and D. Fink (2006), Data report: Radiocarbon dating and sedimentation rates for Holocene-upper Pleistocene sediments, Eastern Equatorial Pacific and Peru continental margin, *Proceedings of the Ocean Drilling Program, Scientific Results*, 201.
- Sohm, J. A., J. A. Hilton, A. E. Noble, J. P. Zehr, M. A. Saito, and E. A. Webb (2011), Nitrogen fixation in the South Atlantic Gyre and the Benguela Upwelling System, *Geophys. Res. Lett.*, 38(16), L16608.
- Somes, C. J., A. Schmittner, and M. A. Altabet (2010a), Nitrogen isotope simulations show the importance of atmospheric iron deposition for nitrogen fixation across the Pacific Ocean, *Geophys. Res. Lett.*, 37(23), L23605.
- Somes, C. J., A. Schmittner, E. D. Galbraith, M. F. Lehmann, M. A. Altabet, J. P. Montoya, R. M. Letelier, A. C. Mix, A. Bourbonnais, and M. Eby (2010b), Simulating the global distribution of nitrogen isotopes in the ocean, *Global Biogeochem. Cycles*, 24(4), GB4019.
- Sonzogni, C., Bard, E., Rostek, F., Lafont, R., Rosell-Melé, A., and Eglinton, G. (1997). Core-top calibration of the alkenone index vs sea surface temperature in the Indian Ocean. *Deep Sea Research Part II: Topical Studies in Oceanography* 44, 1445-1460.
- Stramma, L., G. C. Johnson, J. Sprintall, and V. Mohrholz (2008), Expanding Oxygen-Minimum Zones in the Tropical Oceans, *Science*, 320(5876), 655-658.
- Stramma et al (2009), Cruise Report M77 Leg 3, 2009., <http://www.ifm.zmaw.de/control-station-meteormerian/meteor-cruises/>.
- Stramma, L., S. Schmidtke, L. A. Levin, and G. C. Johnson (2010), Ocean oxygen minima expansions and their biological impacts, *Deep Sea Research Part I: Oceanographic Research Papers*, 57(4), 587-595.
- Stríkis, N. M., Cruz, F. W., Cheng, H., Karmann, I., Edwards, R. L., Vuille, M., Wang, X., de Paula, M. S., Novello, V. F., and Auler, A. S. (2011). Abrupt variations in South American monsoon

- rainfall during the Holocene based on a speleothem record from central-eastern Brazil. *Geology*.
- Strub, P. T., J. M. Mesias, V. Montecino, J. Rutlant, and S. Salinas (1998), Coastal ocean circulation off Western South America, *Robinson, A.R., Brink, K.H. (Eds.). The Global Coastal Ocean, Wiley, New York*, pp. 273-314.
- Suess, E., L. D. Kulm, and J. S. Killingley (1987), Coastal upwelling and a history of organic-rich mudstone deposition off Peru, *Geological Society, London, Special Publications*, 26(1), 181-197.
- Tachikawa, K., Cartapanis, O., Vidal, L., Beaufort, L., Barlyaeva, T., and Bard, E. (2011). The precession phase of hydrological variability in the Western Pacific Warm Pool during the past 400 ka. *Quaternary Science Reviews* 30, 3716-3727.
- Takahashi, T., Sutherland, S. C., Sweeney, C., Poisson, A., Metzl, N., Tilbrook, B., Bates, N., Wanninkhof, R., Feely, R. A., Sabine, C., Olafsson, J., and Nojiri, Y. (2002). Global sea-linear CO₂ flux based on climatological surface ocean pCO₂, and seasonal biological and temperature effects. *Deep Sea Research Part II: Topical Studies in Oceanography* 49, 1601-1622.
- Takashima, R., H. Nishi, B. T. Huber, and R. M. Leckie (2006), Greenhouse world and the Mesozoic Ocean, *Oceanography*, 19, pp. 82-93.
- Ternois, Y., Sicre, M. A., Boireau, A., Conte, M. H., and E. G. (1997). Evaluation of long-chain alkenones as paleo-temperature indicators in the Mediterranean Sea. *Deep Sea Research Part I: Oceanographic Research Papers* 44, 271-286.
- Thamdrup, B., T. Dalsgaard, and N. P. Revsbech (2012), Widespread functional anoxia in the oxygen minimum zone of the Eastern South Pacific, *Deep Sea Research Part I: Oceanographic Research Papers*, 65(0), 36-45.
- Thompson, L. G., Davis, M. E., Mosley-Thompson, E., Sowers, T. A., Henderson, K. A., Zagorodnov, V. S., Lin, P.-N., Mikhailenko, V. N., Campen, R. K., Bolzan, J. F., Cole-Dai, J., and Francou, B. (1998). A 25,000-Year Tropical Climate History from Bolivian Ice Cores. *Science* 282, 1858-1864.
- Tjallingii, R., K. Stattegger, A. Wetzel, and P. Van Phach (2010), Infilling and flooding of the Mekong River incised valley during deglacial sea-level rise, *Quaternary Science Reviews*, 29(11-12), 1432-1444.
- Twilley, R. R., et al. (2001), The Gulf of Guayaquil and the Guayas River estuary, Ecuador, *Ecological studies*, 144(Seelinger, U., and Kjerfve, B., (eds), Coastal marine ecosystems in Latin America.), p. 245-264.
- van Breukelen, M. R., H. B. Vonhof, J. C. Hellstrom, W. C. G. Wester, and D. Kroon (2008), Fossil dripwater in stalagmites reveals Holocene temperature and rainfall variation in Amazonia, *Earth and Planetary Science Letters*, 275(1-2), 54-60.
- Villagrán, C., and Varela, J. (1990). Palynological evidence for increased aridity on the central Chilean coast during the Holocene. *Quaternary Research* 34, 198-207.
- Voss, M., Altabet, M. A., and Bodungen, B. v. (1996). $\delta^{15}\text{N}$ in sedimenting particles as indicator of euphotic-zone processes. *Deep Sea Research Part I: Oceanographic Research Papers* 43, 33-47.
- Wada, E., and A. Hattori (1978), Nitrogen isotope effects in the assimilation of inorganic nitrogenous compounds by marine diatoms, *Geomicrobiology Journal*, 1(1), 85 - 101.
- Walker, G. T. (1923): Correlations in seasonal variations of weather, VIII. A preliminary study of world weather I, Mem. Indian Meteorol. Dept., 23, 75-131.
- Walker, G. T. (1924): Correlation in seasonal variations of weather IX: A further study of world weather, Mem. Indian Meteorol. Dept., 24, 275-332.
- Wang, X., A. S. Auler, R. L. Edwards, H. Cheng, P. S. Cristalli, P. L. Smart, D. A. Richards, and C.-C. Shen (2004), Wet periods in northeastern Brazil over the past 210 kyr linked to distant climate anomalies, *Nature*, 432(7018), 740-743.
- Wang, X., R. L. Edwards, A. S. Auler, H. Cheng, and , and E. Ito (2007), Millennial-Scale Interhemispheric Asymmetry of Low-Latitude Precipitation: Speleothem Evidence and

- Possible High-Latitude Forcing, *AGU Geophysical Monograph 173, Ocean Circulation: Mechanisms and Impacts.*, p. 279-294.
- Wanninkhof, R., and Mc Gillies, W. R. (1999). "A cubic relationship between air-sea CO₂ exchange and wind speed." American Geophysical Union, Washington, DC, Etats-Unis.
- Waser, N. A. D., P. J. Harrison, B. Nielsen, S. E. Calvert, and D. H. Turpin (1998), Nitrogen isotope fractionation during the uptake and assimilation of nitrate, nitrite, ammonium, and urea by a marine diatom, *Limnology and Oceanography*, 43(2), 215-224.
- Wells, L. E. (1990), Holocene history of the El Niño phenomenon as recorded in flood sediments of northern coastal Peru, *Geology*, 18(11), 1134-1137.
- Weltje, G. J., and R. Tjallingii (2008), Calibration of XRF core scanners for quantitative geochemical logging of sediment cores: Theory and application, *Earth and Planetary Science Letters*, 274(3-4), 423-438.
- Witt, C. s., and J. Bourgois (2010), Forearc basin formation in the tectonic wake of a collision-driven, coastwise migrating crustal block: The example of the North Andean block and the extensional Gulf of Guayaquil-Tumbes Basin (Ecuador-Peru border area), *Geological Society of America Bulletin*, 122(1-2), 89-108.
- Wolf, A. (2002), Zeitliche Variationen im peruanischen Küstenauftrieb seit dem letzten glazialen Maximum – Steuerung durch globale Klimadynamik, *University of Kiel, Germany, Ph.D. Thesis.*
- Wyrski, K. (1981), An Estimate of Equatorial Upwelling in the Pacific, *Journal of Physical Oceanography*, 11(9), 1205-1214.
- Ziegler, C. L., R. W. Murray, T. Plank, and S. R. Hemming (2008), Sources of Fe to the equatorial Pacific Ocean from the Holocene to Miocene, *Earth and Planetary Science Letters*, 270(3-4), 258-270.
- Ziegler, M., Jilbert, T., de Lange, G. J., Lourens, L. J., and Reichert, G.-J. (2008). Bromine counts from XRF scanning as an estimate of the marine organic carbon content of sediment cores. *Geochem. Geophys. Geosyst.* 9, Q05009.

Tables

Table 2. Surface sediment data used for this study

Stations	Latitude (S)	Longitude (W)	Water Depth (m)	$\delta^{15}\text{N}$ (‰)	TN (%)	Corg (%)	C/N	SSTalk	Alkenone concentration (ng/g)	SiO ₂ (wt%)	Chlorine	$\delta^{13}\text{C}$ (‰)
M772-076-2	00°05.45'N	80°33.40'	290	4.84	0.073	0.756	10.33	26.65	418.17	1.64	0.165	-22.46
M772-076-2	00°13.00'N	80°39.44'	1314	4.78	0.276	2.625	9.49	26.50	2378.24	4.49	0.203	-21.78
M772-067-2	01°45.14'	82°37.47'	2075	4.74	0.198	1.655	8.35	24.37	1325.12	8.23	0.153	-21.22
M772-064-1	01°53.50'	81°11.76'	529	4.81	0.296	3.015	10.18	25.87	3506.29	2.97	0.142	-21.66
M772-065-2	01°57.01'	81°07.23'	206	4.62	0.114	0.962	8.48	25.99	885.67	1.49	0.191	-21.32
M772-062-2	02°30.01'	81°14.71'	1678	4.52	0.094	3.970	8.73	24.78	6366.30	8.00	0.195	-21.32
M772-071-1	02°48.99'	80°50.72'	100	4.66	0.094	1.054	11.23	25.93	822.25	2.16	0.204	-21.29
M772-072-2	02°49.01'	81°00.53'	425	4.59	0.205	2.005	9.64	25.22	1664.61	1.12	0.187	-21.29
M772-070-2	03°07.00'	80°38.84'	59	5.24	0.045	0.449	9.93	26.09	177.73	8.73	0.199	-21.60
M772-069-2	03°16.02'	80°56.87'	339	4.62	0.169	1.555	9.17	25.24	1696.71	2.16	0.150	-21.47
M772-056-1	03°45.01'	81°07.29'	350	4.78	0.322	3.025	9.39	24.47	3627.86	3.12	0.216	-21.47
M772-060-1	03°51.09'	81°15.49'	701	4.39	0.391	3.340	8.53	24.09	4069.36	3.27	0.235	-21.46
M772-059-2	03°56.95'	81°19.16'	995	4.27	0.349	3.270	8.05	23.92	4107.93	7.02	0.144	-21.46
M772-053-1	05°28.94'	81°34.03'	2607	3.97	0.411	3.310	8.05	21.19	4523.48	11.49	0.326	-20.50
M772-052-3	05°29.01'	81°27.01'	1252	4.26	0.370	3.380	9.13	21.00	4757.53	8.79	0.188	-20.21
M772-054-2	05°29.01'	81°18.35'	297	4.46	0.399	2.815	7.06	21.79	2424.52	4.99	0.235	-20.21
M772-047-3	07°52.01'	80°31.36'	625	4.49	0.566	4.649	8.22	20.15	7350.15	3.64	0.719	-20.64
M772-045-3	07°59.99'	80°20.51'	359	5.14	0.994	8.881	8.94	20.12	19656.35	8.17	0.242	-20.64
M772-050-1	08°01.04'	80°30.13'	1013	4.21	0.517	5.073	9.80	19.50	8957.42	5.26	0.166	-20.63
M772-031-2	09°02.97'	79°26.88'	114	5.27	0.159	1.800	11.29	21.84	2155.00	1.30	0.222	-20.16
M772-028-1	09°17.69'	79°53.86'	1105	4.45	0.832	4.905	8.28	20.15	11174.14	4.55	0.358	-20.75
M772-029-5	09°17.70'	79°37.11'	437	4.53	0.932	8.445	10.15	21.24	19521.96	3.53	0.270	-20.77
554	10°26.37'	78°54.73'	521	6.83	0.408	4.160	10.20	21.82	5084.79	1.21	0.173	-21.13
M772-026-3	10°45.13'	78°28.43'	424	6.59	0.740	6.047	8.17	22.29	9459.92	3.01	0.263	-20.65
M772-022-2	10°53.22'	78°46.38'	1923	5.04	0.361	2.960	8.26	21.56	6138.41	3.55	0.147	-20.88
450	10°59.98'	78°10.04'	319	6.28	1.760	12.198	6.93	21.22	35313.29	9.12	0.212	-20.65
457	11°00.05'	78°19.26'	467	7.27	0.709	6.865	9.67	21.41	13207.03	2.43	0.341	-20.88
519	11°00.01'	78°16.28'	410	6.63	0.568	6.147	10.83	21.18	13330.89	2.83	0.798	-20.88
520	11°00.02'	78°1.87'	196	6.23	1.231	10.400	8.45	21.53	38905.42	15.35	0.297	-20.65
460	11°00.01'	78°35.16'	1245	4.72	0.309	3.215	10.37	21.53	7246.16	1.82	0.206	-20.77
469	11°00.06'	77°56.6'	145	6.02	0.911	7.480	8.21	20.62	30422.47	17.62	0.206	-20.77
458	11°00.12'	78°25.59'	698	5.01	0.713	6.550	9.18	21.06	17864.37	2.44	0.498	-20.94
M772-024-3	11°05.01'	78°00.91'	208	6.12	0.772	13.983	8.54	18.15	15084.07	9.78	0.629	-20.79
581	11°1.22'	78°81.17'	352	6.35	1.637	9.490	7.88	20.40	39468.01	5.72	0.669	-20.79
589	11°14.27'	78°14.66'	495	6.23	1.204	9.490	7.88	20.71	19007.28	6.93	0.641	-20.79
590	11°15.1'	78°16.42'	547	5.76	0.981	8.650	8.81	21.28	20091.58	1.25	0.825	-21.014
602	11°16.03'	78°18.38'	618	5.65	0.781	6.865	8.79	21.26	15722.46	4.52	0.371	-20.94
604	11°17.98'	78°22.40'	877	4.82	0.409	3.930	9.61	21.76	7562.60	1.99	0.149	-20.94
582	11°19.70'	78°4.865'	301.5	6.09	1.389	10.245	7.37	20.72	48217.98	9.64	0.149	-20.94
574	11°9.99'	78°55.30'	310	6.68	1.768	12.319	6.97	20.52	51422.06	9.87	0.139	-20.94
M772-005-5	12°05.66'	77°40.07'	214	6.67	1.201	8.850	7.69	18.64	23564.01	9.89	0.243	-20.99
620	12°18.64'	77°19.16'	152	7.23	1.149	8.850	7.69	19.41	40265.38	17.39	0.243	-20.99
608	12°32.52'	77°30.493'	583	5.02	0.363	3.270	9.016	21.94	1749.89	2.27	0.141	-20.73
623	12°38.178'	77°34.593'	1084	5.82	0.769	6.084	7.91	20.75	15111.55	4.94	1.010	-20.73
M772-002-5	15°04.75'	75°44.00'	290	9.41	0.928	6.240	6.72	18.11	19663.81	20.64	0.146	-20.57
420	15°11.36'	75°34.89'	516	7.36	0.814	6.740	8.28	17.97	17416.69	2.73	0.185	-20.57
398	17°28.05'	71°52.44'	496	8.61	0.250	2.370	9.47	19.34	5633.17	2.73	0.185	-20.57
407	17°34.37'	71°56.00'	788	8.31	0.358	3.515	9.82	20.31	5470.48	2.75	0.141	-20.99
409	17°38.36'	71°58.25'	920	8.19	0.292	2.760	9.46	20.43	4467.63	3.86	0.141	-20.99
411	17°47.16'	72°44.7'	2167	8.54	0.417	2.935	7.04	20.56	5294.52	5.61	0.141	-20.99
403	17°26.00'	71°51.41'	296	9.18	0.160	1.695	10.56	20.46	3153.46	2.22	0.141	-20.99
440	10°39.96'	78°30.05'	928	4.64	0.429	4.295	10.00	21.65	9556.85	1.70	0.141	-21.25
488	11°00.02'	78°23.18'	580	6.18	0.793	4.748	5.99	21.28	15723.09	2.93	0.141	-21.25
543	10°59.99'	77°47.4'	77	4.82	0.499	3.260	6.53	19.74	6058.91	12.88	0.141	-21.25
396	17°26.01'	71°51.40'	299	9.93	0.527	4.910	9.32	17.35	20496.59	6.06	0.141	-21.25

Table 3. Radiocarbon dates (^{14}C -AMS) used for the studied cores

Depth (cm)	Radiocarbon age (yrsBP)	Age range, cal. yrs BP (2σ)	Cal. Age (yrs BP) mean	Methods
M772-056				
2	0	0	0	N. Dutertrei
48	1085 ± 25 BP	416 - 616	516	N. Dutertrei
138	2575 ± 30 BP	1850 - 2153	2001	N. Dutertrei
138	5265 ± 30 BP	5298 - 5559	5428	<i>Non Soluble fraction</i>
138	3245 ± 25 BP	2712 - 2953	2832	<i>Humic acid</i>
198	3255 ± 25 BP	2717 - 2965	2841	N. Dutertrei
338	4960 ± 30 BP	4850 - 5225	5037	N. Dutertrei
338	7190 ± 35 BP	7386 - 7596	7491	<i>Non Soluble fraction</i>
338	5660 ± 30 BP	5688 - 5970	5829	<i>Humic acid</i>
398	5510 ± 40 BP	5563 - 5853	5708	N. Dutertrei
508	6620 ± 35 BP	6735 - 7088	6911	N. Dutertrei
508	9730 ± 40 BP	10233 - 10522	10377	<i>Non Soluble fraction</i>
508	9040 ± 40 BP	9385 - 9663	9524	<i>Humic acid</i>
598	7430 ± 35 BP	7574 - 7826	7700	N. Dutertrei
693	8220 ± 60 BP	8326 - 8678	8502	N. Dutertrei
693	10215 ± 35 BP	10754 - 11158	10956	<i>Non Soluble fraction</i>
693	9045 ± 40 BP	9390 - 9668	9529	<i>Humic acid</i>
768	8960 ± 45 BP	9271 - 9538	9404	N. Dutertrei
893	10085 ± 45 BP	10596 - 11060	10828	N. Dutertrei
893	12710 ± 50 BP	13783 - 14144	13963	<i>Non Soluble fraction</i>
893	10780 ± 70 BP	11369 - 12115	11742	<i>Humic acid</i>
998	11030 ± 50 BP	12052 - 12561	12306	N. Dutertrei
M772-059				
13	830 ± 25 BP	124 - 420	272	N. Dutertrei
148	3490 ± 30 BP	2957 - 3303	3130	N. Dutertrei
203	4325 ± 45 BP	3985 - 4385	4185	N. Dutertrei
303	5725 ± 50 / -45 BP	5732 - 6097	5914	N. Dutertrei
403	7815 ± 65 BP	7922 - 8273	8097	N. Dutertrei
658	10470 ± 50 BP	11128 - 11427	11277	N. Dutertrei
803	11855 ± 60 BP	12916 - 13309	13112	N. Dutertrei
803	12060 ± 130 BP	13081 - 13673	13377	N. Dutertrei
1033	13140 ± 70 BP	14200 - 15119	14659	N. Dutertrei
1343	15270 ± 150 BP	17251 - 18121	17686	N. Dutertrei
M772-029				
3	1185 ± 30 BP	971 - 1396	1183	<i>Non Soluble fraction</i>
3	1260 ± 25 BP	418 - 757	623	<i>Humic acid</i>
38	4480 ± 35 BP	4072 - 4685	4378	<i>Non Soluble fraction</i>
38	4250 ± 35 BP	3766 - 4358	4062	<i>Humic acid</i>
48	6500 ± 40 BP	6170 - 7046	6608	N. Dutertrei
48	7895 ± 40 BP	7329 - 8402	7865	<i>Non Soluble fraction</i>
48	7605 ± 30 BP	7016 - 8146	7581	<i>Humic acid</i>
113	10520 ± 40 / -35 BP	10268 - 11862	11065	<i>Non Soluble fraction</i>
113	10325 ± 40 BP	10003 - 11419	10711	<i>Humic acid</i>
203	11785 ± 45 BP	12014 - 13329	12671	<i>Non Soluble fraction</i>
203	11715 ± 45 BP	11904 - 13295	12599	<i>Humic acid</i>
333	13090 ± 45 BP	13457 - 15098	14277	<i>Non Soluble fraction</i>
333	12775 ± 50 BP	13127 - 14626	13876	<i>Humic acid</i>
423	13640 ± 50 BP	14054 - 16409	15231	<i>Non Soluble fraction</i>
423	13095 ± 55 BP	13457 - 15105	14281	<i>Humic acid</i>

Depth (cm)	Radiocarbon age (yrsBP)	Age range, cal. yrs BP (2 σ)	Cal. Age (yrs BP) mean	Methods
583	14340 + 60 / -55 BP	15197 - 16988	16092	Non Soluble fraction
583	13805 ± 60	14428 - 16604	15516	Humic acid
743	15520 ± 80	17078 - 18365	17722	Non Soluble fraction
743	14092 ± 60	14975 - 16862	15918	Humic acid
823	15925 ± 60 BP	17558 - 18787	18172	Non Soluble fraction
823	14245 ± 50 BP	15157 - 16907	16032	Humic acid
938	16040 ± 60 BP	17669 - 18854	18261	Non Soluble fraction
938	14515 ± 55 BP	15257 - 17230	16243	Humic acid
948	15780 ± 70 BP	17382 - 18653	18017	Non Soluble fraction
948	14770 ± 70 BP	16027 - 17770	16898	Humic acid
1103	17465 ± 60 BP	19227 - 20342	19784	Non Soluble fraction
1103	14750 ± 50 BP	15920 - 17713	16816	Humic acid
1113	19680 ± 100 BP	21558 - 23048	22303	Non Soluble fraction
1113	14990 ± 80 BP	16654 - 17923	17288	Humic acid
1263	20110 ± 90 BP	22252 - 23658	22955	Non Soluble fraction
1263	15335 ± 55 BP	16887 - 18089	17488	Humic acid
M772-003				
8	1240 ± 25 BP	445 - 772	608	Non Soluble fraction
8	1100 ± 25 BP	302 - 642	472	Humic acid
48	2465 ± 20 BP	1596 - 2097	1846	Non Soluble fraction
48	2135 ± 20 BP	1269 - 1692	1480	Humic acid
208	4015 ± 25 BP	3456 - 3992	3724	Non Soluble fraction
208	3945 ± 25 BP	3390 - 3896	3643	Humic acid
348	5085 ± 25 BP	4872 - 5419	5145	Non Soluble fraction
348	5100 ± 25 BP	4885 - 5435	5160	Humic acid
453	6260 ± 25 BP	5561 - 6783	6172	Non Soluble fraction
453	6155 ± 30 BP	5439 - 6663	6051	Humic acid
598	8620 ± 30 BP	8014 - 9313	8663	Non Soluble fraction
598	8465 ± 30 BP	7848 - 9142	8495	Humic acid
703	9570 ± 35 BP	9138 - 10485	9811	Non Soluble fraction
703	9505 ± 35 BP	9035 - 10405	9720	Humic acid
853	12120 ± 55 BP	12575 - 13666	13120	Non Soluble fraction
853	11590 ± 50 BP	11632 - 13186	12409	Humic acid
1008	15625 ± 60 BP	17183 - 18559	17871	Non Soluble fraction
1008	14965 ± 60 BP	16635 - 17903	17269	Humic acid
1018	15590 ± 70 BP	17155 - 18550	17852	Non Soluble fraction
1018	14650 ± 70 BP	15608 - 17572	16590	Humic acid
1028	16460 ± 90 BP	18442 - 19406	18924	Non Soluble fraction
1028	15070 ± 60 BP	16753 - 17947	17350	Humic acid
1038	38670 + 470 / -440 BP	41612 - 43134	42373	Non Soluble fraction
1038	34150 + 410 / -390 BP	36702 - 38933	37817	Humic acid
1063	41570 + 570 / -530 BP	43404 - 45401	44402	Non Soluble fraction
1063	38490 + 780 / -710 BP	41075 - 43421	42248	Humic acid
1103	43010 + 470 / -440 BP	44613 - 46241	45427	Non Soluble fraction
1103	39940 + 730 / -670 BP	42180 - 44415	43297	Humic acid
1303	46000 + 640 / -600 BP	46638 - 49886	48262	Non Soluble fraction
1303	41620 + 90 / -810 BP	43075 - 45736	44405	Humic acid
1453	46800 + 670 / -620 BP	47334 - 50000	48667	Non Soluble fraction
1453	39370 + 660 / -610 BP	41884 - 44009	42946	Humic acid

Table 4. Data of core M772-056-5

M772-056-5								
Depth (cm)	Age (yrs)	$\delta^{15}\text{N}$ (‰)	TN (%)	SST (°C)	Alkenone concentration (ng/g)	Corg (%)	C/N	SiO ₂ (wt%)
3	131.6	4.66	0.345	24.61	2824.91	3.210	9.32	2.10
8	174.3	4.27	0.350	24.58	3703.26			1.32
13	217.0	4.33	0.338	24.58	3663.23	3.220	9.51	3.00
18	259.7	4.46	0.338	24.61	3502.29			1.01
23	302.4	4.26	0.334	24.64	3095.71	3.150	9.44	1.45
28	345.2	4.47	0.332	24.70	3526.66			1.24
33	387.9	4.67	0.334	24.70	3208.48	3.060	9.16	1.25
38	430.6	4.25	0.318	24.58	3093.05			1.23
43	473.3	4.47	0.321	24.70	3288.67	3.000	9.35	3.22
48	516.0	4.44	0.311	24.76	2466.15			
53	598.5	4.61	0.309	24.64	3079.07	2.950	9.56	2.58
58	681.1	4.58	0.304	24.67	2913.15			
63	763.6	4.48	0.292	24.45	2901.21	2.810	9.62	1.98
68	846.1	4.59	0.301	24.42	2920.10			
73	928.6	4.45	0.302	24.39	3440.69	2.990	9.90	2.31
78	1011.2	4.63	0.315	24.48	2974.84			
83	1093.7	4.65	0.312	24.36	3184.75	3.060	9.80	2.00
88	1176.2	4.48	0.308	24.42	2789.72			
93	1258.8	4.58	0.304	24.76	2487.85	2.990	9.82	0.26
98	1341.3	4.77	0.317	24.45	2605.20			
103	1423.8	4.44	0.314	24.27	2964.50	3.010	9.59	0.76
108	1506.3	4.40	0.310	24.64	2353.59			
113	1588.9	4.52	0.312	24.42	2795.90	2.960	9.49	1.32
118	1671.4	4.56	0.296	24.52	2652.53			
123	1753.9	4.36	0.307	24.39	2899.87	2.970	9.68	2.39
128	1836.4	4.45	0.303	24.58	2475.52			
133	1919.0	4.41	0.308	24.33	2984.80	3.020	9.82	0.51
138	2001.5	4.30	0.310	24.06	3144.74			
143	2071.5	4.62	0.314	24.36	2796.73	2.930	9.33	2.44
148	2141.4	4.50	0.301	24.15	2698.79			
153	2211.4	4.83	0.300	24.12	2706.27	2.820	9.39	1.81
158	2281.3	4.12	0.291	24.15	2571.10			
163	2351.3	4.52	0.298	24.03	2581.15	2.970	9.97	1.75
168	2421.3	4.59	0.296	23.82	2657.76			
173	2491.2	4.20	0.282	23.76	2380.97	2.710	9.60	0.00
178	2561.2	4.34	0.281	23.88	2278.59			
183	2631.1	4.48	0.285	23.94	2259.71	2.740	9.63	4.39
188	2701.1	4.56	0.290	24.06	2105.26			
193	2771.0	4.21	0.279	24.12	2313.76	2.800	10.05	2.83
198	2841.0	4.52	0.296	24.18	1905.43			
203	2919.5	4.73	0.296	24.36	2084.30	2.800	9.45	3.64
208	2997.9	4.73	0.285	24.21	2059.45			
213	3076.3	4.38	0.278	24.18	2234.81	2.730	9.80	1.83
218	3154.8	4.41	0.285	24.24	2092.59			
223	3233.2	4.42	0.278	24.24	2049.15	2.710	9.76	3.48
228	3311.7	4.51	0.280	24.12	2107.57			
233	3390.1	4.77	0.278	24.30	1907.28	2.720	9.79	1.11
238	3468.6	4.88	0.293	24.24	2194.47			
243	3547.0	4.74	0.276	24.30	2154.80	2.660	9.63	2.40
248	3625.5	4.67	0.265	24.18	2019.01			
253	3703.9	4.43	0.272	23.79	2236.36	2.720	9.99	2.51
258	3782.4	4.66	0.273	23.91	2143.90			
263	3860.8	4.26	0.265	24.33	2003.43	2.620	9.89	2.57
268	3939.3	4.66	0.268	24.94	1763.95			
273	4017.7	4.93	0.275	24.73	2050.44	2.600	9.44	2.12

M772-056-5

Depth (cm)	Age (yrs)	$\delta^{15}\text{N}$ (‰)	TN (%)	SST (°C)	Alkenone concentration (ng/g)	Corg (%)	C/N	SiO ₂ (wt%)
278	4096.1	4.87	0.272	24.61	2337.68			
283	4174.6	4.51	0.270	24.64	2093.84	2.660	9.87	0.30
288	4253.0	4.96	0.282	24.45	2400.77			
293	4331.5	4.73	0.277	24.27	2625.16	2.740	9.91	1.41
298	4409.9	4.88	0.271	24.45	2444.83			
303	4488.4	4.75	0.255	24.55	2289.00	2.640	10.35	0.83
308	4566.8	4.66	0.262	24.45	2376.03			
313	4645.3	4.65	0.269	24.36	2713.28	2.770	10.30	0.00
318	4723.7	4.68	0.262	24.03	2770.00			
323	4802.2	4.74	0.273	24.03	3037.83	2.760	10.11	2.71
328	4880.6	4.79	0.271	24.06	2924.66			
333	4959.1	5.27	0.293	24.00	2598.39	2.840	9.70	2.52
338	5037.5	5.03	0.286	24.15	3090.88			
343	5093.4	4.90	0.280	24.30	2907.25	2.700	9.63	2.26
348	5149.3	5.02	0.269	24.30	2755.44			
353	5205.1	5.18	0.274	24.30	2896.58	2.700	9.86	2.31
358	5261.0	5.12	0.276	24.27	3204.95			
363	5316.9	4.78	0.268	24.45	2914.62	2.720	10.14	2.56
368	5372.8	4.82	0.271	24.45	3037.06			
373	5428.6	4.80	0.266	24.48	3001.09	2.680	10.08	2.60
378	5484.5	4.69	0.266	24.55	2844.96			
383	5540.4	4.80	0.265	24.52	2653.92	2.630	9.93	1.37
388	5596.3	5.37	0.268	24.55	2585.97			
393	5652.1	4.97	0.267	24.58	2794.01	2.670	10.01	2.68
398	5708.0	4.96	0.261	24.48	2889.25			
403	5762.7	4.97	0.264	24.45	2835.56	2.640	9.99	2.73
408	5817.4	4.74	0.256	24.45	2729.51			
413	5872.1	4.82	0.258	24.48	2595.49	2.630	10.21	1.36
418	5926.8	4.91	0.254	24.52	2866.21			
423	5981.5	4.94	0.257	24.52	2745.28	2.650	10.30	4.10
428	6036.2	4.83	0.252	24.55	2625.55			
433	6090.9	5.03	0.254	24.55	2623.43	2.580	10.16	2.81
438	6145.6	4.72	0.258	24.52	2095.86			
443	6200.3	4.95	0.267	24.55	2467.38	2.570	9.64	2.03
448	6255.1	5.18	0.266	24.61	2653.76			
453	6309.8	4.61	0.252	24.64	2637.62	2.630	10.42	2.75
458	6364.5	5.28	0.262	24.64	2872.56			
463	6419.2	4.77	0.251	24.52	3063.72	2.580	10.27	1.63
468	6473.9	4.92	0.257	24.64	2565.15			
473	6528.6	4.98	0.247	24.52	2812.41	2.590	10.50	2.10
478	6583.3	4.96	0.240	24.36	2202.91			
483	6638.0	4.96	0.249	24.55	2418.70	2.590	10.39	2.68
488	6692.7	5.05	0.254	24.42	2610.65			
493	6747.4	5.18	0.254	24.42	2637.91	2.570	10.11	1.81
498	6802.1	4.93	0.258	24.45	2528.41			
503	6856.8	5.11	0.261	24.52	2594.37	2.610	10.01	0.00
508	6911.5	4.72	0.255	24.42	2968.15			
513	6955.3	5.01	0.262	24.45	2705.75	2.690	10.27	2.39
518	6999.1	4.96	0.266	24.42	2896.62			
523	7042.9	4.55	0.254	24.30	2713.29	2.670	10.50	2.40
528	7086.7	5.05	0.267	24.30	2747.58			
533	7130.5	4.65	0.247	24.33	2620.13	2.620	10.61	2.07
538	7174.3	4.80	0.249	24.33	2597.39			
543	7218.1	4.96	0.244	24.24	2007.50	2.540	10.42	2.97
548	7261.9	5.11	0.236	24.30	2467.53			

M772-056-5

Depth (cm)	Age (yrs)	$\delta^{15}\text{N}$ (‰)	TN (%)	SST (°C)	Alkenone concentration (ng/g)	Corg (%)	C/N	SiO ₂ (wt%)
553	7305.8	5.27	0.243	24.27	2237.14	2.550	10.49	2.04
558	7349.6	4.77	0.242	24.30	2145.53			
563	7393.4	5.20	0.250	24.27	2412.82	2.600	10.39	2.75
568	7437.2	4.99	0.253	24.36	2350.56			
573	7481.0	5.09	0.251	24.30	2054.59	2.610	10.42	2.33
578	7524.8	4.84	0.239	24.24	2297.74			
583	7568.6	5.11	0.246	24.85	1771.87	2.610	10.62	2.10
588	7612.4	4.68	0.243	24.18	2687.73			
593	7656.2	5.04	0.245	24.03	2578.16	2.560	10.45	2.67
598	7700	5.13	0.242	23.88	2735.65			
603	7747.0	5.21	0.254	23.91	2862.14	2.590	10.21	1.96
608	7794.1	5.23	0.258	24.00	2803.73			
613	7841.1	4.74	0.250	24.12	2549.22	2.630	10.51	0.91
618	7888.1	4.97	0.249	24.12	2291.64			
623	7935.1	4.92	0.235	24.00	2310.54	2.500	10.65	2.25
628	7982.2	5.14	0.240	23.85	2458.78			
633	8029.2	4.99	0.234	23.97	2255.16	2.420	10.33	1.87
638	8076.2	5.01	0.235	23.85	2339.33			
643	8123.2	4.81	0.228	23.88	2333.37	2.360	10.36	1.67
648	8170.3	4.84	0.236	23.76	2410.95			
653	8217.3	5.20	0.234	23.79	2153.24	2.400	10.28	2.17
658	8264.3	5.25	0.235	23.76	2129.72			
663	8311.3	4.66	0.230	23.76	2091.31	2.370	10.30	2.19
668	8358.4	4.60	0.221	23.64	2030.30			
673	8405.4	4.88	0.228	23.61	2077.49	2.390	10.46	2.17
678	8452.4	4.93	0.228	23.67	1848.29			
683	8499.5	5.10	0.237	23.55	2180.43	2.410	10.17	1.33
688	8546.5	4.81	0.234	23.55	2072.13			
693	8593.5	5.31	0.230	23.70	1913.67	2.390	10.39	2.52
698	8647.6	5.30	0.225	23.88	1853.18			
703	8701.6	5.53	0.230	23.88	1939.99	2.390	10.40	1.85
708	8755.7	5.25	0.226	23.82	1799.00			
713	8809.8	5.71	0.246	23.94	1764.27	2.400	9.77	3.23
718	8863.8	5.35	0.222	23.70	1788.82			
723	8917.9	5.65	0.228	23.55	2003.74	2.410	10.57	1.70
728	8972.0	5.59	0.228	23.64	1553.47			
733	9026.0	5.70	0.221	23.61	1604.74	2.380	10.77	1.40
738	9080.1	5.59	0.221	23.45	1640.74			
743	9134.2	5.76	0.222	23.36	1628.44	2.400	10.83	0.96
748	9188.2	5.60	0.220	23.27	1698.27			
753	9242.3	5.51	0.218	23.64	1396.94	2.410	11.05	1.43
758	9296.4	5.73	0.224	23.45	1576.09			
763	9350.4	5.72	0.218	23.42	1425.17	2.370	10.90	0.72
768	9404.5	5.71	0.226	23.30	1515.43			
773	9461.4	5.74	0.225	23.33	1555.75	2.390	10.64	2.73
778	9518.4	5.59	0.219	23.39	1492.99			
783	9575.3	5.93	0.226	23.45	1412.51	2.440	10.80	2.72
788	9632.2	5.59	0.216	23.45	1516.32			
793	9689.2	5.82	0.219	23.52	1478.81	2.460	11.22	2.44
798	9746.1	5.75	0.232	23.42	1581.10			
803	9803.1	5.93	0.229	23.42	1675.51	2.420	10.57	1.67
808	9860.0	5.26	0.211	23.39	1544.36			
813	9917.0	5.64	0.219	23.48	1549.03	2.330	10.63	0.32
818	9973.9	5.84	0.225	23.30	1329.85			
823	10030.8	5.34	0.207	23.21	1378.39	2.230	10.76	2.93

M772-056-5

Depth (cm)	Age (yrs)	$\delta^{15}\text{N}$ (‰)	TN (%)	SST (°C)	Alkenone concentration (ng/g)	Corg (%)	C/N	SiO ₂ (wt%)
828	10087.8	5.04	0.203	23.30	1419.71			
833	10144.7	5.48	0.208	23.09	1335.50	2.260	10.88	0.83
838	10201.7	5.86	0.209	23.18	1076.08			
843	10258.6	5.73	0.207	23.36	869.46	2.130	10.27	2.00
848	10315.5	5.76	0.206	23.42	851.43			
853	10372.5	5.47	0.197	23.33	865.51	2.140	10.86	0.49
858	10429.4	5.48	0.199	23.45	976.76			
863	10486.4	5.66	0.205	23.58	882.37	2.190	10.70	2.55
868	10543.3	5.75	0.206	23.45	964.68			
873	10600.2	5.81	0.206	23.58	989.03	2.170	10.51	1.19
878	10657.2	5.79	0.208	23.73	885.12			
883	10714.1	5.90	0.205	23.61	1026.47	2.060	10.06	3.55
888	10771.1	5.39	0.190	23.67	897.85			
893	10828.0	5.98	0.202	23.79	839.21	2.030	10.03	2.19
898	10898.4	5.73	0.197	23.64	822.78			
903	10968.8	5.58	0.194	23.64	796.54	2.040	10.49	0.35
908	11039.2	5.52	0.196	23.52	844.50			
913	11109.6	5.59	0.192	23.42	864.96	2.040	10.60	0.82
918	11180.0	5.32	0.193	23.61	859.71			
923	11250.4	5.14	0.189	23.48	894.67	2.010	10.62	1.40
928	11320.8	5.50	0.190	23.39	709.22			
933	11391.2	5.51	0.185	23.24	890.96	1.940	10.47	0.55
938	11461.6	5.44	0.184	23.21	721.26			
943	11532.1	5.53	0.187	22.97	961.95	1.940	10.40	2.75
948	11602.5	5.37	0.179	22.97	937.61			
953	11672.9	5.61	0.186	22.85	952.88	1.940	10.42	0.15
958	11743.3	5.67	0.189	22.88	895.91			
963	11813.7	5.75	0.192	22.94	959.18	1.890	9.84	1.68
968	11884.1	5.42	0.181	22.76	1051.80			
973	11954.5	5.87	0.191	22.82	1066.45	1.880	9.84	0.84
978	12024.9	5.63	0.190	22.76	1019.54			
983	12095.3	5.37	0.180	22.76	1063.74	1.820	10.08	3.49
988	12165.7	5.52	0.177	22.73	996.03			
993	12236.1	5.66	0.189	22.76	1092.13	1.790	9.48	1.68
998	12306.5	5.69	0.191	22.61	1042.32			
1003	12368.2	5.88	0.196	22.61	1089.18	1.810	9.26	3.02
1008	12429.8	5.40	0.182	22.94	1225.12			
1013	12491.5	5.91	0.186	22.61	1138.79	1.820	9.79	1.52
1018	12553.1	5.83	0.181	22.55	1012.10			
1023	12614.8	5.91	0.187	22.45	1156.17	1.770	9.45	0.97
1028	12676.4	5.68	0.182	22.55	1053.07			
1033	12738.1	5.42	0.182	22.61	1077.51	1.820	10.03	1.73
1038	12799.8	5.75	0.185	22.55	993.77			
1043	12861.4	5.35	0.178	22.82	1175.44	1.790	10.08	2.32
1048	12923.1	5.51	0.179	22.82	1075.14			
1053	12984.7	5.59	0.175	22.64	996.89	1.810	10.36	1.94
1058	13046.4	5.66	0.180	22.73	923.27			

Table 5. Data of core M772-059-1

M772-059-1							
Depth (cm)	Age (yrs)	$\delta^{15}\text{N}$ (‰)	TN (%)	SST (°C)	Alkenone concentration (ng/g)	Corg (%)	C/N
3	62.77	3.65	0.367	23.06	3287.12	3.193	8.70
8	167.38	3.55	0.358	22.06	2411.50		
13	272.00	3.74	0.357	21.94	2009.02	3.083	8.65
18	377.85	4.21	0.359	22.39	1847.80		
23	483.70	3.98	0.348	22.03	1728.20		
28	589.56	4.12	0.347	21.94	1680.51	2.932	8.45
33	695.41	4.11	0.329	21.97	1587.48		
38	801.26	4.00	0.342	21.45	1407.32		
43	907.11	3.68	0.341	21.91	1506.67	2.906	8.53
48	1012.96	3.98	0.349	21.85	1457.67		
53	1118.81	4.21	0.384	22.00	2043.91		
58	1224.67	4.33	0.368	21.27	1541.39	3.250	8.82
63	1330.52	4.35	0.370	21.70	1831.01		
68	1436.37	4.43	0.380	21.55	1702.71		
73	1542.22	4.19	0.353	21.85	1622.52	3.118	8.83
78	1648.07	4.22	0.358	21.91	1737.52		
83	1753.93	4.21	0.356	22.09	1718.81		
88	1859.78	4.35	0.356	22.52	1570.29	3.121	8.78
93	1965.63	4.13	0.350	21.48	1535.94		
98	2071.48	4.26	0.359	21.58	1647.38		
103	2177.33	3.96	0.343	21.88	1672.83	2.995	8.72
108	2283.19	4.01	0.336	22.24	1697.39		
113	2389.04	4.09	0.346	22.48	1758.32		
118	2494.89	3.98	0.356	22.21	1818.55	2.995	8.42
123	2600.74	3.99	0.349	21.91	1869.97		
128	2706.59	3.69	0.341	21.73	1594.02		
133	2812.44	3.82	0.332	21.94	1587.46	2.793	8.41
138	2918.30	4.25	0.341	21.91	1708.68		
143	3024.15	3.88	0.354	21.91	1753.62		
148	3130.00	4.38	0.361	22.24	1829.58	3.170	8.78
153	3225.91	4.21	0.365	21.82	1983.89		
158	3321.82	4.24	0.367	21.97	1950.34		
163	3417.73	4.08	0.364	22.27	2057.44	3.125	8.58
168	3513.64	4.37	0.357	22.73	2001.97		
173	3609.55	4.15	0.362	22.64	1830.89		
178	3705.45	4.43	0.358	22.61	1591.76	2.924	8.16
183	3801.36	4.05	0.344	22.58	1570.55		
188	3897.27	4.17	0.356	22.48	1824.85		
193	3993.18	4.19	0.364	22.48	1765.63	3.069	8.43
198	4089.09	4.19	0.357	22.06	1586.42		
203	4185.00	4.47	0.350	22.21	1807.94		
208	4271.48	4.54	0.348	22.67	1735.18	2.978	8.56
213	4357.95	4.34	0.340	22.30	1600.26		
218	4444.43	4.17	0.341	22.30	1628.11		
223	4530.90	4.03	0.339	21.55	1607.32	2.895	8.54
228	4617.38	3.92	0.338	22.09	1832.14		
233	4703.85	4.16	0.341	21.61	1414.94		
238	4790.33	4.10	0.343	22.00	1372.65	2.971	8.66
243	4876.80	3.86	0.351	21.79	1528.24		

M772-059-1

Depth (cm)	Age (yrs)	$\delta^{15}\text{N}$ (‰)	TN (%)	SST (°C)	Alkenone concentration (ng/g)	Corg (%)	C/N
248	4963.28	3.87	0.362	22.03	1587.91		
253	5049.75	3.85	0.338	21.94	1598.88	2.976	8.80
258	5136.23	4.16	0.336	22.18	1776.73		
263	5222.70	4.62	0.340	22.58	1671.50		
268	5309.18	4.37	0.332	22.21	1734.81	2.957	8.90
273	5395.65	4.24	0.333	22.48	1494.40		
278	5482.13	4.34	0.338	22.27	1755.31		
283	5568.60	4.37	0.338	22.24	1089.43	2.962	8.77
288	5655.08	4.57	0.338	22.48	1201.47		
293	5741.55	4.55	0.325	22.73	1530.45		
298	5828.03	4.44	0.325	22.73	1523.61	2.849	8.78
303	5914.50	4.22	0.318	22.61	1358.35		
308	6023.65	4.66	0.334	22.82	1566.10		
313	6132.80	4.33	0.334	22.88	1222.93	2.907	8.70
318	6241.95	4.08	0.329	22.79	1804.74		
323	6351.10	4.53	0.336	22.58	1688.09		
328	6460.25	4.66	0.333	22.88	2287.55	2.842	8.53
333	6569.40	4.36	0.333	21.82	1552.57		
338	6678.55	4.79	0.346	21.70	1605.47		
343	6787.70	4.34	0.342	22.09	1857.88	2.860	8.37
348	6896.85	4.51	0.346	21.97	1850.91		
353	7006.00	4.59	0.338	21.61	1603.23		
358	7115.15	4.80	0.341	22.33	1812.04	2.769	8.11
363	7224.30	4.69	0.330	22.85	1712.58		
368	7333.45	4.64	0.330	22.39	2254.85		
373	7442.60	5.07	0.333	22.06	1944.18	2.831	8.51
378	7551.75	5.09	0.347	21.58	1880.14		
383	7660.90	4.60	0.349	21.73	2185.42		
388	7770.05	4.51	0.339	21.58	2098.33	2.921	8.61
393	7879.20	4.32	0.330	21.30	1986.42		
398	7988.35	4.64	0.328	21.33	2026.98		
403	8097.50	4.70	0.330	21.48	1957.31	2.735	8.28
408	8159.85	4.31	0.317	20.97	1766.04		
413	8222.21	4.98	0.315	21.55	1793.60		
418	8284.56	4.66	0.316	21.82	1697.22	2.735	8.66
423	8346.91	4.75	0.321	21.91	2029.77		
428	8409.26	4.64	0.312	21.24	1465.25		
433	8471.62	4.94	0.328	21.94	1830.50	2.775	8.46
438	8533.97	5.26	0.328	21.94	1675.79		
443	8596.32	4.85	0.307	21.91	1512.38		
448	8658.68	4.80	0.308	21.82	1412.60	2.800	9.08
453	8721.03	5.30	0.319	21.73	1400.80		
458	8783.38	4.81	0.308	21.88	1616.86		
463	8845.74	5.26	0.312	21.79	1402.26	2.728	8.75
468	8908.09	5.59	0.322	21.61	1632.33		
473	8970.44	5.33	0.312	21.91	1241.13		
478	9032.79	5.03	0.296	22.24	1276.60	2.745	9.27
483	9095.15	5.45	0.311	22.06	1447.76		
488	9157.50	4.63	0.286	21.91	1255.32		

M772-059-1

Depth (cm)	Age (yrs)	$\delta^{15}\text{N}$ (‰)	TN (%)	SST (°C)	Alkenone concentration (ng/g)	Corg (%)	C/N
493	9219.85	5.38	0.300	22.12	1232.59	2.592	8.63
498	9282.21	4.98	0.285	22.00	1120.05		
503	9344.56	5.44	0.308	21.67	1362.97		
508	9406.91	5.39	0.297	21.97	1378.02	2.579	8.68
513	9469.26	5.15	0.286	21.91	819.29		
518	9531.62	5.12	0.286	22.27	976.92		
523	9593.97	5.47	0.307	22.33	843.90	2.640	8.61
528	9656.32	5.01	0.280	22.33	985.60		
533	9718.68	5.24	0.285	22.39	554.04		
538	9781.03	5.02	0.292	22.67	953.11	2.552	8.73
543	9843.38	4.97	0.277	22.70	744.98		
548	9905.74	5.50	0.298	22.79	790.90		
553	9968.09	5.37	0.284	22.82	742.81	2.361	8.32
558	10030.44	4.96	0.286	22.70	1054.28		
563	10092.79	5.42	0.281	22.58	1064.90		
568	10155.15	5.30	0.283	22.58	985.97	2.390	8.45
573	10217.50	5.33	0.280	22.70	828.37		
578	10279.85	5.39	0.284	22.55	915.95		
583	10342.21	5.39	0.284	22.39	983.24	2.324	8.17
588	10404.56	5.22	0.267	22.52	799.20		
593	10466.91	5.44	0.279	22.55	1005.16		
598	10529.26	5.10	0.285	22.18	1132.01	2.341	8.21
603	10591.62	5.08	0.297	22.33	1327.21		
608	10653.97	5.37	0.277	22.45	950.48		
613	10716.32	5.16	0.263	22.58	1027.38	2.273	8.64
618	10778.68	5.09	0.268	22.58	1050.76		
623	10841.03	5.13	0.269	22.30	1002.98		
628	10903.38	5.19	0.256	21.97	940.26	2.198	8.58
633	10965.74	5.57	0.262	22.30	743.29		
638	11028.09	5.25	0.253	22.15	1009.36		
643	11090.44	5.48	0.260	22.00	869.11	2.195	8.45
648	11152.79	4.99	0.247	22.18	978.77		
653	11215.15	5.16	0.258	21.79	1160.49		
658	11277.50	5.23	0.252	22.06	1048.69	2.199	8.71
663	11345.34	5.71	0.267	21.73	961.51		
668	11413.17	5.19	0.255	21.61	987.52		
673	11481.01	5.32	0.263	21.70	1056.95	2.169	8.25
678	11548.84	5.03	0.248	22.00	1251.51		
683	11616.68	5.41	0.249	21.76	1256.97		
688	11684.52	4.72	0.244	21.85	1275.90	2.149	8.81
693	11752.35	5.21	0.251	21.42	1110.91		
698	11820.19	5.43	0.255	21.61	1090.56		
703	11888.03	5.45	0.261	21.61	1153.25	2.132	8.18
708	11955.86	5.20	0.254	21.45	1021.59		
713	12023.70	5.31	0.266	21.52	780.74		
718	12091.53	4.74	0.243	21.39	1272.65	2.083	8.56
723	12159.37	5.30	0.260	21.82	1488.92		
728	12227.21	4.86	0.248	21.42	1250.72		
733	12295.04	5.16	0.257	21.67	1328.45	2.073	8.07

M772-059-1

Depth (cm)	Age (yrs)	$\delta^{15}\text{N}$ (‰)	TN (%)	SST (°C)	Alkenone concentration (ng/g)	Corg (%)	C/N
738	12362.88	5.31	0.260	21.58	1334.85		
743	12430.72	4.92	0.227	21.27	1184.84		
748	12498.55	5.36	0.243	21.58	1409.59	2.018	8.29
753	12566.39	5.39	0.226	20.85	1321.18		
758	12634.22	5.20	0.225	19.73	1313.22		
763	12702.06	5.30	0.231	19.67	1169.64	1.931	8.38
768	12769.90	5.27	0.225	19.70	1061.48		
773	12837.73	5.55	0.223	20.21	995.71		
778	12905.57	5.49	0.225	20.27	1030.12	1.893	8.40
783	12973.41	5.65	0.226	20.52	1053.05		
788	13041.24	5.29	0.221	20.00	1008.50		
793	13109.08	5.69	0.227	19.79	981.16	1.820	8.02
798	13176.91	5.26	0.216	20.33	986.65		
803	13244.75	5.50	0.214	20.42	880.22		
808	13275.51	5.88	0.224	20.94	972.61	1.737	7.76
813	13306.26	5.76	0.217	21.09	697.34		
818	13337.02	5.39	0.213	20.39	756.02		
823	13367.77	5.75	0.223	20.27	688.39	1.761	7.91
828	13398.53	5.83	0.225	21.73	668.64		
833	13429.28	5.89	0.223	21.12	699.70		
838	13460.04	5.56	0.212	20.67	762.81	1.748	8.24
843	13490.79	5.71	0.213	20.45	691.14		
848	13521.55	5.61	0.223	20.85	748.11		
853	13552.30	5.69	0.216	20.85	768.62	1.769	8.18
858	13583.06	5.81	0.221	20.70	770.74		
863	13613.82	5.27	0.209	20.45	740.55		
868	13644.57	5.43	0.211	20.79	679.92	1.716	8.14
873	13675.33	6.22	0.221	21.58	721.96		
878	13706.08	5.84	0.218	21.55	887.39		
883	13736.84	5.87	0.218	21.76	759.83	1.712	7.86
888	13767.59	5.71	0.208	21.64	789.24		
893	13798.35	5.53	0.205	21.12	807.95		
898	13829.10	6.10	0.218	21.52	738.03	1.723	7.91
903	13859.86	6.36	0.199	21.64	828.21		
908	13890.61	5.43	0.188	21.42	932.56		
913	13921.37	6.03	0.202	21.48	959.39	1.752	8.68
918	13952.13	5.98	0.202	21.48	801.99		
923	13982.88	6.16	0.203	20.82	1021.48		
928	14013.64	5.69	0.189	21.09	816.51	1.705	9.04
933	14044.39	5.46	0.185	21.03	861.45		
938	14075.15	5.66	0.182	21.33	912.66		
943	14105.90	5.80	0.187	21.48	1116.58	1.660	8.85
948	14136.66	5.89	0.191	21.33	1003.08		
953	14167.41	5.51	0.185	21.21	777.01		
958	14198.17	6.06	0.197	20.79	906.07	1.722	8.74
963	14228.92	5.54	0.186	21.64	910.87		
968	14259.68	5.97	0.195	21.85	920.44		
973	14290.43	5.40	0.186	21.88	1022.45	1.675	9.00
978	14321.19	5.61	0.186	21.82	990.69		

M772-059-1

Depth (cm)	Age (yrs)	$\delta^{15}\text{N}$ (‰)	TN (%)	SST (°C)	Alkenone concentration (ng/g)	Corg (%)	C/N
983	14351.95	5.55	0.187	20.82	1051.36		
988	14382.70	5.38	0.183	21.52	1028.74	1.679	9.16
993	14413.46	5.74	0.194	21.64	1028.54		
998	14444.21	5.45	0.189	21.73	1076.59		
1003	14474.97	5.69	0.195	19.79	812.52	1.745	8.95
1008	14505.72	5.56	0.193	20.24	840.92		
1013	14536.48	5.17	0.177	20.03	829.47		
1018	14567.23	5.62	0.189	20.18	805.26	1.676	8.87
1023	14597.99	5.49	0.195	20.18	841.69		
1028	14628.74	5.18	0.190	20.33	794.18		
1033	14659.50	5.04	0.186	19.82	811.05	1.599	8.59
1038	14708.31	4.99	0.184	20.85	945.86		
1043	14757.13	5.59	0.203	19.39	901.57		
1048	14805.94	5.11	0.194	19.36	929.76	1.686	8.70
1053	14854.76	5.04	0.191	20.94	1069.18		
1058	14903.57	5.28	0.200	21.48	911.86		
1063	14952.39	4.90	0.193	19.21	1023.94	1.914	9.94
1068	15001.20	5.03	0.187	19.36	914.58		
1073	15050.02	5.10	0.188	19.33	992.38		
1078	15098.83	5.02	0.186	20.61	1396.74	1.664	8.93
1083	15147.65	5.15	0.193	20.24	1114.56		
1088	15196.46	5.11	0.189	20.76	1251.36		
1093	15245.27	4.93	0.182	20.52	1374.91	1.874	10.28
1098	15294.09	5.00	0.191	20.73	1088.20		
1103	15342.90	5.21	0.194	20.73	1396.33		
1108	15391.72	5.09	0.197	20.58	1371.21	1.948	9.88
1113	15440.53	4.90	0.193	20.52	1524.15		
1118	15489.35	4.99	0.195	20.21	1413.05		
1123	15538.16	4.97	0.193	20.97	1575.52	1.921	9.95
1128	15586.98	5.16	0.198	21.06	1294.39		
1133	15635.79	4.94	0.201	21.21	1222.70		
1138	15684.60	5.39	0.207	20.67	1462.42	1.905	9.21
1143	15733.42	4.85	0.191	21.15	1154.51		
1148	15782.23	4.91	0.203	21.30	1239.28		
1153	15831.05	5.32	0.221	21.00	1388.09	1.765	7.99
1158	15879.86	5.56	0.223	20.61	1504.84		
1163	15928.68	5.57	0.204	20.82	1424.23		
1168	15977.49	5.46	0.206	20.67	1416.29	1.911	9.29
1173	16026.31	5.14	0.196	20.73	1507.91		
1178	16075.12	4.94	0.191	21.00	1347.10		
1183	16123.94	5.37	0.196	21.33	1163.93	1.713	8.76
1188	16172.75	4.97	0.189	21.33	1413.63		
1193	16221.56	5.34	0.193	20.67	1478.20		
1198	16270.38	4.99	0.193	21.48	1418.30	1.707	8.82
1203	16319.19	5.12	0.194	21.15	1465.02		
1208	16368.01	5.05	0.191	20.85	1450.81		
1213	16416.82	4.62	0.185	20.70	1281.79	1.876	10.16
1218	16465.64	5.23	0.187	21.12	1193.55		
1223	16514.45	4.67	0.174	20.82	1093.11		

M772-059-1

Depth (cm)	Age (yrs)	$\delta^{15}\text{N}$ (‰)	TN (%)	SST (°C)	Alkenone concentration (ng/g)	Corg (%)	C/N
1228	16563.27	4.94	0.184	20.82	1274.08	1.574	8.54
1233	16612.08	4.94	0.187	20.48	833.11		
1238	16660.90	4.81	0.188	20.91	1372.12		
1243	16709.71	4.62	0.181	20.91	1292.53	1.743	9.65
1248	16758.52	4.99	0.193	20.82	1467.21		
1253	16807.34	4.81	0.185	20.82	1298.11		
1258	16856.15	4.52	0.180	20.67	1375.68	1.571	8.71
1263	16904.97	4.49	0.189	20.70	1457.55		
1268	16953.78	4.35	0.180	21.12	1332.98		
1273	17002.60	4.71	0.179	21.21	1215.51	1.778	9.92
1278	17051.41	4.42	0.178	20.76	1346.30		
1283	17100.23	4.41	0.175	21.30	1203.56		
1288	17149.04	4.65	0.162	20.79	980.10	1.676	10.32
1293	17197.85	4.53	0.178	21.06	1275.37		
1298	17246.67	4.32	0.173	20.70	1310.88		
1303	17295.48	4.34	0.175	20.94	1386.51	1.508	8.63
1308	17344.30	4.57	0.182	21.15	1323.49		
1313	17393.11	4.78	0.180	21.21	925.99		
1318	17441.93	4.36	0.179	21.58	1501.70	1.670	9.34
1323	17490.74	4.52	0.186	21.15	1561.87		
1328	17539.56	4.46	0.188	20.97	1461.51	1.648	8.78
1333	17588.37	4.43	0.185	21.06	1767.01	1.672	9.04
1338	17637.19	4.40	0.182	21.06	1981.19		
1343	17686.00	4.58	0.190	20.88	1713.56		
1348	17751.85	4.40	0.195	21.48	1453.70	2.071	10.65

Table 6. Data of core M772-029-3

M772-029-3

Depth (cm)	Age (yrs)	$\delta^{15}\text{N}$ (‰)	TN (%)	SST (°C)	Alkenone concentration (ng/g)	Corg (%)	C/N	SiO ₂ (wt%)
3	623.50	4.47	0.930	21.85	19329.27	8.600	9.22	3.23
8	1114.71	4.12	0.910	21.88	17804.11			
13	1605.93	4.11	0.800	21.85	17007.49	7.390	9.22	
18	2097.14	4.38	0.950	22.03	21214.13			
23	2588.36	4.09	0.860	22.18	19274.25	7.960	9.21	5.92
28	3079.57	4.03	0.830	22.61	14319.75			
33	3570.79	3.88	0.740	22.18	17440.57	7.140	9.68	
38	4062.00	4.39	0.210	21.97	2515.80			
43	5821.50	4.59	0.200	22.15	2941.46	2.010	10.02	1.96
48	7581.00	4.55	0.250	22.45	2892.61			
53	7821.77	4.91	0.370	22.33	5272.23	3.910	10.59	
58	8062.54	4.84	0.560	23.00	9780.76			
63	8303.31	4.70	0.370	22.97	6392.26	4.010	10.87	4.61
68	8544.08	4.80	0.440	22.70	6911.85			
73	8784.85	4.65	0.480	22.39	7082.85	5.220	10.76	
78	9025.62	4.72	0.500	22.70	6189.53			
83	9266.38	4.99	0.510	22.88	7050.00	5.350	10.54	4.30
88	9507.15	4.90	0.510	23.06	6087.86			
93	9747.92	5.11	0.680	23.06	6992.50	7.230	10.62	
98	9988.69	5.35	0.550	22.39	5495.97			
103	10229.46	5.25	0.620	22.52	6857.49	6.480	10.51	6.43
108	10470.23	6.24	0.580	22.03	7650.67			
113	10711.00	5.29	0.680	22.30	10083.52	7.690	11.27	
118	10815.92	5.09	0.620	21.45	8686.06			
123	10920.83	5.36	0.630	22.58	6144.57	7.010	11.11	8.28
128	11025.75	4.84	0.570	22.79	8411.10			
133	11130.67	5.45	0.490	21.94	8696.79	5.290	10.86	
138	11235.58	6.17	0.680	22.30	12142.20			
143	11340.50	5.98	0.700	22.03	11653.90	7.150	10.23	15.36
148	11445.42	5.48	0.670	21.85	12202.89			
153	11550.33	5.96	0.590	21.06	14764.91	6.180	10.39	
158	11655.25	6.11	0.680	21.33	11647.41			
163	11760.17	5.87	0.490	21.09	6693.27	5.120	10.44	12.74
168	11865.08	5.44	0.520	21.03	10579.46			
173	11970.00	5.73	0.520	21.06	9958.70	5.280	10.07	
178	12074.92	5.83	0.530	19.82	8877.31			
183	12179.83	5.51	0.360	19.85	6439.53	3.780	10.47	17.84
188	12284.75	5.98	0.440	20.15	7689.30			
193	12389.67	6.42	0.480	20.88	9741.34	4.900	10.29	
198	12494.58	6.45	0.550	21.12	9268.32			
203	12599.50	6.27	0.510	20.94	10418.32	5.270	10.28	26.32
208	12648.62	5.80	0.480	21.15	5480.48			
213	12697.73	5.71	0.390	20.52	6600.23	3.800	9.86	
218	12746.85	5.92	0.480	21.18	4628.73			
223	12795.96	6.71	0.400	20.70	7250.20	3.910	9.66	11.11
228	12845.08	6.41	0.410	20.85	7665.05			
233	12894.19	5.99	0.460	21.67	6760.58	4.770	10.42	
238	12943.31	6.04	0.550	21.52	10270.39			
243	12992.42	6.03	0.460	21.39	8021.85	4.760	10.27	16.93
248	13041.54	5.73	0.420	22.03	9932.96			
253	13090.65	6.27	0.530	21.58	10408.87	5.530	10.46	
258	13139.77	5.88	0.540	21.58	11510.13			
263	13188.88	7.16	0.400	21.88	8030.20	3.970	9.84	13.13
268	13238.00	6.58	0.470	21.97	11240.58			
273	13287.12	7.06	0.420	21.58	8706.17	4.240	10.13	

M772-029-3

Depth (cm)	Age (yrs)	$\delta^{15}\text{N}$ (‰)	TN (%)	SST (°C)	Alkenone concentration (ng/g)	Corg (%)	C/N	SiO ₂ (wt%)
278	13336.23	7.45	0.460	21.79	6265.18			
283	13385.35	7.53	0.430	22.09	7703.73	4.420	10.40	17.94
288	13434.46	6.51	0.510	22.30	8174.00			
293	13483.58	6.77	0.510	21.45	7202.80	5.140	10.18	
298	13532.69	6.35	0.430	21.58	10215.70			
303	13581.81	6.05	0.440	21.82	9263.21	4.220	9.63	15.43
308	13630.92	6.16	0.470	22.00	7318.09			
313	13680.04	6.41	0.450	22.00	11075.29	4.680	10.29	
318	13729.15	6.32	0.470	22.30	9386.52			
323	13778.27	7.65	0.520	21.97	12834.76	5.180	10.05	22.83
328	13827.38	6.95	0.430	22.48	11062.95			
333	13876.50	6.88	0.600	22.24	9525.09	6.130	10.25	
338	13898.97	7.63	0.560	21.79	10610.85			
343	13921.44	7.84	0.560	21.97	9377.61	5.400	9.70	19.99
348	13943.92	8.11	0.590	21.39	11688.31			
353	13966.39	7.10	0.440	21.76	6762.71	4.090	9.26	
358	13988.86	8.36	0.600	22.15	11121.67			
363	14011.33	8.55	0.490	22.06	8490.16	4.590	9.40	28.59
368	14033.81	8.90	0.500	22.21	8683.98			
373	14056.28	8.30	0.540	22.12	11760.08	5.120	9.57	
378	14078.75	7.77	0.550	22.48	6769.57			
383	14101.22	9.37	0.420	21.94	7285.04	4.000	9.55	30.36
388	14123.69	8.79	0.460	22.70	6716.42			
393	14146.17	8.17	0.520	22.24	6509.30	5.040	9.71	
398	14168.64	7.66	0.550	22.88	5081.65			15.92
403	14191.11	8.69	0.470	21.88	8293.98	4.460	9.48	
408	14213.58	9.20	0.400	22.06	4616.23			
413	14236.06	6.91	0.440	22.45	4370.56			
418	14258.53	8.10	0.520	22.42	5653.94			19.04
423	14281.00	8.34	0.350	21.97	5144.60	3.220	9.33	
428	14319.61	8.16	0.420	22.00	5628.40			
433	14358.22	6.62	0.430	22.61	5316.20			
438	14396.83	8.60	0.320	22.06	2808.45			32.12
443	14435.44	7.82	0.410	22.45	5190.37	3.690	8.90	
448	14474.05	5.97	0.360	21.00	3969.32			
453	14512.66	7.36	0.390	21.91	5693.52			
458	14551.27	5.95	0.360	20.76	5342.30			
463	14589.88	7.01	0.370	20.24	4296.58	3.410	9.13	26.59
468	14628.48	7.26	0.350	20.03	5150.81			
473	14667.09	6.71	0.350	21.33	5801.29			
478	14705.70	6.90	0.330	20.82	5774.29			
483	14744.31	7.07	0.350	20.48	6520.05	3.100	8.78	21.23
488	14782.92	7.65	0.290	20.18	4087.71			
493	14821.53	7.36	0.390	21.15	7726.91			
498	14860.14	6.48	0.320	20.39	7822.87			
503	14898.75	6.90	0.350	19.85	9111.36	3.150	8.97	20.44
508	14937.36	6.96	0.340	20.97	5684.21			
513	14975.97	8.27	0.350	20.79	2876.56			
518	15014.58	8.02	0.320	20.67	3294.08			
523	15053.19	7.61	0.340	20.55	5680.65			22.69
528	15091.80	8.65	0.350	20.39	3386.08			
533	15130.41	8.50	0.370	21.48	6971.60			
538	15169.02	6.48	0.340	19.76	5015.63			
543	15207.63	6.30	0.300	20.64	3807.63	2.610	8.68	23.79

M772-029-3

Depth (cm)	Age (yrs)	$\delta^{15}\text{N}$ (‰)	TN (%)	SST (°C)	Alkenone concentration (ng/g)	Corg (%)	C/N	SiO ₂ (wt%)
548	15246.23	7.28	0.280	20.91	4290.27			
553	15284.84	6.78	0.310	21.33	3667.90			
558	15323.45	6.98	0.400	20.42	4659.92			
563	15362.06	7.31	0.400	20.73	4754.80			28.51
568	15400.67	8.48	0.350	21.12	3833.61			
573	15439.28	7.19	0.360	21.33	3825.87			
578	15477.89	6.64	0.350	19.30	4398.49			
583	15516.50	8.39	0.390	21.12	6675.72	2.930	7.42	46.30
588	15529.06	7.14	0.340	20.61	9456.35			
593	15541.63	7.33	0.380	20.18	7285.19			
598	15554.19	7.28	0.360	20.48	6835.19			
603	15566.75	7.21	0.350	20.33	6337.12			39.05
608	15579.31	7.46	0.370	19.88	8257.13			
613	15591.88	7.53	0.370	20.76	8695.00			
618	15604.44	8.32	0.350	21.24	8237.66			
623	15617.00	6.86	0.360	20.76	7196.48	3.010	8.36	27.03
628	15629.56	8.07	0.390	20.73	7446.18			
633	15642.13	7.47	0.340	19.94	3937.94			
638	15654.69	6.74	0.380	19.06	12447.04			
643	15667.25	6.56	0.390	20.06	6708.99			36.24
648	15679.81	7.34	0.390	20.24	8394.05			
653	15692.38	8.48	0.360	20.45	5869.57			
658	15704.94	7.24	0.390	20.30	7553.13			
663	15717.50	6.91	0.360	18.64	6610.91	2.980	8.24	32.37
668	15730.06	7.53	0.380	19.61	6428.69			
673	15742.63	6.54	0.410	20.18	7252.74			
678	15755.19	7.96	0.390	19.42	6467.44			
683	15767.75	7.21	0.350	19.61	5451.82			33.14
688	15780.31	7.68	0.340	18.97	4818.27			
693	15792.88	7.13	0.340	20.91	4726.64			
698	15805.44	7.64	0.340	19.15	5798.17			
703	15818.00	7.44	0.360	19.39	4108.21	2.890	8.10	27.35
708	15830.56	7.42	0.360	21.27	2500.76			
713	15843.13	6.88	0.340	20.52	4317.85			
718	15855.69	7.90	0.350	20.88	4325.46			
723	15868.25	7.74	0.360	20.61	4831.12			37.09
728	15880.81	7.32	0.360	20.30	2944.63			
733	15893.38	8.46	0.330	20.79	5577.54			
738	15905.94	7.87	0.310	20.45	5486.70			
743	15918.50	7.35	0.330	20.36	4848.13	2.850	8.57	20.61
748	15925.59	8.21	0.350	19.94	6148.23			
753	15932.69	7.53	0.330	20.36	3176.18			
758	15939.78	7.52	0.340	20.73	3285.69			
763	15946.88	7.48	0.320	20.15	2962.40			27.29
768	15953.97	8.48	0.300	20.21	2587.14			
773	15961.06	8.23	0.320	21.15	5470.45			
778	15968.16	8.41	0.310	21.79	1946.44			
783	15975.25	8.80	0.310	20.97	1736.40	2.470	7.97	39.29
788	15982.34	7.38	0.330	22.03	3216.01			
793	15989.44	8.08	0.310	20.64	2709.57			
798	15996.53	7.83	0.310	21.67	3038.05			
803	16003.63	7.64	0.290	20.09	1733.00			27.25
808	16010.72	7.49	0.300	21.09	1218.80			
813	16017.81	9.16	0.310	20.52	1224.43			
818	16024.91	8.76	0.340	20.15	3635.29			

M772-029-3

Depth (cm)	Age (yrs)	$\delta^{15}\text{N}$ (‰)	TN (%)	SST (°C)	Alkenone concentration (ng/g)	Corg (%)	C/N	SiO ₂ (wt%)
823	16032.00	7.73	0.310	20.45	3500.59	2.730	8.74	29.74
828	16054.46	7.11	0.300	19.82	4009.10			
833	16076.92	7.46	0.300	21.00	4701.99			
838	16099.38	7.83	0.350	22.24	3399.17			
843	16121.83	7.76	0.320	19.94	5798.74			31.38
848	16144.29	8.11	0.310	19.21	5065.60			
853	16166.75	7.71	0.300	18.91	3914.78			
858	16189.21	7.41	0.290	20.42	3868.47			
863	16211.67	7.23	0.280	20.76	2169.89	2.230	8.09	14.51
868	16234.13	7.34	0.330	20.45	2970.93			
873	16256.58	7.28	0.330					
878	16279.04	9.93	0.340	20.61	3418.13			
883	16301.50	8.63	0.350	20.94	3044.16			21.45
888	16323.96	8.71	0.350	20.33	2215.20			
893	16346.42	8.32	0.350	20.06	1707.38			
898	16368.88	6.96	0.330	19.58	2137.94			
903	16391.33	6.92	0.300	19.67	2609.15	2.290	7.53	26.73
908	16413.79	7.54	0.340	20.45	2634.28			
913	16436.25	7.12	0.310	20.52	3325.10			
918	16458.71	6.39	0.290	18.97	1739.39			
923	16481.17	8.09	0.320	19.30	4105.08			28.03
928	16503.63	8.69	0.330	19.67	3079.78			
933	16526.08	8.07	0.300	19.76	3446.25			
938	16548.54	8.10	0.330	19.82	3373.12			
943	16571.00	10.39	0.270	19.30	1503.73	1.940	7.32	42.55
948	16585.59	7.60	0.330	19.79	2283.07			
953	16600.18	8.23	0.340	19.52	1965.17			
958	16614.77	7.69	0.280	18.91	1695.31			
963	16629.36	6.59	0.290	19.33	1712.90			21.23
968	16643.95	7.33	0.350	19.73	1878.24			
973	16658.55	7.77	0.340	19.36	2489.07			
978	16673.14	7.31	0.290	18.61	1809.42			
983	16687.73	7.36	0.310	19.73	1973.42	2.300	7.50	21.81
988	16702.32	6.37	0.250	20.30	1347.75			
993	16716.91	6.32	0.230	20.27	1554.40			
998	16731.50	6.67	0.250	18.48	919.93			
1003	16746.09	6.98	0.240	19.79	1227.27			15.15
1008	16760.68	7.23	0.280	18.76	1905.81			
1013	16775.27	8.06	0.290	19.18	1555.56			
1018	16789.86	7.33	0.290	20.21	2296.33			
1023	16804.45	8.25	0.310	19.79	1950.90	2.400	7.71	34.20
1028	16819.05	7.39	0.280	19.12	1180.16			
1033	16833.64	7.47	0.280	20.06	1681.62			
1038	16848.23	6.80	0.280	20.39	1625.90			
1043	16862.82	6.44	0.250	19.64	1034.41			24.05
1048	16877.41	6.68	0.250	20.27	1653.96			
1053	16892.00	6.50	0.280	20.42	1713.45			
1058	16906.59	6.47	0.240	19.33	1551.99			
1063	16921.18	7.66	0.380	19.88	2689.80	2.150	5.66	17.68
1068	16935.77	6.76	0.240	18.18	1871.90			
1073	16950.36	6.68	0.240	18.82	1647.63			
1078	16964.95	6.27	0.260	19.52	1870.75			
1083	16979.55	6.51	0.260	19.24	2616.13			15.61
1088	16994.14	7.25	0.260	18.39	2002.72			
1093	17008.73	6.95	0.260	17.27	1275.52			

M772-029-3

Depth (cm)	Age (yrs)	$\delta^{15}\text{N}$ (‰)	TN (%)	SST (°C)	Alkenone concentration (ng/g)	Corg (%)	C/N	SiO ₂ (wt%)
1098	17023.32	8.38	0.280	18.45	2751.83			
1103	17037.91	7.11	0.330	19.39	2825.38	2.570	7.88	22.51
1108	17052.50	6.71	0.280	19.52	2087.96			
1113	17066.55	6.52	0.280	18.70	1006.76			
1118	17080.60	6.44	0.250	16.18	871.50			
1123	17094.65	5.87	0.250	18.06	1008.34			16.66
1128	17108.69	5.98	0.230	19.52	1378.18			
1133	17122.74	7.23	0.250	18.91	1206.35			
1138	17136.79	6.78	0.230	18.73	1421.03			
1143	17150.84	6.31	0.230	18.85	1330.93	1.880	8.08	14.94
1148	17164.89	6.61	0.230	17.33	1410.44			
1153	17178.94	6.80	0.250	18.09	2080.43			
1158	17192.98	8.00	0.270	18.91	2290.21			
1163	17207.03	7.36	0.270	18.70	2526.89			27.31
1168	17221.08	6.97	0.270	19.82	1606.43			
1173	17235.13	6.69	0.260	19.88	1390.54			
1178	17249.18	6.61	0.260	18.85	1793.29			
1183	17263.23	7.20	0.260	18.52	2092.80	1.990	7.70	24.96
1188	17277.27	6.77	0.260	18.91	2424.80			
1193	17291.32	6.88	0.280	19.61	1713.08			
1198	17305.37	6.23	0.270	19.94	2014.14			
1203	17319.42	6.18	0.250	19.58	858.50			16.95
1208	17333.47	6.21	0.220	19.85	881.07			
1213	17347.52	5.73	0.220	18.15	774.38			
1218	17361.56	5.99	0.220	17.36	653.15			
1223	17375.61	7.39	0.250	17.36	1100.33	1.770	6.96	21.86
1228	17389.66	5.92	0.270	16.03	795.37			
1233	17403.71	6.82	0.260	19.45	1353.87			
1238	17417.76	5.82	0.240	17.97	968.50			
1243	17431.81	6.00	0.220	17.39	982.52			15.70
1248	17445.85	6.28	0.250	18.27	1524.75			
1253	17459.90	6.37	0.250	19.67	1461.03			
1258	17473.95	6.00	0.250	18.12	2286.78			
1263	17488.00	6.57	0.270	17.70	1146.25	1.950	7.29	21.55
1268	17557.23	6.28	0.260	17.36	620.53			
1273	17626.46	6.16	0.260	17.45	724.83			
1278	17695.70	5.84	0.230	17.12	552.76			
1283	17764.93	6.36	0.220	16.48	400.93			18.14
1288	17834.16	7.40	0.194	18.85	641.90			
1293	17903.39	6.78	0.197	17.58	717.78			
1298	17972.62	6.59	0.213	17.97	666.83			
1303	18041.86	7.41	0.240	18.21	1412.61			25.30
1308	18111.09	7.33	0.263	15.58	515.83			
1313	18180.32	6.85	0.219	19.82	2071.97			
1318	18249.55	7.36	0.249	18.48	2573.91			
1323	18318.78	8.73	0.206	17.58	584.98			20.76
1328	18388.02	6.87	0.232	17.94	441.78			
1333	18457.25	8.24	0.232	18.48	1464.43			
1338	18526.48	8.75	0.238	19.24	1192.09			
1343	18595.71	8.26	0.246	18.70	1136.02			25.82
1348	18664.94	12.32	0.210	18.61	1525.32			
1353	18734.18	7.89	0.258	18.67	1568.56			

Table 7. Data of core M772-003-2

M772-003-2

Depth (cm)	Age (yrs)	$\delta^{15}\text{N}$ (‰)	TN (%)	SST (°C)	Alkenone concentration (ng/g)	Corg (%)	C/N	SiO ₂ (wt%)
3	177.00	5.46	0.601	20.27	10091.70	5.555	0.27	26.11
8	472.00	5.92	0.740	20.97	10504.21			
13	598.06	6.58	0.463	20.15	7476.84	4.110	0.20	
18	724.13	6.51	0.476	21.36	5214.27			
23	850.19	5.89	0.590	21.06	11920.44	5.510	0.26	27.05
28	976.25	5.98	0.548	21.82	9807.37			
33	1102.31	7.23	0.477	21.27	6345.56	4.410	0.21	
38	1228.38	6.93	0.568	22.15	8302.53			
43	1354.44	6.14	0.605	21.97	8462.04	5.430	0.25	24.07
48	1480.50	5.92	0.567	21.94	6786.19			
53	1548.08	7.28	0.573	21.48	5864.65	5.330	0.25	
58	1615.66	7.20	0.387	21.73	2367.76			
63	1683.23	6.09	0.728	22.06	8042.29	6.640	0.30	30.87
68	1750.81	6.23	0.602	21.52	9499.05			
73	1818.39	6.37	0.720	21.91	9857.60	6.700	0.31	
78	1885.97	7.23	0.614	21.94	9931.91			
88	2021.13	4.89	0.652	20.00	3979.56			21.03
93	2088.70	5.02	0.587	20.58	7991.87	5.650	0.27	
98	2156.28	5.55	0.692	21.09	8167.54	6.580	0.31	
103	2223.86	5.14	0.670	20.48	11008.02	6.360	0.31	
108	2291.44	6.65	0.567	20.91	6290.01			45.66
113	2359.02	4.68	0.526	21.03	7570.51	4.850	0.23	
118	2426.59	4.51	0.563	20.76	8133.43			
123	2494.17	5.33	0.736	21.52	9312.80	6.750	0.31	
128	2561.75	4.70	0.620	21.91	9651.30			18.62
133	2629.33	4.91	0.632	21.82	10380.92	5.870	0.27	
138	2696.91	4.66	0.649	22.09	10815.32	6.560	0.30	
143	2764.48	5.75	0.696	22.06	11890.90	6.150	0.28	
148	2832.06	5.89	0.628	22.06	11082.50			33.43
168	3102.38	5.10	0.684	22.18	10710.50	6.300	0.28	
173	3169.95	7.23	0.574	22.21	6926.33	5.300	0.24	
178	3237.53	6.55	0.548	22.45	10436.48			
183	3305.11	5.00	0.670	21.36	9102.26	6.350	0.30	24.52
188	3372.69	6.30	0.546	21.42	7419.94			
193	3440.27	5.67	0.686	21.64	8790.56	6.510	0.30	
198	3507.84	4.96	0.669	21.67	9372.24			
203	3575.42	6.14	0.670	21.36	9703.93	6.575	0.31	39.31
208	3643.00	6.62	0.606	21.15	9630.88			
213	3697.18	6.95	0.655	20.88	9239.70	6.510	0.31	
218	3751.36	5.26	0.589	21.06	8847.08			
223	3805.54	5.67	0.657	21.06	11453.80	6.230	0.30	21.69
228	3859.71	4.88	0.582	21.09	6920.24			
233	3913.89	4.82	0.614	21.03	6759.85	6.000	0.29	
238	3968.07	5.53	0.602	20.79	8757.56			
243	4022.25	5.63	0.602	19.76	7244.21	5.980	0.30	30.87
248	4076.43	6.04	0.580	19.82	6122.37			
253	4130.61	6.19	0.600	20.70	6766.87	6.110	0.30	
258	4184.79	5.16	0.675	20.03	7727.52			
263	4238.96	5.83	0.543	20.09	6212.09	5.020	0.25	31.80
268	4293.14	8.51	0.407	19.21	2764.48			
273	4347.32	6.20	0.591	20.39	7205.73	5.820	0.29	
278	4401.50	5.02	0.627	19.76	5076.54			
283	4455.68	6.27	0.585	19.97	6071.03	5.700	0.29	43.02
288	4509.86	5.27	0.782	20.15	9411.48			

M772-003-2

Depth (cm)	Age (yrs)	$\delta^{15}\text{N}$ (‰)	TN (%)	SST (°C)	Alkenone concentration (ng/g)	Corg (%)	C/N	SiO ₂ (wt%)
293	4564.04	5.61	0.514	19.52	4509.66			
298	4618.21	7.13	0.388	19.61	2442.16	5.050	0.26	
303	4672.39	4.81	0.536	19.45	4401.34			
308	4726.57	7.42	0.340	18.97	1917.22	5.300	0.27	33.95
313	4780.75	6.43	0.349	19.88	2499.74			
318	4834.93	5.51	0.689	19.03	8786.78	3.180	0.16	
323	4889.11	6.13	0.596	19.91	8712.48			
328	4943.29	5.51	0.763	21.15	9483.41	5.800	0.29	33.54
333	4997.46	5.49	0.657	20.48	8316.79			
338	5051.64	5.96	0.670	20.94	8156.17	6.520	0.32	
343	5105.82	5.95	0.705	20.70	9181.53			
348	5160.00	6.43	0.464	20.61	3626.34	6.910	0.33	30.38
353	5202.43	8.35	0.306	19.85	1322.23			
358	5244.86	5.50	0.541	20.55	5409.56	2.900	0.15	
363	5287.29	3.68	0.547	20.76	5217.04			
368	5329.71	3.89	0.468	19.85	6053.71	5.340	0.26	17.72
373	5372.14	4.87	0.662	20.82	9360.23			
378	5414.57	4.59	0.580	20.18	6627.38	6.460	0.31	
383	5457.00	3.97	0.527	19.79	6185.17			
388	5499.43	4.82	0.663	20.33	9364.53	5.180	0.26	25.09
393	5541.86	4.55	0.588	20.15	7140.50			
398	5584.29	5.23	0.439	20.70	4187.72	5.780	0.29	
403	5626.71	4.11	0.571	18.85	7758.74			
408	5669.14	5.02	0.566	20.03	7217.94	5.675	0.30	18.89
413	5711.57	5.21	0.594	20.03	6893.99			
418	5754.00	5.04	0.555	20.15	6784.76	6.020	0.30	
423	5796.43	5.19	0.592	20.61	7979.44			
428	5838.86	5.42	0.589	20.91	4544.98	6.060	0.29	29.72
433	5881.29	4.82	0.534	20.21	5416.12			
438	5923.71	4.88	0.628	20.97	6110.20	5.470	0.27	
443	5966.14	5.06	0.607	20.09	5724.92			
448	6008.57	5.36	0.627	20.48	6836.50	6.330	0.32	26.87
453	6051.00	4.55	0.583	20.79	6476.03			
458	6135.28	4.84	0.537	20.55	4161.31	6.025	0.29	
463	6219.55	4.53	0.563	20.91	6718.73			
468	6303.83	5.24	0.580	20.85	7924.53	5.780	0.28	28.23
473	6388.10	5.06	0.571	20.18	8897.38			
478	6472.38	6.20	0.490	20.33	4493.12	5.650	0.28	
483	6556.66	4.62	0.532	20.67	5607.59			
493	6725.21	4.05	0.513	20.52	7441.63	5.340	0.26	30.32
498	6809.48	4.59	0.499	20.88	6304.42	5.120	0.25	
503	6893.76	5.24	0.478	20.24	6370.10			
508	6978.03	5.15	0.484	18.61	4879.14	4.905	0.24	28.66
513	7062.31	5.16	0.443	19.55	5206.48			
518	7146.59	4.55	0.496	20.61	5014.07	4.260	0.22	
523	7230.86	4.40	0.448	20.15	4866.47			
528	7315.14	5.45	0.587	20.70	6692.80	4.430	0.22	20.68
533	7399.41	4.55	0.544	20.67	6050.51			
538	7483.69	5.96	0.589	21.33	5052.39	5.480	0.27	
543	7567.97	5.18	0.478	19.76	6229.96			
548	7652.24	6.06	0.414	19.82	5763.63	4.690	0.24	31.45
553	7736.52	7.11	0.325	19.18	2128.19			
558	7820.79	6.55	0.572	19.55	3795.52	3.095	0.16	
563	7905.07	6.52	0.429	19.88	3416.31			
568	7989.34	4.30	0.426	20.21	2833.92	4.290	0.22	36.68

M772-003-2

Depth (cm)	Age (yrs)	$\delta^{15}\text{N}$ (‰)	TN (%)	SST (°C)	Alkenone concentration (ng/g)	Corg (%)	C/N	SiO ₂ (wt%)
573	8073.62	4.88	0.419	20.82	4694.26			
578	8157.90	5.08	0.462	20.39	4812.75	4.070	0.20	
583	8242.17	5.04	0.478	20.27	3548.82			24.39
588	8326.45	5.06	0.470	21.18	5868.12	4.820	0.24	
593	8410.72	4.91	0.378	21.18	4979.75			
598	8495.00	5.86	0.503	21.55	3872.53	3.640	0.17	
603	8553.33	5.79	0.439	21.15	5923.02			29.18
608	8611.67	5.65	0.496	21.21	7509.51	4.355	0.21	
613	8670.00	6.03	0.514	21.00	6884.10			
618	8728.33	6.07	0.453	21.39	5502.17	5.160	0.25	
623	8786.67	6.49	0.506	21.33	6505.55			24.52
628	8845.00	5.81	0.455	22.00	6568.12	5.040	0.24	
633	8903.33	5.93	0.517	22.39	6638.02			
638	8961.67	6.02	0.519	22.30	5924.81	5.070	0.23	
643	9020.00	6.78	0.495	22.30	5413.94			27.76
648	9078.33	6.30	0.505	22.15	6442.15	4.770	0.21	
653	9136.67	6.91	0.413	22.06	5858.40			
658	9195.00	7.75	0.364	22.39	4189.51	4.150	0.19	
663	9253.33	6.16	0.405	22.06	4903.15			22.29
668	9311.67	6.49	0.534	22.27	5940.03	3.950	0.18	
673	9370.00	6.90	0.410	22.36	5235.58			
678	9428.33	6.75	0.450	21.94	6280.89	3.990	0.18	
683	9486.67	7.14	0.418	22.24	4409.95			34.76
688	9545.00	5.87	0.427	22.09	5349.66	3.960	0.18	
693	9603.33	7.90	0.373	22.18	2551.59			
698	9661.67	6.46	0.480	22.39	4492.23	3.570	0.16	
703	9720.00	6.66	0.520	21.82	6702.76			19.91
708	9809.63	6.53	0.460	22.42	4655.36	5.185	0.24	
713	9899.27	8.73	0.417	22.18	4116.18			
718	9988.90	7.01	0.540	22.55	4800.08	3.990	0.18	
723	10078.53	7.02	0.500	22.18	5149.09			17.39
728	10168.17	6.65	0.520	22.09	5467.44	4.800	0.22	
733	10257.80	6.97	0.436	22.09	4970.38			
738	10347.43	6.72	0.490	22.21	5629.16	4.330	0.20	
743	10437.07	7.95	0.572	21.55	5815.95			20.85
748	10526.70	8.33	0.465	22.58	5538.15	3.890	0.18	
753	10616.33	7.26	0.469	22.24	6401.59			
758	10705.97	6.55	0.333	22.09	5451.53	4.875	0.22	
763	10795.60	7.36	0.401	21.61	4623.23			13.52
768	10885.23	6.66	0.334	21.76	4720.88	4.080	0.19	
773	10974.87	6.35	0.313	21.76	3899.92			
778	11064.50	6.74	0.345	21.64	5082.17	3.180	0.15	
783	11154.13	6.52	0.322	21.58	4532.60			9.55
788	11243.77	7.78	0.375	21.82	6393.50	3.110	0.14	
793	11333.40	7.24	0.380	20.76	5824.14			
798	11423.03	7.17	0.400	20.79	4105.73	3.790	0.18	
803	11512.67	7.86	0.488	20.88	6600.94			15.89
808	11602.30	7.55	0.420	19.70	6345.70	5.105	0.24	
813	11691.93	8.26	0.453	19.64	7236.17			
818	11781.57	7.82	0.480	18.73	5917.10	4.440	0.23	
823	11871.20	7.82	0.549	20.18	8397.74			23.58
828	11960.83	7.87	0.400	20.09	8389.42	5.570	0.28	
833	12050.47	7.81	0.344	18.27	6078.85			
838	12140.10	7.72	0.370	19.70	5117.78	3.550	0.19	
843	12229.73	8.05	0.350	20.12	4313.67			21.44

M772-003-2

Depth (cm)	Age (yrs)	$\delta^{15}\text{N}$ (‰)	TN (%)	SST (°C)	Alkenone concentration (ng/g)	Corg (%)	C/N	SiO ₂ (wt%)
848	12319.37	8.40	0.380	20.70	6080.20	3.410	0.17	
853	12409.00	8.51	0.350	19.91	5729.20			
858	12550.27	8.01	0.433	21.45	5986.45	3.460	0.17	
863	12691.53	7.46	0.437	20.76	4957.94			24.29
868	12832.80	8.06	0.370	19.91	4219.28	4.360	0.21	
873	12974.06	7.93	0.350	19.61	3529.52			
878	13115.33	7.79	0.375	19.97	4279.77	3.410	0.17	
883	13256.59	7.39	0.325	18.85	4801.81			18.03
888	13397.86	7.51	0.315	19.82	4541.99	3.240	0.17	
893	13539.13	8.10	0.397	20.97	6274.18			
898	13680.39	7.73	0.353	20.97	5317.17	3.930	0.19	
903	13821.66	7.12	0.311	20.88	5503.13			18.58
908	13962.92	8.24	0.370	21.48	6028.72	3.130	0.15	
913	14104.19	8.14	0.360	21.30	5394.74			
918	14245.45	7.88	0.334	21.64	5049.31	3.510	0.16	
923	14386.72	9.25	0.359	22.09	7308.33			16.34
928	14527.98	8.86	0.421	22.24	5570.49	3.610	0.16	
933	14669.25	9.41	0.353	22.21	5925.27			
938	14810.52	9.18	0.420	22.33	6058.91	3.470	0.16	
943	14951.78	9.26	0.440	22.21	7118.88			12.02
948	15093.05	8.63	0.350	22.15	5654.20	4.370	0.20	
953	15234.31			22.06	6374.83			
958	15375.58	8.98	0.320	21.85	5696.92	3.295		
963	15516.84	8.98	0.330	22.06	5901.53			22.05
968	15658.11	9.26	0.290	21.85	5651.34	3.160	0.14	
973	15799.38	8.78	0.300	21.94	6815.59			
978	15940.64	8.73	0.300	20.94	6554.95	2.900	0.13	
983	16081.91	8.40	0.265	20.55	7140.67			19.96
988	16223.17	9.35	0.245	21.55	4970.30	2.640	0.13	
998	16505.70	9.23	0.264	21.88	4214.27			
1003	16646.97	9.94	0.262	21.76	3756.96	2.410	0.11	26.28
1008	16788.23	10.38	0.273	21.52	4666.67	2.525	0.12	
1013	16929.50	9.60	0.286	21.09	4801.38			
1018	17069.67	8.59	0.360	21.00	5161.88	2.820	0.13	
1023	17209.83	8.82	0.330	20.88	5360.13			19.85
1028	17350.00	7.58	0.350	21.03	4725.85	3.150	0.15	
1033		7.25	0.324	20.61	4007.77			
1038	37817.50	5.33	0.310	21.18	3219.63	3.200	0.16	
1043	38703.60	5.94	0.309	20.36	8516.90			40.28
1048	39589.70	5.65	0.273	20.36	5478.48	3.360	0.17	
1053	40475.80	6.29	0.310	19.12	9556.62			
1058	41361.90	5.80	0.360	20.48	9176.33	3.480	0.18	
1063	42248.00	4.42	0.263	20.42	5499.53			26.96
1068	42379.19	4.98	0.320	19.58	5956.91	2.970	0.15	
1073	42510.38	5.24	0.330	20.18	6652.35			
1078	42641.56	5.20	0.330	20.21	6962.88	3.650	0.18	
1083	42772.75	5.53	0.300	20.06	5185.54			37.33
1088	42903.94	6.63	0.431	21.15	11125.50	3.180	0.16	
1093	43035.13	6.34	0.400	21.00	13884.93			
1098	43166.31	6.28	0.380	21.09	8510.95	4.460	0.21	
1103	43297.50	5.43	0.330	20.70	6369.57			31.49
1108	43325.20	5.75	0.380	20.88	10481.71	3.565	0.17	
1113	43352.90	5.70	0.340	20.73	6506.59			
1118	43380.60	5.36	0.340	20.64	6587.99	3.620	0.17	
1123	43408.30	5.48	0.320	21.27	6133.48			28.68

M772-003-2

Depth (cm)	Age (yrs)	$\delta^{15}\text{N}$ (‰)	TN (%)	SST (°C)	Alkenone concentration (ng/g)	Corg (%)	C/N	SiO ₂ (wt%)
1128	43436.00	6.15	0.290	20.85	6512.07	3.330	0.16	
1133	43463.70	7.69	0.233	20.15	4448.14			
1138	43491.40	6.14	0.290	19.91	5281.86	2.300	0.11	
1143	43519.10	6.43	0.310	19.88	5358.84			35.37
1148	43546.80	5.28	0.228	20.45	4244.79	3.210	0.16	
1153	43574.50	5.65	0.280	20.73	5395.63			
1158	43602.20	5.90	0.250	21.36	6051.70	2.960	0.14	
1163	43629.90	5.92	0.300	21.24	6970.39			34.12
1168	43657.60	5.27	0.380	21.39	10259.90	3.400	0.16	
1173	43685.30	5.67	0.251	22.15	8442.13			
1178	43713.00	6.09	0.300	21.61	7888.42	2.860	0.13	
1183	43740.70	6.15	0.320	21.91	9021.56			34.77
1188	43768.40	6.43	0.290	21.21	5927.03	3.580	0.16	
1193	43796.10	6.61	0.330	21.33	8242.04			
1198	43823.80	6.93	0.370	21.88	11699.67	3.710	0.17	
1203	43851.50	5.89	0.290	21.06	6899.47			42.48
1208	43879.20	6.23	0.320	21.09	7220.28	3.155	0.15	
1213	43906.90	5.95	0.400	22.03	9113.52			
1218	43934.60	6.26	0.370	21.48	8421.45	4.470	0.20	
1223	43962.30	6.49	0.300	21.03	7138.78			31.00
1228	43990.00	6.40	0.350	21.12	9784.34	3.310	0.16	
1233	44017.70	7.02	0.345	22.00	8270.75			
1238	44045.40	6.86	0.400	22.15	12264.25	3.950	0.18	
1243	44073.10	6.92	0.320	21.12	6994.56			42.05
1248	44100.80	7.85	0.267	22.36	8272.09	3.540	0.17	
1253	44128.50	7.02	0.350	22.06	10643.55			
1258	44156.20	7.60	0.280	21.55	5934.45	3.825	0.17	
1263	44183.90	7.04	0.290	21.00	4286.51			38.71
1268	44211.60	6.23	0.310	21.00	4622.60	3.020	0.14	
1273	44239.30	6.22	0.300	21.00	4476.37			
1278	44267.00	5.75	0.280	21.06	5998.06	3.310	0.16	
1283	44294.70	6.38	0.310	20.36	6487.02			36.92
1288	44322.40	6.01	0.390	20.67	8736.72	3.320	0.16	
1293	44350.10	6.11	0.360	21.61	8042.63			
1298	44377.80	7.04	0.480	22.15	10751.76	4.030	0.19	
1303	44405.50	6.12	0.410	22.00	6602.77			34.44
1308	44433.20	6.23	0.330	21.67	7985.19	4.505	0.20	
1313	44460.90	7.47	0.251	21.00	2108.41			
1318	44488.60	6.41	0.270	20.24	3164.31	2.730	0.13	
1323	44516.30	6.35	0.310	19.21	5004.29			26.62
1328	44544.00	6.51	0.403	21.70	8525.69	3.390	0.18	
1333	44571.70	5.78	0.312	22.12	6241.30			
1338	44599.40	5.53	0.448	22.36	8540.92	3.400	0.15	
1343	44627.10	6.96	0.360	21.33	6569.32			40.88
1348	44654.80	6.73	0.350	21.09	7577.19	4.050	0.19	
1353	44682.50	7.86	0.290	21.45	7865.55			
1358	44710.20	5.74	0.280	20.73	7570.30	3.230	0.15	
1363	44737.90	5.99	0.270	19.42	7918.11			28.42
1368	44765.60	5.93	0.270	18.79	8978.73	3.040	0.16	
1373	44793.30	6.31	0.290	20.03	6557.49			
1378	44821.00	6.20	0.280	19.03	11069.00	3.200	0.16	
1383	44848.70	6.03	0.290	19.21	10854.45			31.76
1388	44876.40	7.67	0.310	21.09	6690.65	3.360	0.17	
1393	44904.10	7.76	0.330	20.94	7554.10			
1398	44931.80	8.90	0.340	21.45	6977.61	3.550	0.17	

M772-003-2

Depth (cm)	Age (yrs)	$\delta^{15}\text{N}$ (‰)	TN (%)	SST (°C)	Alkenone concentration (ng/g)	Corg (%)	C/N	SiO₂ (wt%)
1403	44959.50	5.82	0.330	21.06	8763.33			33.05
1408	44987.20	5.97	0.400	18.91	11543.20	3.600	0.17	
1413	45014.90	5.83	0.450	21.24	8744.23			
1418	45042.60	5.92	0.330	21.79	7371.83	4.750	0.22	
1423	45070.30	5.37	0.310	22.00	5778.58			30.01
1428	45098.00	6.26	0.330	21.82	6084.46	3.220	0.15	
1433	45125.70	5.94	0.272	19.03	4404.92			
1438	45153.40	8.32	0.320	20.00	6675.26	3.080	0.16	
1443	45181.10	5.80	0.310	20.73	8386.74			36.29
1448	45208.80	5.51	0.320	20.70	7036.05	3.490	0.17	
1453	45236.50	5.32	0.417	21.36	11687.12			
1458	45264.20	6.09	0.370	19.36	6145.89	4.800	0.22	
1463	45291.90	6.70	0.360	21.36	9529.40			31.85
1468	45319.60	5.83	0.350	20.70	7358.90	3.950	0.18	
1473	45347.30	7.30	0.291	20.36	6508.97			
1478	45375.00	5.44	0.349	20.33	7627.68			
1483	45402.70	4.72	0.323	21.18	8177.80			33.27
1488	45430.40	4.72	0.383	20.85	8857.86			